UNIVERSITY OF OKLAHOMA

GRADUATE COLLEGE

THREE-DIMENSIONAL MODELING OF HYDRAULIC AND NATURAL FRACTURE INTERACTIONS AND ITS APPLICATIONS IN RESERVOIR STIMULATION

A DISSERTATION

SUBMITTED TO THE GRADUATE FACULTY

in partial fulfillment of the requirements for the

Degree of

DOCTOR OF PHILOSOPHY

By

AMIRHOSSEIN KAMALI
Norman, Oklahoma
2020

THREE-DIMENSIONAL MODELING OF HYDRAULIC AND NATURAL FRACTURE INTERACTIONS AND ITS APPLICATIONS IN RESERVOIR STIMULATION

A DISSERTATION APPROVED FOR THE
MEWBOURNE SCHOOL OF PETROLEUM AND GEOLOGICAL ENGINEERING

BY THE COMMITTEE CONSISTING OF

Dr. Ahmad Ghassemi, Chair

Dr. Gerald Miller

Dr. Jean-Claude Roegiers

Dr. Mashhad Fahs

Dr. Catalin Teodoriu

Dedication

To my mother and sister for their endless support.

Acknowledgements

I wish to express my deepest gratitude to my adviser and chair of committee, Dr. Ahmad Ghassemi, for his continuous support and guidance throughout my doctorate program. I had the opportunity to learn about different aspects of geomechanics through involvement in many practical projects under his supervision. His expertise in the field of geomechanics and coupled processes had a huge impact on the outcome of this study.

I would also like to thank my committee members, Dr. Roegiers, Dr. Miller, Dr. Fahes and Dr. Teodoriu for their comments and suggestions along the way which helped improve my dissertation.

Last but certainly not least, many thanks to my friends and colleagues in the reservoir geomechanics and seismicity research group at the University of Oklahoma for making this long journey a pleasant experience.

Table of Contents

List of Figures

Chapter 1

Chapter 2

Chapter 3

Chapter 4

Chapter 5

Abstract

The ultralow permeability of the unconventional and geothermal reservoirs can be increased for economic production by hydraulic fracturing. Natural fractures and other discontinuities are inseparable elements of unconventional reservoir rock masses. During stimulation, hydraulic fractures often interact with the natural fractures to form a fracture network which communicates with the rock matrix. This study is an effort to develop numerical models for simulation of these interactions and cast light on the mechanisms involved in the stimulation of naturally-fractured reservoir.

State-of-the-art simulators are developed to investigate the different aspects of stimulation in naturally-fractured rocks. The models include a 2D elastic model that couples rock deformation and fluid flow, a 2D fully-coupled poroelastic model, and an integrated 3D HF-NF model with pressure dependent leak-off. Rock deformation and stresses are modeled using two- and three-dimensional displacement discontinuity (DD) method. Contact elements are used to represent the closed natural fractures along with the Mohr-Coulomb criterion to determine the contact status of the fractures. Fracture propagation is modeled using a mixed-mode propagation scheme. A novel fracture coalescence scheme is integrated in the 3D HF-NF model to investigate intersection problems for a wide range of NF dip angles and strikes.

The simulation results indicate that propagation from critically-stressed and favorably-oriented natural fractures significantly contributes to the stimulation of enhanced geothermal systems (EGS). Wing-crack propagation which starts at injection pressures below the minimum horizontal stress and continues at pressures slightly above the

minimum stress may lead to the generation of NF networks in *en echelon* pattern. The analyses regarding the stress conditions revealed that wing-cracks are likely to form when the confining stress is not significantly high. Conditions that lead to higher leakoff and development of back-stress such as high rock permeability, low reservoir pressure, and low injection rates were found to limit the propagation of wing-cracks. The simulation results indicate that hydraulic fractures experience pressure drop upon intersection with permeable natural fractures. The pressure drop is followed by an increase in the injection pressure as the hydraulic fracture pressurizes the natural fracture. Moreover, the results show that the HF may propagate in other directions away from the NF when it is partially arrested by the natural fractures. Simultaneous interaction with multiple NFs and/or stress barriers was found to result in complex HF geometries with non-uniform fracture aperture distributions that could, in turn, affect proppant placement. The simulation results indicate that the increase in the injection pressure that follows a period of pressure drop in the EGS field experiments is likely caused by fracture containment near natural fractures and stress barriers.

The DFIT results revealed that the interaction between the hydraulic and natural fractures impact the pressure transient behavior. Our results show that the closure of natural fractures which often precedes that of the HF could result in a signature similar to that of the system stiffness/compliance. The simulation result indicate that the multiple closure humps that is observed in some filed data such as one in the FORGE EGS site can be explained by the closure of a HF-NF system.

Chapter 1

Introduction

1. 1. Overview

Rock mechanics, as a distinct discipline, has come to be recognized only since the 50's. This was mostly motivated by the significant growth in the complex engineering activities involving rocks such as those in civil, and mining. The interdisciplinary subject of rock mechanics concerns the response of rock masses to different loading conditions and finds application in geology, geophysics, geotechnics, civil, transportation, petroleum, and mining engineering. Applications of geomechanics have constantly grown in the oil and gas industry due to the more challenging reservoirs. The advent of hydraulic fracturing was a turning point in the application of geomechanics in petroleum engineering.

Hydraulic fracturing has been extensively studied in the past few decades using analytical, experimental, and numerical approaches. Our understanding of this complex multi-physics coupled process has increased over the years owing to the research, field implementation, and feedback from the real life field examples. Historically, hydraulic fracturing has been viewed as a tensile-dominated fracture with symmetric planar wings contained within the payzone. In fact, this is reflected in the famous fracturing models namely, PKN, and KGD (see Fig. 1. 1). Until recently, the vast majority of the fracture designs relied on these widely-used models. While being easy to implement, KGD and PKN models compromise many factors such as: nonplanar fracture propagation, interaction between hydraulic

fractures (fracture-to-fracture stress shadowing), and interaction with pre-existing fractures.

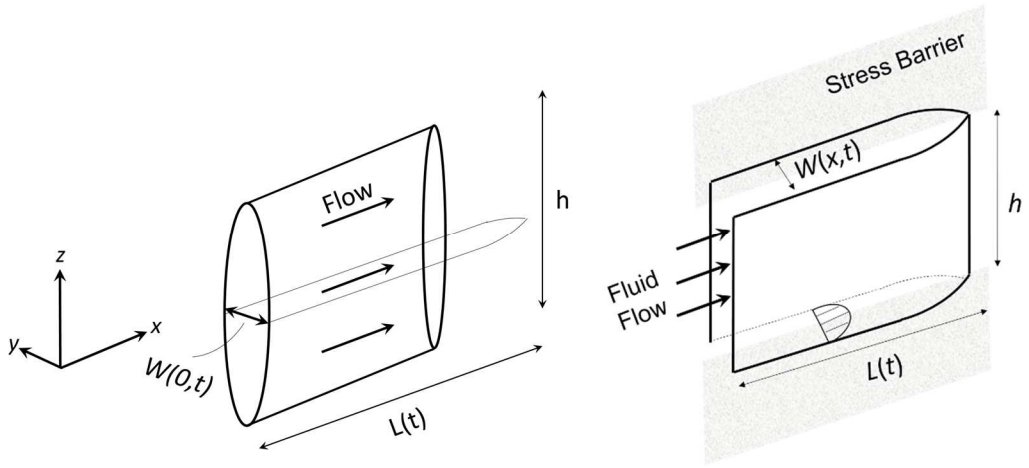

Fig. 1. 1. (Left) PKN fracture model, (Right) KGD fracture geometry.

The development of naturally-fractured and unconventional reservoirs drew attention towards the role of natural fractures in the stimulation and production from such reservoirs. Mechanical and hydraulic interaction between the induced fractures, pre-existing natural fractures, and the reservoir rock matrix are some governing factors that determine the success of a stimulation design. Failure to incorporate the effect of natural fractures in the stimulation design could have drastic consequences such as ineffective clusters, screenouts, severe fluid loss, and overestimation of effective propped area, all of which results in economic losses.

In addition to the oil and gas industry, the geothermal energy sector also relies on fracture network creation via activating pre-existing natural fractures. Currently, engineered geothermal systems strive to maximize heat extraction by increasing the contact area between the injected water and the hot reservoir rocks. To achieve this goal, the impact of

natural fractures on the stimulation mechanisms should be closely examined. Conceptual models should be revisited to integrate natural fractures and their responses to the injection/production process. These responses include: shear slip, tensile opening, propagation, coalescence with other fractures, and closure. Some of these phenomena are likely to occur simultaneously resulting in complex natural fracture behaviors.

1. 2. Motivations and Objectives

Improving current stimulation designs is tied to a better understanding of the interaction between the induced and natural fractures. Whether a naturally-fractured hydrocarbon reservoir or a geothermal reservoir, economic energy production relies on effective communication with the pre-existing natural fractures. Permeability enhancement via shear slip is commonly accepted as the main stimulation mechanism in enhanced geothermal systems (EGS), and at times in unconventional shale reservoirs. However, the mechanisms involved appear not to be well understood and often has been limited to shear dilation. This has often been perceived to exclude the propagation in tensile and shear mode of the natural fractures that experience slip leading to the claims of discovery of new mechanisms, namely stimulation via wing crack propagation. However, natural fracture propagation in general and wing cracks in particular, are an integral part of the shear slip stimulation mechanism.

Wing-crack propagation is a well-established concept which is extensively studied in several disciplines (Bobet and Einstein, 1998a; Brace and Bombolakis, 1963; Dyskin et al., 2003; Hoek and Bieniawski, 1965; Lehner and Kachanov, 1996; Petit and Barquins, 1988). Although these works provide valuable insight into the subject of wing-crack propagation, the actual reservoir stress path under injection conditions is not represented in these works.

This has motivated us to define a framework which helps us to analyze the hydro-mechanical response of naturally-fractured reservoirs during stimulation. This is done by developing a model that integrates several processes such as rock deformation, fluid flow, propagation, and fracture coalescence into a coupled simulator, to enable:

- Studying the injection pressure profiles in problems involving natural fracture propagation in elastic rocks
- Analyzing fracture propagation trajectory under different conditions
- Examining the impact of in-situ stress and operational parameters on the stimulation mechanisms
- Determining the conditions that promote wing and shear fracture propagation as compared to those that favors stimulation via dilation

The elastic model helps shed light on the subject of wing and shear crack formation and propagation in elastic rocks during stimulation. To our knowledge, aside from the work of Min (2013), there are not any studies which discuss the role of poroelasticity in the formation of wing and shear cracks with injection into the matrix. In view of the importance of wing and shear cracks in reservoir stimulation, the elastic model is then extended to account for the role of poroelasticity in the stimulation of naturally-fractured reservoirs. While the elastic model mostly concerned direct contact with the natural fractures, the poroelastic model enabled study of problems with injection outside the natural fractures, into the rock matrix. The main objectives of developing a poroelastic model are to:

- Take a closer look at the impact of poroelasticity on the reservoir stimulation in the presence of natural fractures

- Examine the effect of matrix permeability, and pore pressure on the injection pressure profile and the fracture geometry
- Investigate the impact of pumping rate on the wing-crack propagation
- Study stimulation via activation of pre-existing natural fractures by injecting into the rock matrix

One of the questions that has attracted researchers over the years is the interaction of hydraulic and natural fractures upon their intersection. Many studies have addressed this subject given its immense role in the success of any stimulation design. Earlier studies have discussed how hydraulic fractures propagate near discontinuities such as natural fractures. Several fracture crossing criteria have been proposed ranging from simpler ones involving orthogonal intersection of hydraulic and natural fractures to more sophisticated ones for arbitrary intersection angles. Only a limited number of these studies explicitly model the propagation of hydraulic fractures after intersection. Moreover, considering the complexity in 3D modeling of HF-NF interaction, almost all of the HF-NF propagation models are either 2D or pseudo-3D. The lack of a robust 3D HF-NF simulator provided motivation to develop a 3D model with a robust crossing conditions that allows for hydraulic and natural fracture interaction before and after intersection. This integrated model is used to:

- Predict realistic pumping pressure profiles for different HF-NF intersection scenarios
- Study fracture geometry in the presence of multiple natural fractures with arbitrary shapes, dip angles, and strikes
- Investigate the response of natural fractures upon intersection with the approaching hydraulic fracture

1. 3. Dissertation Outline

The remainder of the dissertation outlies the steps taken to develop a numerical model to study reservoir stimulation in naturally-fractured elastic and poroelastic rocks. Using the knowledge and experience from the 2D models, a 3D HF-NF model is developed that is capable of capturing hydraulic fracture propagation in the presence of natural fractures. A summary of the dissertation chapters is as follows:

- In Chapter 2, the foundation is set for developing a 2D fully-coupled hydro-mechanical model to study the response of natural fractures to injection. The numerical model is based on the displacement discontinuity method (DDM) and couples rock/fracture deformation with fluid flow. This model is used to investigate the mixed-mode propagation of closed natural fractures that are subject to direct water injection. A number stimulation problem of interest in geothermal reservoirs are treated to gain a better understanding of the stimulation mechanisms in such reservoirs. This chapter is based on my journal article "Analysis of Injection-Induced Shear Slip and Fracture Propagation in Geothermal Reservoir Stimulation" that was published in *Geothermics* (Vol. 76, pp. 93-105).
- Chapter 3 discusses the steps involved in extending the elastic model to account for poroelastic effects. This chapter provides an overview of poroelasticity in the context of reservoir stimulation in naturally-fracture rocks, leading to the description of a poroelastic displacement discontinuity fracture propagation model. The elastic analyses of wing crack formation is extended further by looking at the parameters that govern the poroelastic response of the reservoir. This chapter is based on my journal article "On the Role of Poroelasticity in the Propagation Mode

of Natural Fractures in Reservoir Rocks" that was published in the journal of *Rock Mechanics and Rock Engineering*.

- In chapter 4, a 3D HF-NF model capable of capturing fracture coalescence in 3D is presented. This chapter discusses the steps taken to incorporate natural fractures into the 3D HF simulator *GeoFrac 3D*. This model uses boundary elements in its mechanical module for stress-displacement calculations and a finite element model for transport problems. The resulting 3D HF-NF model is a first-of-its-kind model which allows for coalescence of 3D fractures of arbitrary geometry with no major assumption concerning the intersection of the hydraulic and natural fractures.
- Chapter 5 is a direct application of the 3D HF-NF simulator to diagnostic fracture injection tests (DIFT). The 3D model is used to shed light on the role of natural fractures on pre- and post-shutin period pressure transients. Moreover, we examine the fracture stiffness (at times referred to as compliance) approach and how it compares to the conventional tangent method in regards to the interpretation of closure stress.

Chapter 2

Reservoir Stimulation in Naturally-Fractured Elastic Rocks

Permeability enhancement via shear slip is commonly accepted as the main stimulation mechanism. However, the mechanisms involved appear not to be well understood and often has been limited to shear dilation. Often this has been perceived to exclude the propagation in tensile and shear mode of the natural fractures that experience slip leading to the claims of discovery of new mechanisms, namely stimulation via wing crack propagation. However, natural fracture propagation in general and wing cracks in particular are an integral part of the shear slip stimulation mechanism because shear slip increases the stress-intensity at the fracture tips, potentially leading to fracture propagation. In an effort to better understand the underlying mechanisms in the geothermal reservoir stimulation process, a displacement discontinuity (DD) model is developed and used to simulate secondary crack propagation associated with natural fracture slip. The fully coupled DD-FDM model uses Mohr-Coulomb contact elements and rigorously accounts for fracture propagation based on linear-elastic fracture mechanics. The model is applied to explore the conditions conducive to shear and tensile mode fracture propagation. Natural fractures undergo shear slip due to direct and indirect water injection. Out-of-plane wing (tensile) cracks form and propagate at injection pressures below the minimum in-situ stress level and turn toward the maximum in-situ stress direction as they grow longer. It was found in our results that the injection pressure is stabilized at approximately the minimum in-situ

stress level. Secondary cracks form as Wing crack and shear cracks. The predominance of wing cracks and their lengths and propagation paths were found to be controlled by the relative value of differential and mean stresses as well as rock and natural fracture frictional properties. In deeper geothermal reservoir with relatively low differential stress conditions and/or high mean stress levels, the shear crack propagation could play a major role in fracture network formation and permeability enhancement.

2. 1. Introduction

Geothermal energy from EGS is produced by injecting cool water into deep hot rocks and extracting it at higher temperatures. Water injection may cause shearing on critically-stressed natural fractures by reducing the effective normal stress on the pre-existing fractures. Permeability enhancement through shear slip is a commonly accepted stimulation mechanism (Murphy et al., 1999; Pine and Batchelor, 1984). On the surface, this appears to exclude the formation of secondary cracks via propagation in tensile and shear modes of the natural fractures that experience slip. The misconception, has led some to even claim the discovery of a new stimulation mechanism via the formation of wing cracks (McClure and Horne, 2013). But, wing cracks are essentially an integral part of the shear slip stimulation mechanism because shear slip increases the stress-intensity at the fracture tips, potentially leading to fracture propagation. These processes have been implicitly and/or explicitly considered as instrumental in Soultz EGS stimulation (Cornet et al., 2007; Evans, 2005; Jung, 2013). This understanding motivated the development of mixed-mode fracture propagation models for geothermal reservoirs (Huang et al., 2013; Min et al., 2010). The formation of wing-cracks is particularly the case when the natural fractures are directly subjected to water injection. The possibility of natural fracture

propagation and coalescence is suggested in several studies as a viable stimulation mechanism (Huang et al., 2013; Jung, 2013; Kamali and Ghassemi, 2016a, 2016b; Min et al., 2010). An analytical treatment of this problem was provided by Jung (2013) based on field evidence while focusing exclusively on the possibility of propagation in the shear mode. Kamali and Ghassemi (2016a) have explicitly simulated the phenomenon during injection and have shown that shear slip occurs at injection pressures below the minimum in-situ stress and triggers the out-of-plane wing-cracks (Huang et al., 2013; Jung, 2013; Kamali & Ghassemi, 2016a, 2016b; Min et al., 2010). Further propagation and coalescence might be achieved by maintaining the injection at pressures slightly higher than the minimum in-situ stress.

The wing-crack propagation is a well-established concept which is extensively studied in several disciplines such as mining, civil engineering, and rock mechanics (Bobet and Einstein, 1998a; Bombolakis, 1973; Brace and Bombolakis, 1963; Dyskin et al., 2003; Hoek and Bieniawski, 1965; Horii and Nematnasser, 1986; Lehner and Kachanov, 1996; Petit and Barquins, 1988; Shen and Stephansson, 1994; Steif, 1984). These works include experimental, analytical and numerical modelling approaches to the problem of two and three-dimensional cracks under bi-axial compressive stresses. Although these works provide valuable insight into the wing-crack problem, the actual reservoir stress path under injection conditions is not represented in these works. Therefore, a displacement discontinuity model is developed and used in this work to analyze the response of the closed natural fractures to direct water injection.

2. 2. Model development

Injection into naturally-fractured reservoirs is a coupled process which involves rock and fracture deformation in addition to fluid flow. This section outlines the relevant governing equations which are required to quantify this problem. The numerical implementation and discretization of these equations are described at the end of this section.

2. 2. 1. Governing equations of elasticity

The solution of an elastic body deformation must satisfy the governing equations for a given set of stress/displacement boundary conditions. The formulation of elasticity problems relies on the stress tensor partial differential equations and strain-displacement equations. The solution is then completed through a constitutive equation relating the stresses to the strains. Assuming static equilibrium, isotropic and homogenous body, and linear elasticity, the constitutive equation is given as (Timoshenko and Goodier 1970):

$$\varepsilon_{ij} = \frac{1}{E}\left[(1+v)\sigma_{ij} - v\sigma_{kk}\delta_{ij}\right] \tag{2. 1}$$

Where ε_{ij} are the strain tensor components, σ_{ij} are the stress tensor components, E is the Young's modulus, v is the Poisson's ratio, δ_{ij} is the Dirac delta function, and σ_{kk} represents summation over normal stress components.

2. 2. 2. Numerical methodology

To model fractures, the displacement discontinuity method (DDM) used in this work. The DDM (Crouch and Starfield, 1983) which is an indirect Boundary Element Method (BEM) is proved to be a powerful tool in coupled natural fracture and fluid flow analysis (Asgian, 1988; Farmahini-Farahani and Ghassemi, 2016; Ghassemi and Tao, 2016; Safari and Ghassemi, 2015, 2016; Tao et al., 2011; Verde and Ghassemi, 2015), and simulation of

hydraulic fracturing (Ghassemi and Roegiers, 1996; Kumar and Ghassemi, 2016; Sesetty and Ghassemi, 2015; Vandamme and Curran, 1989). A two-dimensional displacement discontinuity model is therefore developed and used to calculate fracture normal and shear displacements along the natural fractures. Displacement discontinuities are defined as the difference between the displacements of the negative and the positive sides of a DD element (Crouch and Starfield, 1983) and is calculated as follows:

$$D_i = u_i(x,0_-) - u_i(x,0_+) \qquad i = x,y \qquad (2.\ 2)$$

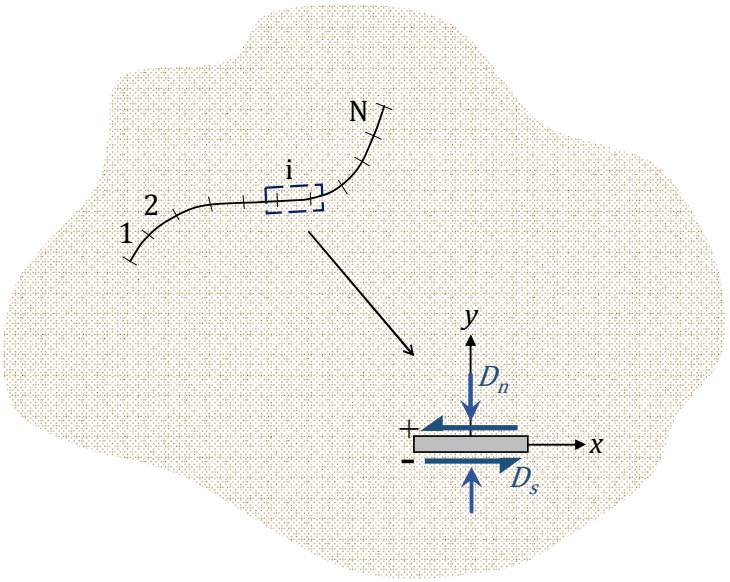

Fig. 2. 1. An elastic rock containing *N* linear crack segments. Positive values of shear and normal DD are shown on a displacement discontinuity element.

Where u_i is the displacement vector in the local coordinate of the crack element. For a rock containing *N* displacement discontinuity elements, the original DD formulation (Crouch and Starfield, 1983) is modified to account for contact elements and fluid pressure as follows:

$$\overset{i}{\sigma_n^{\infty}} + \sum_{j=1}^{N} \overset{ij}{A_{ns}} \overset{j}{D_s} + \sum_{j=1}^{N} (\overset{ij}{A_{nn}} - \delta_{ij} K_n) \overset{j}{D_n} - p_i = 0 \quad (2.3)$$

$$\overset{i}{\sigma_s^{\infty}} + \sum_{j=1}^{N} (\overset{ij}{A_{ss}} - \delta_{ij} K_s) \overset{j}{D_s} + \sum_{j=1}^{N} \overset{ij}{A_{sn}} \overset{j}{D_n} = 0 \quad (2.4)$$

Where σ_n^{∞} and σ_s^{∞} are the farfield normal and shear stresses acting on crack elements, p_i is the fluid pressure at element *i*, K_s and K_n are the shear and normal stiffness, and $\overset{ij}{A_{kl}}$ is the influence coefficient relating the normal (shear) stress of element *i* to the normal (shear) DD of element *j*. These influence coefficients reflect the mechanical interaction between the crack elements. The details of elastic kernel computation is summarized in Appendix A.

2. 2. 3. Contact elements constitutive equations

The closed natural fractures are represented by contact displacement discontinuity elements (Asgian, 1988; Tao et al., 2011). The contact elements are considered mechanically-closed as long as their effective normal stress is compressive. Despite mechanical closure, contact elements may be hydraulically open and therefore transmit the injected fluid (Safari and Ghassemi, 2015, 2016). The normal (shear) displacements of the contact elements are related to their normal (shear) stress using normal (shear) stiffness as follows (Goodman et al., 1968):

$$\sigma_n^{'} = K_n D_n \quad (2.5)$$

$$\sigma_s = K_s D_s \quad (2.6)$$

Where $\sigma_n^{'}$ is the effective normal stress, σ_s is the shear stress, K_n and K_s are the normal and shear stiffness, D_n and D_s are the normal and shear displacement discontinuities along

the crack surfaces. It should be emphasized that these equations hold only when the contact elements are mechanically-closed. The shear and normal stiffness are zero for open cracks.

2. 2. 4. Friction law and inelastic shear slip

Natural fractures are likely to experience shear slip as a result of normal stress reduction due to injection. Therefore, a proper friction law should be used to capture the full range of elastic and inelastic fracture deformation in the transverse direction. Mohr-Coulomb criterion is imposed on the contact elements to identify the state of contact in the transverse direction as follows:

$$\left|\sigma_s\right| \le c + \sigma_n^{'} \tan\phi \tag{2. 7}$$

Where c and ϕ are the natural fracture's cohesion and friction angle which differ from that of the intact rock. Two distinct modes of contact are then defined based this criterion; *stick* mode, which implies that that the contact element deforms elastically and *slip* mode, which occurs when the shear stress reaches the shear strength of a particular element. It is worth noting that the shear stiffness drops to zero for the elements in the *slip* mode. The contact elements are allowed to switch between the stick and slip mode from one time step to another. Once the contact status is identified, the boundary conditions are specified accordingly; for elements in the stick mode, the original set of coupled equations (i.e., eq. 3, 4, and 12) are used whereas for elements in the slip mode the right-hand-side of the shear DD equation (i.e., eq. 4) is modified such that it meets the Mohr-Coulomb criterion:

$$\overset{i}{\sigma_s^{\infty}} + \sum_{j=1}^{N} \overset{ij}{A_{ss}}\, \overset{j}{D_s} + \sum_{j=1}^{N} \overset{ij}{A_{sn}}\, \overset{j}{D_n} = c + \overset{i}{\sigma_n}{}' \tan\phi \tag{2. 8}$$

2. 2. 5. Fluid flow inside natural fractures

A simple and effective approach to modelling fluid flow inside fracture is by assuming flow between two smooth parallel plates separated by an aperture, *w*, (Witherspoon et al., 1980; Zimmerman and Bodvarsson, 1996). Assuming smooth variation of fracture aperture in space and time, the laminar flow of an incompressible fluid can be represented as follows:

$$q(x,t) = -\frac{w^3(x,t)h}{12\mu}\frac{dp}{dx} \tag{2. 9}$$

Where q is the volumetric flow rate, w is the local fracture aperture, h is the fracture height which can be regarded as unity for 2D fracture model (i.e., 1D fluid flow inside fracture), μ is the fluid viscosity and p is the fluid pressure. The coupled fluid flow equation can then be written for a fracture of unit height using the continuity equation as follows:

$$\frac{\partial q}{\partial x} + \frac{\partial w}{\partial t} - \frac{Q_{inj}}{2a}\delta(X_{inj}) = 0 \tag{2. 10}$$

Where Q_{inj} is the injection rate per unit thickness, a is the half-length of the injection element, and X_{inj} is the location of the injection well.

2. 2. 6. Numerical implementation

The continuity equation can be further expanded to form an equation in terms of fluid pressure. The changes of the local fracture apertures could be substituted with that of the normal opening displacement as follows:

$$\frac{\partial}{\partial x}\left(\frac{w^3(x,t)}{12\mu}\frac{dp}{dx}\right) + \frac{\partial D_n}{\partial t} + \frac{Q_{inj}}{2a}\delta(X_{inj}) = 0 \tag{2. 11}$$

An implicit finite difference scheme is then used to discretize this equation and find the fluid pressures in this coupled system. The final form of the discretized continuity equation is given as:

$$T^k_{i-1/2}p^k_{i-1} - (T^k_{i-1/2} + T^k_{i+1/2})p^k_i + T^k_{i+1/2}p^k_{i+1} + \frac{\overset{i}{D}{}^k_n - \overset{i}{D}{}^{k-1}_n}{\Delta t} + \frac{Q_{inj}}{2a}\delta(X_{inj}) = 0 \qquad (2.\ 12)$$

Where k is the time index, Δt is the time-step size, and transmissibility term, T, is defined as:

$$T^k_{i-1/2} = \frac{1}{12\mu}\frac{1}{\Delta x^2}\left(\frac{w(x_i,t_k) + w(x_{i-1},t_k)}{2}\right)^3 \qquad (2.13)$$

Where μ is the injected fluid viscosity, and Δx is the element size. In order to solve the fluid flow problem, a no-flow boundary condition is prescribed at the natural fracture tips (see Fig. 2. 2):

$$w\big|_{x=\pm\ell} = 0, \quad \frac{w^3}{12\mu}\frac{\partial p}{\partial x}\bigg|_{x=\pm\ell} = 0 \qquad (2.\ 14)$$

Where ℓ is the natural fracture length. A constant injection rate is also applied at the injection well as follows:

$$q\big|_{X_{inj}} = Q_{inj} \qquad (2.\ 15)$$

A system of $3N$ algebraic equations is formed using equations 3, 4, and 12 which could be solved for the shear and normal displacement discontinuities and fluid pressure along the natural fractures. An iterative scheme is required to find the local fracture width in each time-step during the simulation. First, guess values of fracture apertures are used to begin

the simulation at each time step. Once the fluid pressure, p, and fracture openings, D_n, are found using equations 3, 4, and 12, apertures are updated as follows:

$$\left(w_i^k\right)^{h+1} = w_i^{k-1} - \left(\Delta \overset{i}{D}_n\right)^h \tag{2. 16}$$

Where k denotes the time index and h denotes iteration index. This iterative scheme is repeated within each time step until the desired convergence is met.

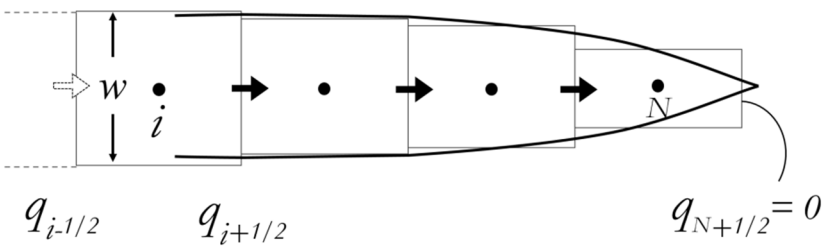

Fig. 2. 2. Fluid flow grid and flow at grid boundaries. No-Flow boundary condition is enforced at fracture tips.

2. 2. 7. Closed crack propagation criterion

A handful of crack propagation schemes have been proposed in the past few decades to capture crack propagation under different loading conditions (Bobet and Einstein, 1998b; Dobroskok et al., 2005; Erdogan and Sih, 1963; Irwin, 1957; Rao et al., 2003; Shen and Stephansson, 1994). These propagation criteria are, in the most general sense, categorized into three classes; the maximum tensile stress criterion, the minimum strain energy density, and the maximum energy release rate (G-criterion). Shen and Stephansson (1994) developed a modified G-criterion as the original criterion fails to accurately predict the propagation path for cracks under compression (Chiang, 1978; Hussain et al., 1974). The original and modified G-criterion are computationally expensive as they require several

iterations to find the propagation angle. In another effort to capture mixed-mode propagation, Dobroskok et al. (2005) developed a unified propagation scheme which is capable of switching between mode I and II during propagation. This scheme, however, does not address the coexistence of wing-cracks (tensile) and shear cracks.

Wing-Cracks propagate in mode I due to the shear slip along the pre-existing crack surfaces. In order to take into account the contribution of both mode I and II stress intensity factors, an equivalent stress intensity approach is used in this study as follows (Erdogan and Sih, 1963):

$$K_{eq} = \frac{1}{2}\cos(\frac{\theta}{2})[K_I(1+\cos(\theta)) - 3K_{II}\sin(\theta)] \tag{2.17}$$

where θ is the angle measured counter-clockwise from the tip of the crack (Fig. 2. 3), K_I and K_{II} are the mode I and II stress intensity factors, respectively which are determined directly from the normal and shear DD values as follows (Yan, 2004):

$$K_I = -\frac{E}{8(1-\nu^2)}\sqrt{\frac{2\pi}{a}}D_n \tag{2. 18}$$

$$K_{II} = -\frac{E}{8(1-\nu^2)}\sqrt{\frac{2\pi}{a}}D_s \tag{2. 19}$$

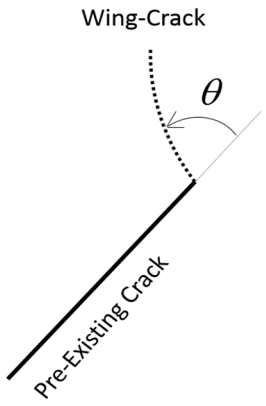

Fig. 2. 3. Wing-Crack configuration and the angle of propagation

The wing cracks start to propagate once the equivalent stress intensity factor, K_{eq}, reaches the mode I fracture toughness, K_{IC}, and the angle of propagation is determined from the following equation (Stone and Babuska, 1998):

$$\theta = \begin{cases} 0 & K_{II} = 0 \\ 2\arctan\left(\frac{1}{4}\left(\frac{K_I}{K_{II}} - \operatorname{sgn}(K_{II})\sqrt{8+\left(\frac{K_I}{K_{II}}\right)^2}\right)\right) & K_{II} \neq 0 \end{cases} \quad (2.\ 20)$$

Stress analysis is carried out at each time step before and after the wing crack propagation to find the local stresses (shear/normal) in the vicinity of the fracture tips. Local shear stresses are then compared to the shear strength obtained from the Mohr-Coulomb criterion. Shear propagation occurs once the local shear stress exceeds the shear strength at that point:

$$\sigma_s(\theta) > c' + \sigma_n(\theta)\tan\phi' \quad (2.\ 21)$$

Notice that c' and ϕ' are the cohesion and friction angle of the intact rock and differ from the natural fracture frictional parameters c and ϕ. It is worth mentioning that the shear strength varies on different planes (different θ) ahead of the kink point due to the variation of normal stress on different planes. Therefore, assigning a single critical shear strength may not serve as a proper shear propagation criterion. The stress analysis in equation 21, in fact, takes this into consideration by calculating the shear strength on each plane and comparing it with the shear stress on that plane.

2. 3. Numerical simulations of mixed-mode fracture propagation

A few numerical examples are presented to shed light on the mechanisms of natural fracture stimulation. Once a clear understanding of mixed-mode natural fracture propagation in response to fracture slip is established, the effect of in-situ stress conditions on the secondary cracks is studied by conducting several sensitivity analyses. Finally, natural fracture connectivity and coalescence is investigated by considering injection into network of *en echelon* fractures.

2. 3. 1. Natural fracture shear slip and propagation in elastic rocks

Stress perturbation caused by injection/extraction processes is known to trigger shearing on critically-stressed natural fractures with possible wing crack propagation. The problem has been treated analytically (Jung, 2013) and numerically (Min et al., 2010; Min, 2013) in the context of reservoir stimulation. It is our objective in this paper to take a closer look at the underlying mechanisms of secondary cracks formation and also show that not only wing cracks but also shear cracks can form, and further describe the reservoir conditions

that exert control on the occurrence of wing cracks. The examples pay particular attention to the case of direct contact between the NFs and the injection well.

Fig. 2. 4 shows a natural fracture subject to the in-situ minimum and maximum horizontal stresses. Water is directly injected into the fracture at a constant injection rate of Q_{inj}. Considering that the vertical extent of the natural fractures are sufficiently larger than their horizontal extent, it is assumed that plain strain condition prevails in the horizontal plane. Therefore, a 2D horizontal slice is chosen for our analyses in which fluid flow is per unit thickness of the fractures. The stress state and the corresponding displacements are monitored along the natural fracture throughout the injection. The natural fracture studied in this example is *5 m* long and is oriented 30^o from the direction of the maximum horizontal stress. Minimum and maximum horizontal stresses are 30 and 35 MPa and the initial reservoir pore pressure is assumed to be 10 MPa. Other rock and natural fracture properties that resembles that of rock samples at Desert Peak geothermal field (Lutz et al., 2010) are summarized in Table 2. 1.

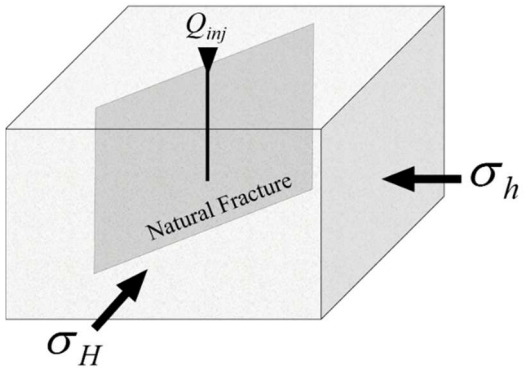

Fig. 2. 4. Natural fracture and the in-situ stress configuration

Table 2. 1. Parameters used in the base case example

Parameter	Value	Parameter	Value
Young's modulus (GPa)	30.0	Intact rock friction angle	30
Poisson's ratio	0.25	Intact rock cohesion (MPa)	20
Normal stiffness	500	Initial hydraulic aperture (mm)	0.10
Shear stiffness (GPa/m)	500	Mode I fracture toughness	2.0
NF friction angle	20	Fluid viscosity (Pa.s)	1.0×10^{-3}
NF cohesion (MPa)	0.25	Injection Rate (m^2/s)	5.0×10^{-5}
NF length (m)	5.0	Orientation with respect to $S_{h,max}$	30^o

Fig. 2. 5 shows a typical injection pressure profile for injection inside a closed natural fracture. It can be observed in this figure that the pressure increases due to the continuous injection of water inside the natural fracture at early times. The effective normal stress decreases accordingly as injection pressure increases. The shear stress remains constant at its initial value (i.e. the projection of the differential stress onto the plane of NF). The shear stress starts to decrease once the corresponding shear strength drops below the shear stress acting on the plane of the natural fracture (see Mohr-Coulomb plot in Fig. 2. 6). The sudden drop of the shear stress and transitioning into the slip mode results in a significant amount of shear slip which might trigger the wing-cracks. It can be seen in Fig. 2. 5 that the deflection point on the pressure plot coincides with the beginning of the shear stress drop. This is in fact the onset of wing-crack propagation which will be illustrated below.

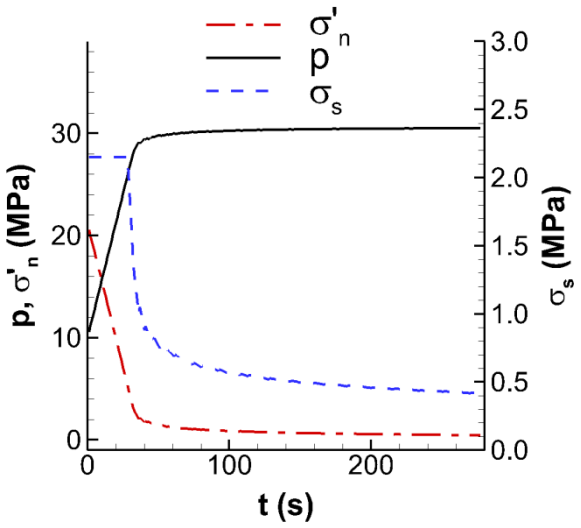

Fig. 2. 5. Variation of the normal and shear stresses and the injection pressure at the center of the fracture (injection well).

Another representation of the stress state at the center of the NF is shown in Fig. 2. 6. The Mohr-Coulomb (MC) plot Fig. 2. 6 shows that the effective normal stress decreases while the shear stress remains constant before the MC failure criterion is violated. The shear stress starts to decrease once it exceeds the MC shear strength. The natural fracture elements undergo a significant amount of shear slip at this point which may initiate the wing-cracks by inducing tensile stress at the tips (McClintock, 1962; Steif, 1984) as shown in Fig. 2. 7.

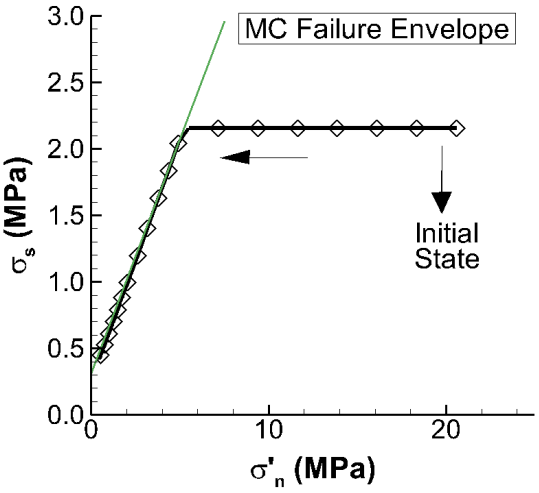

Fig. 2. 6. Stress state in the Mohr-Coulomb space at the center of the fracture.

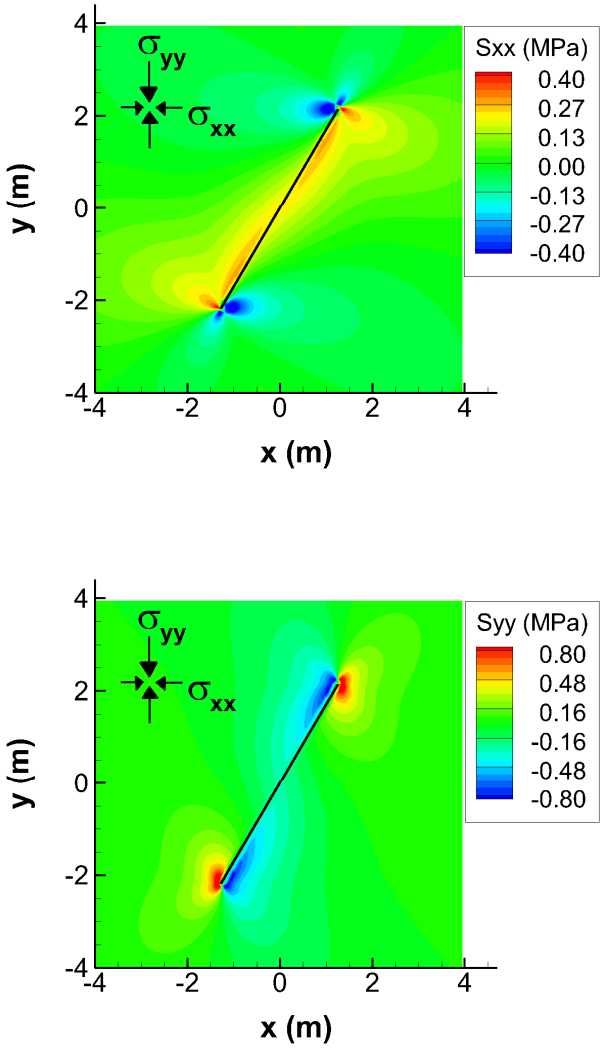

Fig. 2. 7. Induced stresses due to shear slip along the natural fracture. Both σ_{xx} (left) and σ_{yy} (right) contour plots show tensile zones (negative) in the proximity of the tips.

The changes of shear DD at the center of the natural fracture is shown in

Fig. 2. 8. Three distinctive regions may be recognized in this figure; (I) the first region in which the shear DD remains almost unchanged, (II) the second region which is marked by

a sudden rise in the shear DD, (III) and the third region in which the slope of the shear DD plot decreases. It can be observed that the onset of shear slip in

Fig. 2. 8 coincides with that of shear stress drop which is shown in Fig. 2. 5 (t_{inj} ~ 30 seconds). The interaction between the wing-cracks and the pre-existing natural fractures appears to affect the stresses and DDs on the pre-existing crack. Moreover, the injection pressure stabilizes at slightly higher than the minimum horizontal stress value as the wing-cracks propagate as shown in Fig. 2. 5. Therefore, the rate of change of shear DD decreases as wing cracks grow longer. This leads to a transition from a shear-dominated propagation regime at early stages of wing-crack propagation to a tensile-dominated regime. In other words, propagation is mostly controlled by mode I opening caused by fluid pressure rather than the shear slip on the pre-existing natural fracture at later stages.

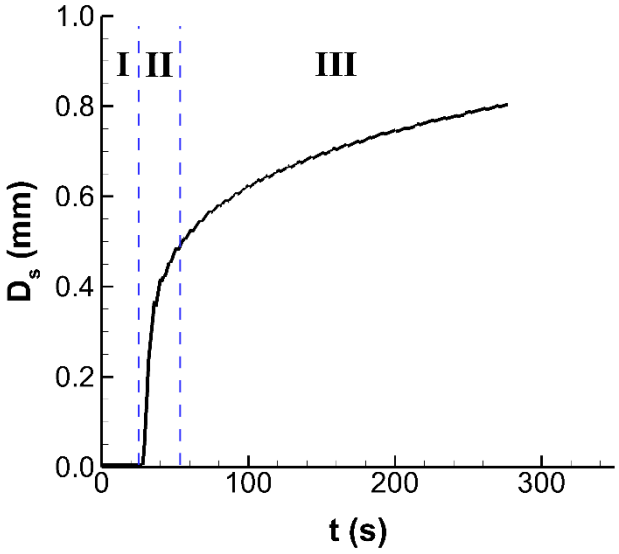

Fig. 2. 8. Evolution of shear displacement during injection at the injection well.

Wing-crack propagation and fracture aperture profile at different injection times is illustrated in Fig. 2. 9. As the effective normal stress decreases with increased injection in

the fracture, the natural fracture shear strength decreases leading to slip and inelastic shear deformation. This, in turn, triggers wing-crack propagation by inducing tensile stress at the tips of the NF. Fig. 2. 9 shows that the wing-cracks are formed at about 70^{o} from the direction of the pre-existing NF and turn toward the direction of maximum horizontal stress as they propagate. This is in accordance with the observations made in the analytical works concerning the propagation of cracks subject to compression (Ashby and Hallam, 1986; Erdogan and Sih, 1963; Lehner and Kachanov, 1996).

There are two factors contributing to the propagation of wing cracks; the first one is the shear slip along the pre-existing fracture which causes initiation and opening of the wings, and the second one is the fluid pressure inside the fracture. The first factor diminishes as wings become longer and sufficiently farther from the main crack. Therefore, the relative dominance of the fluid pressure becomes higher and the wing-cracks grow under a tensile dominated regime. It is interesting to note that the pre-existing crack may remain fully or partially closed while the wing cracks are mechanically open.

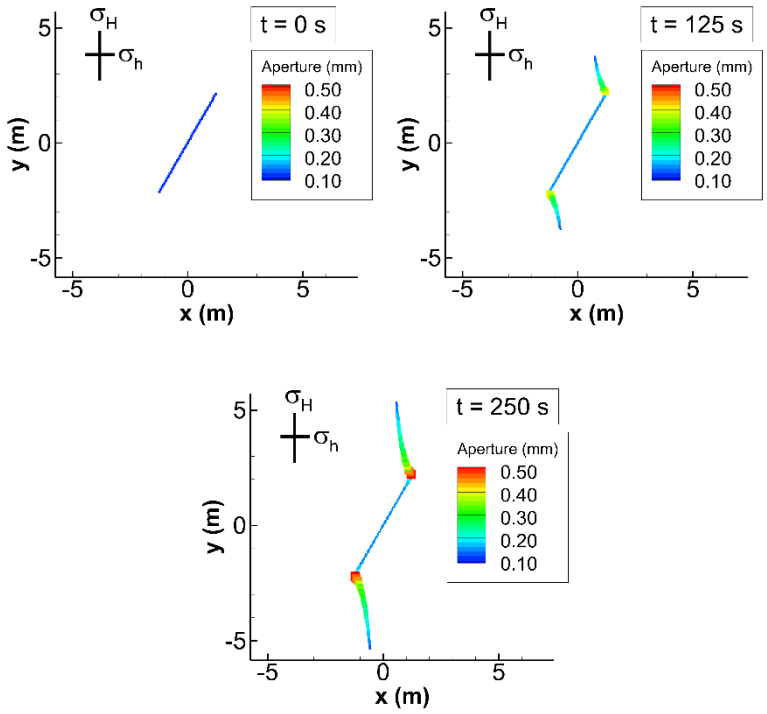

Fig. 2. 9. Wing-crack trajectory and fracture aperture profile at different injection times.

2. 3. 2. The impact of reservoir differential stress

Differential Stress is one of the most important factors contributing to the criticality and destabilization of natural fractures. The impact of the differential stress on the shear slip and propagation of natural fractures is examined in this example. A sensitivity analysis is conducted by changing the differential stress while maintaining the normal stress constant on the pre-existing NF. The stress components and their corresponding differentials stress are summarized in Table 2. 2. All other parameters are the same as the ones used in the base case example.

Table 2. 2. In-Situ stresses and NF configuration in the differential stress example

Case	σ_{xx} (MPa)	σ_{yy} (MPa)	σ_{xy} (MPa)	NF Strike	σ_n on NF (MPa)	$\Delta\sigma$ (MPa)	σ_m (MPa)*
1	31.0	32.0	0.0	N30E	31.25	1.0	31.5
2	30.0	35.0	0.0	N30E	31.25	5.0	32.5
3	29.5	36.5	0.0	N30E	31.25	7.0	33.0

* $\sigma_m = (\sigma_{xx} + \sigma_{yy})/2$

The fluid pressure is monitored at the injection well for all the cases and plotted in Fig. 2. 10. The general trend of the injection pressure profile that was observed in the base case example is preserved in this example for all three cases. It can be observed in this figure that the injection pressure stabilizes at a lower value when the differential stress is higher. It should be mentioned that the highest differential stress corresponds to *case* 3 with the lowest S_{hmin}. Moreover, the long-term pressure behavior of the wing fracture is governed by the minimum horizontal stress. Therefore, *case* 3 with the highest differential stress and the lowest minimum stress requires the least injection pressure to maintain wing propagation. While the stabilized portion of the curve is controlled by the value of the minimum horizontal stress, its deflection point is governed by the differential stress. The deflection point on the pressure plot which essentially signifies the onset of propagation, is controlled by differential stress; Propagation starts earlier and at a lower injection pressure when the differential stress is higher. A simple Mohr-Coulomb analysis reveals that at a given normal stress, a fracture under higher initial shear stress is closer to the critical (failure) point. Therefore, it requires less fluid pressure to initiate the shear slip and propagation. This is, in fact, reflected in Fig. 2. 10. It can be seen in this figure that the curve starts to flatten at a lower pressure and smaller injection time when the differential

stress is higher. So, in reservoirs having higher differential stress, shear slip and dilation as well as wing crack propagation contribute to permeability and surface area increase. The fact that higher differential stress promotes propagation at injection pressures below the minimum horizontal stress value implies that reservoir stimulation could be effectively accomplished by injecting water at reasonably low injection rates when differential is high.

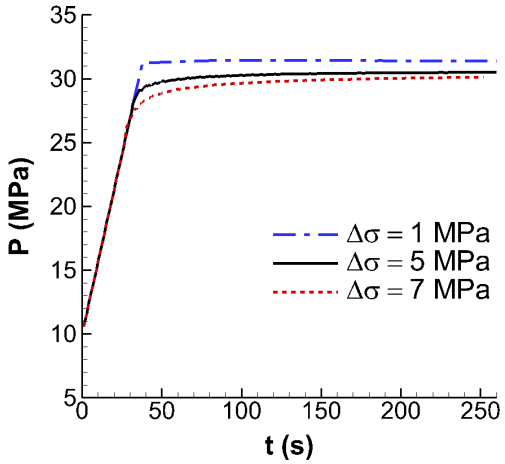

Fig. 2. 10. Injection pressure profile for different differential stress values. The smallest differential stress corresponds to the largest minimum in-situ stress.

Propagation trajectory and width profile for different differential stress values are shown in Fig. 2. 11. The propagated crack geometry is shown for only the upper half of the Natural fracture. Although the overall wing-crack geometry is similar in all cases, there are some differences in terms of the length and hydraulic apertures. It can be observed in this figure that after the same injection volume, a shorter wing-crack is achieved when the differential stress is smaller. A smaller differential stress has two major effects: a) it causes the natural fracture to be farther away from the failure envelope, and b) it provides a smaller window for the total shear slip magnitude before the natural fracture becomes mechanically-open; The first effect delays the onset of propagation and the second one limits the wing-crack

propagation by reducing the driving force on it. It is also interesting to note that the fracture aperture at the bottom of the wing-crack (i.e., the kink point) is higher at higher differential stresses. This could be simply explained by the fact that the higher shearing causes more opening at the bottom of wing-cracks.

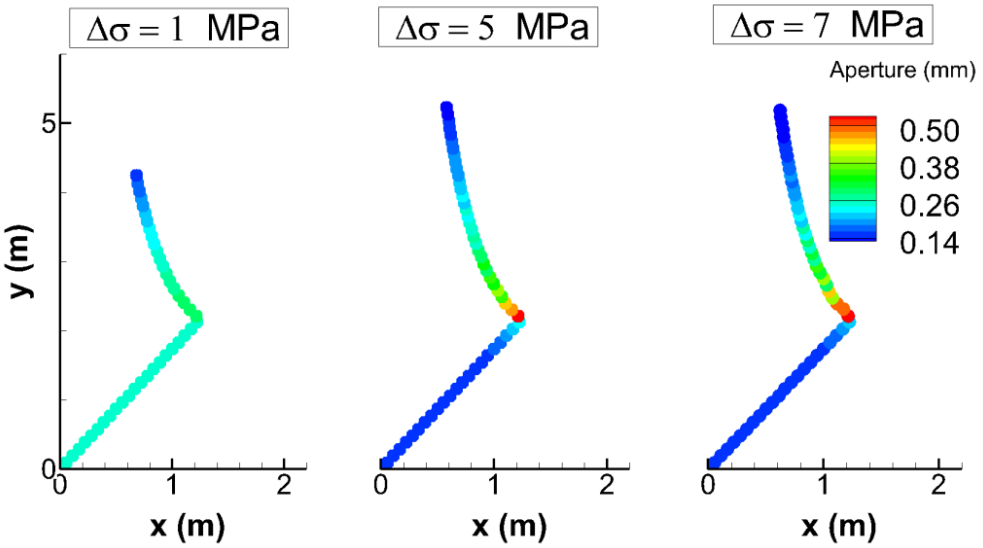

Fig. 2. 11. Propagation trajectory and width profile for different values of differential stress after 250 s of injection. The left plot corresponds to the least differential stress and the right one corresponds to the highest differential stress.

2. 3. 3. The impact of confining stress

Confining stress is known to affect the propagation of *dry* cracks under increasing axial stress (Fairhurst and Cook, 1966; Melin, 1986). The impact of confining stress on the propagation of wing-cracks due to water injection is studied in this example. This analysis is conducted by changing the confining stress (and therefore the mean stress) while maintaining the differential stress at a constant value of 5 MPa. The details of in-situ stresses are summarized in Table 2. 3.

Table 2. 3. In-Situ stresses and NF configuration in the confining stress example.

Case	σ_{xx} (MPa)	σ_{yy} (MPa)	σ_{xy} (MPa)	NF Strike	σ_n on NF (MPa)	$\Delta\sigma$ (MPa)	σ_m (MPa)
1	30.0	35.0	0.0	N30E	31.25	5.0	32.5
2	35.0	40.0	0.0	N30E	36.25	5.0	37.5
3	40.0	45.0	0.0	N30E	41.25	5.0	42.5

The injection pressure profiles for cases 1-3 are shown in Fig. 2. 12. This figure shows that the pressure required for maintaining the propagation increases as the confining stress increase. It should be noted that the confining stress (i.e., σ_{xx}) represents the minimum horizontal stress in this example. Similar to the case of hydraulic fracturing, a higher injection pressure is required to maintain fracture propagation in the presence of a higher minimum stress. Apart from the stabilized portion of the pressure vs. time profile, one can notice the change in the onset of wing crack propagation marked by the deflection points on the plot. This is explained by the fact that the higher confining in-situ stress causes more stability along the natural fracture (assuming constant differential stress).

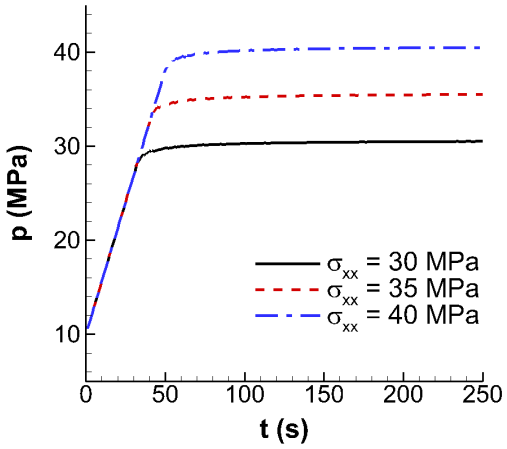

Fig. 2. 12. Injection pressure profile for different confining stresses. This figure shows that the pressure required for propagation increases when the confining stress increases.

Fracture geometry and wing-crack's length are also compared between these cases to investigate the impact of confining stress on the wing-crack propagation. The overall fracture geometry is found to be similar with differences in terms of wing-crack's length as shown in Fig. 2. 13. This figure shows that the wing-cracks become shorter when the confining stress increases. This is, in fact, in agreement with the results of dry-crack propagation due to mechanical loading. It is widely known in the classical wing-crack literature that the high confining stress has a hindering impact on the propagation. Considering the fact that the propagation of dry-cracks (as of in the classical wing-crack literature) is purely shear-driven, one can expect a different degrees of hindering of wing propagation between this case and wing-crack propagation due to mechanical loading.

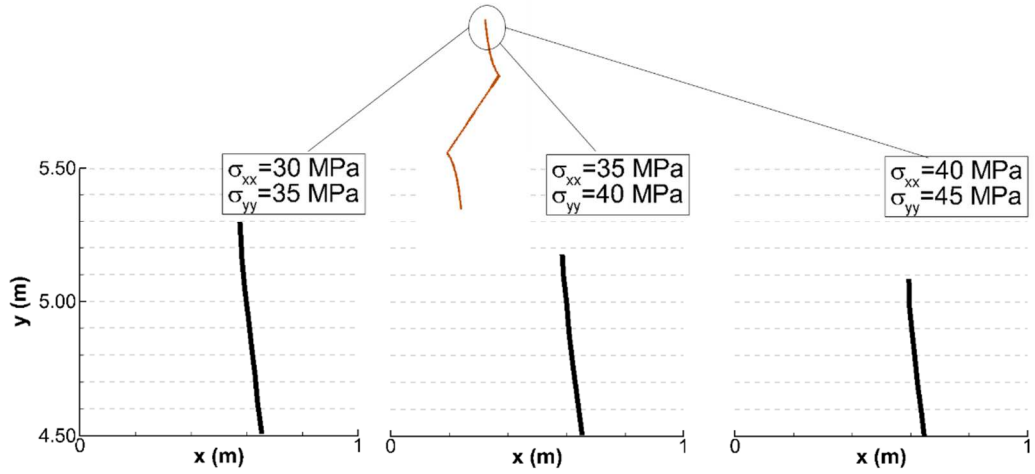

Fig. 2. 13. The difference between wing-crack's length subject to different confining stresses after 250 s of injection. Longest wings under the lowest mean stress, σ_m=32.5 MPa (left) and the shorter wings under higher mean stresses, σ_m=37.5 MPa (middle), and σ_m=42.5 MPa (right).

2. 3. 3. The impact of natural fracture's length

A wide range of natural fracture lengths is usually encountered in naturally fractured rocks. The response of natural fractures to injection could vary based on their initial length. To investigate the impact of natural fracture's length on the shear slip and propagation, a sensitivity analysis is conducted using different lengths of natural fractures. The NF's lengths used in this example are 5 and 10 *m*. The injection rate is held constant at 5.0 x 10^{-5} m^3/s and the rest of the parameters are listed in Table 2. 1.

The variation of the shear displacement due to injection is shown in Fig. 2. 14 (a). This figure shows that the onset of shear slip which is marked by the sudden rise of the shear displacement, is delayed in the case of the longer natural fracture. The higher initial volume of the longer fracture results in a slower pressure buildup given that the injection rate is the

same for both cases. Therefore, it takes a longer time for the longer natural fracture to fail in shear. Having said that, the ultimate shear slip is higher for the longer natural fracture. This could potentially lead to seismic events of higher magnitude as compared to the seismic events caused by the shorter fracture.

The pressure plot in Fig. 2. 14 (b) shows that pressure increases at a lower rate in the case of injection into a longer fracture. This is, in fact, because of the higher volume of the longer fracture leading to a slower pressure buildup. It is noteworthy that the separation of the deflection points on the pressure plot agrees with the difference in the onset of shear slip in Fig. 2. 14 (a). Although, both injection pressures stabilize at slightly higher than the minimum horizontal stress value, the pressure requirement appear to be slightly lower for the longer fracture. This could be attributed to the higher levels of shear slip along the longer natural fracture.

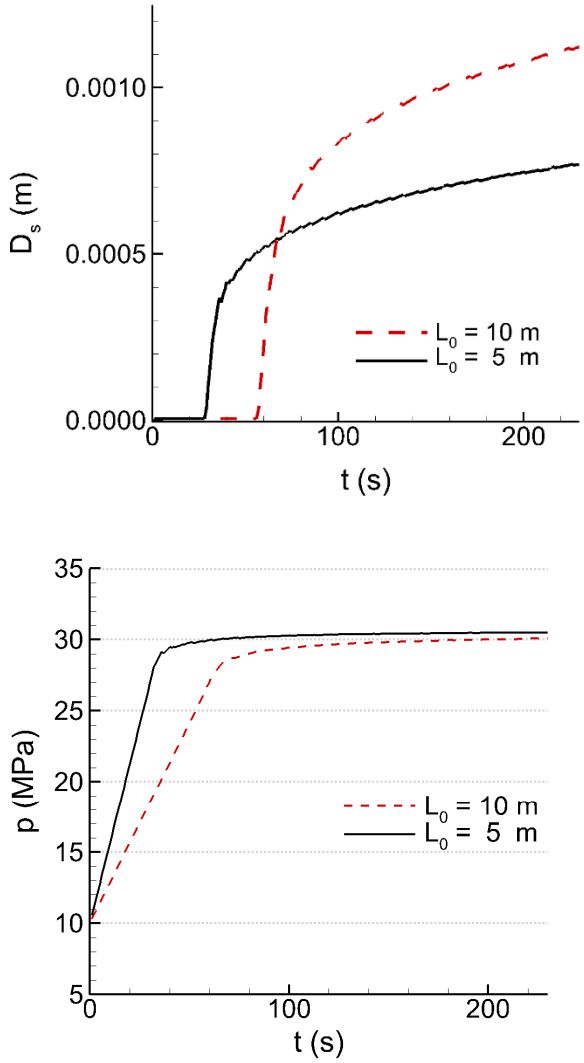

Fig. 2. 14. (a) Evolution of shear slip at the center of the natural fractures of different length. The onset of shear slip is earlier in the shorter fracture while experiencing a smaller slip at later stages. (b) Injection pressure profile for different values of natural fracture's length.

2. 3. 4. Coexistence of wing and shear cracks

Although, mode I propagation almost always prevails in brittle materials (Rao et al., 2003), there exists evidence of shear crack propagation under certain conditions that can contribute to seismicity and permeability enhancement. This example is designed to illustrate the importance of the shear strength of the intact rock and how it impacts different modes of propagation. The natural fracture used in this example is subject to a higher differential stress. A lower value of intact rock cohesion is used as compared to that of the base case example. The simulation parameters are summarized in Table 2. 4.

Table 2. 4. Simulation parameters used in the shear propagation example

Parameter	Value	Parameter	Value
Young's modulus	30.0	Intact rock friction angle	30
Poisson's ratio	0.25	Intact rock cohesion (MPa)	10
σ_{xx} (MPa)	20	Initial hydraulic aperture (mm)	0.10
σ_{yy} (MPa)	30	Mode I fracture toughness	2.0
NF friction angle	20	Fluid viscosity (Pa.s)	1.0×10^{-3}
NF cohesion (MPa)	0.25	Injection Rate (m^2/s)	5.0×10^{-5}
NF length (m)	2.0	Orientation with respect to σ_{yy}	30^o

Fig. 2. 15 shows the propagation trajectory at different injection times. It can be observed in this figure that wing-cracks are the dominant propagation mode at earlier stages ($t < 50s$). Shear propagation begins once the local shear stress at the tip of the pre-existing natural fracture exceeds the local shear strength. It is interesting to note that the shear crack extend along the direction of the pre-existing natural fracture. The slight deviation from the original crack plane is believed to be due to the influence of the wing-cracks on the local

stresses at the kink point. This example shows that Mode I and Mode II propagation are both likely to occur in response to injection and the existence of shear cracks should not be neglected in reservoir stimulation. Furthermore, Mode II propagation in a closed natural fracture is closely related to the shear strength of the intact rock. Moreover, shear propagation becomes equally as important as wing cracks in the rocks with low shear strength rock or highly fractured rock. Therefore, shear propagation is more likely to occur in rocks that have many small crack and micro-cracks. It is emphasized in (Petit and Barquins (1988)) that a dense population of defects (orders of magnitude smaller than the pre-existing NF) has to be present in order achieve mode II propagation. This is likely the case near faults zones where dense distribution of natural fractures reduces the shear strength of the rock and could possibly be the case in Soultz geothermal reservoir. Although, propagation of secondary cracks in the form of wing is hypothesized in a few studies, formation of shear cracks is generally overlooked as a plausible stimulation mechanism.

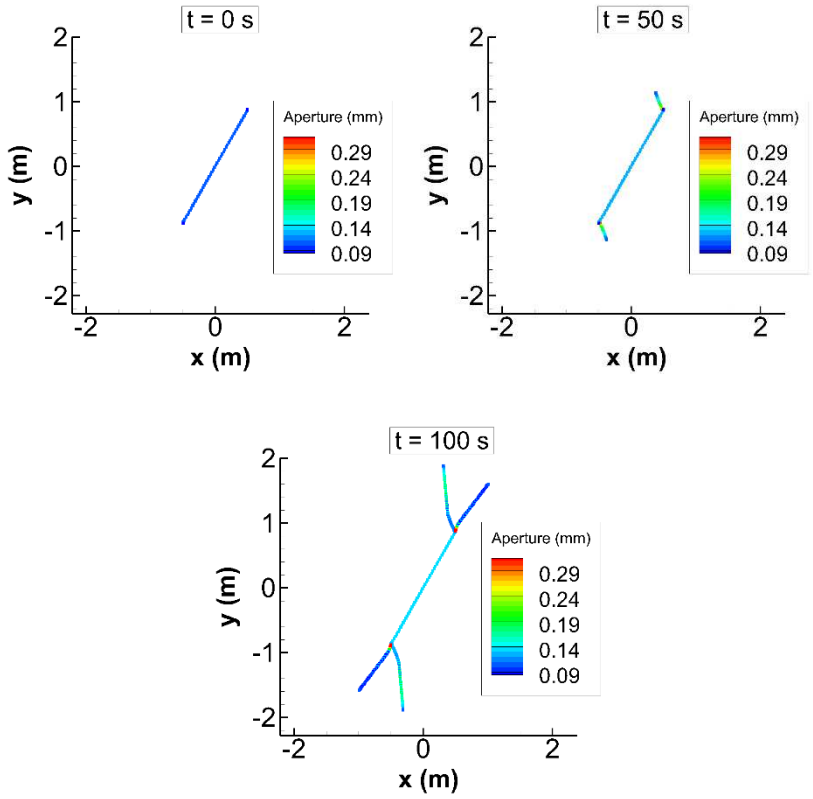

Fig. 2. 15. Propagation of wing-cracks and shear cracks from the pre-existing natural fracture.

2. 3. 5. Natural fracture coalescence

Propagation of multiple natural fractures is investigated in this example to highlight some of the key characteristics of this system. The objective of this example is to analyze the propagation, coalescence, and the final geometry of the natural fractures. The initial configuration consists of three parallel natural fractures that are vertically separated by the same distance in an *en echelon* configuration. Water is injected in the middle natural fracture and the other fractures are not in direct contact with the injection well. The details of this configuration are summarized in Table 2. 5. Other simulation parameters are similar to the ones that are used in the previous examples.

Table 2. 5. Natural fracture configuration in the multiple NF propagation example

Natural fracture length (m)	5.0
NF strike	N30E
Vertical offset [center-to-center] (m)	5.0
Horizontal offset [center-to-center]	0.0
σ_{xx} (MPa)	30.0
σ_{yy} (MPa)	35.0
σ_{xy} (MPa)	0.0
Initial pore pressure (MPa)	10.0

The propagation trajectory and the aperture profiles are shown at different injection times in Fig. 2. 16. As mentioned previous, water is injected directly into the middle natural fracture and the other natural fractures are not in direct contact with the injection well. Therefore, it is reasonable to expect wing-crack propagation from the middle fracture. The top right plot in Fig. 2. 16 shows propagation of wing-cracks from the middle fracture after 120 seconds of injection. The wing-cracks curve toward the direction of maximum horizontal stress (i.e. σ_{yy}) and therefore approaching the adjacent fractures. Natural fracture coalescence is, therefore, a likely scenario in this particular configuration. The propagation trajectory after 200 seconds of injection shows the moment before coalescence occurs. Upon intersection, water is transmitted to the neighboring fractures and reduces the effective normal stress which is acting on the top and bottom fractures. This reduction, in turn, initiates shear slip and triggers wing-cracks from the top and bottom natural fractures. The aperture profiles consistently show that the aperture is higher in the wing-crack

segments as opposed to the pre-existing natural fractures. It is worth noticing that the aperture of the wing-cracks emanating from the middle natural fracture decreases after they intersect with the neighboring fractures. This is in part because of the pressure reduction in the middle fracture upon coalescence and partly due to the shear slip along the adjacent fractures. The shear slip along the newly intersected fractures tend to reduce the aperture at the upper portions of the wing-cracks which are closer to the intersection.

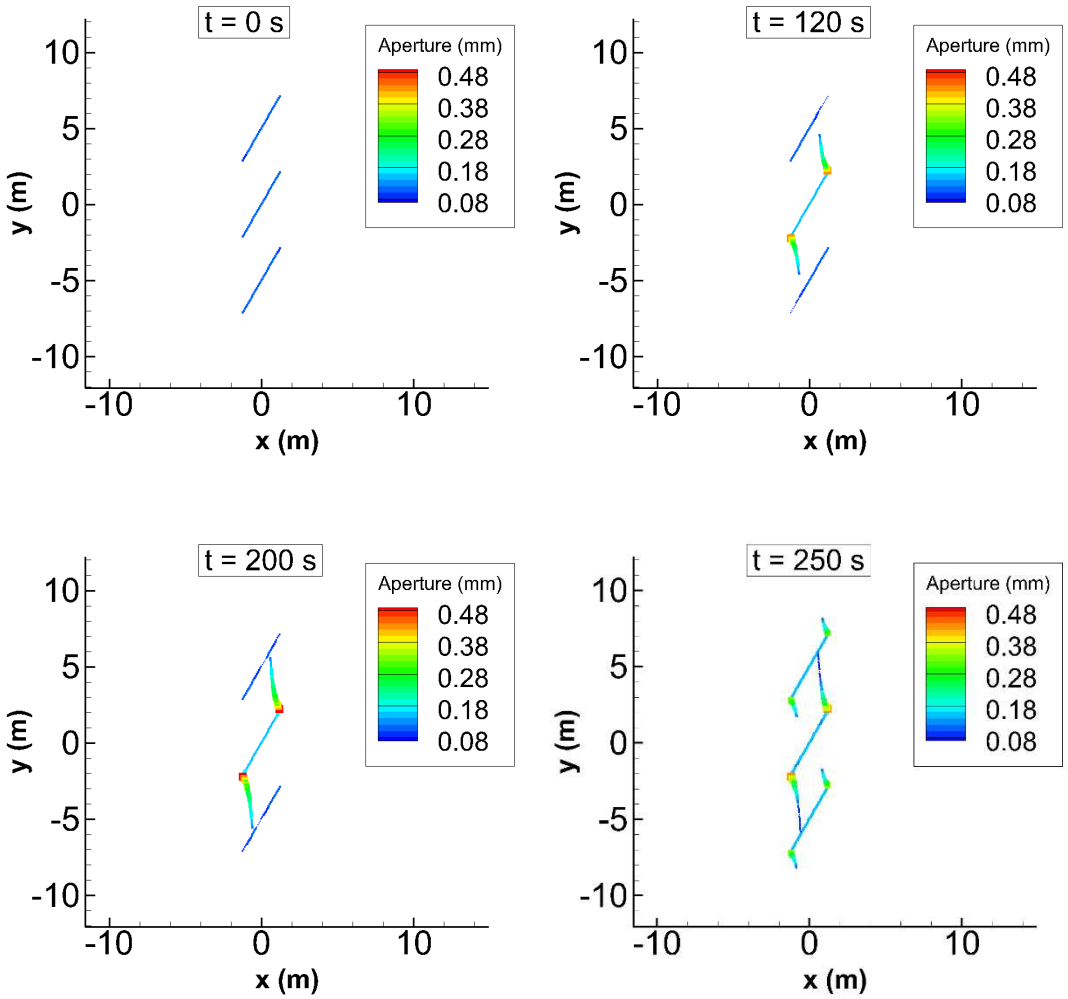

Fig. 2. 16. Natural fracture propagation and aperture profiles before and after coalescence. The initial configuration is shown at t=0 s (top left), the top right shows the central fracture propagation after 120 s of injection, the bottom left shows the moment right before coalescence and the bottom right picture shows the final configuration after 250 s.

The injection pressure profile is shown in Fig. 2. 17. The short-term behavior of the injection pressure resembles that of the previous examples; a buildup segment and stabilization at a pressure slightly above the minimum horizontal stress. It can be observed in this figure that the injection pressure drops at t=200 s which coincides with the moment of wing-crack coalescence with the adjacent fractures. The pressure, however, increases

due to continuous injection in order to maintain the propagation. This type of coalescence can be pictured on a larger scale which leads to natural fracture connectivity in a reservoir with couple of hundreds of natural fractures. Therefore, natural fracture coalescence can be regarded as a plausible stimulation mechanism in naturally-fractured rocks.

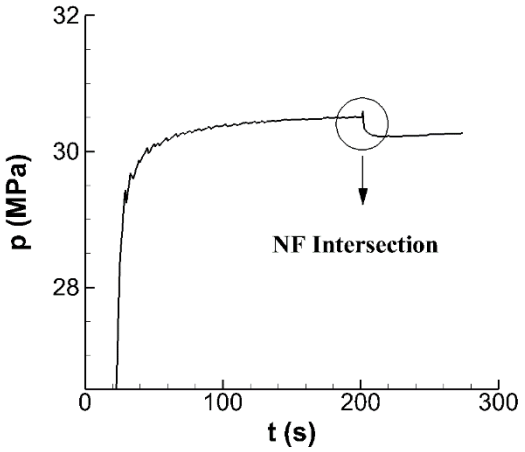

Fig. 2. 17. Pressure recorded at the injection well in the middle fracture. The moment of intersection and NF coalescence is marked by a sudden pressure drop on the plot.

The evolution of a connected fracture network is investigated using two different initial configurations. The first set contains 9 parallel natural fractures with 5 *m* of vertical spacing in an *en echelon* configuration as shown in Fig. 2. 18. All other parameters are similar to the previous examples. Water is injected in the middle fracture to initiate wing-cracks which causes subsequent intersection of wing-cracks and the neighboring fractures. It can be observed in this figure that a fully connected network is developed after 1300 seconds of injection.

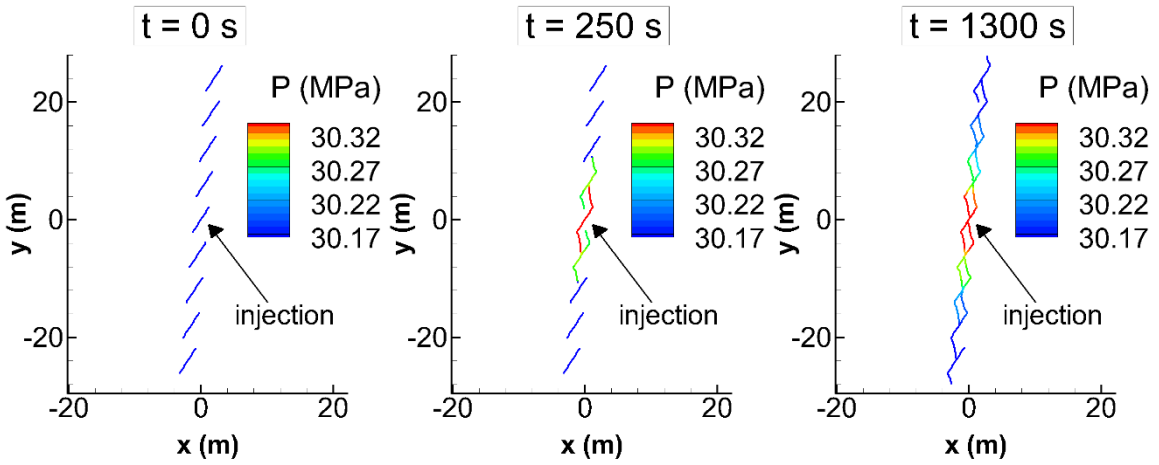

Fig. 2. 18. Evolution of a complex fracture network through natural fracture coalescence from an *en echelon* configuration. Propagation trajectory is shown at different injection times. A fully connected network is developed after 1300 s of injection.

In a different setting, natural fractures are divided into two clusters of parallel fractures. The horizontal spacing between these clusters are 10 *m* while the vertical spacing between the natural fractures in each cluster is 5 *m*. Water is injected inside the middle fractures in each cluster as shown in Fig. 2. 19. Wing-crack propagation and intersection with the adjacent fractures causes fracture coalescence in both clusters. Given the smaller number of natural fractures in each cluster, fracture connectivity is achieved earlier as compared to the previous configuration.

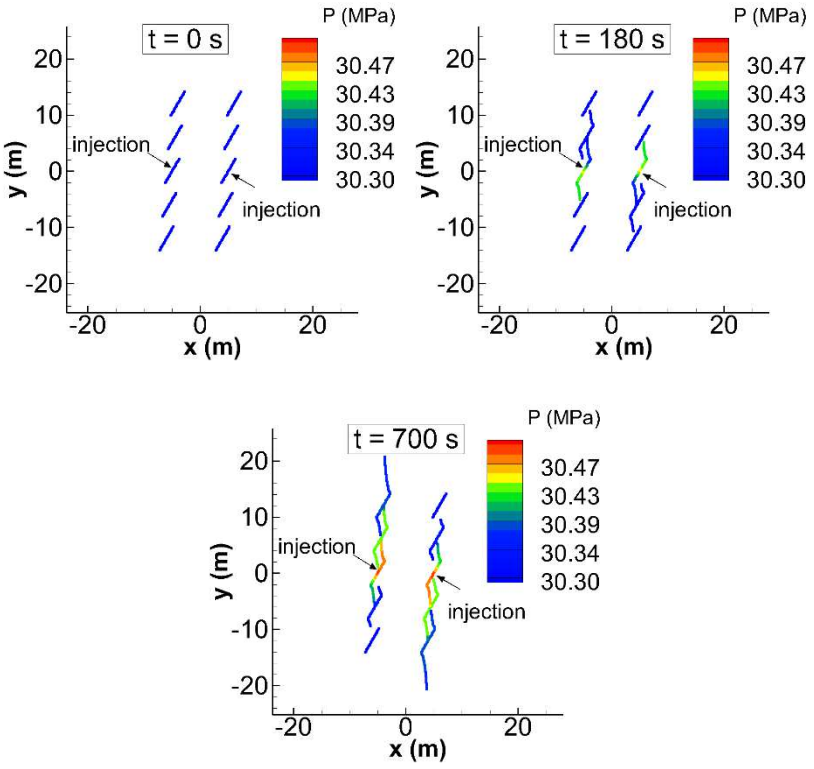

Fig. 2. 19. Natural fracture coalescence in two clusters of *en echelon* fractures. Water is injected in the middle fracture in each cluster. Fracture connectivity is achieved through wing-crack coalescence.

2. 4. Discussion

Evans et al. (2005) and Evans (2005) provided a pre- and post-stimulation assessment of an injection well in Soultz EGS highlighting the increase in the number of medium- to high-permeability natural fractures as a result of injection. The observation that not all critically-stressed fractures experienced permeability enhancement led to the conclusion that stress criticality is a necessary but not sufficient condition for shearing and permeability enhancement. Cornet et al. (2007) also investigated the shear failure of the rock mass during stimulation of Soultz EGS using detailed analysis of microseismicty and the stress state. The authors proposed two mechanisms for failure namely slip on pre-

existing weakness planes and generation and coalescence of new fracture to form a larger failure zone in conjunction with pre-existing feature. In accordance with these assessments, our simulation results indicate that the stress state in Soultz (Evans, 2005) having a differential stress exceeding 15 MPa and a mean stress in the range of 40-50 MPa could potentially lead to permeability enhancement via shear slip. Moreover, our study suggests that the propagation of secondary cracks in the form of wing and shear fractures could also be a plausible stimulation mechanism.

In a more detailed effort to better understand the stimulation mechanism in EGS systems, Jung (2013) explored the relationships between the test parameters and results in major EGS projects. Given the 2D geometry of the seismic cloud and the occurrence of seismic events at injection pressure below the minimum principal stress, Jung (2013) hypothesized that the formation of wing-cracks and their coalescence are in fact the main stimulation mechanism. A simple yet effective analytical treatment was then used to find the length of the linear wing-cracks. That formulation is, however, suitable for the prediction of wings crack's length only at injection pressures below the minimum principal stress because of singular terms. As pointed out by Jung (2013), network connectivity and wing-crack coalescence could happen at injection pressures not significantly higher than the pressure for wing-crack initiation. As illustrated in our numerical examples, natural fracture coalescence could be achieved through shear slip and propagation of secondary cracks in the tensile and shear modes. Shear propagation becomes important in reservoirs with low shear strength (or e.g., with highly fractured rock). Therefore, shear propagation is more likely to occur in rocks that have many small crack and micro-cracks and/or when the differential stress is low and the mean stress is high. It is emphasized in (Petit and Barquins

(1988)) that a dense population of defects (orders of magnitude smaller than the pre-existing NF) has to be present in order achieve mode II propagation. This is likely the case near faults zones where dense distribution of natural fractures reduces the shear strength of the rock and could possibly be the case in Soultz geothermal site. Finally, it is worth mentioning that the vertical spacing in *en echelon* networks could impact the injection pressure required to achieve coalescence. The illustrative example in Jung's hypothesis contains a closely-spaced network and therefore the injection pressure is assumed to remain below the minimum principal stress value. Natural fracture coalescence could still occur in networks with higher vertical spacing at slightly higher injection pressure as illustrated in our numerical examples.

2. 5. Conclusions

Reservoir stimulation is regarded as an integral part of any reservoir development plan in the oil and gas industry. This topic has lately gained a significant amount of attention in the engineered geothermal systems. The underlying stimulation mechanisms could be vastly different in the presence of natural fractures. In an effort to shed more light on the stimulation mechanisms in naturally fractured reservoir a numerical model is developed and used in this study.

Despite the commonly accepted hydro-shearing concept, our results indicate that wing-crack propagation is a likely scenario when there is a direct contact between the injection well and the natural fractures. Our simulation results show that the wing-crack propagation starts at pressures below the minimum horizontal stress. Once the wing-cracks are formed, the injection pressure still rises and then stabilizes slightly above the minimum horizontal stress. It was found that the wing-cracks propagate in a curvilinear manner by turning

toward the direction of maximum horizontal stress. Higher confining stresses were found to hinder the propagation. This observation is in agreement with that of the wing-crack propagation in *dry* cracks. Our results also indicate that longer wing-cracks may be achieved for the same amount of injection under higher differential stresses.

The propagation of natural fractures in a simple *en echelon* configuration revealed that, fracture coalescence could happen as a result of wing-crack intersection with the neighboring fractures. This is, in fact, regarded as a plausible stimulation mechanism in geothermal reservoir. This type of NF connectivity increases the contact area between the injected water and the rock matrix which improves the heat transfer process.

Chapter 3

Injection-Induced Natural Fracture Slip and Propagation in Poroelastic Rocks

Almost all reservoir rocks contain natural fractures. The presence of such discontinuities affects reservoir stimulation to a certain degree. The interaction between the natural and hydraulic fractures determines the overall fracture trajectory and the stimulated reservoir volume. In contrast to conventional hydraulic fracturing, natural fractures do not propagate in a tensile-dominated regime. Propagation of mechanically-closed fractures lies in the mixed-mode propagation regime which differs from that of open fractures. Therefore, the response of natural fractures to pore pressure and stress perturbations should be carefully addressed within the context of reservoir stimulation. This study aims at investigating the response of closed natural fractures to water injection in poroelastic rocks. A poroelastic displacement discontinuity (DD) model is developed and used to shed light on the propagation of closed natural fractures. Mohr-Coulomb contact elements are used in this study to identify the contact status of the elements in the transverse direction. Moreover, fracture propagation is effectively accounted for based on linear elastic fracture mechanics. Hydro-mechanical coupling is achieved by combining an implicit finite difference scheme with the poroelastic DD model. Our simulation results indicate that natural fracture shear slip and propagation is likely to occur when the closed natural fractures are subject to direct water injection. The injection pressure required to maintain the propagation in poroelastic rocks was found to be consistently higher than the pressure in its elastic counterpart. The

propagation trajectory of the *wing-cracks* was, on the other hand, found to be similar to that in elastic rocks. It was found in our results that the formation of wing-cracks and shear (secondary) cracks is an integral part of the reservoir stimulation in geothermal systems where natural fractures are in direct contact with the injection wells. This point is often overlooked or poorly treated and has led to erroneous interpretations from the reservoir stimulation standpoint.

3. 1. Introduction

The majority of unconventional oil and gas and geothermal resources occur in reservoirs that contain at least some natural fractures which needs to be considered in reservoir development activities. The fluid flow aspect of this problem is extensively studied in the reservoir engineering community with special focus on the interaction between the matrix and natural fractures (Warren and Root 1963; Gringarten 1984).

Geomechanical analyses have also been conducted on such reservoirs (Huang and Ghassemi, 2015; Huang and Ghassemi 2017; Ghassemi and Zhou 2011; Safari and Ghassemi 2015; Tao et al. 2011; Zhou and Ghassemi 2011) in order to investigate the response of natural fractures to injection and production.

In addition to normal opening and closure, natural fractures often undergo shear deformation and slip which is particularly important in reservoir stimulation. The possibility of shear slip and fracture propagation of critically-stressed natural fractures in response to pore pressure changes is addressed in the context of reservoir stimulation (Cornet et al. 2007; Evans 2005; Jung 2013; Kamali and Ghassemi 2018; Murphy et al. 1999; Pine and Batchelor 1984). Fracture mechanics studies have revealed that shear slip

induces tensile stress at fracture tip potentially leading to the formation of *wing-cracks* (Brace and Bombolakis 1963; Bobet and Einstein 1998b; Dyskin et el. 2003; Hoek and Bieniawski 1965; Horii and Nemat-Nasser 1986; Lehner and kachanov 1996; Petit and Barquins 1988).

These wing cracks tend to form at approximately 70 degrees from the tip of pre-existing closed fractures. Although *wing-cracks* are tensile cracks, they are formed due to shear slip in a mixed-mode propagation regime. Many modeling and experimental studies have been conducted to analyze wing-crack formation and propagation (Bobet and Einstein 1998a; Hoek and Bieniawski 1965). Most of these studies have been performed on dry cracks under axial loading. Uniaxial experiments with low injection pressure have also been published (AlDajani et el. 2018). Despite providing valuable insight into the mechanics of *wing-crack* propagation, these studies do not represent true in-situ stress path that is experienced in oil/gas and geothermal applications. Ye and Ghassemi (2018a, b), and Ye et al. (2018) have performed experiments to investigate wing crack formation and permeability enhancement in granite and shales under triaxial injection conditions demonstrating the impact on flow and permeability increase. In view of the importance of wing crack formation in stimulation, it has been considered in fracture network formation conceptually (Jung 2013) and numerically (Sesetty and Ghassemi 2017). The authors have shown that network complexity can be heavily impacted by wing crack formation which in turn depends on the in-situ stress contrast.

The conditions for formation of wing and shear cracks were studied by Kamali and Ghassemi (2018) in a numerical study. It was shown that in reservoirs with high confining pressure with relatively low shear strength, shear cracks dominate and wing cracks mostly

form in strong rock and high stress contrast. More importantly, wing cracks form even when the injection pressure is lower than the minimum is-situ stress (see also Zhi and Ghassemi 2018). However, to our knowledge aside from the work of Min (2013), the conditions for the formation and shear and wing cracks in poroelastic rock with injection into the matrix has not been studied. In view of the importance of wing and shear (secondary) cracks in reservoir creation, it is necessary to include pore pressure and poroelastic effects in *wing-crack* formation and propagation models to help in stimulation design and better understanding of fracture network formation and the interpretation of micro-seismicity.

For this purpose, a poroelastic displacement discontinuity model is developed and used in this study. The plain strain condition is assumed in this study which implies that the fractures have high dips and are sufficiently long in the vertical direction as compared to their horizontal extent. This assumption is valid for a wide range of problem with rectangular/semi-rectangular fracture geometries. However, the 2D plain strain condition could be violated when dealing with circular fractures. Contact elements are utilized to represent mechanically-closed fractures. Moreover, Mohr-Coulomb criterion is applied to capture shear slip along the natural fractures. An implicit finite difference scheme is used to solve the fluid flow inside natural fractures. The fluid flow and poroelastic DD models are linked through coupling terms, namely, the fluid pressure, fracture width, and the fluid leakoff (diffusion) and the model is applied to investigate the mechanics of wing crack formation due to pore pressure increase in the matrix and natural fractures.

3. 2. Governing Equations for Fracture Propagation in Poroelastic Rock

Injection/extraction in fractured rocks can potentially involve a number of diffusive and transport processes coupled with the rock and fracture deformation. In this paper, we limit our attention to the pore pressure diffusion/deformation coupling within the framework of linear poroelasticity.

3. 2. 1. Poroelasticity

The theory of poroelasticity describes the mechanical behavior of a fluid infiltrated porous medium. This theory, which is an extension of elasticity, quantifies the interaction between the pore fluid and solid deformation. Poroelasticity was first introduced by Biot (1941) and later extended by Verruijt (1969), and Rice and Cleary (1976). Given the broad scope of its concept, poroelasticity has been widely used in petroleum engineering, hydrogeology, civil engineering, soil mechanics and other disciplines. The main characteristic of the deformation in a fluid-saturated medium is its transient nature (Biot 1941). The constitutive equations relating the stress to strain and pore pressure in an isotropic and homogeneous poroelastic material are as follows (Cheng 2016; Rice and Cleary 1976):

$$\sigma_{ij} = 2G\varepsilon_{ij} + \frac{2Gv}{1-2v}\delta_{ij}\varepsilon_{kk} - \alpha\delta_{ij}p \tag{3. 1}$$

$$\zeta = \frac{\alpha(1-2v)}{2G(1+v)}\sigma_{kk} + \frac{\alpha^2(1-2v)^2(1+v_u)}{2G(1+v)(v_u-v)}p \tag{3. 2}$$

Where σ_{ij} is the total stress component, ε_{ij} is the strain tensor component, p is the pore pressure, ζ is the fluid content change per unit volume, δ_{ij} is the Kronecker delta function,

G is the rock shear modulus, v_u and v are the undrained and drained Poisson's ratio, and α is the Biot's coefficient. σ_{kk} represents the first invariant of the stress tensor.

By applying the force balance under the quasi-static condition, the equilibrium equations can be expressed as follows:

$$\frac{\partial \sigma_{xx}}{\partial x} + \frac{\partial \sigma_{yx}}{\partial y} + b_x = 0 \tag{3. 3}$$

$$\frac{\partial \sigma_{xy}}{\partial x} + \frac{\partial \sigma_{yy}}{\partial y} + b_y = 0 \tag{3. 4}$$

Where b_i denotes the body force in i direction.

3. 2. 2. Fluid flow inside fractures

Fluid flow inside natural or hydraulic fractures is a key aspect in studying the hydro-mechanical behavior of fractured rocks. Fluid pressure induces fracture deformation and is, conversely, affected by the changes of fracture aperture leading to a coupled process. Assuming the fluid is incompressible and the flow is one-dimensional along the fracture, the continuity equation can be expressed as follows (Bird et al. 1960; Economides and Nolte 2000):

$$\nabla . q = -\frac{\partial w(x,t)}{\partial t} - 2v_L + \frac{Q_{inj}}{\Delta x}\delta(x - x_{inj}) \tag{3. 5}$$

Where q is the volumetric flow rate, w is the fracture width, v_L is the leakoff velocity, Q_{inj} is the injection flow rate, and x_{inj} denotes the location of the injection well. The flow equation is subject to the following initial and boundary conditions:

$$p(x,0)=p_0 \tag{3. 6}$$

$$q\big|_{x=\pm l}=0 \tag{3. 7}$$

Where p_0 is the initial reservoir pressure, and l represents the fracture half-length. The boundary condition in Equation 5 implies that a no-flow condition is prescribed at the fracture tips. The fluid lag is not considered in this study and we assumed that the fluid front follows the fracture tip at all times (see Garagash, 2006 for more details).

An effective approach to solve the fluid flow equation is by assuming flow between two smooth parallel plates (Witherspoon et al. 1980; Zimmerman and Bodvarsson 1996). The lubrication equation can be written for the laminar flow of an incompressible fluid as follows:

$$q(x,t)=-\frac{w^3(x,t)h}{12\mu}\frac{\partial p}{\partial x} \tag{3. 8}$$

Where μ is the fluid viscosity, and h is the fracture height which could be regarded as unity for a 2D fracture model. The flow equation is then substituted in the continuity equation to form a differential equation in terms of fracture apertures and fluid pressure.

The injected fluid is partially taken by the fracture (stored volume) leading to fracture opening and/or propagation and the rest leaks into the matrix (leakoff volume). Considering that the total injected volume is equal to the fracture volume (stored) plus the cumulative leakoff volume, the global mass balance equation can be expressed as follows:

$$\int_0^t Q_{inj}(t')dt' = \int_{-L(t)}^{L(t)} w(x,t)dx + \int_{-L(t')}^{L(t')} \int_0^t 2v_L(x,t')dxdt' \quad (3.\ 9)$$

3. 2. 3. Contact Elements

Natural fractures maintain their load carrying capacity as long as their surfaces are in mechanical contact. The term *mechanically-closed* is used in this paper to differentiate closed fractures from open hydraulic fractures (see Fig. 3. *1*). This figure shows that the natural fracture may retain some finite hydraulic aperture even when it is mechanically-closed. Displacement discontinuity contact elements (Asgian 1988; Kamali and Ghassemi 2017; Kamali and Ghassemi 2018; Tao et al. 2011) are used in this study to represent the natural fractures in contact. A set of constitutive equations are used to relate the normal/shear stresses to the normal/shear displacements through normal/shear fracture stiffness (Goodman et al. 1968):

$$\Delta\sigma_n^{'} = K_n \Delta D_n \quad (3.\ 10\ )$$

$$\Delta\sigma_s = K_s \Delta D_s \quad (3.\ 11)$$

Where $\sigma_n^{'}$ is the effective normal stress acting on the contact element, σ_s is the shear stress, K_n and K_s are the normal and shear fracture stiffness, D_n and D_s are the normal and shear displacement discontinuities. It is worth mentioning that these constitutive equations hold only when the joint is in mechanical contact; transitioning into the open-fracture state causes the fracture stiffness to drop to zero.

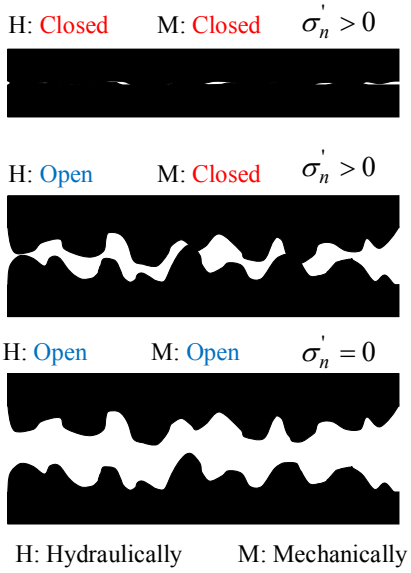

Fig. 3. 1. Mechanical and hydraulic closure of a natural fracture

3. 2. 4. Contact Status and the Friction Law

Shear slip along the natural fractures is the most prominent characteristic that differentiates closed fractures from open fractures (Goodman, 1989). Two distinct modes of contact are considered for mechanically-closed elements: *stick* mode which signifies that the element deforms elastically in the transverse direction, and *slip* mode which implies that the element has experienced inelastic deformation in the transverse direction. The state of contact is determined by the Mohr-Coulomb criterion as follows:

$$\left|\sigma_s\right| \le c' + \sigma_n' \tan\phi' \qquad (3.\ 12)$$

Where c' is the natural fracture's cohesion, and ϕ' is the natural fracture's friction angle. The right-hand-side of this inequality denotes the shear strength of the fracture. The contact element undergoes shear slip once the shear stress exceeds the shear strength of that particular element.

3. 3. Propagation Criterion

Propagation of closed natural fractures differs from that observed in hydraulic fracturing. Conventional hydraulic fracturing is a tensile-dominated process whereas closed fractures often propagate under a mixed-mode regime. Therefore, mode I and II propagation are equally important in the propagation of natural fractures. Several propagation criteria are proposed (Bobet and Einstein 1998; Dobroskok et al. 2005; Erdogan and Sih 1963; Irwin 1957; Shen and Stephansson 1994) to capture the propagation of closed fractures. These criteria fall under three main categories: the maximum tensile stress criterion, the minimum strain energy density, and the maximum energy release rate criterion (*G*-criterion). To account for the contribution of mode I and II stress intensity factors in the propagation of closed fracture, an equivalent stress intensity approach (Erdogan and Sih 1963) is utilized in this study:

$$K_{eq} = \frac{1}{2}\cos(\frac{\theta}{2})[K_I(1+\cos(\theta)) - 3K_{II}\sin(\theta)] \tag{3. 13}$$

Where K_I and K_{II} are the mode I and mode II stress intensity factors, θ is the angle of propagation measured counter-clockwise from the tip of the crack (Stone and Babuska 1998). The stress intensity factors are calculated directly from the normal and shear displacement discontinuities at the tip (Yan 2004):

$$K_I = -\frac{E}{8(1-v^2)}\sqrt{\frac{2\pi}{a}}D_n \tag{3. 14}$$

$$K_{II} = -\frac{E}{8(1-v^2)}\sqrt{\frac{2\pi}{a}}D_s \tag{3. 15}$$

Where E is the Young's modulus, v is the Poisson's ratio, and a is the element half-length. Considering the fact that *wing-cracks* are tensile by nature, crack propagation occurs once the equivalent stress intensity factor reaches the mode I fracture toughness.

It should be noted that the propagation criterion that is used in our paper is for tensile wing-cracks that are generated under a mixed-mode loading regime. Wing-cracks are naturally tensile cracks and therefore the propagation criterion should take this into account. This is why the equivalent stress intensity $K_{eq} = K_{eq}(K_I, K_{II})$ is compared against the mode I toughness ($K_{eq} = K_{IC}$). We are not excluding the shear cracks or mode II propagation. In fact, mode II propagation is checked using a stress analysis approach rather than direct use of stress intensities .The reason for adopting this approach is that once the wing-cracks are initiated, the shear cracks are no longer emanated from a classic crack tip and they are initiated from the kink-points.

3. 4. Numerical Implementation

The coupled poroelastic models often yield a set of partial different equations which should be solved for stress/displacements, fluid pressure, and pore fluid diffusion. These equations are usually not amenable to analytical treatments even for simple geometries and boundary conditions. Researchers, therefore, resort to numerical methods to solve problems involving poroelasticity. Hydraulic fracture problems in poroelastic rock are effectively treated using the DD method (Ghassemi and Roegiers 1996; Ghassemi and Tao 2016; Ghassemi and Zhang 2004; Kumar and Ghassemi 2015, 2018; Sesetty and Ghassemi 2017, 2018; Vandamme et al. 1989; Vandamme and Roegiers 1990). The displacement discontinuities quantify the separation between the negative and positive crack surfaces in the normal and transverse direction:

$$D_i = u_i(x,0_-) - u_i(x,0_+) \qquad i = x, y \qquad (3.16)$$

Where u is the displacement vector in the local coordinate of the boundary element. Fig. 3. *2* shows a discretized crack with positive normal and shear displacement discontinuities along one of its elements.

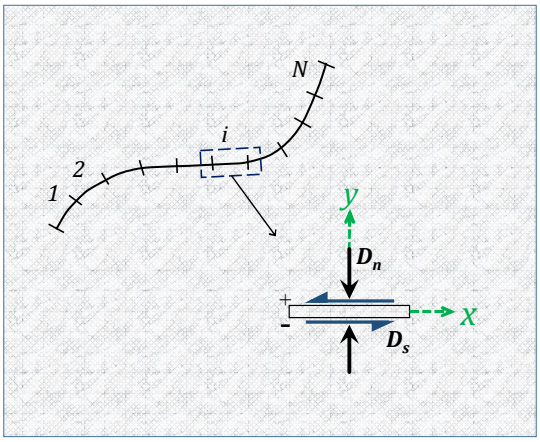

Fig. 3. 2. Normal and shear displacement discontinuities along a discretized crack

This section provides an overview to the DD numerical discretization of the coupled poroelastic model that is used in this study. The following integral equations quantify the stresses and pressure along a fracture in a poroelastic rock:

$$\sigma_{ij}(X,t) = \int_0^t \int_\Gamma \begin{bmatrix} \sigma_{ijk}^{iD}(X-\chi;t-\tau) D_k(\chi,\tau) + \\ \sigma_{ij}^{iq}(X-\chi;t-\tau) D_q(\chi,\tau) \end{bmatrix} d\Gamma(\chi) d\tau \qquad X = (x_1, x_2) \qquad (3.17)$$

$$p(X,t) = \int_0^t \int_\Gamma p^{iq}(X-\chi;t-\tau) D_q(\chi,\tau) d\Gamma(\chi) d\tau \qquad X = (x_1, x_2) \qquad (3.18)$$

Where $\sigma_{ij}(X,t)$ represents the stress tensor components at location X and time t, σ_{ijk}^{iD} and σ_{ij}^{iq} denote induced stress due to instantaneous unit point DD and fluid source at location χ and time, τ, D_k and D_q are the strength of the point DD and fluid source, and p^{iq}

represents the induced pore pressure due to an instantaneous unit point fluid source. These equations imply that a one-way poroelastic coupling is implemented in this study in which stresses are affected by both the fluid source and displacements while pore fluid diffusion is only affected by the fluid source. The temporal integration is carried out by using a time marching algorithm as shown in Fig. 3. *3*.

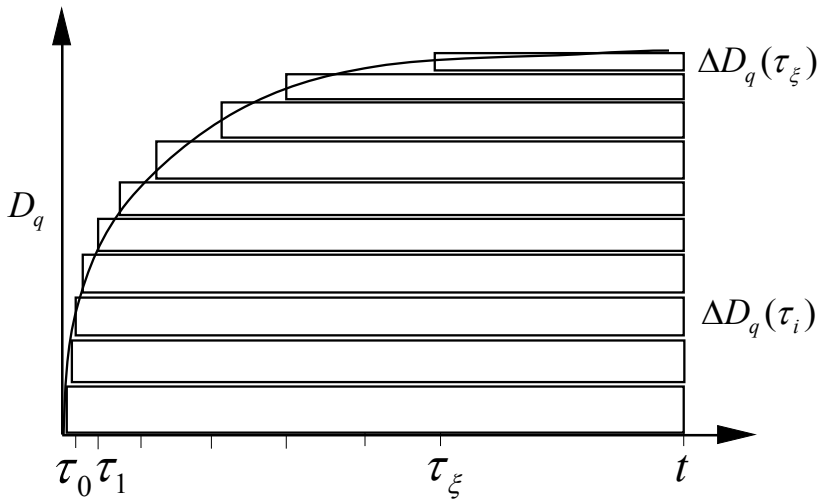

Fig. 3. 3. Time marching scheme used for temporal integration of poroelastic equations (Curan and Carvalho 1987)

The integral equations can be implemented numerically using the time marching scheme and discretizing the fracture into *M* boundary elements. The final form of the poroelastic DD equations are formed considering farfield stress components (i.e., non-equilibrium joint formulation), fluid pressure, and fracture stiffness as follows:

$$\overset{i}{\sigma}{}_s^{\infty} + \sum_{j=1}^{M} (\overset{ij}{A}_{ss} - \delta_{ij} K_s) \overset{j}{D}_s + \sum_{j=1}^{M} \overset{ij}{A}_{sn} \overset{j}{D}_n + \sum_{h=0}^{\xi} \sum_{j=1}^{M} \overset{ij}{A}_{sq} (t - \tau_h) \Delta \overset{j}{D}{}_q^h = 0 \qquad (3.\ 19)$$

$$\overset{i}{\sigma}_n^{\infty} + \sum_{j=1}^{M} \overset{ij}{A}_{ns} \overset{j}{D}_s + \sum_{j=1}^{M} (\overset{ij}{A}_{nn} - \delta_{ij} K_n) \overset{j}{D}_n + \sum_{h=0}^{\xi} \sum_{j=1}^{M} \overset{ij}{A}_{nq} (t - \tau_h) \Delta \overset{j}{D}_q^h - p_i = 0 \qquad (3.\ 20)$$

$$\sum_{h=0}^{\xi} \sum_{j=1}^{M} \overset{ij}{A}_{pq} (t - \tau_h) \Delta \overset{j}{D}_q^h = p_i - p_0 \qquad (3.\ 21)$$

Where σ_s^{∞} and σ_n^{∞} are the farfield shear and normal stresses, A_{kl} is the influence coefficient relating displacement discontinuities and fluid source to stresses and pressure, p_o is the initial pore pressure, h is the dummy time index for time marching, and p_i is the fluid pressure inside DD element i. The details of the stress kernel calculation are summarized in Appendix-A (Curran and Carvalho, 1987; Crouch and Starfield, 1983). It is worth noticing that the poroelastic DD equations could be solved for the displacement discontinuities and the fluid source intensities. The fluid pressure which appears in equations 20 and 21 is calculated from the fluid flow equation.

The fluid flow equation is discretized using an implicit finite difference scheme. Central differences is used for spatial discretization and forward differences is used for temporal discretization of the flow equation. The FDM form of the fluid flow equation is expressed as follows:

$$\sum_{j=NB_{i,1}}^{NB_{i,2}} T_{ij}^{m+1} p_j - \left(\sum_{j=NB_{i,1}}^{NB_{i,2}} T_{ij}^{m+1} \right) p_i + \frac{\overset{i}{Q}_{inj}}{\Delta x} - 2 \overset{i}{v}_L + \frac{\overset{i}{D}_n^{m+1} - \overset{i}{D}_n^{m}}{\Delta t} = 0 \qquad (3.\ 22)$$

Where m denotes the time index, T_{ij}^{m+1} is the transmissibility term evaluated at the current time step $m+1$, NB denotes the neighboring element index. This procedure is repeated until the desired tolerance is met. A no-flow boundary condition, as outlined in the model development section, is prescribed at the fracture tips in order to solve the fluid flow

equation. Considering that the transmissibility term depends on the fracture width which is not known at time step m+1, an iterative procedure is required to solve the fluid flow equation. The iterations begin with an initial guess value for the fracture width at each element, and the fracture apertures are updated after each iteration on the fluid pressure and fracture openings within a specific time step. The fracture aperture and normal displacement discontinuity are related through the following expression:

$$w^t = w^{t-1} - \Delta D_n^t \tag{3. 23}$$

Where superscript t denotes time-step number and ΔD_n shows the changes of normal displacement discontinuity. It should be noted that fracture opening is regarded negative in our DD formulation.

As an implicit scheme, numerical instability is not a concern however choosing very large time steps results in erroneous pressure/width calculations and mass balance error. Moreover, the time step size is constrained when enforcing a stress intensity criterion to capture stable fracture propagation. For problems involving direct injection into the fracture the time step size was of the order of 1-10 seconds and for the injection outside the fracture the time step ranged from seconds in the beginning to couple of minutes at the end.

Fluid leakoff appears in the diffusion equation and the fluid flow equation as a coupling term. This term which is evaluated using a 2D diffusion equation (D_q in equation 21) and gives rise to the poroelastic stress components affects the fluid flow by controlling the leakoff and stored volumes.

3. 5. Poroelastic Model Verification

A verification example is provided in this section to check the validity of the proposed poroelastic model. The response of a pressurized crack is studied and the results are compared against the analytical solution of this problem. This problem consists of a fracture of length L in an infinite poroelastic rock which is subject to an internal pressure p^*. It should be noted that the fluid pressure p^* acts as the traction boundary condition on the crack surfaces as well as the pore pressure boundary condition in the poroelastic rock. The former which is often termed as "Mode I" poroelastic loading (not to be confused with normal and shear loading terminology) causes fracture opening and the latter which is the pore pressure loading is termed as "mode II" poroelastic loading. Fig. 3. 4 shows the loading decomposition and the boundary conditions in each sub-problem. It should be noted that mode I causes fracture opening and mode II results in fracture closure over time. The combined effect leads to a transient fracture opening behavior with known early-time and late-time solutions.

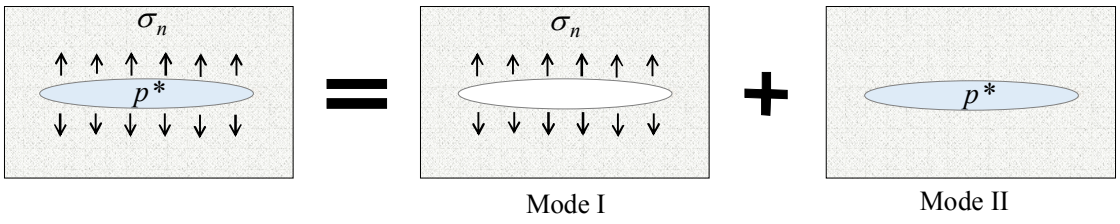

Fig. 3. 4. Load decomposition of a pressurized crack in a poroelastic rock

This problem is decomposed into two sub-problems of a pore pressure loading and a stress loading (Carter and Booker 1981; Cheng 2016; Vandamme et al., 1989) whose solutions are given by (Vandamme et al., 1989):

$$\underset{t\to 0^+}{D_n} = -\frac{4(1-v_u^2)}{E} p^* b \tag{3. 24}$$

and

$$\underset{t\to \infty}{D_n} = +\frac{4(1-v^2)}{E} \eta p^* b \tag{3. 25}$$

Where v and v_u are the drained and undrained Poisson's ratio, respectively and b is the crack's half-length and η is the poroelastic stress coefficient,

$$\eta = \frac{\alpha(1-2v)}{2(1-v)} \tag{3. 26}$$

Table 3. 6 summarizes the input parameters that are used in the verification example.

Table 3. 6. Input parameters used in the verification example

Parameter	Unit	Value
E	GPa	50.0
v_u	-	0.30
v	-	0.25
p^*	MPa	1.0
k	m^2	$1.0x10^{-17}$
α	-	0.80
b	m	0.5

Fig. 3. 5 shows the variations of crack opening at the center of the pressurized crack predicted by the model and the analytical solution of this problem at sufficiently large times. It can be seen in this figure that the pressurized crack has the highest opening during

the early stages of pressurization (negative D_n indicates opening). The crack opening then decreases due to the impact of pore fluid diffusion (i.e., mode II loading). The rate of closure and crack opening variation becomes smaller after sufficiently large times of pressurization. This figure shows that the poroelastic DD results are in a good agreement with the large-time asymptote of this problem.

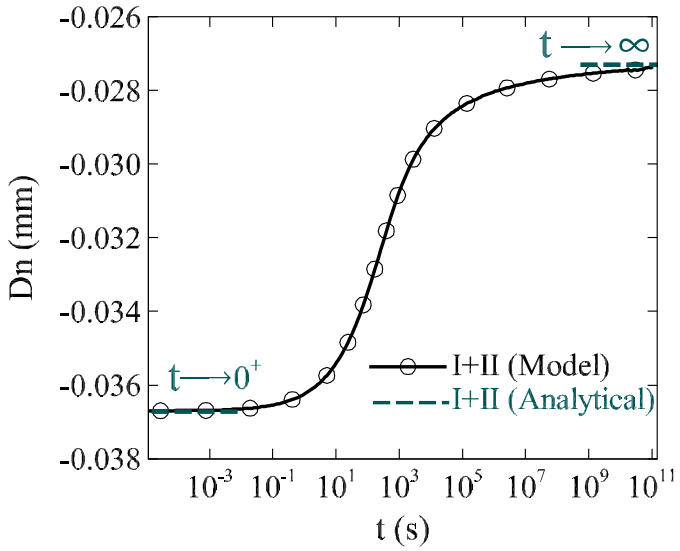

Fig. 3. 5. Variations of crack opening at the center of a pressurized crack. Comparison between the poroelastic DD model and analytical solution for mode I and II loading scenarios

3. 6. Wing Cracks in Poroelastic Rock

The poroelastic displacement discontinuity model is used in this section to analyze the response of closed natural fractures to direct and indirect (into the matrix) water injection. The numerical examples illustrate the fundamental condition for the formation and propagation of wing-cracks in poroelastic rocks including their propagation trajectory, injection pressure profile and stress path. Sensitivity analyses are conducted to investigate

the impact of rock matrix and poroelastic properties on the propagation of natural fractures. Although our attention is focused on the propagation of wing-cracks in this paper, it should be emphasized that shear (secondary) cracks are also likely to form under certain circumstances. As discussed in our previous paper (Kamali and Ghassemi 2018), the relative dominance of wing-cracks decreases at higher confining stresses. Weaker intact rocks or rocks containing an array of smaller-scale discontinuities are expected to be more conducive to the formation of shear (secondary) cracks. A schematic of a natural fracture under plane strain condition and subjected to in-situ stresses is shown in Fig. 3. 6.

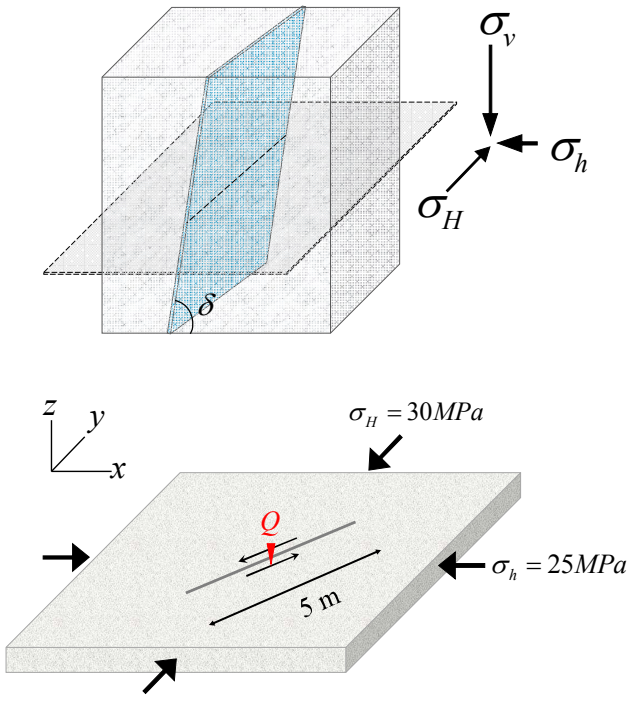

Fig. 3. 6. (Left) 3D view and (Left) 2D Natural fracture and in-situ stress configuration. This figure shows a natural fracture with very high dipping angle that is extended in the vertical direction. A horizontal slice is chosen for analysis.

It is assumed in the first example that the injection well is in direct contact with the natural fractures as shown in Fig. 3. 3. The example serves to illustrate the essential aspects of natural fracture propagation in poroelastic rocks. Water is injected at a constant rate into a closed natural fracture with an initial length of 5 meters. This natural fracture is oriented 30° from the maximum horizontal stress direction. Table 3. 7 summarizes the input parameters and assumed values of rock properties for a granitic formation used in this example. A time-step size of 0.5 second is used throughout the sensitivity analyses in this paper and the pre-existing crack is discretized into 50 displacement discontinuity elements which results in an element size of 0.10 m along the crack.

Table 3. 7. Input parameters used in the base case example.

Parameter	Unit	Value
σ_{xx}	MPa	25.0
σ_{yy}	MPa	30.0
σ_{xy}	MPa	0.0
p_o	MPa	15.0
E	GPa	50.0
ν_u	-	0.30
ν	-	0.25
k	m^2	1.0×10^{-17}
α	-	0.80
Q_{inj}	m^3/s	5.0×10^{-5}
μ	Pa.s	1.0×10^{-3}
K_{IC}	$MPa.m^{0.5}$	2.0
K_n	GPa/m	100.0
K_s	GPa/m	100.0
c'	MPa	0.0
φ'	°	20.0

The stress path or the variations of the shear and effective normal stresses of the injection element is shown in Fig. 3. 7. The Mohr-Coulomb failure envelope is also shown in this figure to determine the state of a contact element during injection. This figure shows that this particular element at the center of the fracture is stable prior to the injection. Injecting water causes the fluid pressure to rise which reduces the effective normal stress. Further reduction of the effective normal stress and the shear strength leads to shear slip. This corresponds to the point where the stress path intersects with the Mohr-Coulomb failure envelop as shown in Fig. 3. 7. The shear stress acting on the fracture keeps dropping as a result of continuous injection until the fracture becomes mechanically open.

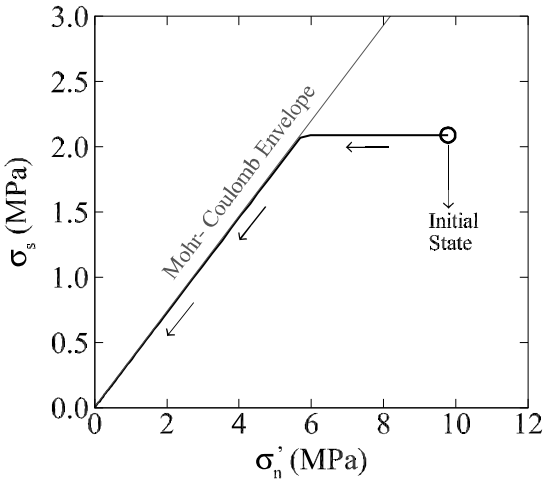

Fig. 3. 7. Changes of shear and effective normal stresses at the injection point. Note that both total stress and effective stresses change but because of the small diffusivity the diffusion time scale is much larger than the injection time scale so that total stress changes are relatively small

The shear displacement is monitored at the injection element during the simulation and is shown in Fig. 3. 8. It can be observed in this figure that the shear displacement discontinuity

remains constant at earlier stages of injection. Continuous water injection triggers shear slip at the injection well which is marked by a sudden increase in the shear displacement in Fig. 3. 8. The shear slip along the natural fracture creates tension in the vicinity of the natural fracture tips with maximum tension at a 70° plane from the fracture tip. Further shear slip could potentially result in fracture propagation in the form of tensile wing-cracks (Bobet and Einstein 1998a; Kamali and Ghassemi 2018).

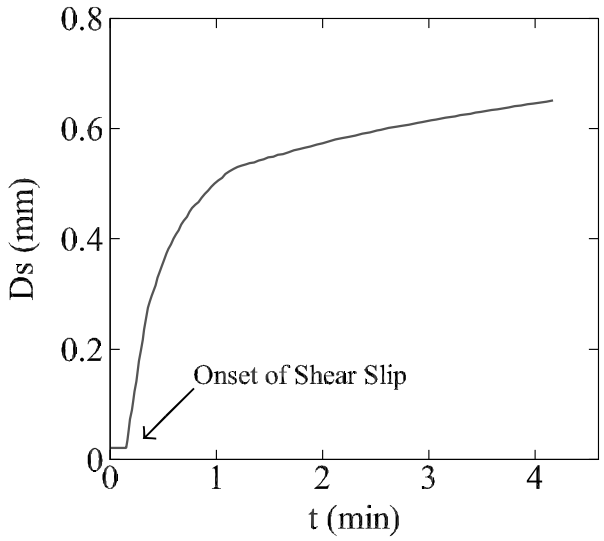

Fig. 3. 8. Shear slip history at the injection well. The natural fracture undergoes a sudden increase in the shear DD due to the continuous water injection. Note that there is a small initial elastic deformation which is caused by the far-field stresses (non-equilibrium formulation). There is no increment of Ds after that until the joint fails

To highlight the main differences between the elastic and poroelastic response the stress contours are plotted for each case after 18 seconds of injection (Fig. 3. 9). The elastic stress field is shown in the top row whereas the poroelastic field is in the bottom row. It can be observed in this figure that the stress fields are vastly different both in the magnitude and

the shape because the elastic joint slips earlier during injection. The induced $\sigma_{x'x'}$ at the crack tip (tensile) is higher in the elastic case than in in the poroelastic case. This is because of the faster pressure buildup and larger shear slip caused by the same injected volume (i.e., 1.8 L). However, the normal stress component on the fracture plane ($\sigma_{y'y'}$) is lower in the central region of the fracture for the poroelastic case which is due to the leakoff and pressure buildup in the matrix. It should be emphasized that these contours are obtained for the same amount of injection in both cases. It appears from the induced tension at the crack tips that wing-crack propagation is more likely to happen in impermeable rock (see Appendix-C for more details).

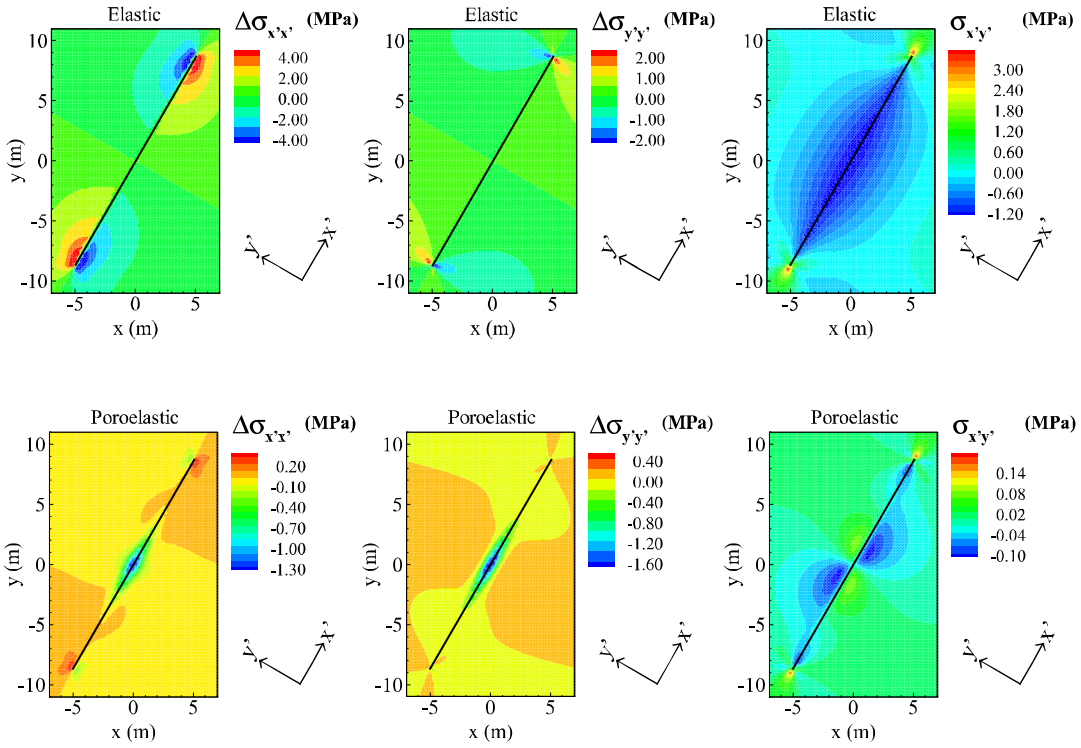

Fig. 3. 9. A comparison between the induced stress fields around a natural fracture in elastic (top row) and poroelastic (bottom row) rocks after 18 s of injection (1.8 L). Stresses are

rotated and plotted in the local coordinate of the natural fracture (i.e. 60° from the global x-axis). Compression is regarded positive

The shear slip along the natural fracture triggers the wing-cracks out of the fracture plane at approximately 70° from the crack tip. The wing-cracks grow longer due to the shear slip on the pre-existing natural fracture and the fluid pressure at the tip of the fracture. Wing-cracks tend to re-orient and propagate in the direction of the maximum horizontal stress leading to a curvilinear propagation path. Fig. 3. 10 shows the fracture aperture profile and the fracture geometry before injection and after 4 minutes of injection. It can be seen in this figure that the wing-cracks are aligning themselves with the maximum horizontal stress direction as they grow longer. The fracture aperture profile reveals that the initiation points of the wing-cracks have the highest aperture despite being farther away from the injection point. This is mainly due to the shear slip along the pre-existing fracture that induces more opening at the root of the wing-cracks.

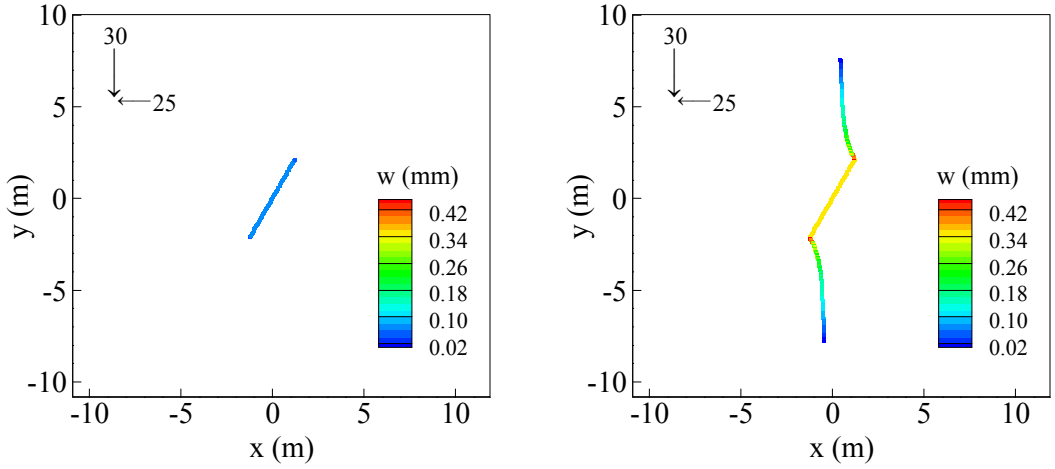

Fig. 3. 10. Natural fracture and wing-cracks geometry and fracture apertures at different injection times. a) Pre-existing natural fracture prior to the injection. b) Natural fracture and the wing-cracks after 4 mins of injection

3. 6. 1. Influence of Rock Matrix Permeability

Rock diffusivity is an important parameter among other factors which controls the pore fluid diffusion and therefore the poroelastic effects. Matrix permeability directly governs the fluid leakoff across the fracture surfaces. It is classically known in the hydraulic fracturing literature that higher leakoff results in higher poroelastic stress or "*back-stress"* (the additional compressive stress induced by the pore fluid diffusion which increases the normal stress on the fracture surfaces) to make fracturing more difficult and increases the fluid pressure required to maintain the propagation (Cleary 1980; Ghassemi and Roegiers 1996; Vandamme and Roegiers 1990). The sensitivity analysis in this example sheds light on the effect of rock permeability on the propagation of natural fractures in poroelastic rocks. The base case example with the rock permeability of 1.0×10^{-17} m^2 (0.01 mD) is repeated using two more permeability values. All other simulation parameters are similar to the ones used in the base case example.

The injection pressure profile is shown in Fig. 3. 11 for different values of rock permeability. This figure shows that the pressure increases at a higher rate for lower values of permeability which is attributed to lower leakoff volume and higher storage inside the fracture corresponding to lower permeabilities. It can be observed in Fig. 3. 11 that the injection pressure for all cases rises above the minimum horizontal stress value (i.e. 25 MPa). Furthermore, the pressure required to maintain the propagation is higher when the

rock permeability is higher. Higher leakoff causes a stronger back-stress leading to higher injection pressures. The kink points where the slope of the injection pressure profile changes shows the onset of propagation; the newly created volume due to propagation causes the pressure profile to flatten and increase at a lower rate.

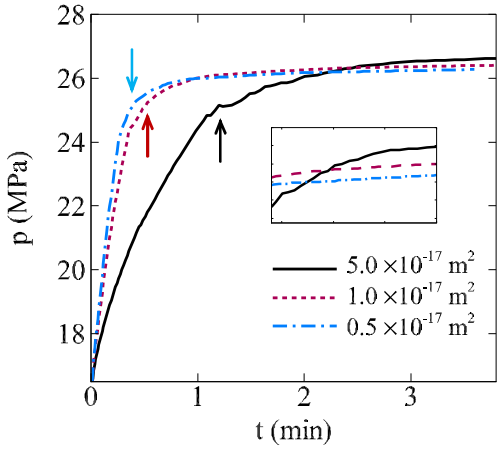

Fig. 3. 11. Comparison of the injection pressure profile at the injection well for different permeability values. The figure shows that higher permeability leads to slower pressure buildup and higher pressure requirement.

The fluid leakoff associated with higher permeabilities is expected to affect the length of propagation. The final crack geometry is shown in Fig. 3. 12 for different permeabilities. This figure shows that the length of the wing-crack achieved after 4 minutes of injection is longer for lower permeabilities. The higher stored volume inside the fracture and smaller leaked volume in the case of lower permeability helps obtaining a longer fracture. Therefore, rock permeability manifests itself in not only the injection pressure but also in the wing crack dimensions with higher permeability reducing the wing crack length.

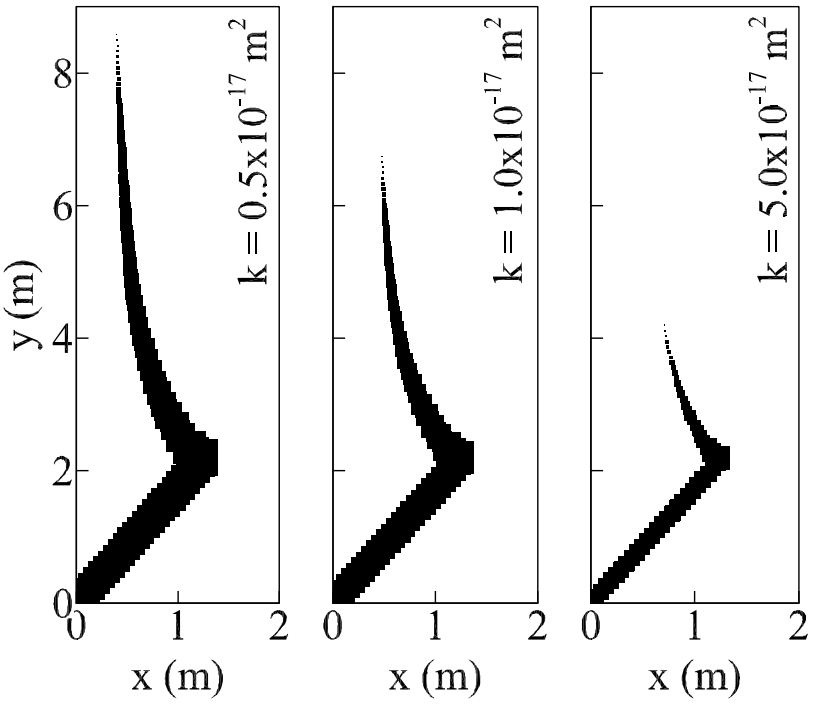

Fig. 3. 12. Wing-crack's length after 4 mins of injection for different values of permeability. A higher permeability results in shorter wing-cracks because of the higher leakoff and smaller stored volume

3. 6. 2. Influence of Initial Pore Pressure

Initial reservoir pressure is another factor that determines the tendency to leakoff. Lower initial pore pressures results in a higher pressure gradient between the fracture and the matrix leading to higher leakoff volume. Therefore, initial pore pressure contributes to the poroelastic behavior of rocks. In this example, the variation of wing-crack's length and the injection pressure of three pore pressure values are studied.

Fig. 3. *13* shows the wing-cracks variations with time for different pore pressure values. It can be seen in this figure that the wing-cracks are noticeably longer when the background pore pressure is higher. This is, in fact, due the lower leakoff and lower back-stress caused

by the smaller pressure gradient between the natural fracture and the matrix (see a detailed analysis of this problem in Appendix-D). Reservoir pore pressure changes the effective stresses and controls the stress criticality of natural fractures (by reducing the effective normal stress) in an elastic rock. In addition to changing the effective stresses, reservoir pore pressure impacts the amount of leakoff and the corresponding back-stress caused by diffusion in a poroelastic rock. The latter effect is absent in elastic rocks.

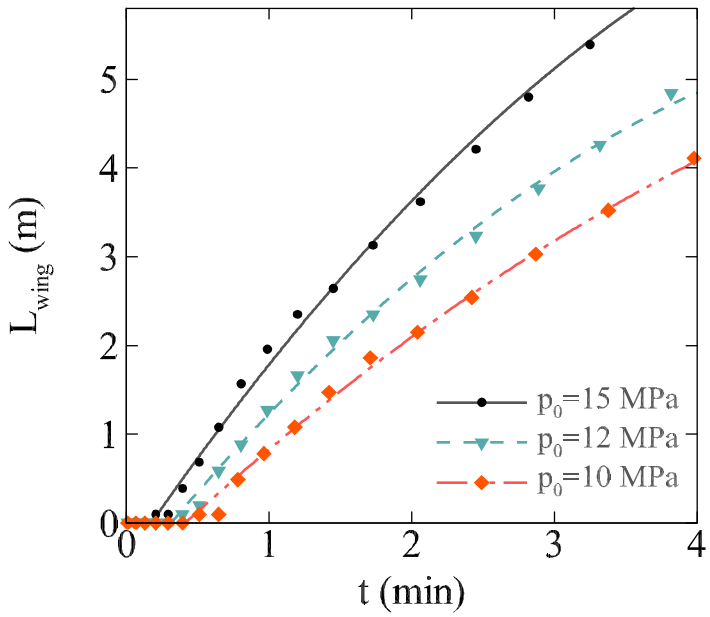

Fig. 3. 13. Comparison of wing-crack's length vs injection time for different values of initial pore pressure. The figure shows that lower pore pressures result in shorter wings for the same amount of injected volume

The injection pressure profile for this example is shown in Fig. 3. *14*. This figure shows that the pressure requirement is higher for the lower pore pressure values in the stabilized portion of the plot. This confirms that the higher leakoff associated with low pore pressure gives rise to higher compression on the fracture and increases the required injection

pressure. This example implies that longer fractures may be achieved using lower injection pressures when the initial pore pressure is higher in certain formations.

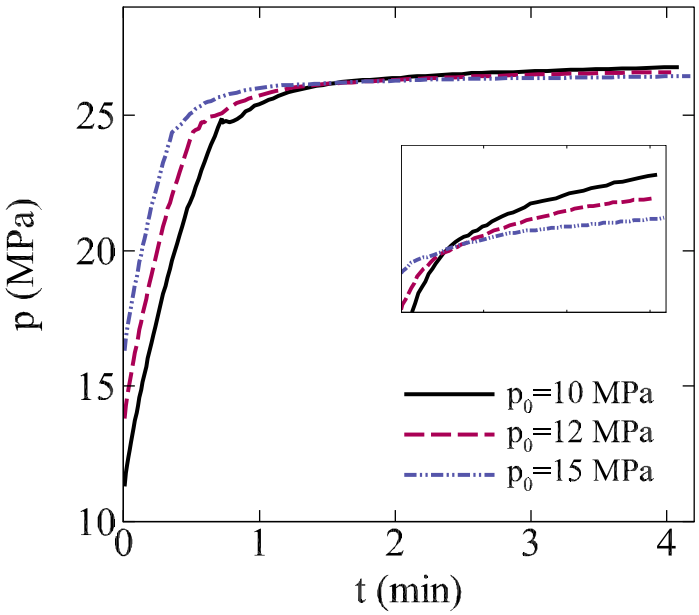

Fig. 3. 14. Injection pressure profile for different pore pressure values. The pressure requirement is higher when the pore pressure is lower in the stabilized portion of the plot

3. 6. 3. Influence of Pumping Rate

The rigidity or softness of a poroelastic medium is controlled by how fast or slow the medium is loaded. Although the pumping rate into a fracture may not be directly interpreted as the loading rate but it is our understanding that it has the same effect as the loading rate. Therefore, the impact of pumping rate on the fracture length and width is investigated in this example. The pumping rates used in this example are Q^*=5.0x10^{-3} m^3/s, 0.75Q^*, and 0.50Q^*. Considering that the injection rate varies in each case, fracture length and width are monitored against the injection volume rather than the injection time.

The final fracture geometry is shown in Fig. 3. *15* for the lowest and the highest pumping rate. As can be observed in this figure, longer wing-cracks are created after injecting 12 L of water using a higher pumping rate. Higher injection rate reduces the injection time for any given injection volume which in turn reduces the compressive stresses that are developed on the fracture surfaces due to the diffusion. The pumping rate, however, does not affect the overall propagation trajectory of the wing-cracks.

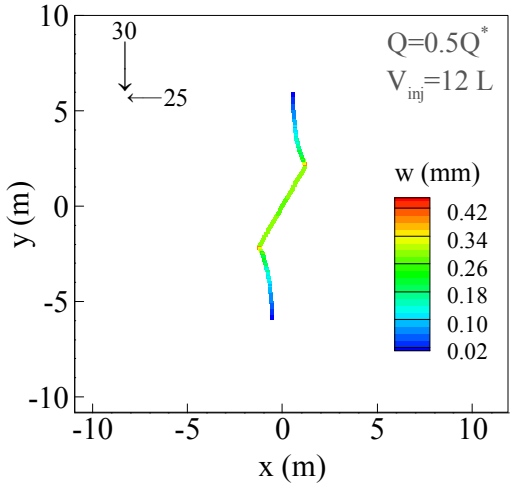

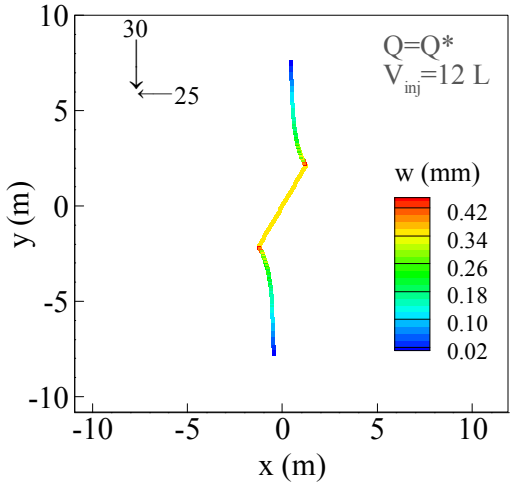

Fig. 3. 15. Final fracture geometry after injecting 12 L of water using a) rate 0.50Q* and b) rate Q*. Higher pumping rate results in longer fracture for the same amount of injected volume.

Fig. 3. 16 shows the variation of the fracture width at the center of the fracture for different pumping rates. It can be observed in this figure that a higher pumping rate results in a higher fracture width after injecting the same volume of water. Higher fracture apertures in the case of higher pumping rate could be justified with the smaller compression that is induced over a smaller injection interval. It is worth noticing that the slope of fracture aperture increases after stabilizing in the mid portion. The inflection point for each curve signifies the transition from the closed natural fracture to an open hydraulic fracture. Unlike two previous parameters, namely, reservoir pore pressure, and permeability, pumping rate could be controlled in the field. Therefore, it can be used as a design parameter to achieve higher efficiencies in the stimulation of naturally fractured poroelastic rocks.

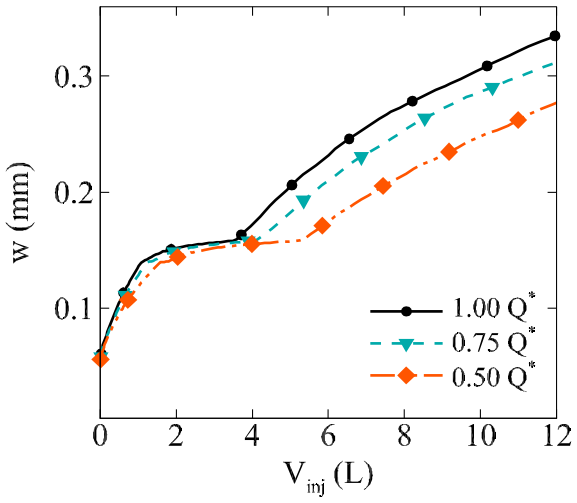

Fig. 3. 16. Variations of the fracture width vs. fluid injection volume at the injection point for three pumping rates. A higher pumping rate results in higher fracture apertures by

reducing the injection interval and consequently the compressive stress induced by diffusion (see also Zhou and Ghassemi, 2011).

3. 6. 4. Injection into the Rock Matrix

Previous examples dealt with the problem of injection into the natural fractures. This is only possible when the natural fractures are in direct contact with the injection well. A more likely scenario is activating the natural fractures by injecting into the rock matrix rather than into the fractures. The injected fluid flows in the rock matrix and may as well be stored in the natural fractures. The changes of pore pressure, total and effective stresses could lead to the destabilization of faults and natural fractures. It is our objective in this example to investigate the behavior of two natural fractures with different strikes in the vicinity of an injection well (see Fig. 3. *17*). Both fractures are 100 *m* long, one with N60E strike (NF 1) and the other with N30E strike (NF 2) as shown in Fig. 3. *17*. The farfield stresses are 25 and 32 MPa in the E-W and N-S directions, respectively. Water is injected at a constant rate of 5×10^{-6} m^3/s into a reservoir with the permeability of 0.10 mD. The rest of the simulation parameters are similar to the ones used in the previous examples.

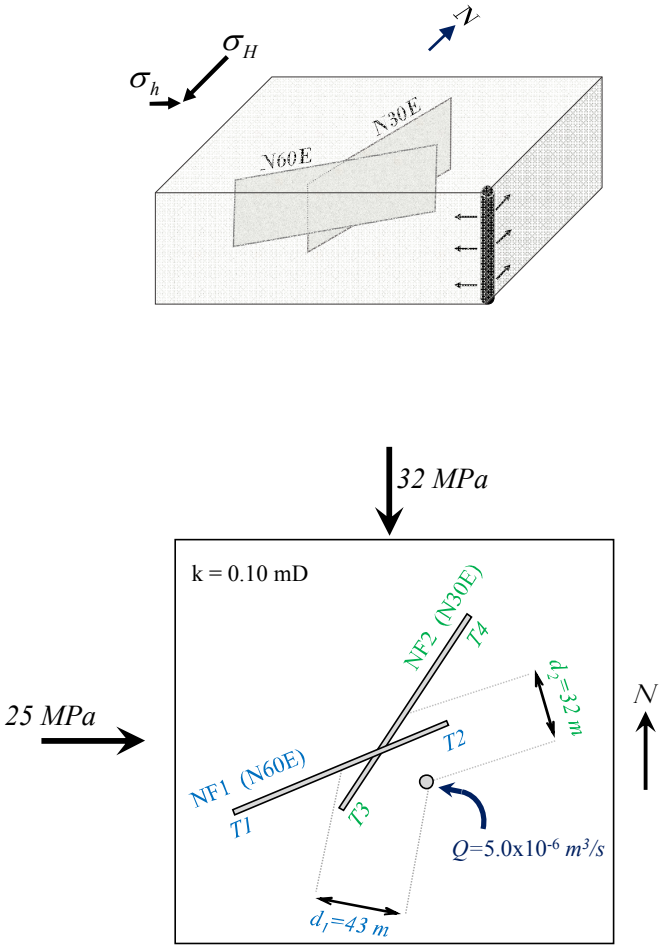

Fig. 3. 17. (Left) 3D view and (Right) plane view configuration of the natural fractures in the vicinity of the injection well. The injection well is drilled in the matrix with no direct contact with the natural fractures.

The stresses and the pore pressure is monitored at certain locations in the domain throughout the injection. Fig. 3. 18 shows the stress state and the pressure at the tip of both natural fractures (*T2*, and *T4*). It can be observed in this figure that the variation of the pressure, effective normal stress and the shear stress have the same trend during the first 50 days of injection. However, the shear stress at the tip of NF 2 (*T4*) starts to drop at a

relatively high rate which signifies shear slip. The mere fact that the initial normal stress is lower along NF 2, makes this fracture more critically-stressed and prone to shear slip.

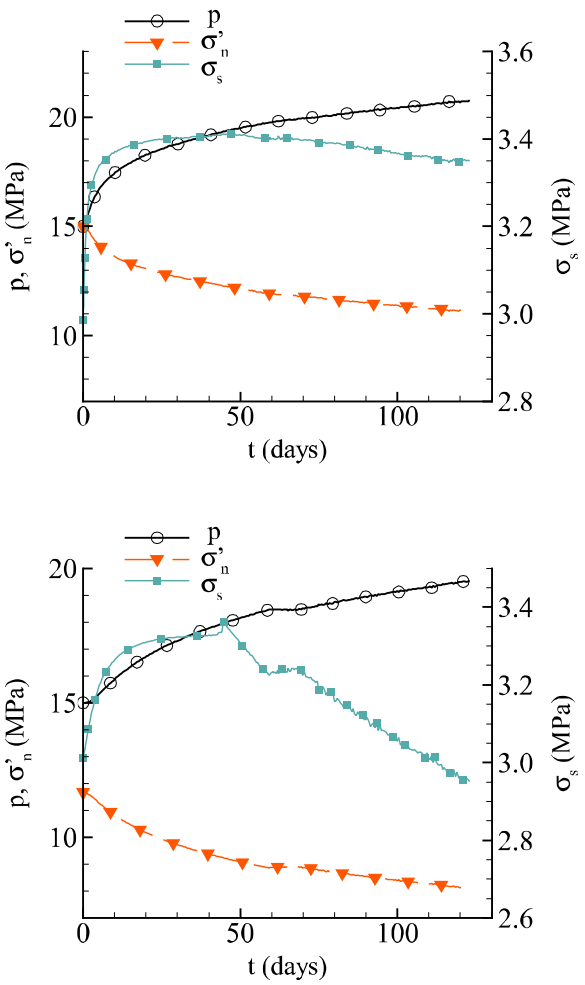

Fig. 3. 18. a) Stress state and pressure at *T2* (left) and b) Stress state and pressure at *T4* (right)

Fig. 3. 19 shows the shear deformation along the natural fractures at the beginning of the simulation and after 4 months of injection. This figures shows that NF 2 undergoes a significant amount of shear slip after 4 months of injection whereas NF 1 only shows slight changes of shear deformation within the elastic range. This is in agreement with the stress

state profiles shown in Fig. 3. 18. Moreover, it is interesting to note that entire fracture does not experience slip in NF 2 which is attributed to the local variation of the stresses and pore pressure caused by the injection.

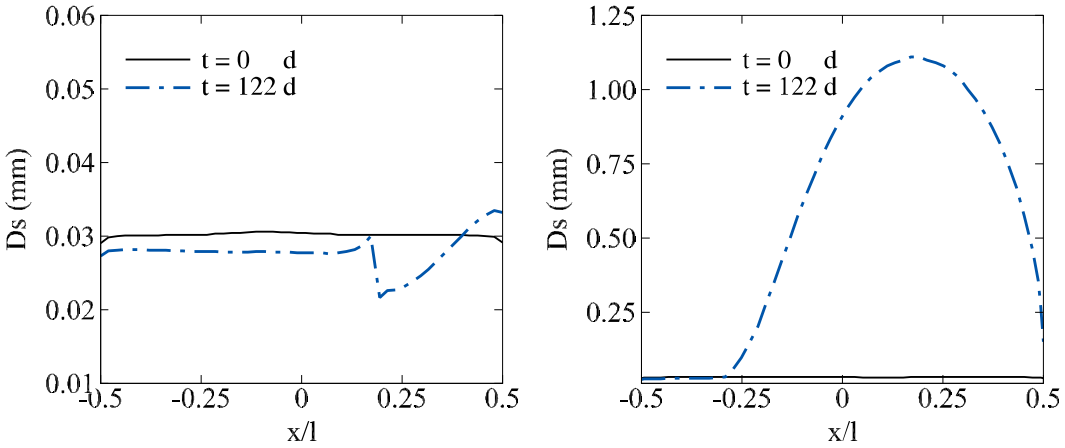

Fig. 3. 19. Shear deformation profile along NF 1 (left) and NF 2 (right) at the beginning of the injection and after 4 months of injection. This figure shows that the NF 2 is destabilized locally and experienced shear slip while NF 1 remained in the stick mode with not any significant changes of shear DD

The shear slip along the natural fractures create a tensile zone around the tip of the fracture and could potentially lead to wing-crack propagation as explained in the previous examples. It can be seen in the final configuration of the natural fractures in Fig. 3. 20, that the shear slip has, indeed, created a wing-crack from the upper tip of NF 2 (i.e., *T4*). It was, however, observed that the wing-crack propagated to some extent and the stopped. The impact of shear slip on the wing propagation diminishes as the wing grows longer and reaches farther away from the pre-existing fracture. Moreover, the pore pressure in this case is not as high as the pressure in the direct injection case. Therefore, it is only reasonable to expect that the wing-crack propagation is not as dominant as it was in the

case of direct injection into the fractures for the same stress state and fracture orientation. However, pore pressure increase enhances slip potential, fracture slip and wing crack formation.

This example implies that reservoir stimulation by wing crack initiation and propagation is possible in both direct and indirect injection scenarios. The direct injection scenario (as in hydraulic fracturing) can lead to stimulation via wing-cracks based on the findings of this study and shear (secondary) crack (Kamali and Ghassemi 2018) propagation in the neighborhood of the major fracture. The indirect injection tends to mainly cause shear slip along the natural fractures leading to their dilation and thus permeability enhancement (Kamali and Ghassemi 2018). These suggest that shear crack formation and shear dilation are both viable stimulation mechanisms and can predominate under particular geologic and injection settings.

A growing number of microseismic and seismic activities have been observed in recent years particularly near geothermal sites and volcanoes which do not fit the profile of double-couple (DC) earthquakes. The departure from idealized DC models, as Foulger and Julian (2015) argue, is believed to be caused by fault curvature and/or rock anisotropy. Earthquake mechanisms can be represented by an equivalent force system. However, the physical source that yields a certain force system may not be uniquely identified because different force systems can have an identical force system. Foulger and Julian (2015) consider "combined tensile and shear faulting" as a potential candidate for non-DC events. This mechanism requires intersected shear and normal faults. The predicted fracture geometry in our study involves shearing along the pre-existing faults/fractures and tensile

opening along the wings, so the ultimate fracture geometry can exhibit paired-tensile-shear behavior. This is, of course, only one possible explanation for the observed non-DC events.

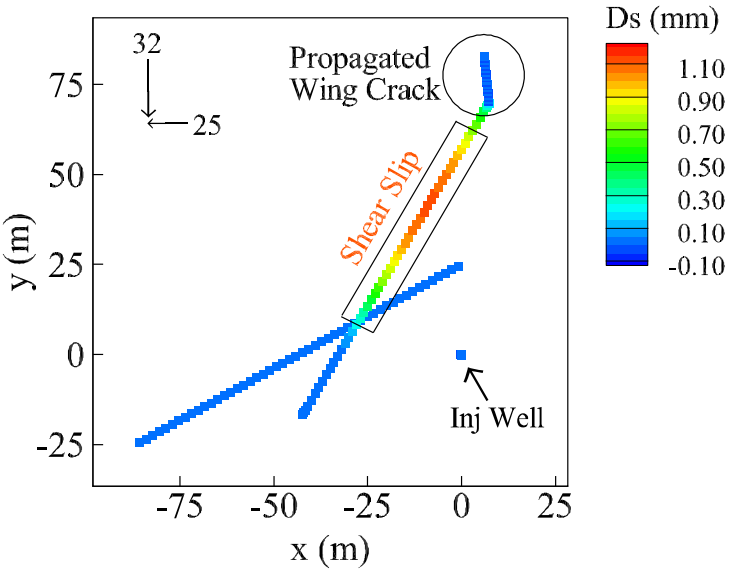

Fig. 3. 20. Shear DD along the natural fracture and asymmetric wing crack growth at the end of the simulation

3. 7. Conclusions

Several simulations were conducted to explore the impact of poroelasticity on the reservoir stimulation mechanisms in naturally fractured reservoirs. The numerical examples were studied under two main categories: injection into the natural fracture and injection into the rock matrix. Our findings in the first scenario indicates that wing-crack propagation is an integral part of the reservoir stimulation when there is direct contact between the well and the natural fractures. The sensitivity analyses on the role of poroelasticity revealed that lower matrix permeability, higher initial pore pressure, and higher pumping rate promote wing-crack propagation. The effect of natural fracture's length was investigated in our previous paper (Kamali and Ghassemi 2018) where it was shown that shorter pre-existing

fractures promote wing-crack propagation whereas longer fractures often experience dilation. The impact of the fracture's length is even more noticeable in poroelastic rocks; higher leakoff from the surfaces of a longer fractures leads to shorter wing-cracks (when compared to elastic rocks). Moreover, higher leakoff from a longer pre-existing fracture results in a slower pressure buildup within the fracture and therefore causes retardation in the formation of the wing-cracks. Although wing-crack propagation was found to be more difficult to achieve in a poroelastic rock due to the back-stress that is developed on the pre-existing fractures, pore pressure enhances the potential for slip and wing crack formation. This is important because it can be argued based on elastic simulations (e.g., Kamali and Ghassmei 2017) that increasing confinement reduces the possibility of wing crack formation in the favor of shear (or secondary) cracks. But as has been shown by Lehner and Kachanov (1996), the presence of a pore pressure mitigates the effect of confinement. Pore pressure action on the wing cracks lowers the effective stresses, promoting wing crack growth. This effect is further enhanced under undrained conditions (e.g., injection into an impermeable fracture) when the driving shear forces remained unaltered. The stimulation mechanism was found to be essentially different when the injection well does not intersect any of the natural fractures. Injection into the rock matrix caused local destabilization along the natural fractures and non-uniform stress state along them. The wing-crack is much shorter in this case and emanates only from one of the fracture tips.

As an extension to our previous paper (Kamali and Ghassemi 2018), this work addresses the role of diffusion and the induced poroelastic stresses on the stimulation of natural fractures. Our findings provide guidance for more efficient stimulation designs in naturally fractured rocks through a detailed analysis of injection pressure profiles, stress fields, and

fracture opening and slip variations. Our results indicate that reservoir stimulation can be achieved at injection pressures below the minimum horizontal stress level and under relatively low injection rates. Natural fracture propagation can be maintained by keeping the injection pressure slightly above the minimum horizontal stress. Based on our findings, overdesign (in terms of injection pressure and rate), which often translates to extra cost, could be avoided by targeting the natural fractures. This framework finds immediate application in the geothermal and unconventional oil and gas reservoirs where stimulation relies mostly on the natural fractures. Also, our simulation results can help further understanding of non-DC seismic events due to simultaneous shear-tensile behavior that is observed along the pre-existing fracture/faults and the wing-cracks.

Chapter 4

3D Modeling of Hydraulic and Natural Fracture Interaction

Natural fractures (NF) and other discontinuities are inseparable elements of rock masses. Outcrop analyses show the presence of natural fractures on a number of different scales. It has been argued that naturally occurring fractures and discontinuities in the outcrops are not solely a result of weathering and surface conditions implying their presence in the reservoir rocks (Nelson, 2001).

Though the fractured nature of reservoir rocks has been well known, accounting for the impact of natural fractures in the coupled rock-fluid processes does not date back to more than a few decades. Production from tight and unconventional oil and gas reservoirs highlighted the immense role of natural fractures in the development of oil and gas reservoirs (Aguilera, 1980). Promising hydrocarbon production from key shale plays motivated a closer examination of the state of natural fractures in several studies (see e.g. Schettler et al., 1989; Gale et al., 2007).

Natural fractures affect the hydrocarbon and geothermal reservoirs during different stages of their lifespan. The first encounter with the natural fractures during the well development happens during drilling. Drilling through heavily fractured formations requires pre-planning to adjust the mud weight and other drilling parameters to avoid severe mud loss. Next interaction, and a critical one, is during stimulation. Hydraulic fracturing in the

presence of natural fractures becomes a complex problem which needs to be carefully examined for better stimulation results. The interaction between the hydraulic (HF) and natural fractures takes different forms and could have positive and negative impacts on the stimulation results. The HF-NF interactions can be summarized as follows:

- Natural fractures affecting the hydraulic fracture propagation path before intersection: This is a purely mechanical interaction caused by the stress perturbations around natural fractures. The stress disturbance around natural fractures could potentially result in curvature and turning in the approaching HF front.
- Hydraulic fracture affecting the natural fractures before intersection: Also a pure mechanical effect (neglecting poroelastic effects) caused by the tensile stress zone ahead of the HF tip zone. This interaction can destabilize the natural fractures and leads to shear slip and, in some cases, permeability enhancement in the natural fractures.
- Coalescence of hydraulic and natural fractures: This type of interaction has mechanical and hydraulic components and affects both the hydraulic fracture and natural fractures. The overall hydro-mechanical interaction determines the course of propagation after the coalescence. Some of the likely scenarios after coalescence are: HF propagation terminates upon intersecting the NF; HF continues to propagate by crossing the natural fractures; HF propagates along the natural fracture or other discontinuities such as beddings; HF propagates with an offset from its original plane; HF preferential propagation around the natural fracture resulting in an engulfing pattern. Additionally, this type of interaction

affects the proppant transport behavior if the natural fractures are not sealed. This effect has implications in the reservoir productivity as it controls the effective propped area after shut-in.

Natural fractures provide highly conductive path to the hydrocarbons and therefore contribute to the overall well performance during production. This effect is even more pronounced in unconventional reservoirs because of the ultra-low permeability of the rock matrix in comparison to the natural fractures.

This section seeks to acquaint the reader with the different aspects of hydraulic and natural fracture interaction through a summary of the literature on this subject. The summary presented here include experimental, analytical, and simulation studies.

4. 1. Introduction

Lamont and Jessen (1963) provided an experimental work on the extension of hydraulic fractures in rocks with pre-existing fractures. Their experiments were conducted on relatively small rectangular rock samples by varying the joint angle, width, and stress conditions. Surprisingly, hydraulic fractures were found to cross the closed fractures in almost all of the cases with no significant impact of the stress conditions and angle of inclination on the results. They note that the stress magnitudes are admittedly lower than the ones under in-situ conditions. They also report considerably high propagation rates as compared to the field treatments raising the question of unstable fracture propagation.

As one of the earlier works on the subject of interaction of hydraulic and natural fractures, Daneshy (1974) discussed hydraulic fracturing near planes of weakness and supported his arguments with a few block experiments. The planes of weakness were categorized based

on their size (relative to the hydraulic fracture) and their open/closed status. Daneshy (1974) argued that small- to medium-sized (several inches for small-scale and up to several feet for the medium-scale category) flaws have no noticeable effect on the trajectory of hydraulic fracture, regardless of their opening mode. These type of flaws can, at most, have local effects on the fracture trajectory. Large flaws, on the other hand, can influence the propagation trajectory depending on their opening status. Hydraulic fractures tend to reorient themselves to become parallel to large open flaws (because of zero normal stress on the plane of weakness) when approaching them. The hydraulic fracture may extend in its original plane once it grows beyond the disturbance zone. Danehsy (1974) found that hydraulic fractures are most likely to cross closed natural fractures and continue to propagate in their original propagation plane (see Fig 4. 1).

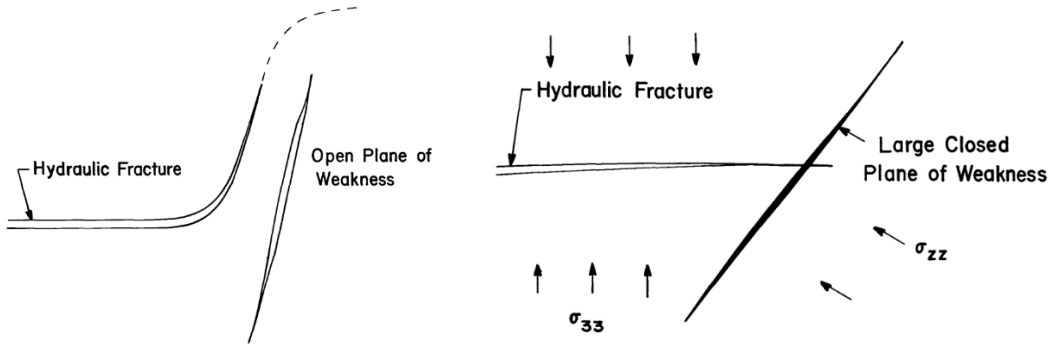

Fig. 4. 1. Plausible propagation path for a hydraulic fracture approaching (left) a large open flaw and (right) a large closed flaw (after Daneshy, 1974).

Anderson (1981) examined hydraulic fracturing near unbonded rock interfaces in a series of small-scale experiments. The experiments were mainly performed to determine the conditions leading to fracture crossing the interface using sandstone and limestone samples. As demonstrated in his experiments, shear resistance of the interface was a critical

factor in whether the hydraulic fracture crosses the interface. The frictional properties of the interface which was the centerpiece of this work was varied using different preparation techniques such as lubrication, and mechanical roughening. Anderson's result indicate that a lubricated interface with reduced friction require a higher compressive stress on the interface to allow fracture crossing (Fig 4. 2). Anderson (1981) also showed that the presence of water affect the normal stress threshold for crossing differently depending on the rock sample (limestone and sandstone in this particular study) implying the importance of rock-mineral interaction.

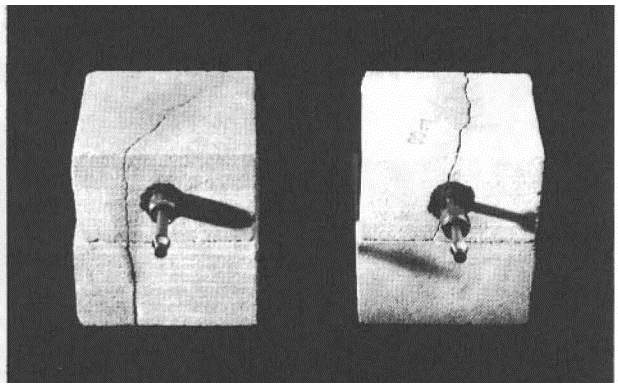

Fig. 4. 2. Hydraulic fracture crossing an unbonded interface in the left block and arrested in the right rock blocks. The left block is loaded above the normal stress threshold to facilitate crossing conditions (after Anderson, 1981).

In yet another experimental study, Blanton (1982) investigated the hydraulic fracture morphology in pre-fractured Devonian shale and hydrostone under tri-axial stress state. His work mainly concerned the impact of the intersection angle and the differential stress. Blanton (1982) provided a more comprehensive analysis to justify his observations by adopting Hanson's stress intensity approach (Hanson et al., 1981) and applying proper stress analysis near the intersection zone. Blanton noticed a pattern when plotting the

interaction types (i.e., cross, arrest, open) in terms of the angle of approach and the differential stress leading to an early version of intersection criterion. Blanton's experiments suggest that fracture crossing is only possible at very high intersection angles and high differential stresses (which results in a higher normal stress on the interface). Blanton (1982) fails to clarify that the differential stress is increased by increasing the maximum horizontal stress while keeping the minimum horizontal stress unchanged. In other words, the normal stress on the pre-existing fracture is not constant in his experiments. Nonetheless, Blanton argued that symmetrical, bi-wing and vertical fractures are not likely to form in naturally fractured reservoirs given the impact of natural fractures.

Jeffrey et al. (1987) developed a two-dimensional displacement discontinuity (DD) model to study the interaction of a propagating hydraulic fracture with natural fractures. Using elastic-perfectly-plastic Mohr-Coulomb elements along the natural fracture, Jeffrey et al. (1987) captured shear slip along the natural fracture as a result of hydraulic fracturing. It is pointed out in this study that the slip zone is not limited to the tip of the hydraulic fracture. In fact, natural fractures can experience slip even after a hydraulic fracture crosses the natural fracture. Jeffrey argues that the aperture reduction in the hydraulic fracture upon intersection can lead to proppant bridging and ultimately screen-out. The model did not consider hydraulic communication between the hydraulic and natural fractures limiting its applicability to treating larger scales problems.

To cast light on the complex behavior of hydraulic fracture in the presence of geological discontinuities, Warpinski and Teufel (1987) analyzed mineback experiments and lab tests involving hydraulic fractures and discontinuities like joints, and faults. Their mineback experiments revealed that hydraulic fractures are often offset when they cross natural

fractures (see Fig. 4. 3). They observed multiple hydraulic fractures emanating from the intersected joints. Their observations indicate that hydraulic fractures tend to terminate after a short distance of propagation across the faults. This is attributed to the changes of the stress across the faults and not the fault plane itself. They argue that under small differential stresses, the discontinuities with favorable orientation for blunting the hydraulic fractures are likely to experience dilation.

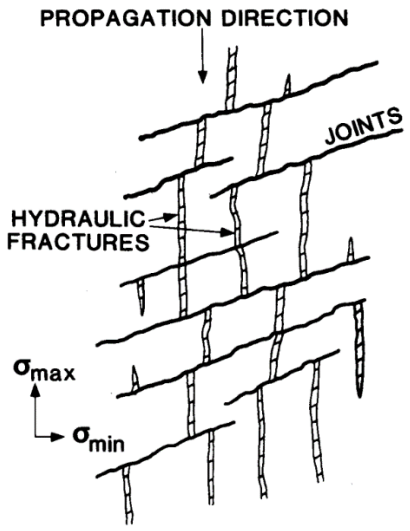

Fig. 4. 3. Fracture treatment in jointed rocks. This figure shows fracture offset pattern in the presence of joints (after Warpinski and Teufel, 1987).

Renshaw and Pollard (1995) developed a crossing criterion for propagation across unbonded frictional interfaces. This work which is based on linear elastic fracture mechanics, focuses only on the case of orthogonal intersection of HF and the interface. They conducted several experiment to test the validity of their proposed crossing criterion. They distinguished between the continuous propagation of the approaching fracture and re-initiation of another crack on the opposite side of the interface (see Fig 4. 4). They advocated the latter mechanism as the primary mechanism of crossing because the first one

fails to justify fracture offsets that are observed in several instances. That said, continuous propagation across the interface as a plausible mechanism was not ruled out. Considering that the stress singularity at the fracture tip diminishes when it contacts the interface, fracture re-initiation on the opposite side is very likely to occur before the intersection. The basis for their crossing criterion can be summarized as follows: 1) the compression on the interface is sufficient to prevent slip along the interfaces and 2) the tensile stress ahead of the fracture tip is enough to initiate a fracture on the opposite side of the interface. The study has two major assumptions which might limit its results; the first major assumption is that the trajectory of the approaching fracture is not influenced by the interface and the second assumption is that the pressure inside the hydraulic fracture is low enough to ensure crossing and not deflection of the HF into the interface.

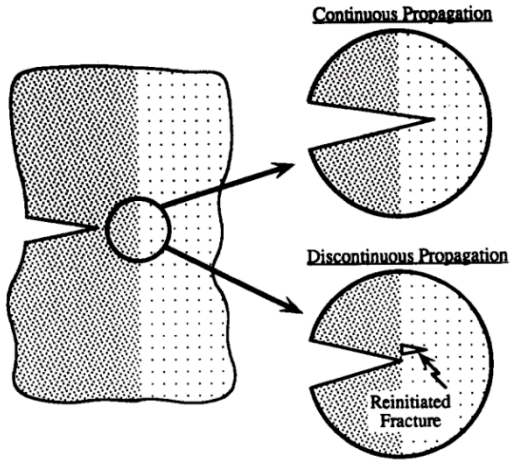

Fig. 4. 4. Fracture crossing as a result of continuous propagation (top) and re-initiation from the opposite side of the interface (bottom) (after Renshaw and Pollard, 1995).

Koshelev and Ghassemi (2003) took a numerical approach to investigate hydraulic fracture propagation in the vicinity of natural discontinuities. Their model is based on a complex variable boundary element method (CV-BEM) and uses Coulomb's law of friction to

quantify sliding along the discontinuities. Fracture propagation is achieved by increasing the fracture pressure to a limit to satisfy the critical stress intensity condition (K_I=K_{IC}). Their comparison between the fracture trajectory in a rock with and without faults shows how the stress disturbance near the fault influence the propagation path (Fig. 4. 5). This study highlights how the shear displacement along the natural discontinuity deflects the HF propagation trajectory. Koshelev and Ghassemi (2003) demonstrated the role of differential stress in the HF-NF interaction; their simulation results indicate that the hydraulic fracture tends to approach the discontinuity under lower differential stresses while turning at shaper angles and extending parallel to the discontinuity under higher differential stresses. This study is limited to the fracture propagation before intersection and does not discuss the coalescence and after-intersection behavior of the HF-NF system.

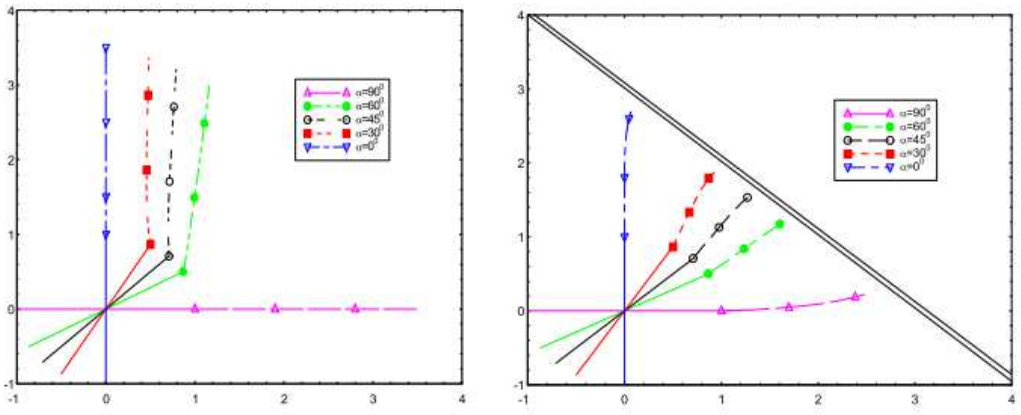

Fig. 4. 5. The impact of stress disturbance near faults on the hydraulic fracture trajectory (after Koshelev and Ghassemi, 2003).

Advocating the speedy analysis of analytical approaches as compared to numerical models, Theircelin and Makkhyu (2007) developed a semi-analytical mode to study the stress fields around natural fractures as a result of hydraulic fracturing. This work is based on the theory

of dislocations and concerns the stress field in the vicinity of natural discontinuities in the presence of an approaching HF. Theircelin's work focuses on the re-activation of natural fractures and seeks to find the most probable location for fracture offset after intersection. It is important to note that this work assumes HF re-initiation on the opposite side of the natural fracture begins before coalescence. Their simulation results indicate that the length of the re-activated (i.e., slipped and/or open) natural fracture decreases as the intersection angle between the HF and NF increases. This activated NF length almost diminishes as the pre-existing NF becomes perpendicular to the HF. Their result also show that higher intersection angles favor fracture crossing. Thiercelin also argues that the zone of maximum tensile stress may not even lie on the natural fracture plane in certain cases which makes the analysis of the HF offset location even harder. Although the study provides useful insight to the problem of HF re-initiation and offset it has several shortcomings; their discussion does not involve the pre-coalescence stage and fluid flow is not explicitly modeled.

A mine-back experiment by Jeffrey and Ghassemi (2001) revealed several types of HF-NF interaction and intersection patterns all in one experiment. Fig. 4. 6 shows a hydraulic fracture that is initiated in a naturally fractured rock. The fracturing fluid is dyed red to facilitate tracing the fracture wings. This figure shows fracture propagation near a major natural fracture that is marked by a yellow rectangle. The hydraulic fracture has penetrated into the natural fracture and crossed the natural fracture with a small offset from its previous plane (marked with a blue arrow). It is interesting to note that the fracturing fluid has opened another vein or perhaps propagated as a wing-crack from one of the adjacent natural fractures (red arrow in the left bottom corner). The observations indicate that the

fracture geometry can become very complex and several intersection patterns can coexist in highly fractured rocks.

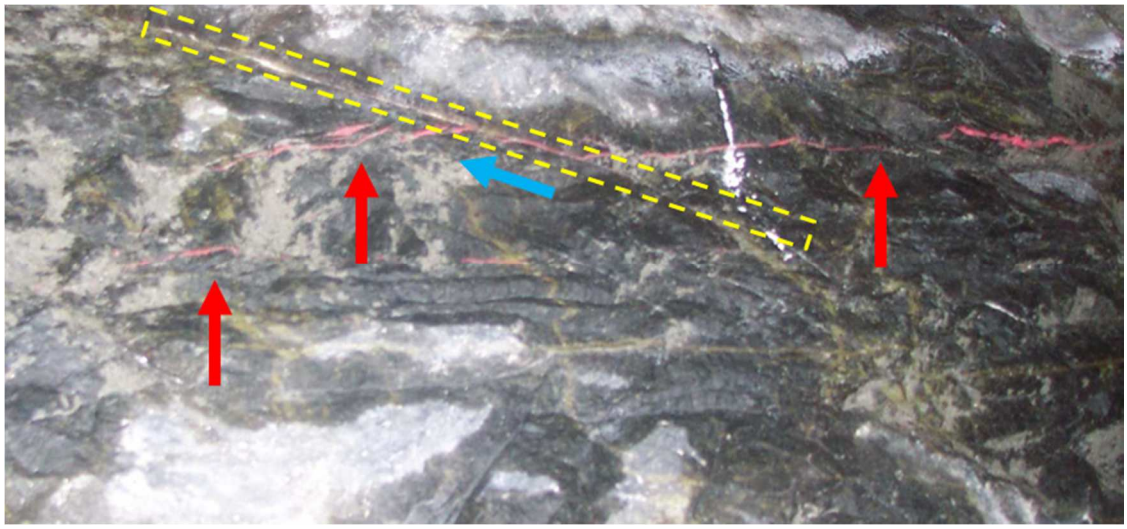

Fig. 4. 6. Mine-back experiment showing HF crossing with a minor offset and a secondary wing-crack propagation parallel to the main HF (Courtesy of Rob Jeffrey, 2001).

Gu et al. (2012) extended Renshaw and Pollard's (1995) criterion to account for non-orthogonal intersection of hydraulic and natural fractures. Their criterion, like that of Renshaw and pollard (1995), applies to the mechanical interaction of the hydraulic and natural fracture before the coalescence to determine if the fracture crosses the natural fracture. Gu et al. (2012) divided the crossing process into the following steps: before the fluid front reaches the intersection point and after the fluid reaches the intersection (as a result of fluid lag). Therefore, they do not account for fluid flow and hydraulic interaction of the HF and NF by focusing particularly on the first step. Their discussion, similar to the rest of literature, re-iterates the fact that fracture crossing occurs only if shear slip is prevented and if the tensile stress is enough to overcome the tensile strength of the rock on the other side of the interface. Their results indicates that fracture crossing is very sensitive

to the intersection angle with higher angle favoring crossing and lower angles favor fracture arrest.

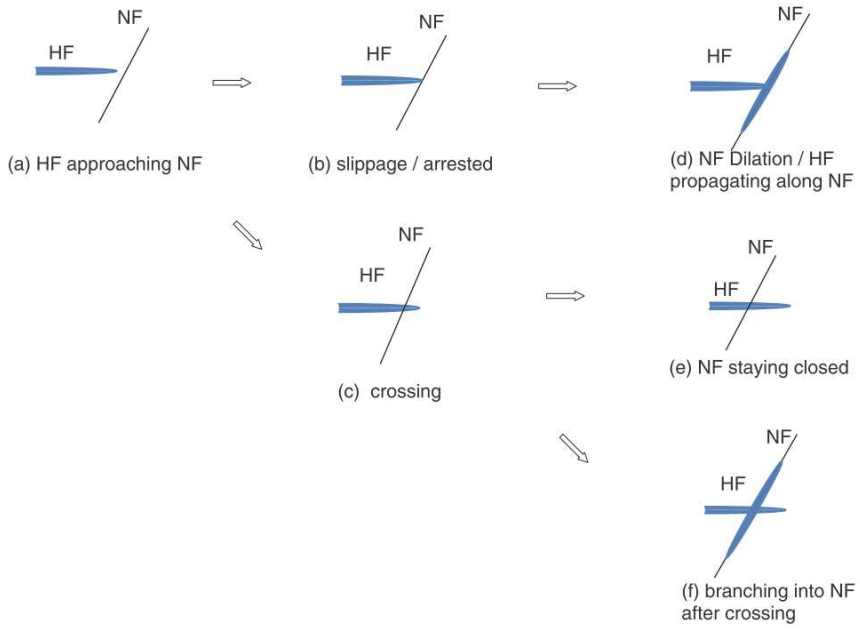

Fig. 4. 7. A summary of hydraulic and natural fracture interaction and likely crossing/arrest scenarios (after Gu et al., 2012).

Sesetty and Ghassemi (2012) developed a two-dimensional displacement discontinuity model by explicitly modeling the fluid flow inside the fractures and accounting for the HF-NF interactions. This study provided the injection pressure profiles for several cases of HF propagation near a natural fracture. The numerical examples consider the case of re-initiation from the natural fracture tips after intersection. This study demonstrates the impact of stress shadowing on the non-uniform distribution of the normal/shear stresses along the natural fracture which, in turn, results in asymmetric fracture trajectories. Their simulation results indicates that the injection pressure rises in order to maintain fracture propagation. This might be an artifact of two-dimensional modeling where fracture tips are

reduced to a single point rather than a tip front as seen in 3D configurations. The width profiles along the HF-NF system provided in Sesetty's work becomes handy in identifying the locations that might cause proppant bridging and eventually screen-outs.

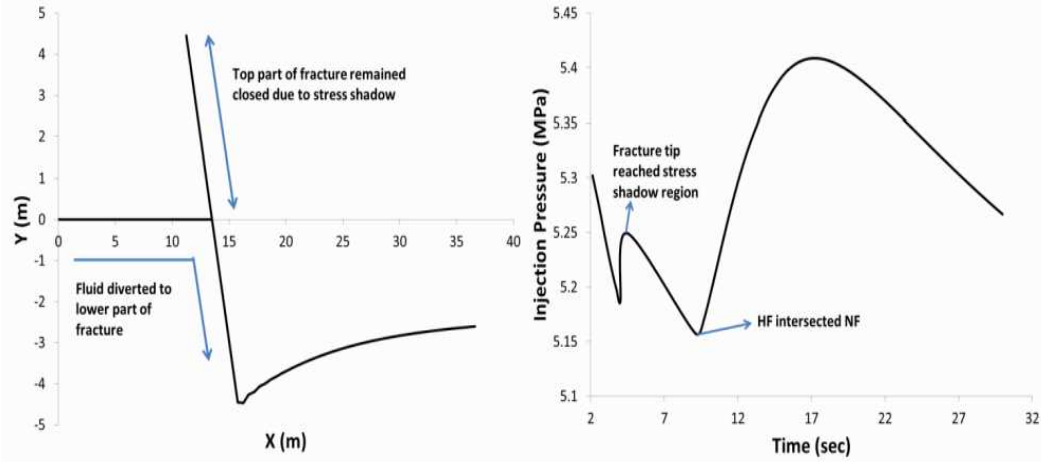

Fig. 4. 8. Re-initiation of HF from the tip of a pre-existing fracture (left) and the corresponding injection pressure profile (after Sesetty and Ghassemi, 2012).

In another numerical study, Dahi Taleghani and Olson (2013) developed an extended finite element (XFEM) model to investigate the impact of pre-existing natural fractures on the geometry of the hydraulic fracture. This 2D model assumes plane-strain condition in the horizontal plane and allows for asymmetric fracture growth and diversion of the fracture trajectory along the natural fractures. Dahi Taleghani conducted several stress analyses on static HF-NF pairs to explain the effect of an approaching hydraulic fracture on the stress state of the natural fracture. Their fracture propagation results highlight the role of in-situ stress anisotropy on the overall natural fracture geometry. Similarly to previous work, their simulations also indicate that higher differential stresses promote hydraulic fracture alignment with the S_{Hmax} direction and deflecting out of the natural fracture plane prior to

reaching the NF tips. Isotropic stress state, on the other hand, results in propagation along the natural fracture planes.

4. 2. Modelling Strategy for HF-NF Interaction Modeling

Hydraulic fracturing involves several processes that are coupled and affect each other. This multi-physics problem includes rock and fracture deformation, fracture propagation, fluid flow inside the fracture, pore fluid diffusion, and heat exchange. The presence of natural fractures further complicates the problem due to the hydraulic and mechanical interaction between the hydraulic and natural fractures. The coupling between these processes ranges from very strong two-way coupling (like the one between the fracture deformation and fluid flow) to weaker one-way interaction (like the one between the thermal stresses and rock deformation). Finding a closed-from solution to this problem, even in its simplest form, is a difficult task, if not impossible. Therefore, a numerical model is developed and used to address hydraulic fracturing near discontinuities. The remainder of this chapter discuss the steps taken to develop this 3D HF-NF model based on linear elastic fracture mechanics by neglecting poro- and thermoelastic effects.

4. 3. Governing equations

This section provides an overview of the equations that are required to develop the 3D HF-NF simulator. First and foremost, the theory of elasticity and its fundamental equations are laid out. Next, fluid flow equations are discussed as another building block of this model.

Contact mechanics, friction law, and propagation scheme are explained at the end of this section.

4. 3. 1. Theory of Elasticity

The solution of an elastic body deformation should satisfy the governing equations for a given set of stress/displacement boundary conditions. Several boundary value problems may be defined depending upon the type of conditions prescribed at the boundaries. The formulation of elasticity problems relies on the stress tensor partial differential equations and strain-displacement equations. The solution is then completed through a constitutive equation relating the stresses to displacements/strains.

The variations of the stress within a body in equilibrium may be derived by generalizing the Newton's law of motion or conservation of linear momentum to a deformable body. This principle states that the rate of the change of linear momentum is equal to the resultant forces acting on the body. Let σ_{ij} denote the Cauchy stress distribution, b_i represent the body forces, v_i denote velocity, and a_i represent acceleration. The resultant force on an arbitrary volume of the body can be expressed as:

$$R_i = \int_V \rho b_i dV + \int_A \sigma_{ji} n_j dA \tag{4. 1}$$

Where ρ is the density. The conservation of the linear momentum can therefore be expanded as follows (Irgens, 2008):

$$\int_V \rho b_i dV + \int_A \sigma_{ji} n_j dA = \frac{d}{dt} \int_V \rho v_i dV \tag{4. 2}$$

Where the right-hand-side of this equation shows the rate of change of the linear momentum. By applying the divergence theorem to the second term on the left-hand-side of the equation and rearranging, the conservation law may be expressed as follows:

$$\int_V (\rho b_i + \sigma_{ji,j} - \rho a_i) dV = 0 \tag{4. 3}$$

Since this integral holds for any volume of the body, it follows that:

$$\rho b_i + \sigma_{ji,j} = \rho a_i \tag{4. 4}$$

For a body with no acceleration this equation simplifies to the equation of static equilibrium:

$$\rho b_i + \sigma_{ji,j} = 0 \tag{4. 5}$$

Assuming static equilibrium, isotropic and homogenous body, the field equations may be summarized as follows:

$$\frac{\partial \sigma_{xx}}{\partial x} + \frac{\partial \sigma_{yx}}{\partial y} + \frac{\partial \sigma_{zx}}{\partial z} + \rho b_x = 0 \tag{4. 6}$$

$$\frac{\partial \sigma_{xy}}{\partial x} + \frac{\partial \sigma_{yy}}{\partial y} + \frac{\partial \sigma_{zy}}{\partial z} + \rho b_y = 0 \tag{4. 7}$$

$$\frac{\partial \sigma_{xz}}{\partial x} + \frac{\partial \sigma_{yz}}{\partial y} + \frac{\partial \sigma_{zz}}{\partial z} + \rho b_z = 0 \tag{4. 8}$$

The second set of equations required to complete the solution are the compatibility equations. The compatibility condition ensures that the displacements u_x, u_y, u_z are

continuous and single-valued and therefore there are not any gaps or overlaps in the displacement fields. The compatibility equations are given below:

$$\frac{\partial^2 \varepsilon_{yy}}{\partial z^2} + \frac{\partial^2 \varepsilon_{zz}}{\partial y^2} = 2\frac{\partial^2 \varepsilon_{yz}}{\partial y \partial z} \qquad \frac{\partial^2 \varepsilon_{xx}}{\partial y \partial z} = \frac{\partial}{\partial x}\left(-\frac{\partial \varepsilon_{yz}}{\partial x} + \frac{\partial \varepsilon_{zx}}{\partial y} + \frac{\partial \varepsilon_{xy}}{\partial z} \right) \tag{4. 9 a,b}$$

$$\frac{\partial^2 \varepsilon_{zz}}{\partial x^2} + \frac{\partial^2 \varepsilon_{xx}}{\partial z^2} = 2\frac{\partial^2 \varepsilon_{xz}}{\partial x \partial z} \qquad \frac{\partial^2 \varepsilon_{yy}}{\partial x \partial z} = \frac{\partial}{\partial y}\left(+\frac{\partial \varepsilon_{yz}}{\partial x} - \frac{\partial \varepsilon_{zx}}{\partial y} + \frac{\partial \varepsilon_{xy}}{\partial z} \right) \tag{4. 10 a,b}$$

$$\frac{\partial^2 \varepsilon_{yy}}{\partial x^2} + \frac{\partial^2 \varepsilon_{xx}}{\partial y^2} = 2\frac{\partial^2 \varepsilon_{xy}}{\partial x \partial y} \qquad \frac{\partial^2 \varepsilon_{zz}}{\partial x \partial y} = \frac{\partial}{\partial z}\left(+\frac{\partial \varepsilon_{yz}}{\partial x} + \frac{\partial \varepsilon_{zx}}{\partial y} - \frac{\partial \varepsilon_{xy}}{\partial z} \right) \tag{4. 11 a,b}$$

The components of the stress and strain tensor are then related through the generalized Hooke's law or the constitutive equation of linear elasticity for an isotropic and homogeneous material (Timoshenko and Goodier, 1970):

$$\sigma_{ij} = 2G\varepsilon_{ij} + \frac{2Gv}{1-2v}\delta_{ij}\varepsilon_{kk} \tag{4. 12}$$

Where G is the shear modulus, v is the Poisson's ratio, and δ_{ij} is the Kronecker delta function.

4. 3. 2. Fluid Flow inside Fractures

Fluid flow inside fractures is another governing process in hydraulic fracturing. Fluid pressure distribution, leakoff, and fracture apertures are quantified using the fluid flow equations along with the mechanical equations describing the rock/fracture deformation. The conservation of mass for a deformable control volume can be expressed as:

$$\nabla.(\rho q)+\frac{\partial(\rho A)}{\partial t}=0 \tag{4. 13}$$

Where ρ is the fluid density, q is the volumetric flow rate, and A is the area normal to the flow. To further expand this and rewrite it in terms of fluid pressure a proper transport law should be used. Darcy's law which has been long used in the soil mechanics and oil and gas industry can be used to write the conservation equation in terms of fluid pressure. The Darcy's law state that the pressure gradient in a medium is directly proportional to the flow rate through a constant called permeability (Batchelor, 1967):

$$q=-\frac{kA}{\mu}\nabla p \tag{4. 14}$$

Where A is the area normal to the flow, μ is the fluid viscosity, and k is the permeability. Substituting q in the continuity equation from the Darcy's equation and assuming incompressible fluid yields:

$$\nabla.\left(-\frac{kA}{\mu}\nabla p\right)+\frac{\partial A}{\partial t}=0 \tag{4. 15}$$

An effective approach to model fluid flow in fractures is by using the lubrication theory assuming flow through two smooth parallel plates that are separated by an aperture, w (Witherspoon et al., 1980). Fractures with slightly rough surfaces could still be modeled using the lubrication theory. Higher degrees of surface roughness could be accounted for by using correction factors such as the one proposed by Lomize (1951). By applying the cubic law and accounting for the leakoff, and sink/source terms, the final form of the continuity equation can be expressed as follows:

$$\nabla.\left(\frac{w^3}{12\mu}\nabla p\right)=\frac{\partial w}{\partial t}-Q_{inj}\delta(X_{inj})+2v_L \tag{4. 16}$$

Where w is the local fracture aperture, v_L is the leakoff velocity, and Q_{inj} is the fluid injection rate per unit area (see Fig. 4. 9).

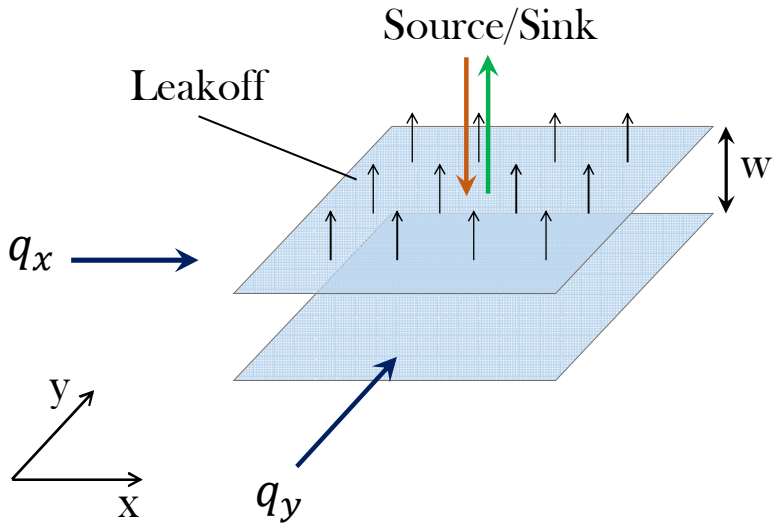

Fig. 4. 9. Fluid flow components through smooth parallel plates separated by an aperture w.

4. 3. 3. Contact Elements

Natural discontinuities such as natural fractures and faults are generally under compressive stresses. Therefore, their surfaces are in contact and maintain their load-carrying capacity. This load-carrying capacity is maintained as long as the fracture surfaces are in contact

with each other. Despite mechanical contact, natural fractures can still act as conduits for fluid flow given their rough surfaces which result in a substantial hydraulic conductivity in most cases (Fig. 4. 10). For a contact element the deformation and the applied stresses are related through the fracture stiffness in the normal and transvers direction (Goodman et al., 1968):

$$\Delta\sigma_n = K_n \Delta D_n \tag{4. 17}$$

$$\Delta\sigma_s = K_s \Delta D_s \tag{4. 18}$$

Where K_n and K_s are normal and shear stiffness and D_n and D_s are normal and shear displacement discontinuities that measure the relative displacement of the two surfaces of the fracture. A more comprehensive discussion of the displacement discontinuities are provided in the numerical implementation section. It is worth mentioning that a *non-equilibrium* joint formulation is adopted to account for the initial deformation of the closed fractures due to the in-situ stresses. The mathematical equations describing the non-equilibrium joint behavior is explained in details in chapter 2, and 3. It should be emphasized that the joint constitutive equations hold only when the fracture is mechanically closed, (i.e., $\sigma'_n > 0$).

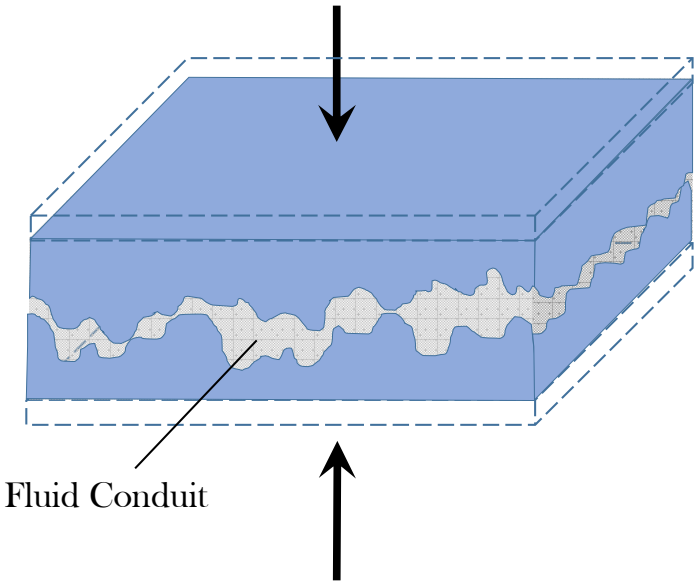

Fig. 4. 10. Rough surfaces of a natural fracture that are in mechanical contact while providing hydraulic conductivity.

4. 3. 4. Friction Law

Rock joints can destabilize and undergo inelastic deformation due to the combined effect of induced stresses and pressure. The shear resistance provided by the compressive in-situ stresses often stabilize the fracture against shear slip (see Fig. 4. 11). However, the reduction of the shear resistance can trigger inelastic shear deformation. Therefore, a proper friction law should be utilized to quantify the shear stress level of a destabilized fracture.

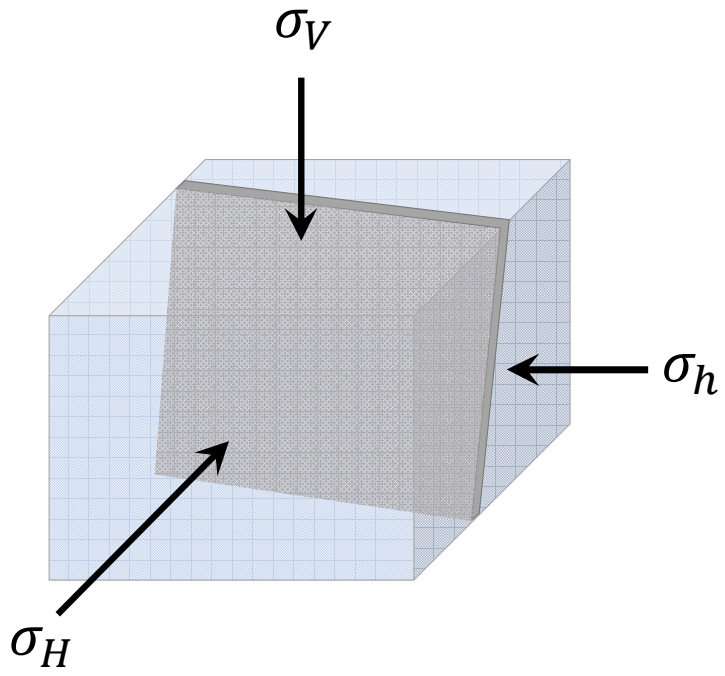

Fig. 4. 11. A stable sub-vertical natural fracture under in-situ stress condition.

The Mohr-Coulomb criterion is used in this study to identify the slip status of the fracture. This criterion, which is categorized as an elastic-perfectly-plastic stress law, relates the shear stress of the natural fracture to its normal stress as follows:

$$\left|\sigma_s\right| \le c^{NF} + \sigma'_n \tan(\phi^{NF}) \tag{4. 19}$$

Where c^{NF} and ϕ^{NF} are the natural fracture cohesion and friction angle, respectively. This inequality states that the shear stress of the fracture cannot exceed its shear resistance (right-hand-side of the inequality). At shear stresses below the threshold, the joint deforms elastically according to equation 4. 18. Beyond that, an iterative scheme, is used to determine the shear stress as described in the numerical section. The shear resistance is mainly controlled by the effective normal stress on the fracture. A graphical representation

of the stress state of the natural fracture and its onset of shear slip is shown in the Mohr-Coulomb stress space in Fig. 4. 12.

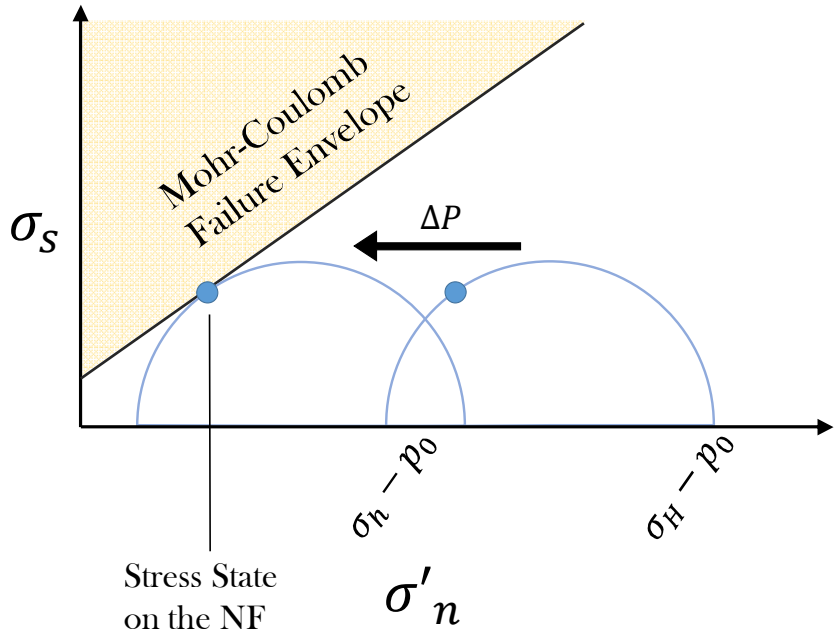

Fig. 4. 12. The onset of natural fracture shear slip caused by the elevated pore pressure due to injection.

4. 3. 5. Fracture Propagation

Introduced by Griffith (1921) and later modified by Irwin (1957), Linear Elastic Fracture Mechanics (LEFM) has been long used in several engineering disciplines to study fatigue, cracking and fracture propagation in solids. This concept assumes linear elastic and isotropic materials and can be studied by either the near-tip stress fields or the energy release rate. Griffith (1921) adopted the theorem of minimum energy to constitute his crack

theory. Let a denote the crack's half-length, γ represent the energy needed to create a unit new surface area (surface energy), the surface energy released by a crack is as follows:

$$W_s = 2(2a\gamma) = 4a\gamma \tag{4. 20}$$

Following Inglis' solution, Griffith calculated the total energy released due to the presence of a crack in an infinite medium:

$$W = \frac{\pi a^2 \sigma^2}{E'} \tag{4. 21}$$

Applying the minimum energy theorem and substituting the energy components yields:

$$\frac{\partial}{\partial a}\left(W - W_s\right) = \frac{\partial}{\partial a}\left(\frac{\pi a^2 \sigma^2}{E'} - 4a\gamma\right) = 0 \tag{4. 22}$$

Solving for the stress to initiate crack extension results:

$$\sigma_c = \sqrt{\frac{2\gamma E'}{\pi a}} \tag{4. 23}$$

Where $E' = E$ for the plane stress condition, and $E' = E/(1-\nu^2)$ for the plane strain condition. It is interesting to note that this work was initially motivated by the discrepancy that was observed between the strength of the material in the atomic level and the strength of the bulk material. It is known that manufactured brittle materials fracture at stresses 10 to 100 times less than the material strength predicted by the theoretical atomistic models. He attributed this discrepancy to the presence of flaws in the brittle materials. A comparison between the failure stress between the atomistic and Griffith model justifies this discrepancy:

$$\sigma_c = \sqrt{\frac{\gamma E}{a_0}} \tag{4. 24}$$

Where a_0 is the equilibrium distance between the atomic planes. Given the fact that $a_0 \ll a$ the failure stress of the bulk material is expected to be much lower than the one predicted in the atomic level (i.e., $\sigma_c^{bulk} \ll \sigma_c^{atomic}$).

The strain energy released per an increment da of the fracture length can be expressed as follows:

$$G = \frac{\pi a \sigma^2}{E'} \tag{4. 25}$$

The failure condition is met when the Griffith energy release rate reaches its critical value $G_c = 2\gamma$ which is a material property and is regarded as the material's resistance to fracture growth. Irwin later recognized that the energy release rate is directly related to the square of stress intensity at the crack tips as follows:

$$G = \frac{K^2}{E'} \tag{4. 26}$$

4. 4. Numerical Implementation

The numerical model developed and used in this study is comprised of two main components; the mechanical module which is implemented to study rock and fracture stress and displacements and the fluid flow module which concerns the fluid flow inside the fractures and its interaction with the matrix via leakoff. These modules work hand-in-hand to provide the solution to the coupled process that was laid out above.

4. 4. 1. Boundary Integral Equations

The numerical scheme used to discretize the fracture domain for stress analysis is based on an indirect boundary element method (BEM) called "displacement discontinuity method" or DDM. The elastic displacement discontinuity formulation is derived by superimposing the singular solution for discontinuity in the displacement field along the fracture. The displacement discontinuity is attributed to the discontinuous jump in the displacement field that is observed along the fracture faces. The displacement discontinuities measure the relative displacement between the negative ($\bar{z} = 0^-$) and positive ($\bar{z} = 0^+$) side of the fracture surfaces as shown in Fig. 4. 13:

$$D_{33} = u_3^- - u_3^+ \tag{4. 27}$$

$$D_{13} = u_1^- - u_1^+ \tag{4. 28}$$

$$D_{23} = u_2^- - u_2^+ \tag{4. 29}$$

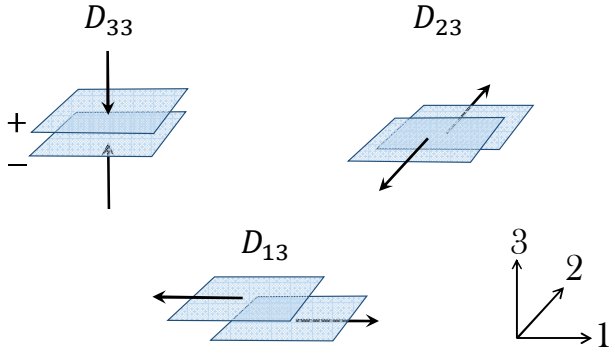

Fig. 4. 13. Three displacement discontinuity components shown in their local coordinate system.

The stresses at each point in the infinite domain may be calculated using the following integral form knowing the intensity of the DD sources as follows:

$$\sigma_{ij}(x) = \int_{\Gamma} T^{dc}_{ijkn}(x - x')D_{kn}(x')d\Gamma(x') + \sigma^{0}_{ij}(x) \tag{4. 30}$$

Where T^{dc}_{ijkn} is the stress component *ij* induced by a unit continuous DD component *kn* in the infinite medium (also called the influence function or stress kernel), D_{kn} is the displacement discontinuity component *kn*, *x* is the location of the field point, and *x'* represents the location of the source point. To establish a relationship between the induced stresses and the source intensity over a finite boundary element the stress kernel can be evaluated over the source element as follows:

$$S^{dc}_{ijkn} = a_{il}a_{jm}\int_{\Gamma_s} T^{dc}_{lmkn}d\Gamma_s \tag{4. 31}$$

where a_{il} is the rotation matrix from the source element to the influenced coordinate system. By discretizing the boundary into *M* boundary elements, the boundary integral equation for the stresses can be expressed as follows:

$$\sigma_{k3}(x) = \sum_{j=1}^{M} S^{dc}_{k3n3}(x)D^{j}_{n3} \tag{4. 32}$$

Where D^{j}_{n3} is the magnitude of the displacement discontinuity at the source element *j*.

The fundamental solution for the displacement discontinuity method which has its roots in the principle of superposition was initially obtained to study mining problems. Some of the early attempts and formulations regarding DD fundamental solutions can be found in

Salamon (1963). Crouch (1976) derived a solution for DD line segments in an infinite media. Later, Crouch and Starfield (1980) extended the solution to three-dimensional and heterogeneous bodies. Point DD solutions are also utilized in the literature to construct DD methods by integrating the solution over a certain element shape. Examples of such derivations may be found in Curran and Carvalho (1987), Vandamme (1986), and Carvalho (1990). Following Cleary (1977) point force solution, Carvalho and Curran (1987) derived a fundamental solution for displacement discontinuity in a poroelastic medium. Ghassemi and Zhang (2006) developed 2D DD for thermo-poroelastic media based on the fundamental solution from Berchenko (1998). It should be noted that spatial integration of the fundamental DD solutions become improper when evaluating the effect of a boundary element on itself (i.e., self-effect influence coefficient). This is due to the singularity in the fundamental solution that arises when the distance between the influencing (source) and the influenced element approaches zero. The singularity should be properly treated to construct a full set of DD equations. Several standard techniques has been proposed and used over the years to treat the singularity (Kellogg, 1929; Banerjee and Butterfield, 1981; Guiggiani et al., 1992). A detailed description of the fundamental solution and its numerical implementation can be found in Kumar and Ghassemi (2016).

4. 4. 2. Fluid Flow Equation

The fluid flow equations are discretized using a Galerkin finite element method (FEM). The numerical implementation of the fracture fluid flow is carried out using the same mesh that was used in our mechanical module for BEM. Assuming linear variation of the fluid pressure across elements, the fluid pressure in a certain element is interpolated from the nodal values as follows:

$$p^e = N^e \tilde{p} \tag{4. 33}$$

Where superscript *e* denotes elemental value, *N* is the interpolation function and $\tilde{p}$ is the nodal pressure vector. The discretized fracture flow equations are given by:

$$[K].\{\tilde{p}\} = \{F\} \tag{4. 34}$$

Where the coefficient matrix *K* and the vector *F* are defined as follows:

$$K = \sum_{e=1}^{M} \int_{\Gamma_e} \frac{w^3}{12\mu} \nabla^T N^e . \nabla N^e d\,\Gamma \tag{4. 35}$$

$$F = -\sum_{e=1}^{M} \int_{\Gamma_e} \frac{\partial w}{\partial t} \mathrm{N}^{eT} d\,\Gamma + \int_{\partial\Gamma^P} \mathrm{N}^P Q_i dS \tag{4. 36}$$

Where *w* is the fracture aperture, *Q* represent the source/sink terms, *M* is the total number of elements. A detailed description of the fluid flow implementation can be found in Kumar and Ghassemi (2016).

4. 4. 3. Fracture Propagation

Fracture propagation is an integral component of our model which captures the incremental growth of a fluid-driven fracture in response to injection. Energy release rate and stress intensity approach were explained in the previous section as two common approaches in studying fracture propagation. We use the stress intensity approach and enforce the critical stress intensity criterion to ensure stable fracture propagation. Considering three modes of propagation (Fig. 4. 14), the stress intensities are given (Aliabadi and Rooke, 1991):

$$K_I = \frac{E}{4(1-\nu^2)}\sqrt{\frac{\pi}{2r}}D_{33}(r) \tag{4. 37}$$

$$K_{II} = \frac{E}{4(1-\nu^2)}\sqrt{\frac{\pi}{2r}}D_{13}(r) \tag{4. 38}$$

$$K_{III} = \frac{E}{4(1+\nu)}\sqrt{\frac{\pi}{2r}}D_{23}(r) \tag{4. 39}$$

Where r measures the distance between the crack edge and the DD estimation point, and K_I, K_{II}, K_{III} are the mode I, II and III stress intensity factors (SIF), respectively. The stress intensity components are evaluated at $r = 0.80L$ in this study (Safari and Ghassemi, 2015).

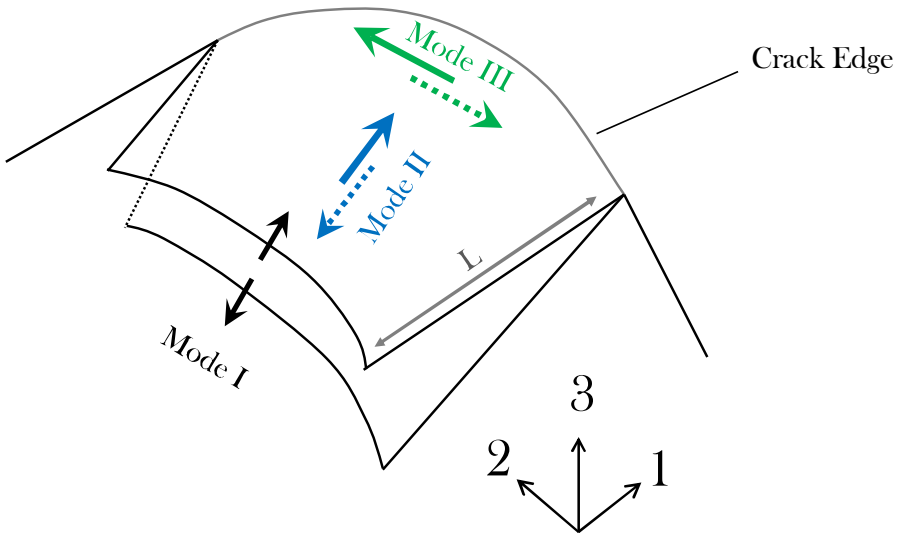

Fig. 4. 14. Fracture propagation modes: mode I corresponds to opening, mode II represents shearing and mode III is the tearing mode.

Hydraulic fracturing has conventionally been viewed as a tensile-dominated fracture with insignificant contribution of in-plane and out-of-plane shearing along it edges. This is often implied in the development of pseudo-3D and even 3D propagation models as it simplifies

the implementation to a great extent. It should be noted that mode II (in-plane shear) loading results in front turning/curving while keeping a continuous fracture tip front. However, mode III loading causes segmentation and tears the fracture front. Therefore, mode III contribution is neglected in this work when calculating the angle of propagation.

Whether the hydraulic fracture crosses a certain natural fracture is determined upon its intersection with the natural fracture. The crossing criterion used in this study is the one developed by Gu and Weng (2012) as an extension to the Renshaw and Pollard's (1995) criterion. This criterion simply takes the tendency of the natural fracture to slip to identify the state of crossing. For a hydraulic fracture to cross an interface, the resultant shear stress on the interface should be such it does not initiate slip. This ensures that the tip stresses are transmitted to the opposite side of the interface to continue propagation. For a frictional rock interface this criterion is expressed as:

$$\left|\tau_\beta\right| < c^{NF} + \sigma_{\beta y}\tan(\phi^{NF}) \tag{4. 40}$$

Where τ_β and $\sigma_{\beta y}$ are the shear and normal stresses acting on the interface when a hydraulic fracture tip is approaching the interface (see Fig. 4. 15). At the HF crack tip, these stresses can be quantified as a function of the stress intensity factor *K* as follows:

$$\tau_\beta = K\sin(\frac{\theta}{2})\sin(\frac{3\theta}{2})\sin(2\beta) + K\sin(\frac{\theta}{2})\cos(\frac{3\theta}{2})\cos(2\beta) - \frac{\sigma_H - \sigma_h}{2}\sin(2\beta) \tag{4. 41}$$

$$\sigma_{\beta y} = K + K\sin(\frac{\theta}{2})\sin(\frac{3\theta}{2})\cos(2\beta) - K\sin(\frac{\theta}{2})\cos(\frac{3\theta}{2})\sin(2\beta) \quad (4.\ 42)$$
$$+\frac{\sigma_H + \sigma_h}{2} - \frac{\sigma_H - \sigma_h}{2}\cos(2\beta)$$

Where the normal and shear stresses are evaluated by setting $\theta = \beta$ (i.e., the intersection angle) and K is calculated using the following quadratic equation:

$$A_1 K^2 + A_2 K + A_3 = 0 \quad (4.\ 43)$$

The details of the quadratic equation parameters may be found in the original paper. This criterion allows to determine whether a hydraulic fracture crosses a natural fracture at any intersection angle.

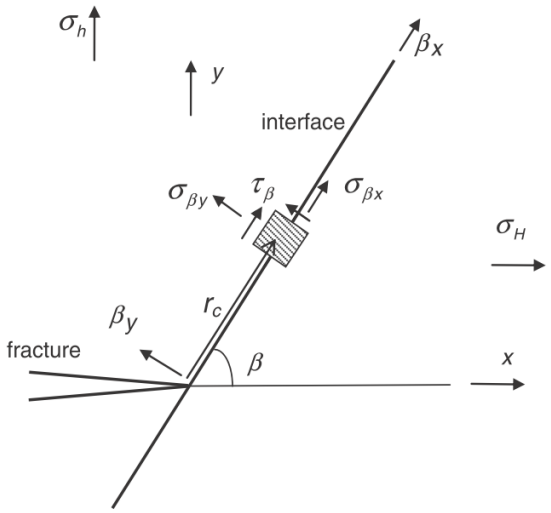

Fig. 4. 15. Schematic of a hydraulic fracture approach an interface (After Gu and Weng 2012).

4. 5. Verification Examples

Two verification examples are provided to check the validity of the 3D displacement discontinuity model used in the study. These examples include the response of a static fracture to constant internal pressurization and it propagation due to a constant injection rate.

4. 5. 1. Pressurized Penny-Shaped Fracture

The first example concerns the normal opening of a pressurized fracture in an infinite rock. The numerical results are compared with a closed-form solution provided by Sneddon (1946). The fracture used in this example is a penny-shaped fracture with radius $a = 1.0\,\text{m}$. This fracture is subjected to a constant internal pressure of 1.0 MPa as shown in Fig. 4. 16. The surrounding rock has a Young's modulus of 25 GPa and a Poisson's ratio of 0.25.

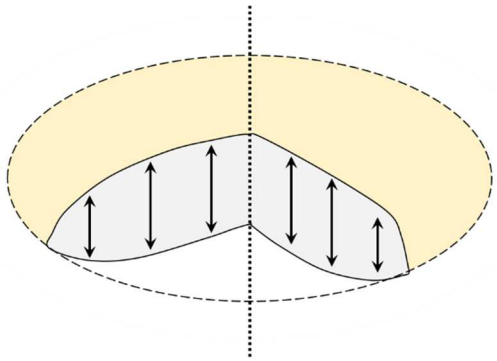

Fig. 4. 16. A penny-shaped fracture subjected to a constant internal pressure P.

Fracture openings are plotted along the radius of the pressurized fracture in Fig. 4. 17. This figure shows that the normal opening has its highest value at the center of the fracture and it decreases towards the edge of the fracture. As can be seen, the numerical DD results are in a good agreement with that of the analytical solution. It should be pointed out that using

constant DD elements results in the overestimation of the displacement discontinuities. The numerical DD values become less accurate closer to the fracture tip. Several methods are proposed to address this issue including using special tip elements. However, this is beyond the scope of this work and we used constant DD elements throughout this study.

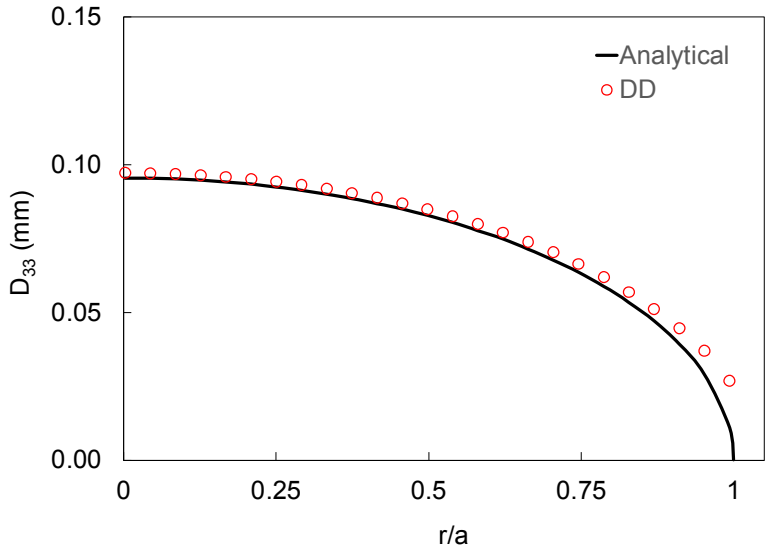

Fig. 4. 17. Comparison between the normal displacements discontinuity obtained numerically using the 3D DD model and the Sneddon's solution.

4. 5. 2. Propagation of a Radial KGD Fracture

Unlike the first verification example which examined the opening of a static fracture, the next example compares the width and length of a propagating fracture obtained numerically to the radial KGD results. Propagation is achieved by pumping water under the constant rate of 1.0×10^{-3} m^3/s in a radial fracture with initial radius of 1.0 m. The Young's modulus of the surrounding rock is 50 GPa and its Poisson's ratio is 0.25.

Fig. 4. 18 shows the changes of the fracture radius and its width at the injection element. It can be observed in this figure that both radius and width show excellent agreement with the radial KGD results. The minor differences are attributed to the fact that the KGD model does not take into account the fracture toughness while we consider this parameter in our model. Nonetheless, the current model shows good agreement with the analytical ones and can be applied to more sophisticated example that are not tractable using analytical approaches.

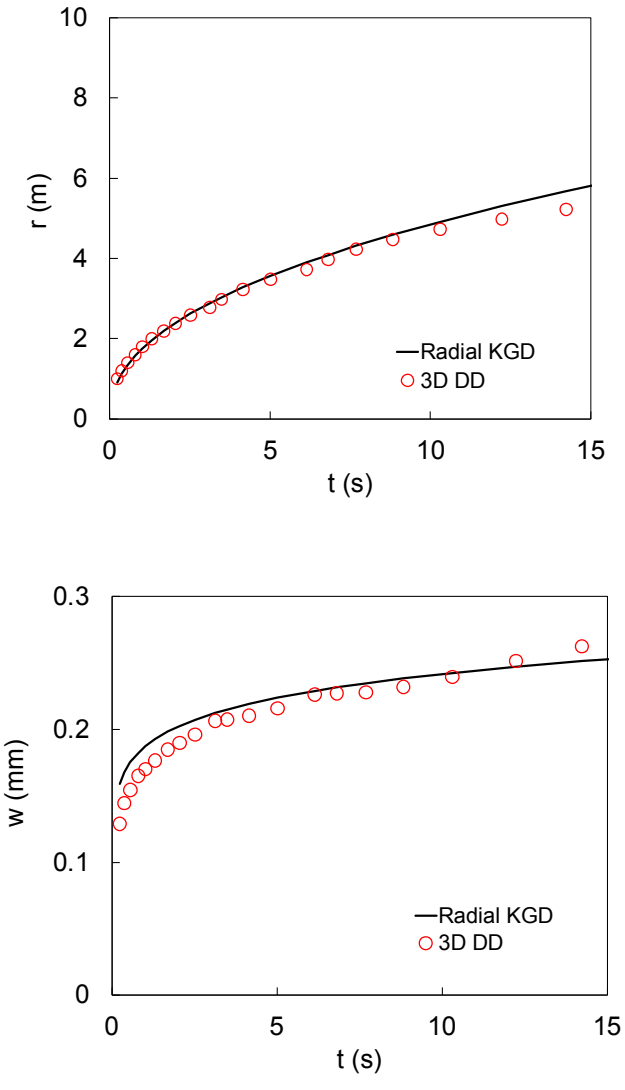

Fig. 4. 18. Comparison between numerical and analytical results for the radius of a penny-shaped fracture (top) and its maximum width at the injection well (bottom).

4. 6. Application Examples

Our integrated 3D HF-NF model is applied to a range of hydraulic fracturing problems involving natural fractures and discontinuities. It is our objective to closely examine the important problem of HF/NF coalescence in 3D which has not been rigorously treated or simulated using very simple static formulation neglecting the dynamics of fracture propagation. In particular, we study the ultimate fracture geometry, treatment pressure and fracture width. Additionally, we highlight the differences between propagation in the vicinity of discontinuities and the propagation of an isolated hydraulic fracture. Moreover, fracture engulfing, a 3D modeling feature, is presented in this section.

The first two examples discuss the fracture crossing and arrest modes and their corresponding injection pressure profiles. The hydraulic fracture is initiated in the *YZ*-plane (Fig. 4. 19), perpendicular to the minimum horizontal stress (i.e., σ_h) at a distance d from the natural fracture. The hydraulic fracture approaches the natural fracture at an intersection angle of 60° and 90° in the first and second example, respectively. Leakoff is neglected (the impact of leakoff on this class of problems is studied in detail in Kamali and Ghassemi, 2019) in the following examples and the rest of the input parameters are listed in Table 4. 1.

Table 4. 1. Input parameters for the 3D HF-NF simulations. The rock mechanical properties are similar to that of the Eagle Ford shale (Hu et al., 2014).

parameter	unit	Value

Young's modulus	GPa	35.0
Poisson's ratio	-	0.25
Minimum horizontal stress	MPa	29.0
Maximum horizontal stress	MPa	32.5
Pore pressure	MPa	24.0
Mode I stress intensity	$MPa.m^{1/2}$	3.0
NF length	m	12.0
NF height	m	4.0
NF distance from wellbore	m	3.0
Injection rate	m^3/s	0.001
fluid viscosity	Pa.s	0.001
NF Cohesion	MPa	0.0
NF friction angle	°	20
Intersection angle	°	60, 90

4. 6. 1. Partial Fracture Arrest

Fracture arrest occurs when the approached natural fracture experiences opening and/or shear slip. This example illustrates a fracture arrest scenario in which the hydraulic fracture propagates towards a natural fracture at a 60° angle. Fig. 4. 19 shows the hydraulic and natural fracture footprint along with the pressure contours before, during, and after intersection. It can be observed in these figures that the hydraulic fracture propagates radially in the uniform stress field before reaching the natural fracture. The pressure in the natural fracture is at the initial reservoir pressure level before being intersected by the hydraulic fracture. Because of the hydraulic communication between the HF and NF upon intersection, the fluid pressure in the natural fracture increases by continued injection. Once the hydraulic fracture attains sufficient energy to propagate, it extends in the other

directions away from the natural fracture. It is interesting to note that the hydraulic fracture tends to grow above and below the natural fracture leading to an *engulfing* pattern. It is needless to say that this geometry cannot be captured using 2D or simpler 3D models that lack rigorous propagation capabilities.

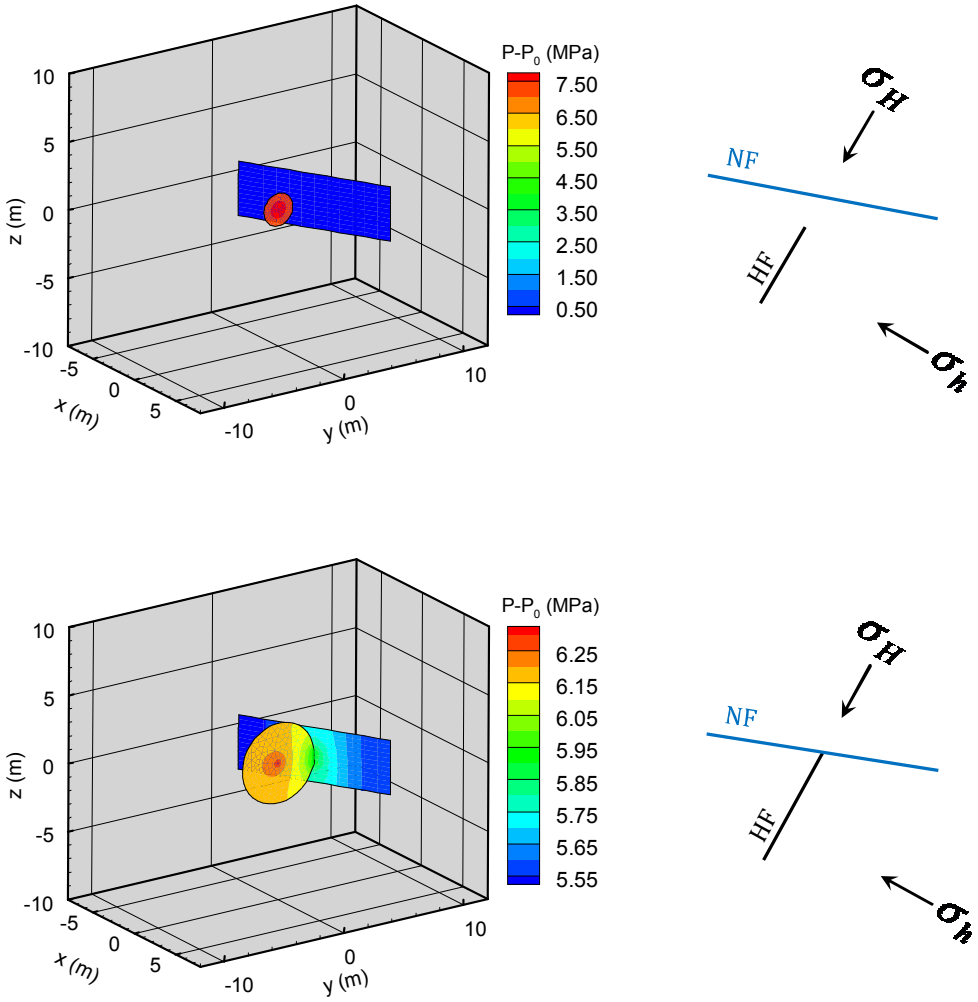

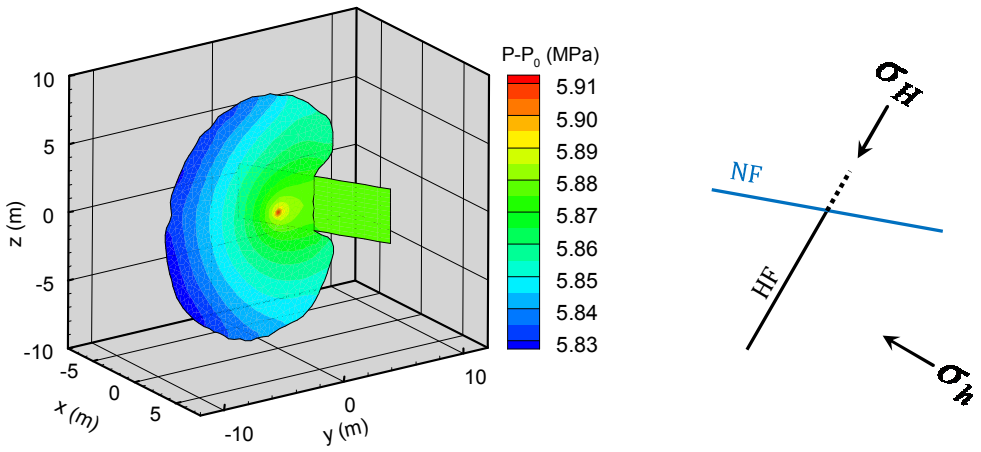

Fig. 4. 19. Hydraulic fracture propagation near a natural fracture. Partial HF arrest at the intersection with NF. The ultimate geometry reveals that the HF can propagate from its other side and even engulf the NF.

The hydraulic and mechanical interaction between the fractures are expected to impact the treatment pressure. The injection pressure profile for this example is shown in Fig. 4. 20. This figure shows several distinct intervals in the pressure profile during the injection (intervals are separated by dashed lines). The first one is the continuous pressure drop early during pumping. This interval corresponds to fracture propagation before intersection. The second interval corresponds to the HF-NF intersection. The start of this interval is marked by an arrow in Fig. 4. 20. A sudden pressure drop is a characteristic of this period which is caused by hydraulic communication between the hydraulic and natural fracture. The pressure starts to increase again which eventually results in further propagation (marked by another arrow). It should be noticed that the pressure response might vary under different conditions.

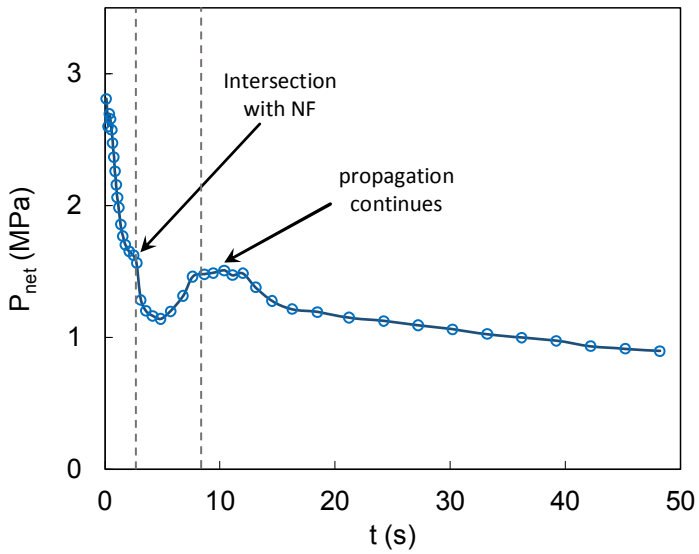

Fig. 4. 20. Pumping pressure history for a hydraulic fracture partially arrested by a natural fracture. The net pressure profile shows a dip consisting of a pressure drop period followed by an increase in the net pressure. This is caused by the intersection with natural fracture. The hydraulic fracture starts to propagate again after it recovers from this pressure drop due to NF pressurization.

The stress state on the natural fracture is affected by an approaching hydraulic fracture. The tensile stress field at the tip of a propagating fracture induces local compression or tension on the natural fracture depending on the angle of approach.

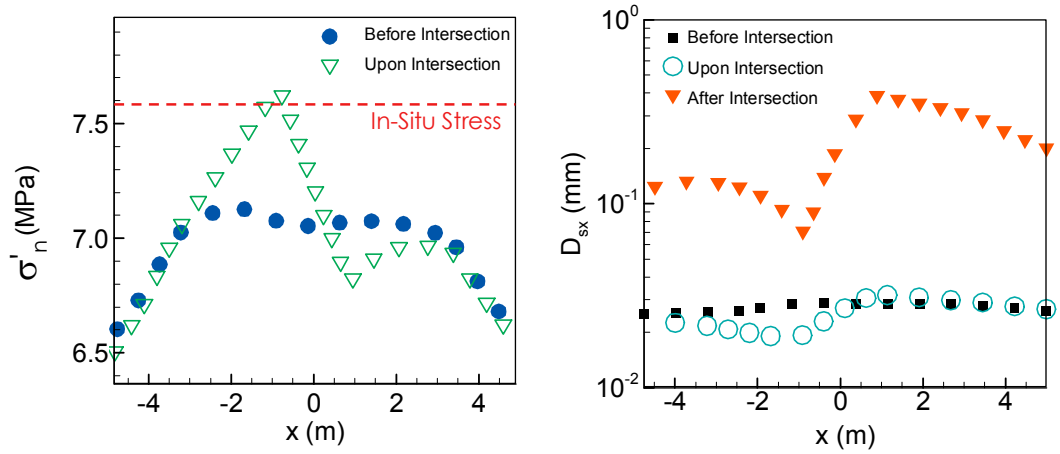

Fig. 4. 21. Changes of the effective normal stress along the natural fracture due to a hydraulic fracture approaching at an angle of 60 degrees (left). Changes of shear displacement along the natural fracture before, at, and after intersection with a hydraulic fracture (right). Considering the non-equilibrium joint formulation and the initial deformation of the natural fractures due to the in-situ stresses, the normal stress along the fault is lower than the in-situ stress.

The variations of the effective normal stress is plotted for a horizontal line (dashed line in Fig. 4. 22) along the center of the natural fractures in Fig. 4. 21. This figure shows the normal stress when the hydraulic fracture intersects the NF and also when it is farther away from the NF. It can be observed in this figure that the normal stress increases on the left side of the natural fracture while it decreases on the right side (when compared to the case where HF is far away). The region under induced compression makes a sharper angle with the HF (see Fig. 4. 22). Similar to the normal stress, the shear displacement is also explored before, during, and after intersection. This figure shows the shear displacement increase by an order of magnitude after intersection. This is, in fact, due to the pressure increase in the NF after intersection which leads to shear slip. It is interesting to note that the shear slip is not symmetric with respect to the center of the NF. This is attributed to an asymmetric

stress profile caused by the intersecting hydraulic fracture (which was arrested and then engulfed the NF).

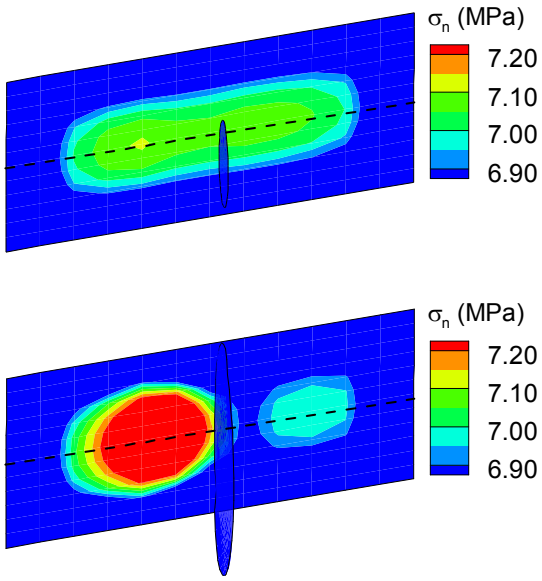

Fig. 4. 22. Effective normal stress on the natural fracture (top) when the HF is far away (bottom) right before intersection.

4. 6. 2. Hydraulic Fracture Crossing a Natural Fracture

Hydraulic fractures are not always arrested by discontinuities in the rock and as shown above they can engulf the NF and so continue to grow. This example presents a case where a hydraulic fracture propagates towards a natural fracture orthogonally. Unlike the previous example, the hydraulic fracture crosses the NF and propagates freely in all directions. This is mainly because of the higher normal stress on the natural fracture and zero shear stress along the NF, which together inhibit the shear slip on the NF and facilitate fracture crossing. Although, the fracture geometry deviates from its radial shape for a limited time upon intersection, the HF recovers its radial shape after crossing the NF as shown in Fig. 4. 23. It is worth noticing that although the HF crosses the NF, there is still hydraulic

connectivity between the fractures increasing the pressure inside the natural fracture. Having said that, the natural fracture remains mechanically closed in this case because it is subjected to a higher in-situ stress as compared to the HF.

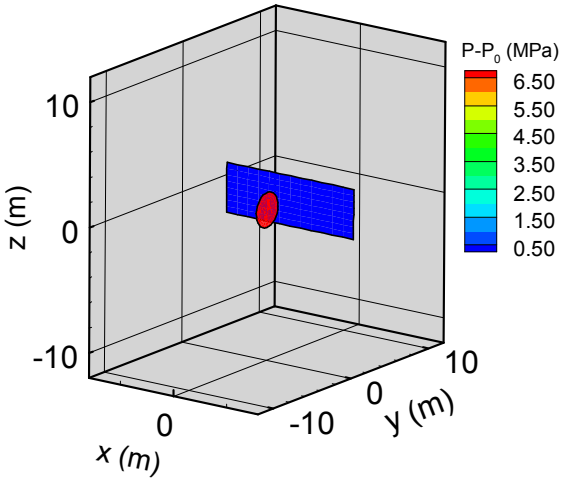

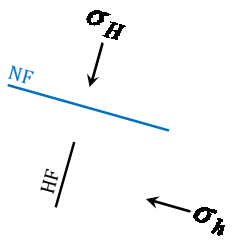

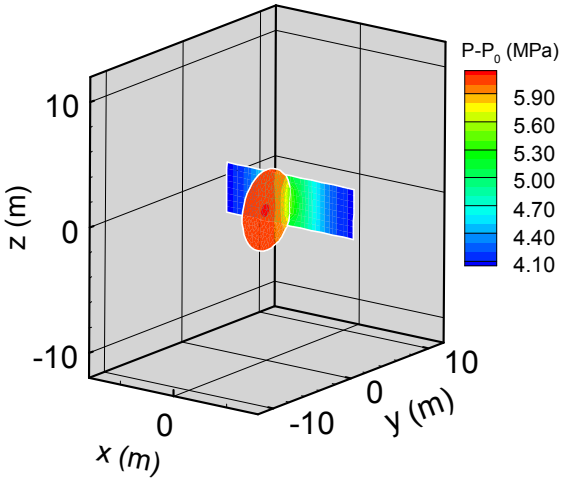

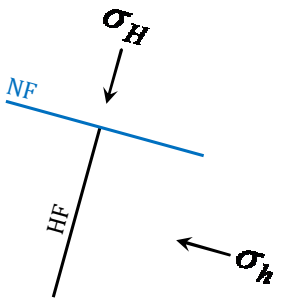

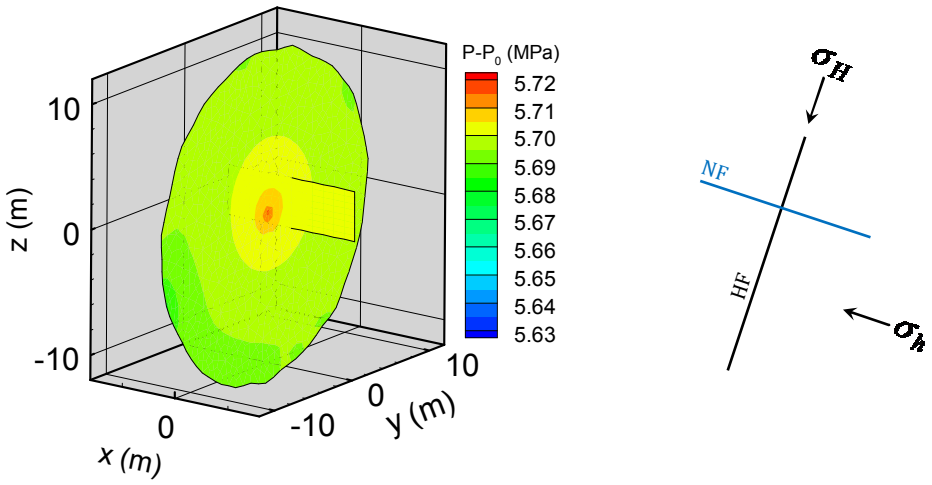

Fig. 4. 23. Hydraulic fracture crossing a natural fracture orthogonally. The fracture edges are not ideally smooth at the end of simulation. This is caused by the relatively coarse elements at the tip which affects the stress intensity calculations. Average mesh size is determined based on the problem geometry and configuration during the dynamic remeshing process. This has been implemented to make the coalescence scheme more robust and to avoid mesh convergence issues.

The injection pressure profile for this example is shown in Fig. 4. 24. It can be seen in this figure that the propagation has multiple stages similar to the previous example. Before intersecting the natural fracture, the pressure decreases similar to that observed in the propagation of an isolated HF. The hydraulic fracture then experiences a sudden pressure drop as it hits the natural fracture. Propagation continues once again after the pressure inside the hydraulic fracture is sufficient for propagation. It is worth noticing that the crossing and arrest cases resulted in similar pressure responses. This is explained by the fact that even under the arrest condition, the majority of the hydraulic fracture edge, except

for a limited portion near the NF, freely propagates. Note that the fracture edges are not ideally smooth at the end of simulation. This is caused by the relatively coarse tip elements which affects the stress intensity calculations.

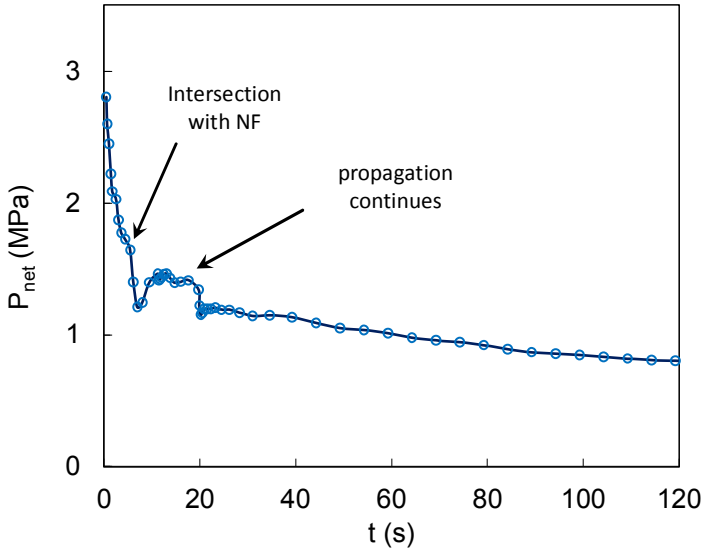

Fig. 4. 24. Pumping pressure history for a hydraulic fracture crossing a natural fracture at a 90° angle. The net pressure plot shows a pressure drop followed by an increase in the net pressure after HF-NF intersection. The onset of pressure drop and intersection is marked by a vector. The stress state and the orientation of the natural fracture result in the fracture crossing mode. The instance of fracture crossing is marked by another pressure drop. The exaggerated pressure drop upon crossing is a modeling artifact due to mesh considerations as explained above.

4. 6. 3. HF Propagation near Natural Fractures and Stress Barriers

To illustrate the combined effect of stress barriers and natural fractures on the hydraulic fracture geometry, a hydraulic fracture is initiated 2 m below a strong stress barrier ($\Delta\sigma$ = 3 MPa) and 3 m away from the natural fracture (Fig. 4. 25). The intersection angle is

assumed to be 60° in this example. The rest of the input parameters are similar to the first example.

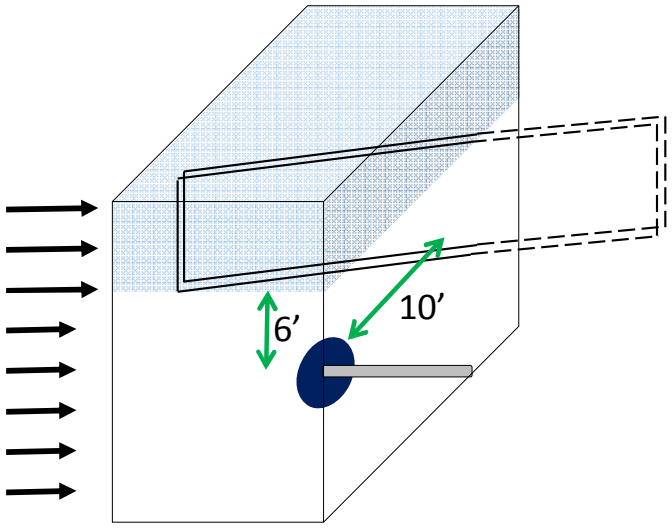

Fig. 4. 25. Stress barrier and the natural fracture configuration.

Unlike the previous examples where the fracture geometry was impacted only by the discontinuities, the propagation pattern is influenced by the NF and the stress barrier in this example. The partial arrest near the stress barrier and the natural fracture and the preferential growth in other directions is expected to yield a complex geometry. Fig. 4. 26 shows the evolution of a hydraulic fracture and its normal opening (Dn) near a natural fracture and a stress barrier. It can be seen in this figure that the fracture propagates like a penny-shaped fracture before reaching the stress barrier and the NF during the earlier stages. However, due to the partial arrest near the NF and also the stress barrier, the fracture soon conforms to the propagation barriers (i.e., NF and the stress barrier) and propagates asymmetrically away from both features. In case of a symmetric stress barrier, it was possible to achieve a PKN type fracture. However, this example involves only one stress

barrier at the top. It should be emphasized that due to the ability of the hydraulic fracture to propagate below the natural fracture (engulfing), it is possible the HF will extend beyond the natural fracture even though, it is partially arrested by the NF. It is worth noticing that, because of the asymmetric fracture growth in this case, the location of the maximum fracture width moves away from the injection point as the fracture extends. In fact, the location of the maximum fracture width shifts 20 ft (6 m) below the injection point after 70 seconds of injection. The intersection line between the HF/NF can serve as a choke for proppant. Also, the maximum aperture shifting to the lower end of the system will prevent uniform proppant distribution in the HF. The final configuration of the hydraulic fracture shows vertical containment near the stress barrier, partial fracture arrest by the natural fracture, and engulfing on the lower side of the natural fracture. This example illustrates the capabilities of our integrated 3D HF-NF simulator in handling complex propagation patterns.

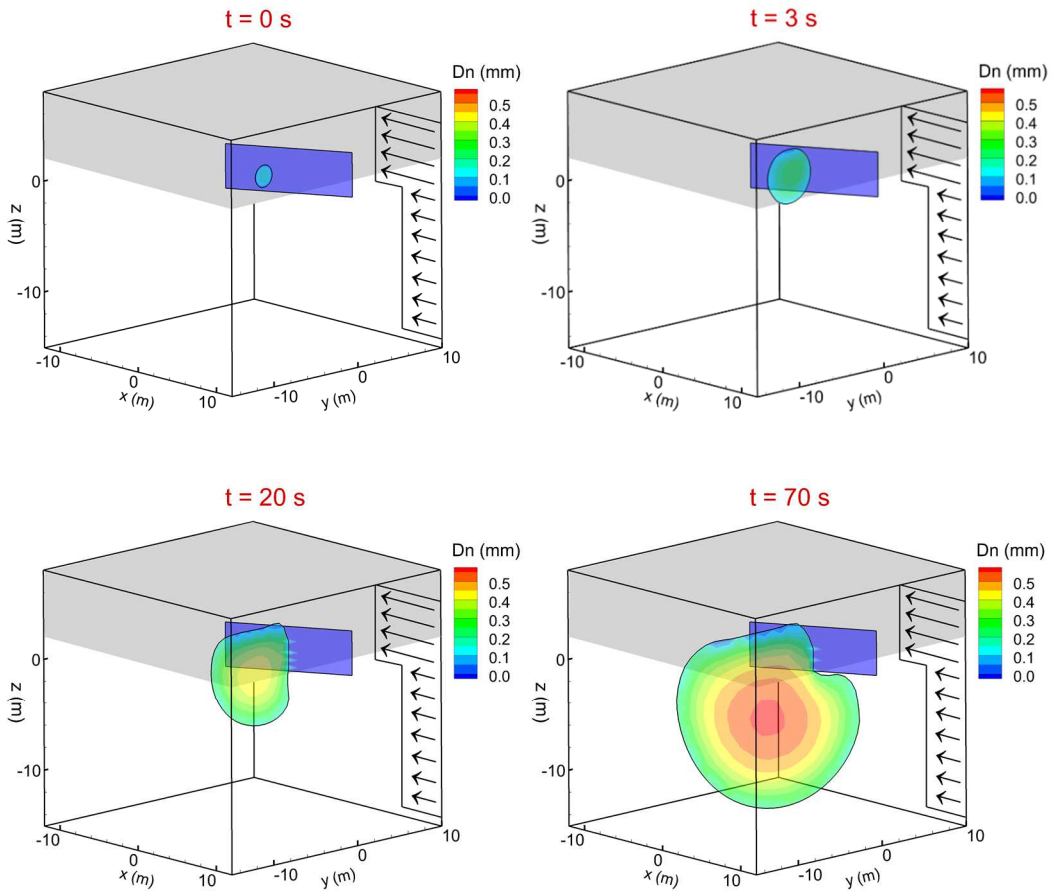

Fig. 4. 26. Evolution of a hydraulic fracture near a stress barrier and a natural fracture. The normal opening contours indicate that the location of the maximum fracture width shifts away from its initial point at the injection well.

4. 6. 4. Intersection with Multiple Natural Fractures

The previous examples outlined the characteristic behavior of a hydraulic fracture approaching a single natural fracture that results in either partial arrest and engulfing or crossing. The injection pressure plot for each case was also discussed to highlight some of the important signatures on the pressure profile. To replicate a more realistic geological setting, the number of natural fractures that are directly approached with the hydraulic fracture is increased. Moreover, the dip and strike of the natural fractures are chosen such

that a mixed cross-arrest behavior is observed. Table 4. 2 summarizes the natural fracture size and configuration used in this example.

Table 4. 2. Natural fracture configuration in the multiple NF example.

Natural Fracture	Dimension (m)	Dip Angle (°)	Strike
1	20 x 10	65	N 125 E
2	20 x 8	80	N 85 E
3	15 x 6	75	N 25 E

The horizontal well is placed between natural fracture 1 and 2 and therefore the hydraulic fracture is initiated between these two natural fractures. Fig. 4. 27 shows the evolution of the hydraulic fracture near the natural fractures. It can be observed in this figure that the HF intersects NF 1, and 2 first. Natural fracture 1 is more favorably oriented for shear given its strike. Therefore, the hydraulic fracture is to be arrested with this natural fracture. However, natural fracture 2 is less likely to slip and can potentially result in hydraulic fracture crossing. Once pressurizing natural fracture 1, and 2 and regaining the required pressure to propagate, the hydraulic fracture crosses NF 2 while being partially arrested by NF 1. The hydraulic fracture continues to propagate toward natural fracture 3. The final intersection between the HF and NF 3 results in partial HF arrest along this natural fracture. Ultimately, the hydraulic fracture is arrested with NF 1, and 3 and is contained in the lateral direction. Having said that, HF can still propagate vertically and also above and below NF 1, and 3 to engulf them.

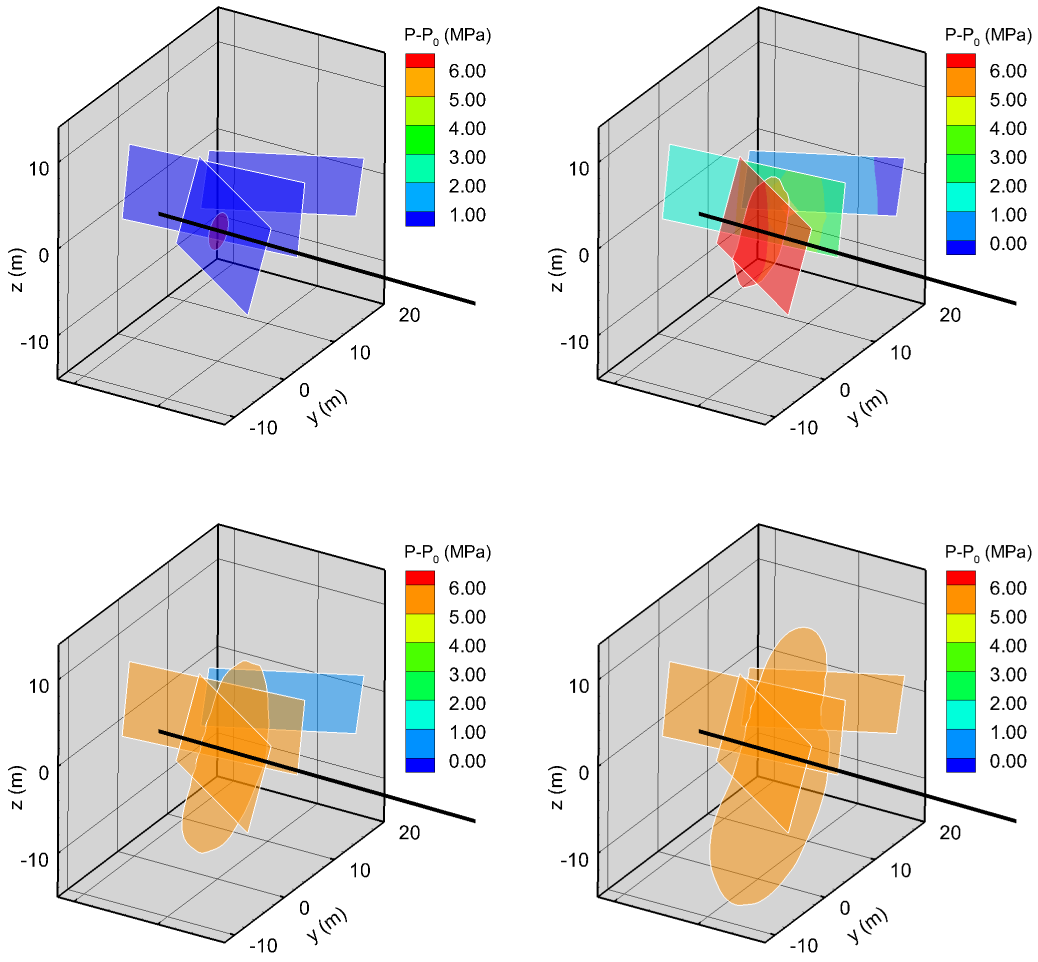

Fig. 4. 27. Evolution of a hydraulic fracture near multiple natural fractures. Fracture geometry and pressure distributions are shown at different injection times.

A side-view of the fracture geometry is shown in Fig. 4. 28. The figure on the left shows that the HF is arrested with NF 1 (left-most NF) while pressurizing NF 2 (middle fracture). After crossing NF 2 and hitting NF 3 the hydraulic fracture stops propagating in the lateral direction as it is arrested by NF 1 and NF 3. However, the HF keeps propagating vertically but mostly downward. This is due to the dip orientation of NF 3 which limits the upward propagation of the HF. This implies that NF configuration potentially impacts the ultimate fracture geometry in case of fracture arrest near natural fractures. A realistic prediction of

fracture geometry calls for accurate characterization of natural fractures and more importantly incorporating them into fracturing models. It is needless to say that simpler models such as pseudo-3D and 2D models fail to predict hydraulic fracture geometries such as this one.

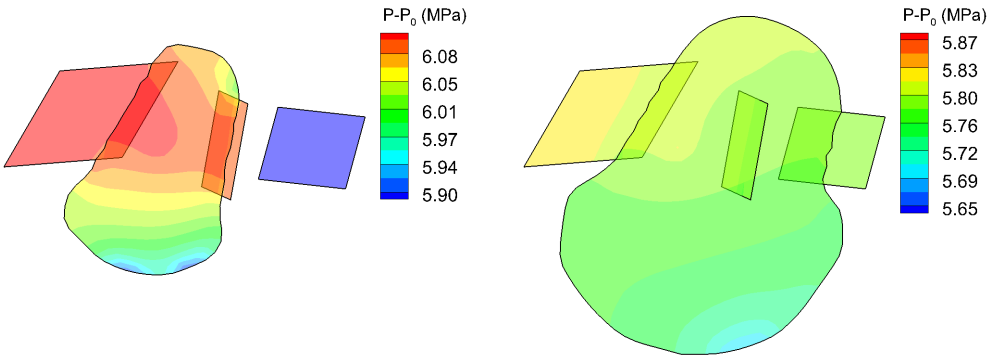

Fig. 4. 28. Side-view of problem showing fracture arrest near NF 1 and 3 and crossing through NF 2. The HF tends to propagate downward because of the dip orientation of NF 1 which limits its upward propagation.

Injection pressure history often includes important information regarding the interaction of hydraulic fractures with other geological features. Fig. 4. 29 shows the net injection pressure for this example. Some of the important features are marked by arrows on this plot. The first arrow marks the intersection of the HF with NF 1 which leads to a sudden pressure drop. The pressure drop is due to the pressurization of the natural fracture which is initially at the reservoir pressure before intersection. The pressure increases again as a result of continuous injection (marked by the second arrow). At this point fracture gain its

energy to continue propagating as shown by the third arrow. Soon after this the HF reaches NF 2 and experience another pressure drop. Once the injection pressure is sufficient, the HF continues propagating mostly in the vertical direction to cover the height of NF 2 before crossing it. The last significant pressure drop is at 90 seconds when HF crosses NF 2 and is shown by the 5th arrow. The pressure drop in this stage is mostly a modeling artifact and might be less severe in field conditions. The portion of the hydraulic fracture that crosses the natural fracture should be allowed to be sufficiently large to avoid mesh generation issues during remeshing. This could potentially lead to a higher length of propagation than is typically needed. The length of propagation across the NF upon fracture crossing is set at ¼ to ⅓ of the natural fracture height in the current version of the program. The hydraulic fracture experiences another pressure drop once intersecting with NF 3. This pressure drop is not as severe as the previous ones. It should be noted that magnitude of the pressure drop decreases upon each intersection (arrow 1, 3, and 6). This is because of the relative volume of the intersected natural fracture to the propagating fracture decreases throughout the stimulation. In other words, the injected fluid is displaced from a larger fracture into a smaller one as time goes by.

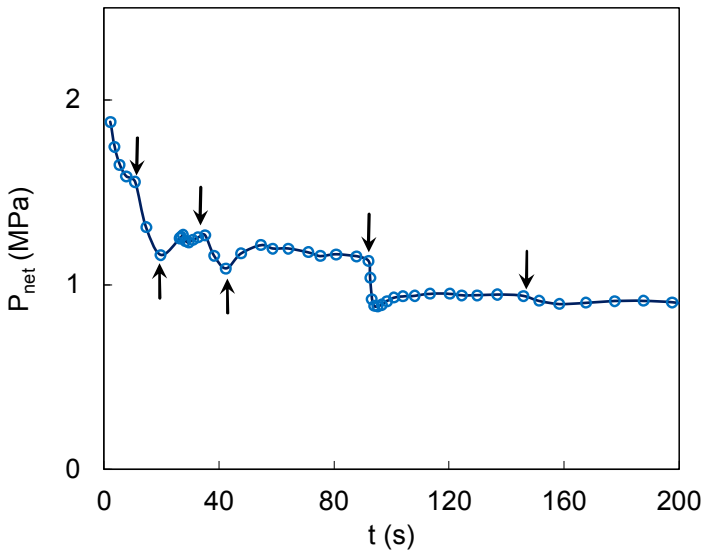

Fig. 4. 29. Net injection pressure of a hydraulic fracture near 3 natural fractures. The pressure profile shows multiple dips consisting of pressure drops and recovery from the pressure drop upon each HF-NF intersection. The HF gets partially terminated after intersecting the first intersection. The pressure drop and the consequent recovery from this intersection is marked by the 1st and 2nd arrows. The HF intersects the middle NF (3rd and 4th arrows) soon after intersection with the first NF. The HF experiences another pressure drop as it crosses the middle NF. The exaggerated pressure drop is a modeling artifact due to meshing considerations.

Fracture width is another important component of stimulation as it determines fracture conductivity and ultimately reservoir productivity. Fig. 4. 30 shows the fracture opening contour plots during early stages on the left and at the end of simulation on the right. The fracture opening distributions are shown to explain how the zone of maximum fracture opening can potentially shift from near the injection well to another part of the fracture. This example show that the zone of maximum fracture opening shifts approximately 10 m away from the injection well. This is mainly because the fracture shape deviated from its

original penny-shaped geometry by conforming to the propagation barriers like natural fractures. It should be emphasized that the fracture geometry can become highly asymmetric even in the absence of stress barriers and solely due to the presence of discontinuities. Fracture asymmetricity translates into asymmetric width profiles which, in turn, affects proppant placement.

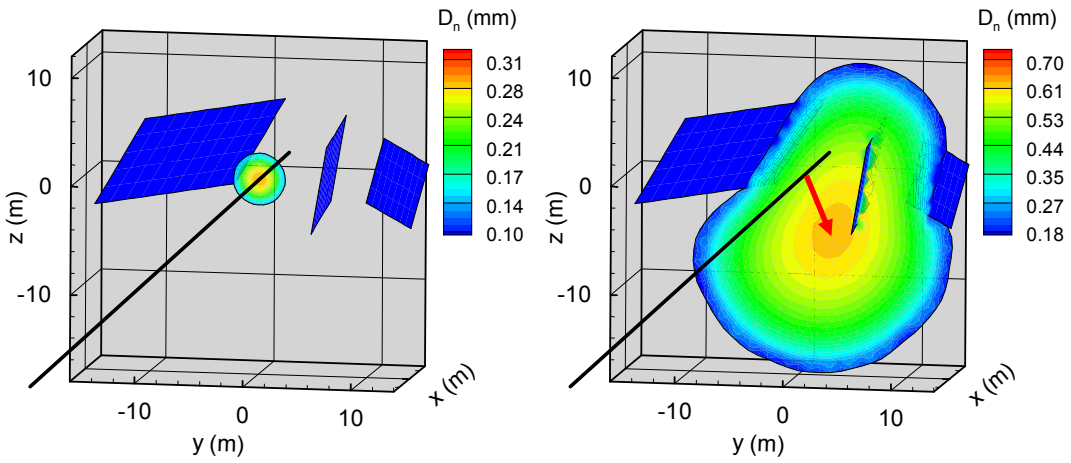

Fig. 4. 30. Fracture opening distribution at early stages (left) versus fracture opening at the end of simulation (right). This figure shows that the zone of maximum opening shifts away from the injection well to the lower right portion of the fracture. HF propagates radially before intersecting the natural fractures. The middle fracture allows the hydraulic fracture to cross whereas the left and right natural fractures lead to fracture arrest due to their orientation. The zone of maximum fracture width which is usually near the injection well, shifts away from the injection well because of the asymmetric fracture growth in the vicinity of natural fractures.

4. 6. 5. Interaction with a Network of Connected Natural Fractures

As an extension to the previous example, hydraulic fracturing is studied near a network of connected natural fractures. In the previous example, the hydraulic connection between the natural fractures were established only after they intersect with the hydraulic fracture. However, in this example the natural fractures are initially connected. The natural fracture configuration is similar to the previous case with two extra natural fractures parallel to the hydraulic fracture which connects the rest of the natural fracture (see Fig. 4. 31).

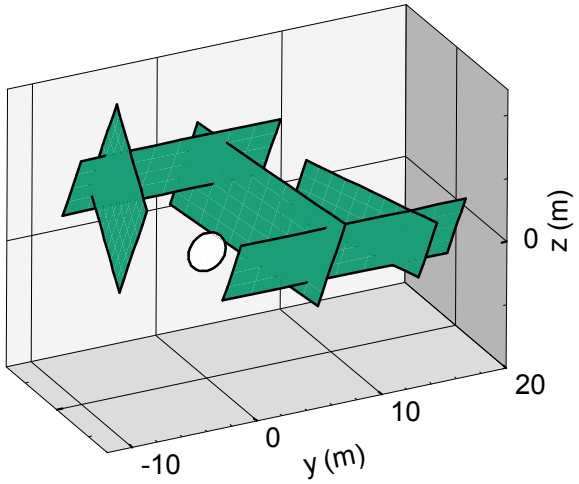

Fig. 4. 31. Natural fracture network prior to injection.

The hydraulic fracture is initiated perpendicular to the minimum horizontal stress. Water is injected into this fracture at a constant rate of 2.65×10^{-3} m^3/s (1.0 BPM). The reservoir rock has an initial pore pressure of 4.0 MPa and is subjected to a very high differential stress (~14 MPa). The input parameters used in this example are summarized in Table 4. 3.

Table 4. 3. Input parameters used in the connected NF network example

Parameter	Unit	Value

E	GPa	35.0
v	-	0.25
σ_h	MPa	21.7
σ_H	MPa	35.5
σ_V	MPa	39.0
p_0	MPa	4.0
Q	m^3/s [BPM]	0.00265 [1.0]
ρ	Kg/m^3	1000.0
μ	Pa.s	0.001
w_0^{NF}	mm	0.05

The hydraulic fracture geometry and pressure distribution in the network is shown in Fig. 4. 32. The first figure shows the fluid pressure in the network after the first HF-NF intersection. It can be seen in this figure that although only one natural fracture is coalesced with the hydraulic fracture, the entire network is pressurized. This is simply because of the hydraulic connectivity between the natural fractures. When compared to the previous example with isolated natural fractures, the elevated pressure in the natural fracture network reduces the pressure difference between the HF and the approached NF. In the previous example all natural fractures were at the initial reservoir pressure level before intersection. However, in this example all natural fractures are pressurized as the HF intersects the first natural fracture. This phenomenon may affect the injection pressure profile as discussed below.

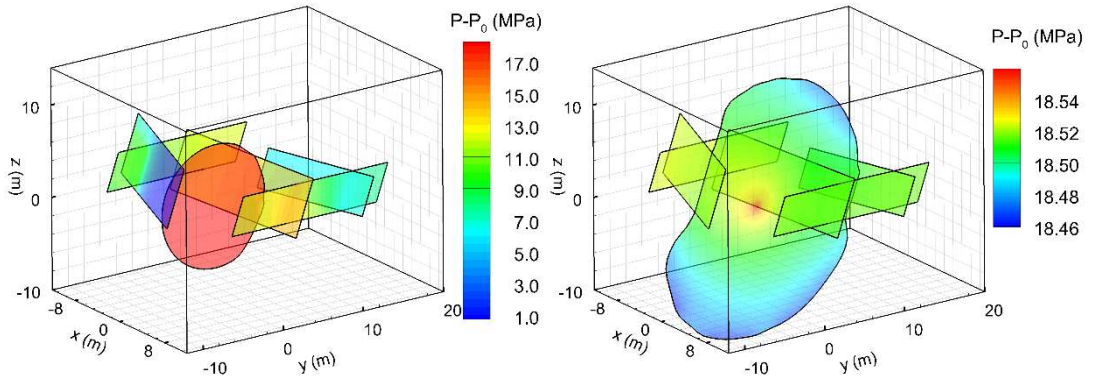

Fig. 4. 32. Hydraulic fracture evolution and pressure distribution in a NF network with hydraulic connectivity. The left figures show the fracture geometry after the first intersection and the right figure is the fracture configuration at the end of simulation.

The variations of the injection pressure for this example are shown in Fig. 4. 33. This figure, like the ones in the previous examples, shows signs of intersection, pressure drop and re-pressurization throughout the injection. The first distinct pressure drop corresponds to the first NF intersection. Unlike previous example where only one NF took fluid upon intersection, the hydraulic fracture pressurizes several fractures simultaneously in this case. After the fluid pressure is sufficient for propagation, the HF continues to propagate and the pressure starts to drop. It is interesting to note that the pressure drop upon the second intersection (3rd arrow) is not as pronounced. This is because the fluid pressure is already elevated in the second natural fracture prior to intersection. The injection pressure plot shows another drop as the hydraulic fracture crosses the middle natural fracture and approaches NF 3. Intersection with the third and last natural fracture does not show any significant pressure change. This is due to the increased fluid pressure in this natural

fracture in response to the continuous injection into the fracture network. This example implies that the intersection signatures on the pressure plot are affected by the fluid pressure inside the natural fractures. The fluid pressure inside the natural fractures are primarily controlled by either matrix-fracture or fracture-fracture interaction. Fluid flow and hydraulic communication is more likely via fracture-fracture interaction given the ultra-low permeability of unconventional reservoirs and the time-scale of a typical stimulation job. That said, changes of pore pressure due to fluid flow in the matrix should not be neglected altogether.

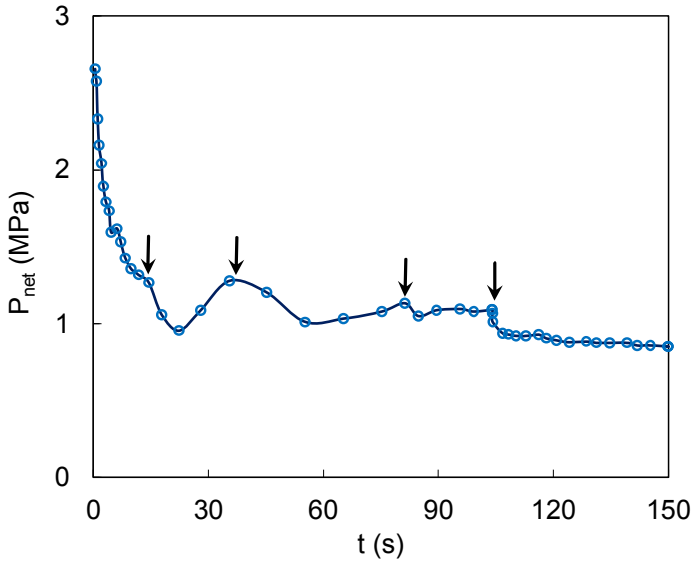

Fig. 4. 33. Injection pressure profile for a hydraulic fracture near a natural fracture network. HF intersection with the first natural fracture is followed by a pressure drop as shown with the first arrow. An increasing pressure trend follows the pressure drop and the HF starts to propagate again (shown with the second arrow). Note that because the NFs are connected the pressurization (dip between the first and second arrow) takes longer and the dip is

wider. Moreover, the pressure drop upon the next intersections become less severe because the pressure in the NF network is already elevated due to previous intersections.

4. 6. 6. Field Example: COLLAB EGS Pilot Test

The last example in this section concerns fracture propagation in a small-scale field site. COLLAB is a Department of Energy (DOE) funded project which aims to increase understanding of Enhanced Geothermal Systems (EGS) to achieve commercial viability. This project provides an opportunity for simulation and experimental works to establish validation against small-scale field tests focusing primarily on permeability enhancement and fracture behavior. The interaction of the induced fracture with the pre-existing fractures, rock fabric, and discontinuities resulted in peculiar injection pressure behaviors that raised many questions some of which are still unanswered. The objective of this example is to provide plausible scenarios that could explain the field observations.

The induced hydraulic fracture was initially thought to be an ideal penny-shaped fracture by the designers despite the fact that the injection pressure profile, and later the micro-seismic activities, did not support this concept. The first injection cycle resulted in a pressure profile that many interpreted as a classic formation breakdown followed by the propagation of a radial fracture. However, the increase in the injection pressure shortly after the breakdown raised questions regarding the validity of the penny-shaped fracture assumption. Two simulation examples are presented here to mimic the COLLAB test conditions and provide plausible scenarios leading to the observed pressure profile. The first example examines the hydraulic fracture evolution in the vicinity of seven natural fractures without stress barriers. The second example includes two symmetric stress barriers in addition to the natural fractures. Input parameters are listed in Table 4. 4.

Table 4. 4. Simulation parameters for the COLLAB example.

Parameter	Unit	Value
E	GPa	71.4
v	-	0.22
σ_h	MPa	21.7
σ_H	MPa	35.5
σ_V	MPa	39.0
p_0	MPa	4.0
Q	L/min	5.0
ρ	Kg/m^3	1000
μ	Pa.s	0.001
k_m	mD	0.001
ϕ_m	-	0.02
w_0^{NF}	mm	0.10
c^{NF}	MPa	0.50
$\emptyset^{NF}$	◦	25.0
L_{NF}	m	[6-15]
H_{NF}	m	[6-8]
K_{IC}	MPa.m$^{0.5}$	2.50
K_n^{NF}	GPa/m	50.0
K_s^{NF}	GPa/m	50.0

Several single-rate and step-rate injection tests were conducted during May and June of 2018 to collect pressure and MEQ data in order to characterize the fracture and formation behavior in COLLAB. The injection rates were as low as 0.20 L/min and did not exceed

5.0 L/min. The longest injection interval lasted up to 3 hours. The first cycle (May 22, 2018) yielded a unique pressure profile in which the injection pressure has a decreasing trend in the beginning followed by an increasing trend later in the test. Fig. 4. 34 shows the field injection pressure and rate for the first injection cycle. The simulation examples in this section focus on this stage of injection in order to provide answers as to why the injection pressure might show a significant trend reversal.

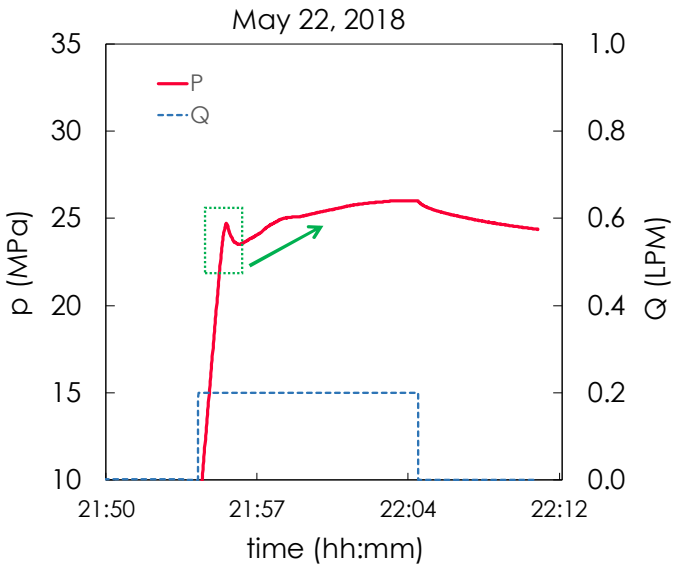

Fig. 4. 34. Field pressure and rate data from the first injection cycle on May 22, 2018. This cycle shows a so-called formation breakdown signature followed by an upward trend which is not typically observed in the case of single HF propagation.

The natural fracture network is constructed based on the actual position of the natural fractures obtained from the formation characterization studies on the COLLAB EGS site (EGS COLLAB experiment 1 report, 2019). Although a significant number of natural fractures are identified in the field, only a limited number of them which could impact the

hydraulic fracture are selected for the simulation examples in this section. The natural fractures are selected based on their distance from the hydraulic fracture and whether or not they intersect the approaching HF. Hydraulic and natural fracture configurations are shown in Fig. 4. 35. This figure shows the top view (x-y plane), side view (y-z plane), and the 3D view of the HF-NF configuration. It should be noted that the hydraulic fracture is initiated as a radial fracture from a horizontal injection well. However, the HF geometry can later change due to the influence of the natural fractures and/or the stress barriers. The first example examines the hydraulic fracture evolution in the vicinity of natural fractures without stress barriers. The injection rate is set at 5 LPM which is the maximum injection rate of the COLLAB test.

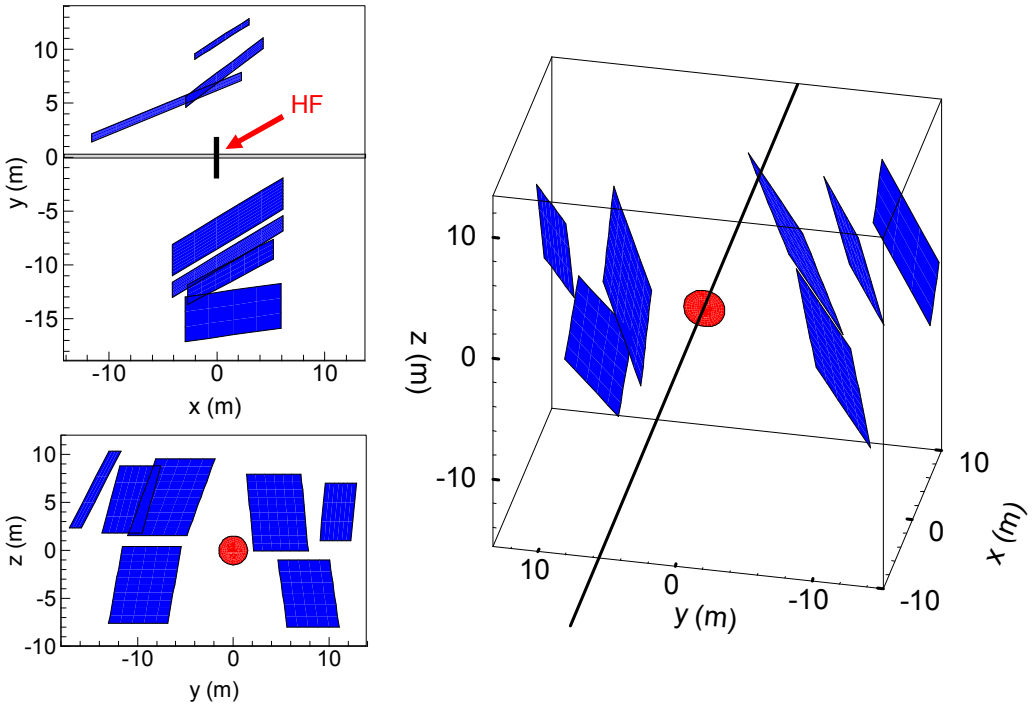

Fig. 4. 35. Hydraulic and natural fractures used in the COLLAB example.

The net injection pressure is recorded throughout the simulation and is shown in Fig. 4. 36. This figure shows some of the characteristics of the HF-NF intersection as discussed in the previous examples. Three instances of pressure drop and recovery can be observed in this figure suggesting HF intersection with multiple natural fractures (. It should be noted that while the pressure plot shows three distinct pressure drops the HF intersected four of the nearest natural fractures (see Fig. 4. 37). This is, in fact, because the hydraulic fracture intersects two natural fractures at the same time after recovering from the first intersection. Consequently, it takes a longer time for the injection pressure to increase after intersecting two NFs simultaneously. The net pressure stabilizes after the last intersection.

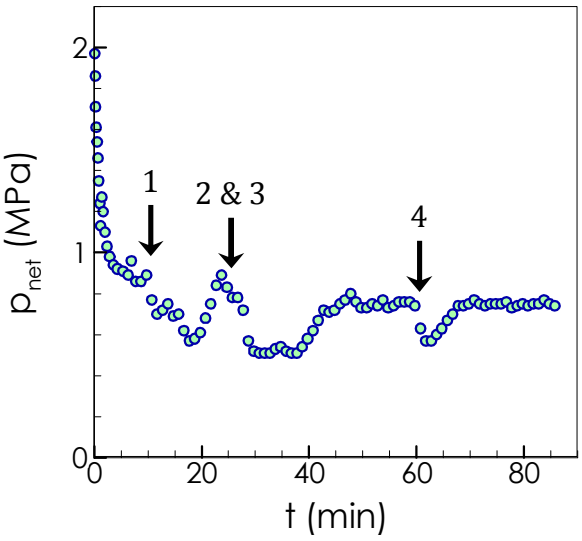

Fig. 4. 36. Simulated injection pressure profile for the COLLAB field example without stress barriers. The net pressure shows a decreasing trend in the early stages which is a characteristic of radial propagation behavior. The instance of intersection with natural fractures are marked by arrows on the pressure plot. The hydraulic fracture experiences a pressure drop upon intersection the first natural fracture and it experience another pressure

drop soon after recovering from the first one. Given that the HF intersects and pressurized two natural fractures on it second intersection the dip is wider. The late time net pressure behavior does not capture the increasing trend observed in the field test.

Fig. 4. 37 shows the hydraulic fracture geometry and the pressure distribution at different injection times. It can be observed in this figure that the HF maintains its radial shape during the early stages before reaching any of the natural fractures. After intersecting the natural fractures and being partially arrested, the HF deviates from its penny-shaped geometry. The hydraulic fracture pressurizes the natural fractures and initiate wing-crack segments from some of the natural fractures as shown in this figure. It should be noted that despite termination near the intersected natural fracture, the HF can still propagate vertically where there are no obstacles in the form of NF or stress barriers. The injection pressure at the later stages of the test is in agreement with the propagation behavior. Although insightful, this example does not capture the increasing trend in the injection pressure as observed in the first cycle of COLLAB (see Fig. 4. 38).

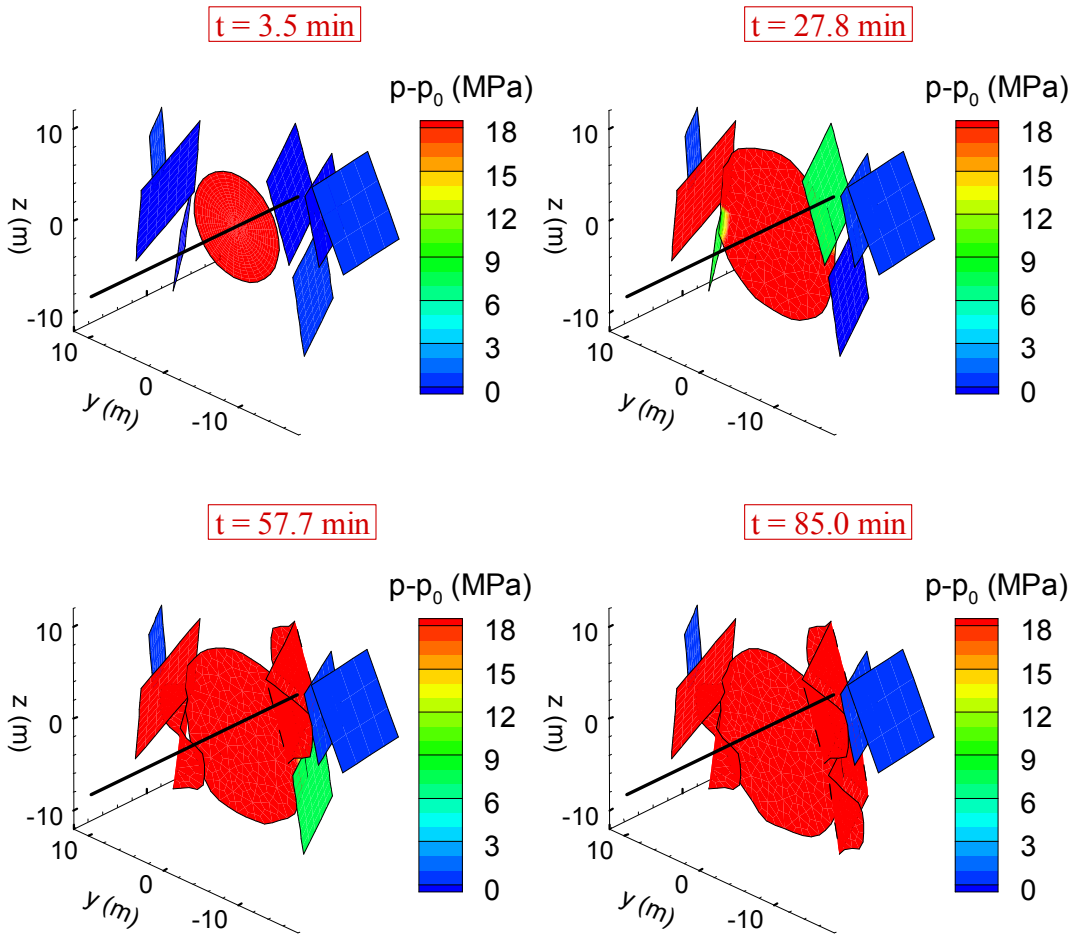

Fig. 4. 37. Hydraulic fracture evolution near natural fractures and the pressure distribution in the system at different injection time. The hydraulic fracture can still propagate in the vertical direction although it is contained in the lateral direction because of the natural fractures.

Next, two symmetric stress barriers are placed 6 m above and below the injection well in the second simulation example. This is simple representation of stress heterogeneity that likely exists because of different lithologies present in the area. The stress barriers are introduced to further contain the fracture in the vertical direction. The injection pressure from the simulation and the field data are shown in Fig. 4. 38. This figure shows a pressure

behavior similar to the previous example until about 50 minutes of injection. However, in contrast to the previous example, the pressure profile starts to show an increasing trend after 50 minutes of injection (marked by an arrow). This type of behavior is caused by continued injection into a fracture that is contained and is stationary or has minimal propagation. The trend resembles that of the field data in the sense that it shows a breakdown followed by a decreasing trend due to propagation, and then an increasing trend in the pressure. As a likely scenario, this example suggest that the increasing trend in the injection pressure is caused by pressurization of a network consisting of the hydraulic fracture and natural fractures that are subjected to a higher normal stress than the HF (due to their orientation). Additionally, this trend dictates very minimal fracture growth as shown in this example. It should be emphasized that this is only one plausible scenario that results in the continuous increasing pressure trend. Others have linked the rise in the injection pressure to poroelasticity. Given the permeability of the rock, the time scale of the first cycle, and the low injection rate the argument regarding poroelasticity does not appear very convincing at least during the first cycle.

Extended injection tests that were conducted during 2019 resulted in pressure buildup rates ranging from approximately 3.0×10^{-3} MPa/hour to 2.0×10^{-2} MPa/hour. Extended injection under a constant rate of 0.4 L/min yields a pressure buildup rate of 0.50 MPa/hr in our simulation. This rate is, however, obtained without accounting for leakoff and the recovered water at the production outlets (which sums up to 85-90% of the injected volume). Accounting for the recovered volume reduces the pressure buildup rate to 0.075 MPa/hour which is closer to the field observations. It should be pointed out that the uncertainties associated with the reservoir properties and the natural fracture network

affects the injection pressure profile and the pressure buildup rate during the extended injection intervals.

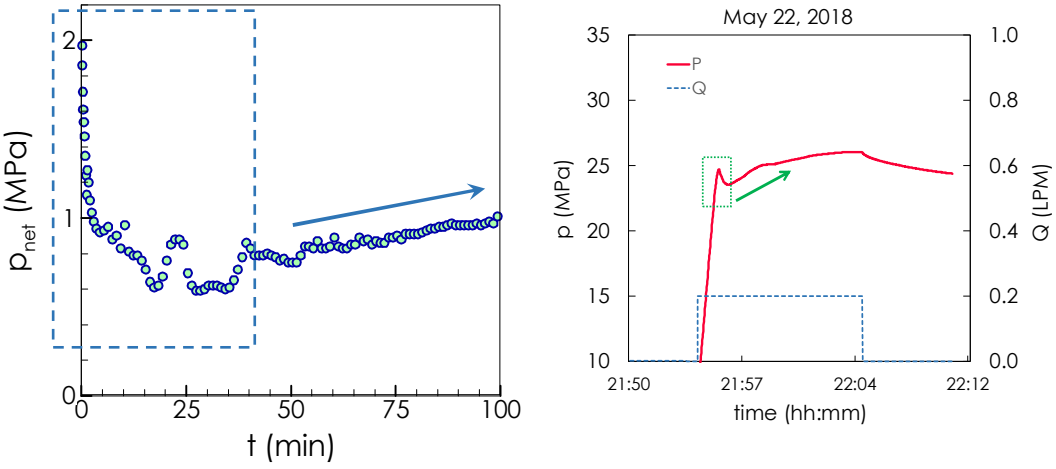

Fig. 4. 38. Injection pressure profile near NFs and stress barriers from simulation (left). Injection pressure plot from the field measurements (right). The rectangle in both plots represent the pressure drop during propagation and the arrows mark the pressure increase due to the pressurization of a contained HF near natural fractures.

The hydraulic fracture evolution and the pressure distribution are shown in Fig. 4. 39. Unlike the first scenario, the hydraulic fracture shows complete containment in the vertical direction due to the stress barriers. A side view of the HF-NF configuration at the end of the simulation shows a fully contained hydraulic fracture, four natural fractures that are pressurized after intersection with the hydraulic fracture, and initiation of wing-cracks from three of the intersected natural fractures.

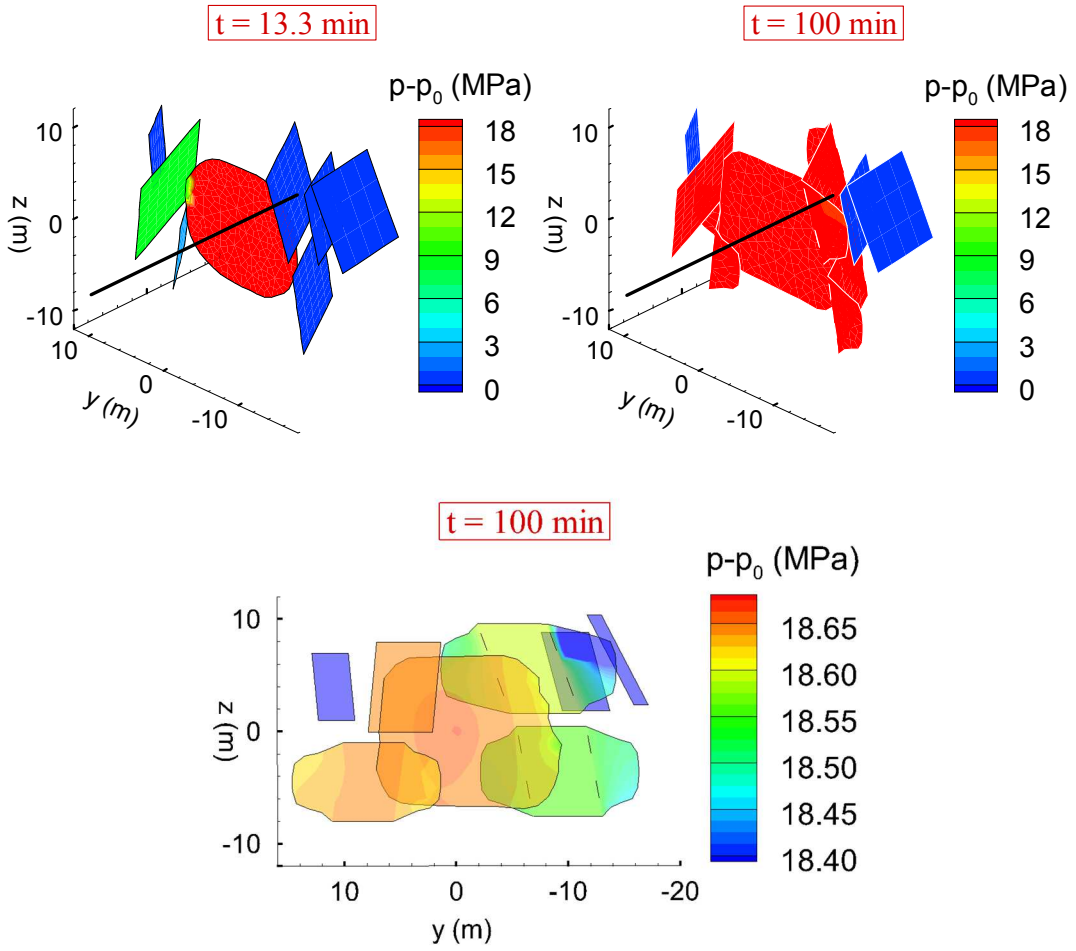

Fig. 4. 39. Hydraulic fracture evolution near natural fractures and stress barriers. This figure shows that the hydraulic fracture is arrested by the natural fractures in the lateral direction and contained in the vertical direction due to the stress barriers. The hydraulic fracture pressurizes the intersected natural fracture and initiates wing-cracks from three of the natural fractures.

4. 7. Extension to Half-Space and Bonded Half-Space Problems

Some reservoir rocks consist of layers with different minerology, thickness, mechanical, and petrophysical properties or are contained within distinct over- and underlying layers.

The variations of the elastic properties such as Young's modulus, and Poisson's ratio could impact the hydraulic fracture geometry. While stiffer layers contain the fracture height, softer formation facilitate the height growth. In addition to altering the fracture geometry, the contrast between the mechanical properties of the rock layers results in asymmetric width profiles along the height of the fractures.

The 3D displacement discontinuity method used in previous portions of is study is based on the fundamental solution of the displacement discontinuity in an infinite medium. Although DDM has been widely used to study fractures in infinite media, very little has been done on the 3D modeling of hydraulic fracturing in layered rocks using displacement discontinuity. This is mainly due to the lack of a boundary integral solution to the generalized half-space problems in 3D. Extending the DD formulation to account for rock layers with different elastic properties faces serious challenges and gets complicated even for very simple configurations.

Shou (1993) developed a 3D displacement discontinuity model for half-space and bonded half-space problems using the theory of images. His model requires an image DD element in addition to the actual DD element to negate the normal stress on the free surface in the case of the half-space problem and an additional supplementary solution for the case of bonded half-space problems. The half-space and bonded half-space configurations, the actual DD element, local and global coordinate systems are shown in Fig. 4. 40. Shou's model concerned crack growth near interfaces under tensile loading. Following Shou's modeling strategy and incorporating a fluid flow model, a fully-coupled planar 3D model is developed to study hydraulic fracturing near rock interfaces. Constant rectangular elements are used in this section to take advantage of analytical integration of the stress

kernels. Also, it should be noted that we limit our analysis to the cases where hydraulic fracture remains in one layer without crossing the interface at this stage.

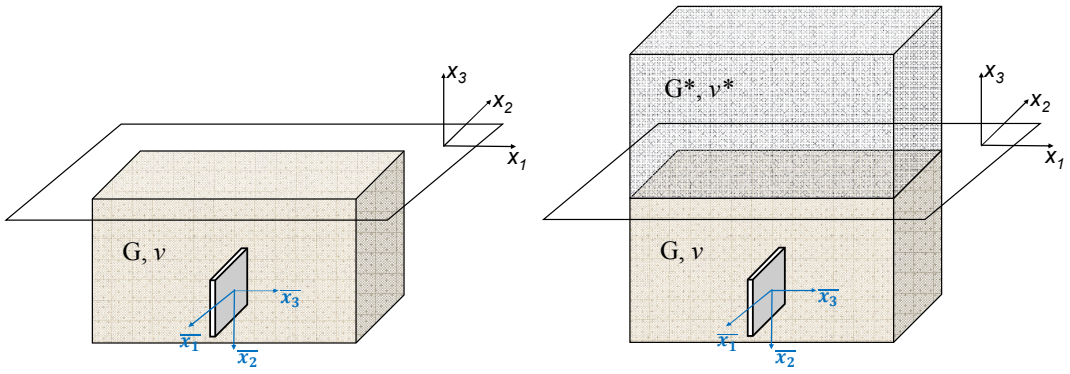

Fig. 4. 40. (Left) half-space model configuration, and (right) bonded half-spaces including two rock layers with different elastic properties.

4. 7. 1. Verification Example

This example investigates the normal opening of a rectangular crack which intersects the surface of the half-space. The result obtained from the 3D displacement discontinuity model is then compared to a 2D analytical model developed by Tada et al. (1973). The crack length (along *y*-direction) is taken to be more than 10 times its height (along *z*-direction) to satisfy the plane-strain condition along section A-B as shown in Fig. 4. 41. The half-space shear modulus and Poisson's ratio are assumed to be 30 GPa and 0.25, respectively and 1 MPa of tensile stress is applied in the *x*-direction. The crack height is 0.40 m. Fig. 4. 41 shows that the highest opening is at the top of the crack which intersects the traction-free surface. It should be noted that the highest crack opening occurs in the center of the crack in an infinite rock.

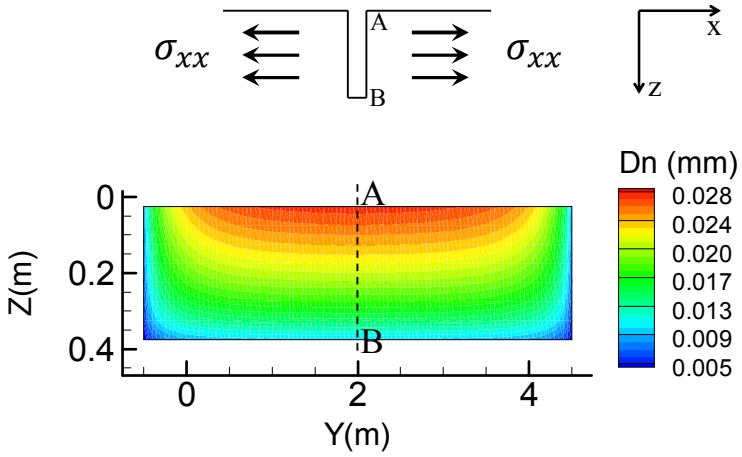

Fig. 4. 41. Rectangular crack intersecting the surface of half-space. Given the high length to height ratio in this example, the fracture height is enlarged for plotting purposes. Maximum crack opening is at point A where the crack intersect the free surface. Maximum crack opening is at the center of the crack in infinite rocks.

The normal opening of the crack along the dashed line A-B is compared to the analytical solution of this problem in Fig. 4. 42. This figure shows that the highest normal opening is at the top of the crack which intersects the free surface at point A. The crack opening decreases as depth increases and the crack closes at point B (i.e. Z/H = 1). The 3D DD model shows an excellent agreement with the analytical solution of the problem (Tada et al., 2000):

$$D_n(z) = \frac{4\sigma}{E'}\sqrt{H^2 - z^2}\, D\left(\frac{z}{H}\right) \tag{4. 44}$$

$$D\left(\frac{z}{H}\right) = 1.454 - 0.727\left(\frac{z}{H}\right) + 0.618\left(\frac{z}{H}\right)^2 - 0.224\left(\frac{z}{H}\right)^3 \tag{4. 45}$$

Where H is the crack height and the positive z direction is downwards.

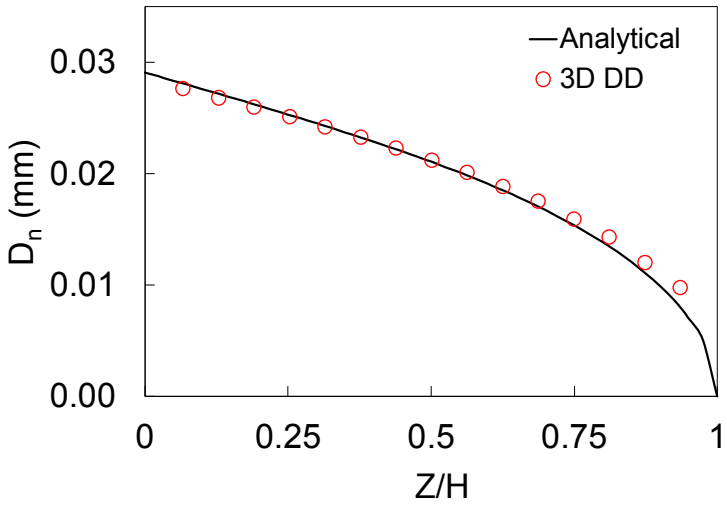

Fig. 4. 42. Normal DD along A-B showing highest opening at the top of the crack.

4. 7. 2. HF Propagation in the Vicinity of a Stiffer Layer

Fracture propagation is influenced by the contrast between the elastic modulus of adjacent layers. The bonded half-space model is used in this example to study the effect of elastic modulus contrast on the overall fracture footprint. The first example investigates propagation of a hydraulic fracture in a host rock (lower half-space) with a stiffer upper half-space. The shear modulus, G, of the lower and upper half-space are 30 and 150 GPa, respectively. In a similar analysis, the fracture propagation is investigated when the upper layer is significantly stiffer than the host rock (i.e., $G_U >> G_L$). Simulation input parameters are listed Table 4. 5.

Table 4. 5. Input parameters of the simulation of HF propagation near a stiffer layer.

Parameter	Unit	value
σ_{xx}	MPa	20
Injection fluid viscosity	Pa.s	1.0×10^{-3}

Injection rate	m^3/s	$1.0x10^{-4}$
Lower H.S. Poisson's ratio, ν_L	-	0.25
Upper H.S. Poisson's ratio, ν_U	-	0.25
Lower H.S. shear modulus, G_L	GPa	30
Upper H.S. shear modulus, G_U	GPa	150
Fracture toughness, K_{IC}	$MPa.m^{0.5}$	2.0

The hydraulic fracture is initiated from a penny-shaped fracture with 1.0 m radius. Water is injected at a constant rate at to the center of the fracture which is located 7.0 below the interface. The fracture geometry and hydraulic aperture profiles are monitored during the simulation.

The fracture geometry and aperture profiles are shown in Fig. 4. 43 at different injection times. This figure shows that the fracture propagates radially and both the fracture geometry and width profile remain symmetric before feeling the influence of the adjacent formation. The fracture starts to extend asymmetrically as the upper tips approach the stiffer layer (upper half-space). This is in fact because propagation is more difficult closer to the stiffer layer. The degree of asymmetry is of course dependent upon the contrast between the elastic modulus of the layers and the distance from interface. Propagation tends to terminate in regions near the interface at higher injection times (see Fig. 4. 43) and deviate from its initial penny-shaped geometry. Moreover, the fracture tends to have a higher hydraulic aperture at the bottom portion which is farther from the stiff half-space (Fig. 4. 43 at t=270 sec).

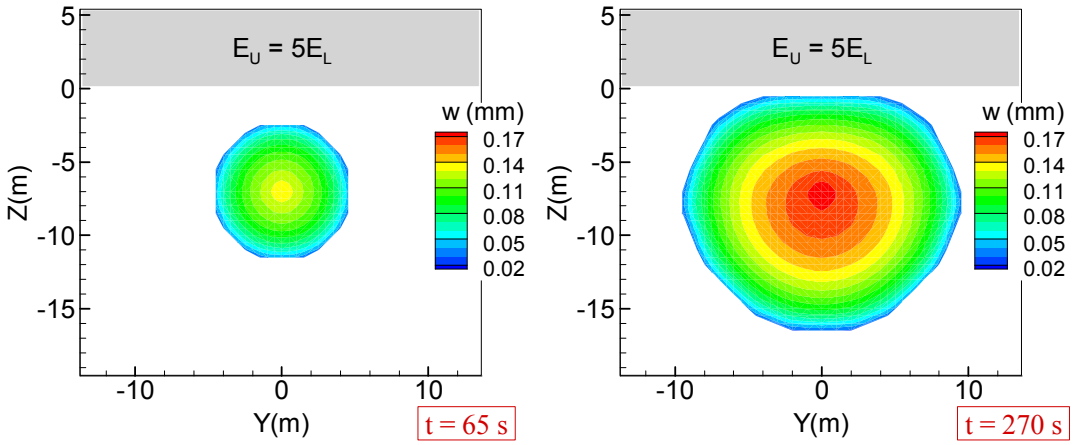

Fig. 4. 43. Fracture geometry and aperture profile in the vicinity of a stiffer half-space.

Fig. 4. 44 shows the fracture geometry in the vicinity of an upper half-space with much higher elastic modulus ($E_U = 100\ E_L$) after 450 seconds of injection. It can be observed that the fracture extends asymmetrically away from the stiffer layer. It should be noted, however, that this is a limit case where the elastic modulus contrast is unrealistically high. Nonetheless, the elastic modulus difference affects the overall fracture footprint and the aperture profile as was observed in the first example. The variation of fracture width along the dashed line is also plotted in this figure. The width profile shows that the fracture extends 7 m upwards before reaching the interface while it extends 15 m below the perforation (marked by asterisk). Moreover, this asymmetric growth and preferential propagation leads to an asymmetric width distribution along the height of the fracture.

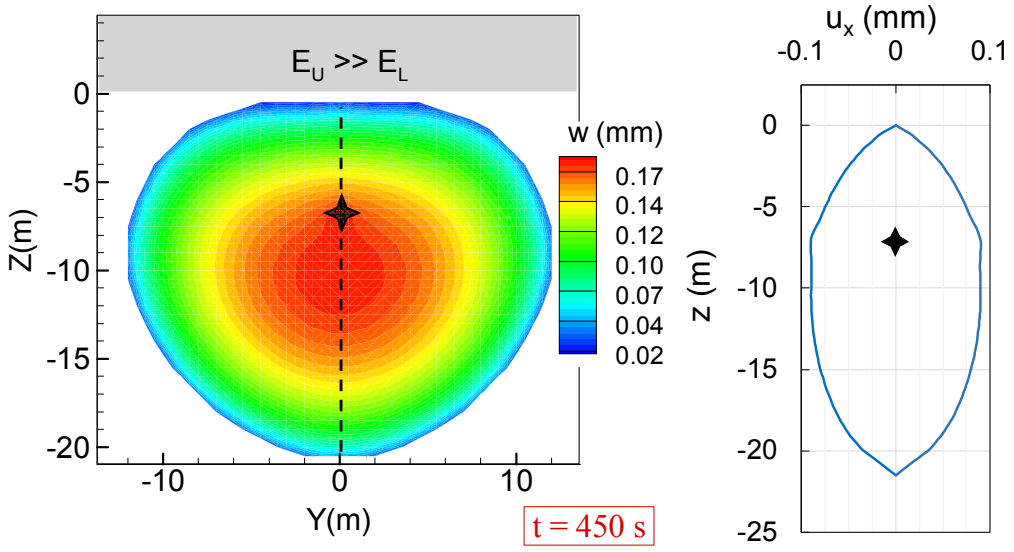

Fig. 4. 44. (Left) fracture geometry near a layer with much higher Young's modulus. (Right) width profile along the dashed line.

4. 7. 3. HF Propagation in the Vicinity of a Softer Layer

A similar example is designed to analyze fracture propagation in the vicinity of a softer upper half-space. The initial fracture geometry and other rock and injection parameters are the same as the ones used in the first example. However, the fracture is initiated at a relatively lower depth of 10 m. The shear modulus of the upper half-space is set to 6 GPa whereas the shear modulus of the host rock (lower half-space) is 30 GPa.

Fracture geometry and aperture profile are shown in Fig. 4. 45. Similar to what was observed in the first example, fracture propagates symmetrically in all directions at early stages. The hydraulic aperture profile also looks uniform. As upper fracture tips approach the softer upper half-space and feel the influence of this layer, the fracture starts to grow asymmetrically. Fracture tips tend to open easier near a softer layer and therefore we observe easier propagation in the vicinity of the interface. It can be observed in Fig. 4. 45

that the fracture elongates in the *z*-direction at later stages of propagation. It should be noted that fracture propagation may become unstable as it approaches the softer half-space. The simulation is terminated once the crack tips reach the interface as the elastic kernels for the upper half-space are not developed in this work. The softer the top layer, the easier for the fracture to propagate towards it. Unstable fracture growth may be avoided by using modeling/simulation prior to the actual hydraulic fracturing. The risk of intersecting softer layers can be mitigated by calculating the injection time required to reach the interface in layered rocks.

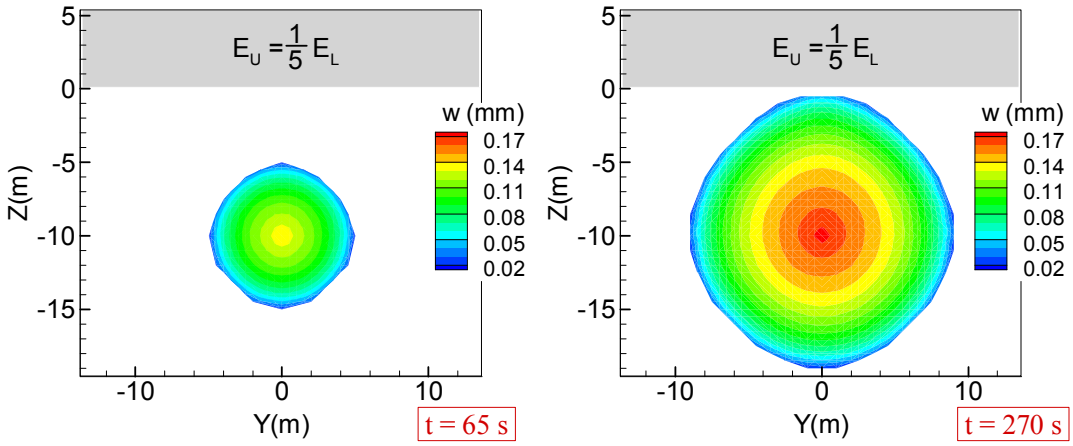

Fig. 4. 45. Fracture geometry and aperture profile in the vicinity of a softer layer.

Chapter 5

Application of the Integrated HF-NF Model to DFIT

Mini-Frac is a technique used for determination of the minimum in-situ stress and can be used in estimating reservoir properties such as pore pressure. Historically, Nolte's G-function has been used to estimate the closure stress by drawing a tangent line to G dp/dG plot (Fig. 5. 1). This method is based on the assumption that a single planar fracture forms with injection. However, the presence of natural fractures and other rock fabric features, as well as coupled process can complicate the pressure data and the interpretation of DIFT (diagnostic fracture injection test). In this work, a 3D integrated HF-NF simulator is used to study the complex interaction of hydraulic and natural fractures and their signatures on the pressure data. The DFIT model consists of a hybrid boundary element and finite element method (BE-FEM) where stresses/deformations are solved using the displacement discontinuity method and the transport processes are modeled using finite element. Additionally, contact elements and Mohr-Coulomb criterion are used to capture the deformation and failure behavior of the fracture. A detailed description of the coupled physics equations is provided in the previous chapter. Here, the model is applied to shed light on the complex pressure data from FORGE and to provide a better estimate of the minimum in-situ stress and reservoir properties.

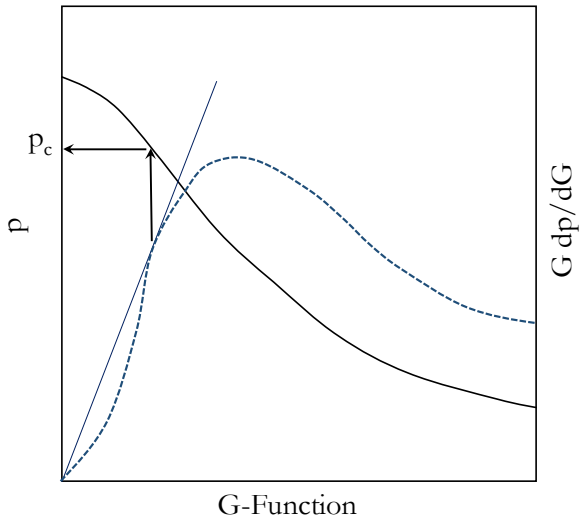

Fig. 5. 1. Closure pressure determination using the tangent method.

5. 1. Introduction

Hydraulic fracturing has been used in the oil and gas industry for several decades as a viable stimulation technique to improve production. The design and placement of hydraulic fractures has advanced and been optimized owing to the extensive modeling and experimental studies on this subject. Creating hydraulic fractures in smaller scales and analyzing the post shut-in pressure profile yields a viable means for the estimation of the minimum in-situ stress. This technique, which is commonly termed as Mini-Frac or DFIT consists of a short pumping period at a relatively low rate (5-10 barrels per minute) to create a hydraulic fracture, After shut-in, the fall-off pressure is monitored to identify the closure pressure.

The fracture pressure diagnostics in its current form started with the seminal work of Nolte (1979) where he proposed using a special time function, namely the G-function to analyze post shut-in pressure transient. G-Function is essentially a dimensionless time function

which linearize the pressure behavior before fracture closure under normal leakoff condition. Nolte (1979) formulated his work based on the material balance under several assumptions including a single planar fracture and constant leakoff from the fracture surfaces. Nolte also assumed constant fracture height which implies perfect containment between stress barriers. This assumption may not always hold especially in reservoir with weak stress barriers or no barriers at all. Additionally, Nolte assumed that injection yields two symmetric wings. It is unrealistic to presume ideally symmetric fracture wings in unconventional reservoirs. Acknowledging that an actual hydraulic fracture deviates from these idealizations, Nolte noted that the validity of his proposed method depends on the degree of deviation from these assumptions. Relying on the bottom-hole pressure measurement from three massive hydraulic fracturing (MHF) treatments which showed an increasing treatment pressure, Nolte assumed a PKN type fracture to develop his model. Nolte (1986) extended his original work to determine closure parameters using other fracture models such as KGD and penny-shaped fractures. The primary step in his analysis involves a type-curve matching process using master type-curves as shown in Fig. 5. 2. The type curves are constructed by using a reference time (typically between zero and one) and plotting G-function vs. the dimensionless time. The same reference time is used to plot pressure difference between a dimensionless time and the reference time vs. the elapsed times since shut-in for a new test. The pressure match is then obtained by overlaying the curve on the type curves so that the reference time matches a dimensionless value, and shifting the y-axis such that the pressure difference matches the master type curves.

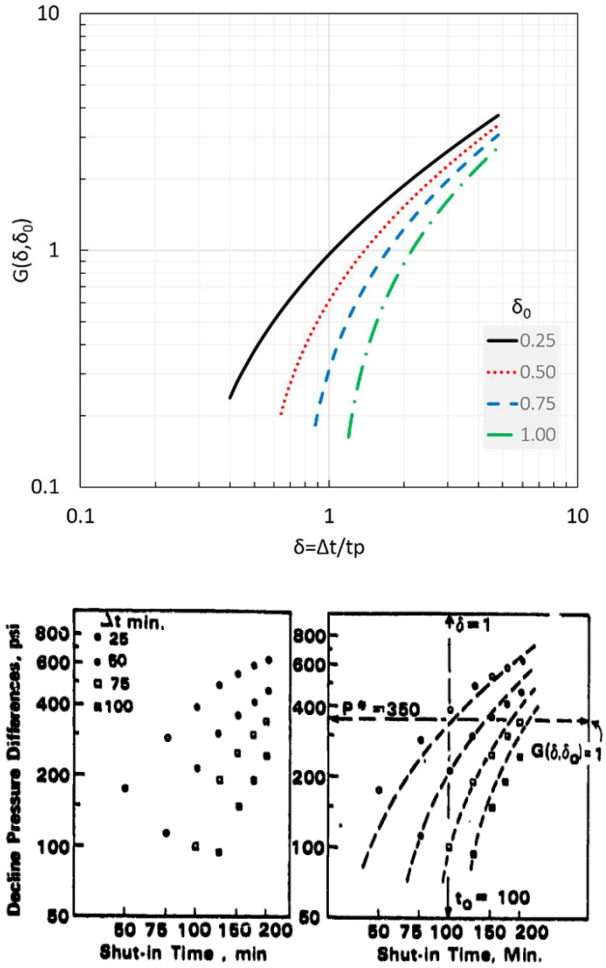

Fig. 5. 2. (Top) Master type-curve used in Nolte's analysis. (Bottom) An example of type curve matching (After Nolte, 1971).

Following Nolte's work, Castillo (1987) improved the pressure decline model by including the pressure-dependent leakoff terms. Castillo (1987) also used a graphical approach to determine the closure pressure and pointed out that the pressure decline curve forms a straight line when plotted against the G-time during the fracture closure (see Fig. 5. 3). Fracture closure is interpreted as the deviation from the linear trend. Since the G-time was proposed to linearize pressure decline behavior before fracture closure, the departure from the linear trend signals fracture closure and transitioning into a different flow regime.

Castillo improved the constant leakoff assumption that was previously used in the Nolte's method by considering other leakoff mechanisms such as filtrate viscosity dominated, and reservoir dominated leakoff and obtained the parameters to use in each case.

Although the use of G-function helped to advance the analysis of the DFIT, it was recognized that pressure vs. G-function plots may lead to non-unique interpretations with regard to the type of the closure mechanism (i.e., tip extension, height recession, fissure opening etc.).

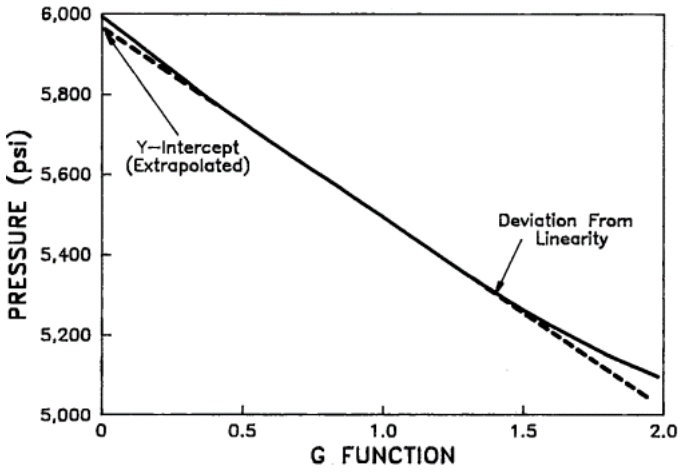

Fig. 5. 3. Plot of pressure vs. G function to identify closure pressure (After Castillo, 1987).

The next extension to the original work of Nolte was proposed by Mukherjee et al. (1991). Mukherjee made note of the fact that a significant part of oil and gas production is from naturally fractured reservoir with pressure dependent leakoff behavior. They argued that Nolte's constant leakoff assumption leads to over-prediction of fluid efficiency when applied to such reservoirs. Fluid efficiency measures the ratio of the fluid volume in the fracture at shut-in to the pumped volume. This could result in a fracture design with inadequate pumping rate and pad volume and consequently, premature screenout. To

remedy this issue, Mukherjee proposed a piece-wise leakoff function which takes into account leakoff due to fissure opening/closure. Their pressure decline function can be expressed as follows:

$$\Delta p_w(\Delta t_{D1}) = KC(p)G(\Delta t_{D1}) \quad (5.\ 1)$$

Where, Δp_w is the pressure decline since shut-in, K is a constant comprised of pumping duration, fracture geometry and fracture's compliance, G is the Nolte's time function, and $C(p)$ is the pressure dependent leakoff function. The proposed leakoff function consisted of a simple exponential function for pressures above fissure closure and a constant leakoff term below that pressure.

Barree and Mukherjee (1996) proposed a graphical approach using pressure and its semi-logarithmic derivative, Gdp/dG, to identify closure pressure and the cause of non-ideal leakoff behavior during the fracture closure. Using this technique, they demonstrated a few cases with non-ideal leakoff behavior such as pressure-dependent leakoff, height recession, and variable fracture compliance. It is important to account for the non-ideal leakoff behaviors especially pressure-dependent leakoff when applying the DFIT to unconventionals. In fact, in a statistical study performed by Craig et al. (2005) on more than 1000 DFIT cases, it was found that the majority of cases exhibit pressure dependent leakoff behavior and the ideal leakoff was rarely observed. Barree's analyses indicate that pressure-dependent leakoff has significant impacts on the fracture geometry and should be accounted for in fracture designs.

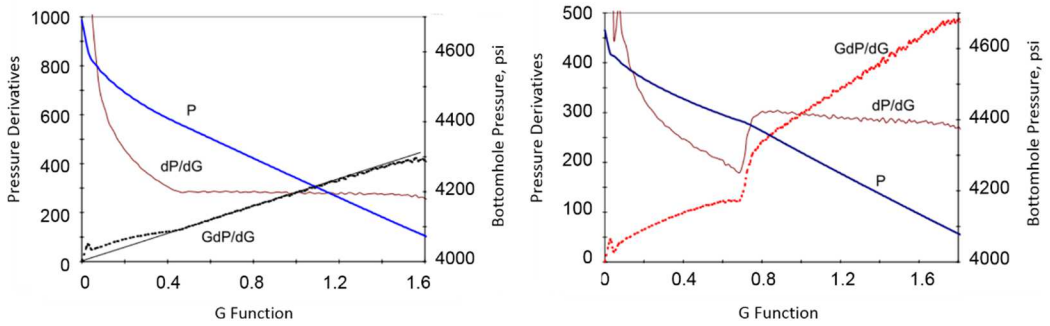

Fig. 5. 4. Semi-log pressure derivative G dp/dG shows sign of pressure dependent leakoff by lying above the tangent line in the concave segment(left), and variable fracture compliance (right). A comprehensive investigation of fracture closure using p, dp/dG, and G dp/dG on the same plot (after Barree and Mukherjee, 1996).

Alternative methods such as the rate-normalized plot (RNP) and simple log-log diagnostics have also been presented and used by Mayerhofer and Ecomomides (1997). In addition to the widely used tangent method, some have suggested the system stiffness/compliance method to determine the closure pressure (see Barree and Mukherjee, 1996; Raaen et al., 2001; Raaen et al., 2005; McClure et al., 2016). Normal stiffness is defined as the changes of the normal stress on the fracture with respect to the fracture closure ($K_n = d\sigma_n/dD_n$). As discussed in one of the earlier studies on the system stiffness approach (Raaen et al., 2001), the system stiffness is expected to change upon closure which, in turn, affects the pressure and pressure derivatives (see Fig. 5. 5). Therefore, the change of system stiffness manifests itself in the diagnostic plots and could help to estimate the fracture closure pressure.

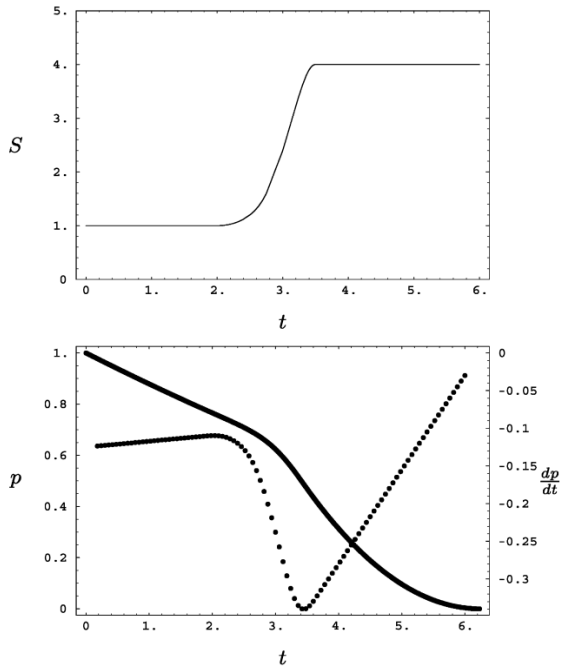

Fig. 5. 5. Assumed time development of system stiffness shown on the top figure and pressure decline and its derivative during fracture closure shown on the bottom figure. Fracture starts to close at 2.5 sec (after Raaen et al., 2001).

In this paper we use a fully coupled 3D simulator to analyze the pressure transient in HF-NF systems where natural fractures and their interaction with the hydraulic fracture are explicitly modeled. The model is first used to shed light on how natural fractures might affect the pressure transient in several complex HF-NF sets. It is then applied to FORGE mini-frac tests to interpret the observed unusual pressure transients.

5. 2. Modelling Strategy

The integrated HF-NF model is applied to investigate fracture pressure transient during shut-in in several examples. The developed model in its current form can handle DFIT problems as it explicitly models fracture closure using contact elements and captures

pressure-dependent leakoff. Considering that leakoff is pressure-dependent and not known in advance, leakoff velocities are required to be calculated and updated within each time step in an iterative scheme. Fan and Economides (1995) proposed a pressure-dependent leakoff model for Frac & Pack treatment in high permeability formations. Assuming a Newtonian fluid (n=1, K'= μ), the fluid flow in the porous medium can be written as:

$$\frac{\partial^2 p}{\partial x^2} = \frac{\mu \phi c_t}{k} \frac{\partial p}{\partial t} \tag{5. 2}$$

Where, μ is the fluid viscosity, ϕ is the porosity, c_t is the system compressibility, k is the permeability. By dividing the reservoir into the invaded (1) and undisturbed (2) zone, the solution to the flow equation is given by Fan and Economides (1995) as follows:

$$p_{frac} - p_0 = \frac{\sqrt{\pi}}{2} \frac{\phi \eta}{k} \left\{ \mu \sqrt{\alpha_1} e^{\left(\frac{\eta}{\sqrt{4\alpha_1}}\right)^2} erf\left(\frac{\eta}{\sqrt{4\alpha_1}}\right) + \mu_r \sqrt{\alpha_2} e^{\left(\frac{\eta}{\sqrt{4\alpha_2}}\right)^2} erfc\left(\frac{\eta}{\sqrt{4\alpha_2}}\right) \right\} \tag{5. 3}$$

Where α_1 and α_2 are the hydraulic diffusivities for the invaded and reservoir zones defined as:

$$\alpha = \frac{k}{\mu \phi c_t} \tag{5. 4}$$

For the cases where the injected and the reservoir fluid are similar (such as in geothermal applications) so that the hydraulic diffusivity of the invaded and reservoir zone, α_1 and α_2 , are the same, the right-hand-side of solution can be simplified (using $erf(u) + erfc(u) = 1$) to yield,

$$p_{frac} - p_0 = \frac{\sqrt{\pi}}{2}\frac{\phi\eta}{k}\left\{\mu\sqrt{\alpha_1}e^{\left(\frac{\eta}{\sqrt{4\alpha_1}}\right)^2}\right\} \tag{5. 5}$$

It should be noted that η is an unknown parameter which should be calculated by solving the pressure equation iteratively. Once η is calculated, the leakoff rate is determined using the following equation,

$$u_L = -\frac{k}{\mu}\frac{dp_1}{dx}\bigg|_{x=0} = -\frac{k}{\mu}\frac{d}{dx}\left(p_{frac} + \frac{\sqrt{\pi}}{2}\left(-\frac{\phi\eta\mu\sqrt{\alpha_1}}{k}e^{\left(\frac{\eta}{\sqrt{4\alpha_1}}\right)^2}\right)erf\left(\frac{x}{\sqrt{4\alpha_1 t}}\right)\right)_{x=0} \tag{5. 6}$$

$$u_L = \frac{\varphi\eta}{2\sqrt{t-\tau}}e^{\frac{\eta^2}{4\alpha_1}} \tag{5. 7}$$

It can be shown that for the simplified case defined by equation 5. 4 the leakoff velocity is:

$$u_L = \frac{C_L(p)}{\sqrt{t-\tau}} \tag{5. 8}$$

Where, the pressure dependent leakoff coefficient is expressed as:

$$C_L(p) = (p - p_0)\sqrt{\frac{k\phi c_t}{\pi\mu}} \tag{5. 9}$$

It is interesting to notice that the leakoff term for this simple case reduced to a form very similar to the Carter's leakoff with a pressure-dependent term.

The pressure decline analysis is mostly conducted using G-function. This function which is essentially a time function is defined as:

$$G(\Delta t_D, \Delta t_D^*) = \frac{4}{\pi}[g(\Delta t_D) - g(\Delta t_D^*)] \tag{5. 10}$$

Where, Δt_D is the dimensionless time since shut-in, and Δt_D^* is a dimensionless reference time which is often selected as zero. The time function $g(\Delta t_D)$ is expressed as follows:

$$g(\Delta t_D) = \frac{4}{3}\left[(1+\Delta t_D)^{\frac{3}{2}} - \Delta t_D^{\frac{3}{2}}\right] \quad (5.\ 11)$$

Where the dimensionless time is defined using the pumping duration, t_p, as follows:

$$\Delta t_D = \frac{t - t_p}{t_p} \quad (5.\ 12)$$

5. 3. Example Applications

A number of simulation examples are provided to highlight some of the primary mechanisms in the fracture closure. The impact of pressure dependent leakoff, change of system stiffness, and natural fracture closure on the closure behavior is studied in the following examples.

5. 3. 1. Change of System Stiffness upon Fracture Closure

The first example in this section concerns the impact of fracture stiffness on the pressure decline during fracture closure. Some studies advocate the stiffness method as a viable technique to determine closure stress. The following example is provided to contrast the closure stress reading from the conventional tangent method and the stiffness approach. The hydraulic fracture used in this example is created using a pumping rate of 1 BPM (2.65×10^{-3} m^3/s) for the duration of 30 seconds. The pressure decline is then monitored during the shut-in period. The simulation parameters are listed in Table 5. 1.

Table 5. 1. Input parameters in the stiffness method example.

parameter	unit	Value

Young's modulus	GPa	37.5
Poisson's ratio	-	0.25
Minimum horizontal stress	MPa	31.0
Pore pressure	MPa	24.0
Mode I stress intensity	$MPa.m^{1/2}$	3.0
Injection rate	m^3/s	0.00265
fluid viscosity	Pa.s	0.001
HF radius	m	10.0
Permeability	μD	10.0
Porosity	-	0.02
Total Compressibility	Pa^{-1}	$2.0x10^{-9}$
HF Normal Stiffness	GPa/m	10.0
Initial Aperture	mm	0.20

Fracture pressure decline and its semi-log derivative, Gdp/dG, are plotted against G-function in Fig. 5. 6. The pressure derivative is used to identify fracture closure and its corresponding pressure. Conventionally, the closure pressure is determined by drawing a tangent line to the Gdp/dG plot. Fracture closure pressure is interpreted as the departure from the linear trend on this plot. The closure pressure reading using the tangent method is approximately 29 MPa as shown on this figure using a black arrow. As an alternative approach, the stiffness method considers the sudden jump in the derivative plot as a sign of change of fracture stiffness and therefore fracture closure. The stiffness approach yields a closure pressure value of approximately 31 MPa (green arrow). It can be observed that the tangent method underestimates the closure pressure by roughly 6%. The system stiffness increases upon closure leading to a higher rate of pressure drop which translates into a sudden increase in Gdp/dG. This is often inferred as the stiffness signature.

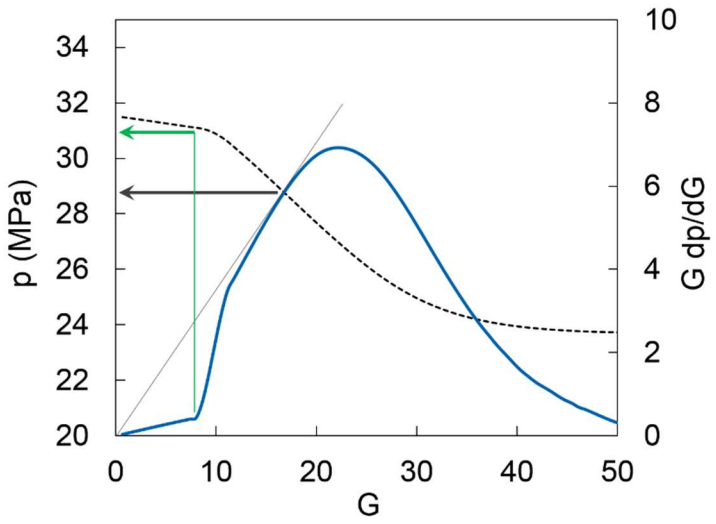

Fig. 5. 6. Closure stress prediction using stiffness method. This plot compares the closure stress reading from the conventional tangent method and the stiffness approach.

A simple pressure derivative plot, dp/dt, is also obtained for this case to compare to a similar plot in Raaen et al. (2001) which was shown in the previous section. Fig. 5. 7 shows the pressure decline (solid) and its derivative (dotted) against shut-in time. It can be observed in this figure that the pressure derivative shows a trend reversal after 0.25 hour of shut-in. The magnitude of the pressure derivative suddenly increases, reaches a maximum and starts to decrease again. This trend reversal, which was also shown in Raaen's work (Fig. 5. 5), is taken as a sign of fracture closure. The early behavior (before sudden reversal) of the pressure derivatives are different. Our example shows a more significant change of pressure derivative before closure as compared to that of Raaen et al. (2001) in Fig. 5. 5 possibly hinting to a stronger pressure dependent leakoff (PDL) behavior. It should be noted that Raaen's work is based on a flow-back test whereas our test is conducted using extended shut-in. This could explain the difference between the pressure derivatives during the pre-closure period.

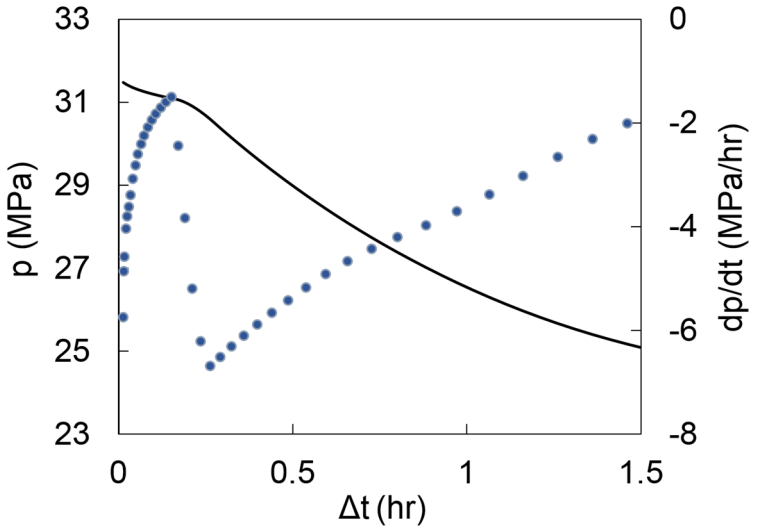

Fig. 5. 7. Pressure and pressure derivative plot vs. the shut-in time. Pressure derivative plot shows a trend reversal indicating fracture closure.

5. 3. 2. The impact of normal stiffness

A sensitivity analysis is conducted on the impact of fracture stiffness on the pressure decline and its G-function derivative. The pressure decline is monitored for three cases with normal stiffness ranging from 8 to 25 GPa/m. Fig. 5. 8 shows the G-function plot for these three cases. It can be observed in this figure a higher normal stiffness results in a higher rate of pressure drop right after fracture closure. Although counterintuitive, the rate of pressure change is higher for stiffer fractures due to the higher changes in the effective normal stress per unit change in the fracture closure ($\Delta(\sigma_n - p) = K_n \Delta D_n$). Additionally, this figure shows that the sudden jump in the Gdp/dG plot is more significant for stiffer fractures. The results indicate that softer fractures tend to have a wider Gdp/dG plot with a lower peak value. The closure pressure for all three cases are equal to 31 MPa using the stiffness signature. However, the tangent method consistently yields lower closure pressure

values. That said, the closure pressure reading using the tangent method is 30.2 MPa (2.5% error) for the stiffest case and 29.5 MPa (4.9% error) for the softest fracture. The closure stress obtained using both methods are actually in good agreement. The results indicate that the tangent method tends to underestimate the closure stress and becomes less accurate for softer fractures. This is, however, under the assumption that the stiffness approach is valid. It is our objective to bring light to this subject through different analyses and comparison with field data. Analysis of the field pressure data and closer examination of the stiffness signature in the following examples helps us to determine the validity of stiffness/compliance method.

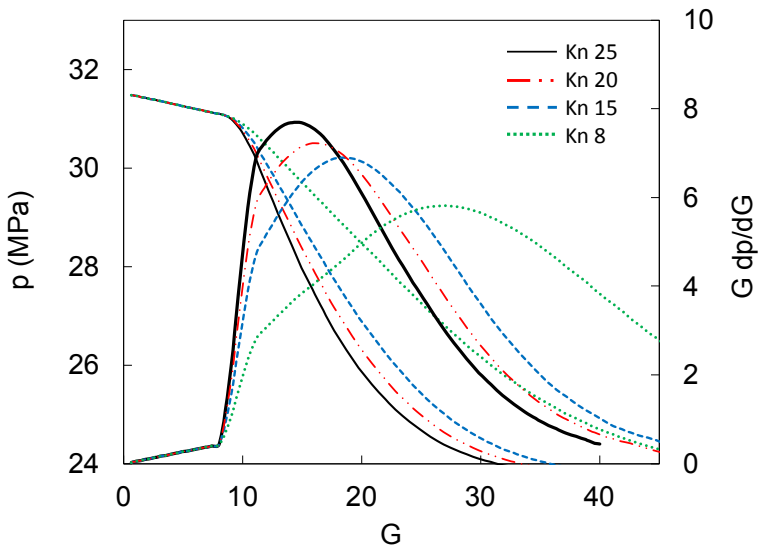

Fig. 5. 8. Comparison between the pressure decline and semi-log derivative of fractures with different normal stiffness.

Fig. 5. 9 shows the pressure derivate dp/dt vs. shut-in time for these cases. It can be observed in this figure that the pressure derivatives are identical during the early stages when the fracture is still open. As the fracture closes, the fracture with highest normal

stiffness shows the highest drop in the pressure derivative. Also, the stiffest fracture attains the lowest pressure derivative of all three cases (largest in magnitude). This is simply because of the higher rate of pressure drop associated with higher fracture stiffness. To explain further, a unit change of fracture closure (or fracture volume) causes a higher change of effective stress and pressure when fracture stiffness is higher. It is interesting to note that second trend reversal (going from minimum pressure derivative back to zero) is also fastest for the fracture with the highest stiffness. This implies that the duration of the pressure decline from closure to the initial reservoir pressure is the shortest for the stiffest fracture.

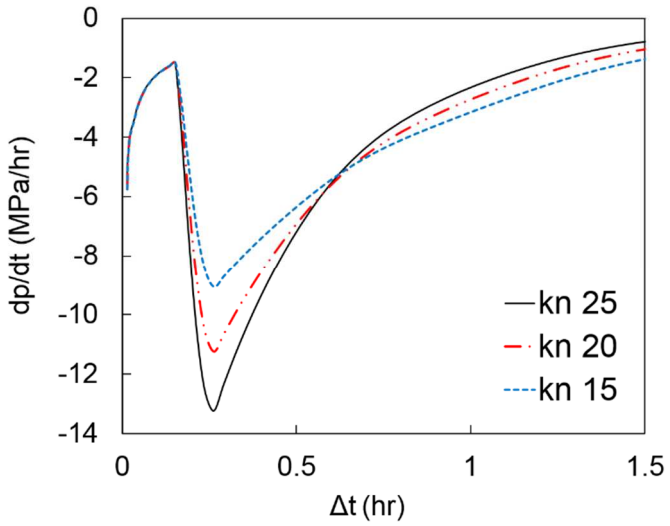

Fig. 5. 9. Pressure derivative plots for fractures with different initial normal stiffness values.

5. 3. 3. The impact of matrix permeability

Matrix permeability is another governing factor in the pressure transient behavior. This parameter controls the rate of leakoff from the fracture to the matrix during shut-in. A

sensitivity analysis is conducted to study the effect of permeability on the pressure decline and its derivative Gdp/dG. In this example, matrix permeability is varied from 5 μD to 20 μD while the fracture stiffness and other input parameters are kept constant. It is important to note that this analysis is conducted on the fractures with the same initial size. Fig. 5. 10 shows the pressure decline and pressure derivative, Gdp/dG, for three matrix permeability values. This figure shows that higher matrix permeabilities results in a higher rate of pressure drop before and after fracture closure (marked by the sudden change of slope on the p vs. G plot). This is due to the higher rate of leakoff from the fracture surface to the matrix when the matrix permeability is higher. The stiffness signature on the derivative plot indicates that fracture closure occurs faster for higher permeability rocks. The closure pressure obtained using the stiffness approach is approximately 31 MPa for all three cases. The tangent method, on the other hand, yields a closure pressure reading of 29 MPa (6.5% error) for all cases. This example shows both methods yields consistent values of closure pressure regardless of the matrix permeability.

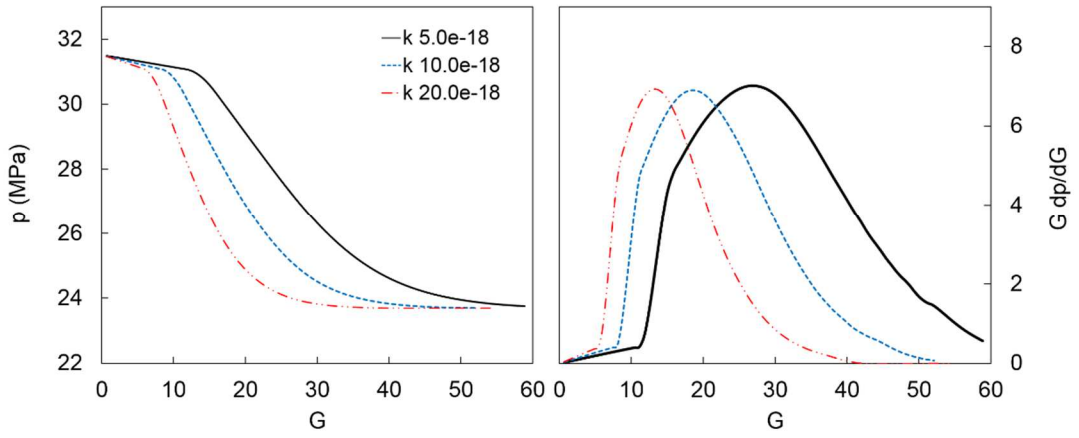

Fig. 5. 10. Pressure decline vs. G (left) and pressure derivative, Gdp/dG, (right) for rocks with different permeabilities.

Fig. 5. 11 shows the pressure derivative plots of this example. The pressure derivative dp/dt shows two trend reversals similar to the previous examples. It should be noticed that the pressure derivative plots differ from one another during the early stages before the first trend reversal. This is in contrast with the previous example where the pressure derivative plots where identical before the first trend change. This is because matrix permeability affects the pressure transient throughout the entire test whereas fracture stiffness impacts the pressure decline only after fracture closure. This figure also shows that higher permeabilities result in a more significant drop in the pressure derivative upon fracture closure (highest in magnitude). After attaining their minima, pressure derivatives show a second trend reversal. It is interesting to note that the pressure derivative approaches zero at a higher rate when the matrix permeability is higher. This is because the fracture pressure drops to the initial reservoir pressure level faster when the matrix permeability is higher.

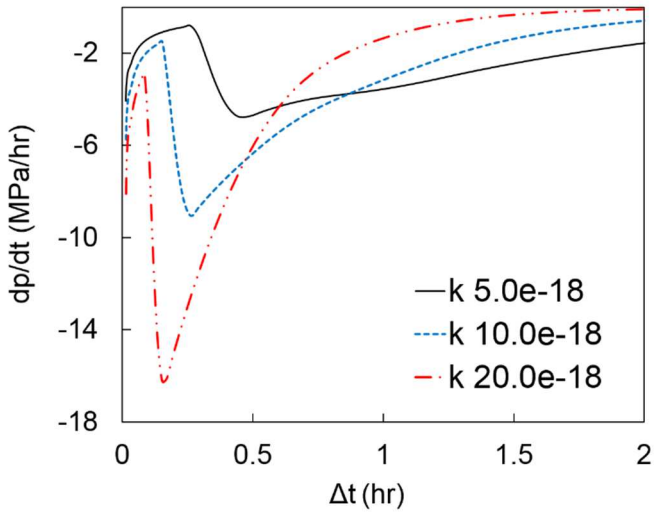

Fig. 5. 11. Pressure derivative profiles during shut-in for different matrix permeability values.

5. 3. 4. Hydraulic fracture intersecting a natural fracture

This example highlights some of the main features of the pressure profile obtained from the HF-NF sets. The hydraulic fracture in this case is assumed to be stationary and connected to one natural fracture via a 60° intersection angle. The test consists of a pumping period of 2.5 minutes at 1.3 L/s followed by a shut-in period. All the simulation parameters and reservoir properties are summarized in Table 5. 2.

Table 5. 2. Input parameters used in the simulation of HF-NF DFIT.

Parameter	Value	Parameter	Value
E (GPa)	50.0	μ (Pa.s)	0.001
ν (-)	0.27	ϕ (-)	0.025
$\sigma_{h\,min}$ (MPa)	31.0	w_0 (mm)	0.1
$\sigma_{H\,max}$ (MPa)	37.9	K_n^{HF} (GPa/m)	24.0
σ_V (MPa)	58.6	K_n^{NF} (GPa/m)	120.0
P_0 (MPa)	23.7	L_{HF} (m)	10.0
k_m (mD)	0.01	L_{NF} (m)	15.0

Fig. 5. 12 shows the fracture opening distribution and the closure status of the hydraulic and natural fractures before and after shut-in. It can be seen in Fig. 5. 12 (a) that the hydraulic fracture has a higher opening compared to the natural fracture as it opens against the minimum horizontal stress. Moreover, the opening is not symmetric and uniform in the natural fracture; the right NF wing has less opening which is due to the stress shadow caused by the hydraulic fracture. This implies that proppant placement is relatively more difficult in the right NF wing unless finer proppants are used (e.g., Kumar et al., 2019). Fig. 5. 12 (b) shows the closure status of the elements 30 minutes after shut-in. It is interesting to note that the right wing closes earlier than the rest of the NF despite being

subjected to the same normal in-situ stress as the rest of the natural fracture. This behavior is due to the higher stress shadow caused by the hydraulic fracture in the sharper corners. This partial closure suggests that the NF closure signature could be less pronounced on the pressure plots.

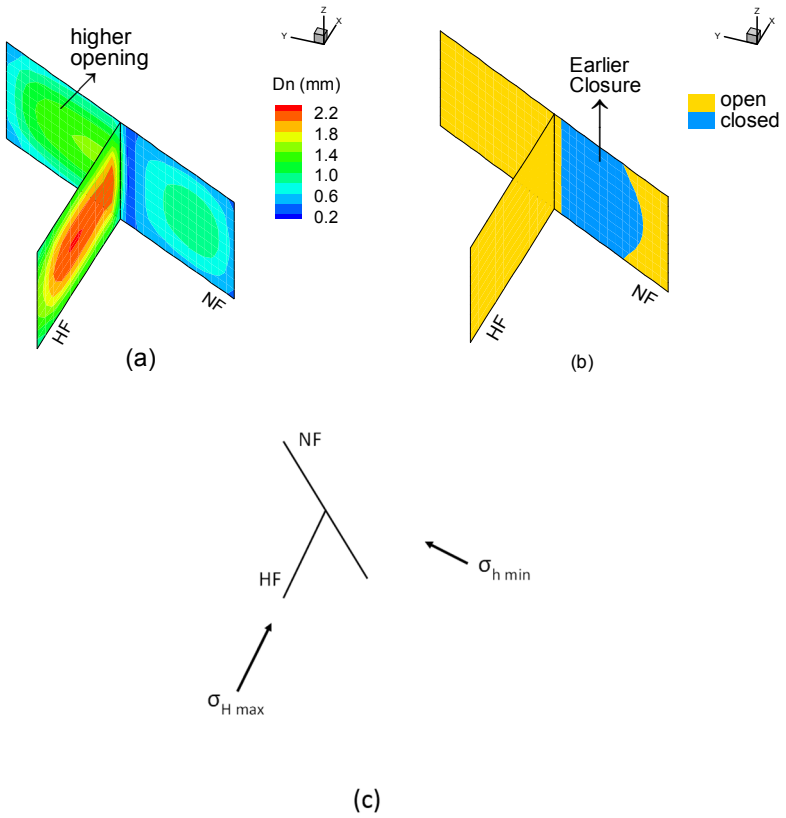

Fig. 5. 12. a) Fracture opening distribution right before shut-in. The stress shadow results in less opening in the right NF wing. b) Closure status after 30 min. shut-in. It can be seen that the right NF wing closes earlier than the left wing due to the stress shadow caused by the HF. The figure on the right shows the top plane-view of the HF-NF set and the in-situ stresses.

The after shut-in pressure profile and the Gdp/dG plots are shown in Fig. 5. 13. The pressure plot shows only one point which could be attributed to the change of system

stiffness between 30 and 35 MPa. Despite having a higher normal stiffness, the NF closure signature is not clearly visible on the pressure profile. This is perhaps because of the gradual closure of the natural fracture as discussed above. It is, however, possible to pick the NF closure signature on the Gdp/dG plot (marked by blue circle). The natural fracture closure is followed by that of the hydraulic fracture (marked by the green circle on Gdp/dG). The closure pressure from the tangent method is also shown on the plot with a black arrow. The tangent method reading is slightly lower than that of the stiffness method but both methods yield reasonably close values for the closure pressure (i.e., 31.0 MPa). A detailed study of the parameters affecting the pressure decline behavior and the diagnostic plots of naturally fractured reservoirs can be found in Kamali and Ghassemi (2019).

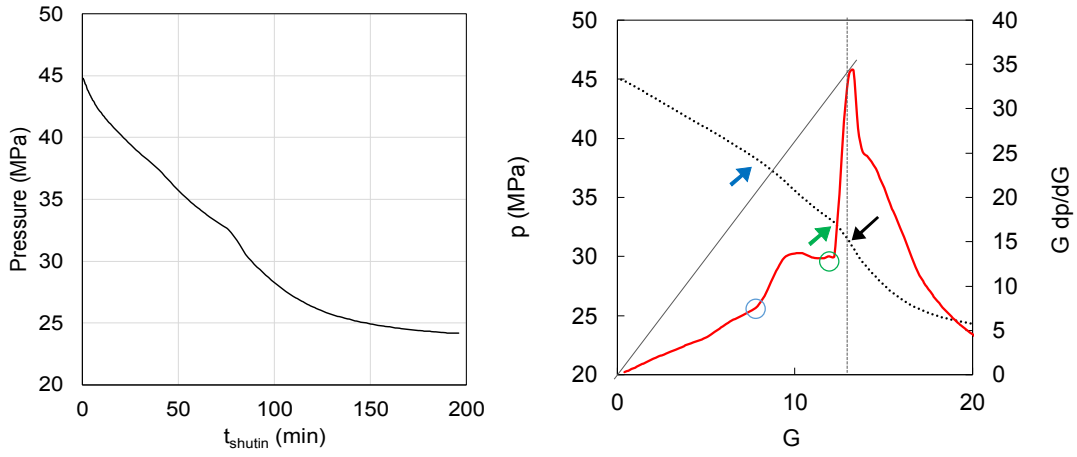

Fig. 5. 13. Pressure profile after shut-in and the Gdp/dG plot for the HF-NF set.

5. 3. 5. Conjugate fracture sets

The analysis of the pressure decline and closure behavior is extended to more complex sets in order to gain a better understanding of fracture closure in naturally fractured rocks. In this example, we study the pressure decline profile and the closure sequence of a network

consisting of a hydraulic fracture intersecting a conjugate natural fracture set. The hydraulic fracture is parallel to the maximum horizontal stress direction and intersects two natural fractures at 60° and 120°, respectively (see Fig. 5. 14-1). Fracture propagation is not considered in the following examples and the HF-NF sets are assumed to be connected from the beginning of the simulation. The minimum and maximum horizontal stresses are 27.6 and 29.6 MPa, respectively. The opening status of the hydraulic and natural fractures is shown in Fig. 5. 14. It can be observed in this figure that all the fractures are fully open prior to the shut-in (Fig. 5. 14-1). It is interesting to note that despite being subjected to the same normal stress, the natural fractures experience partial closure on the wings that make a sharper angle with the hydraulic fracture. This is caused by the stress shadow of the HF on the NFs in those wedges areas. This example shows how the closure process could change due to the interaction between the hydraulic and natural fractures which, in turn, impacts the interpretation of the closure pressure.

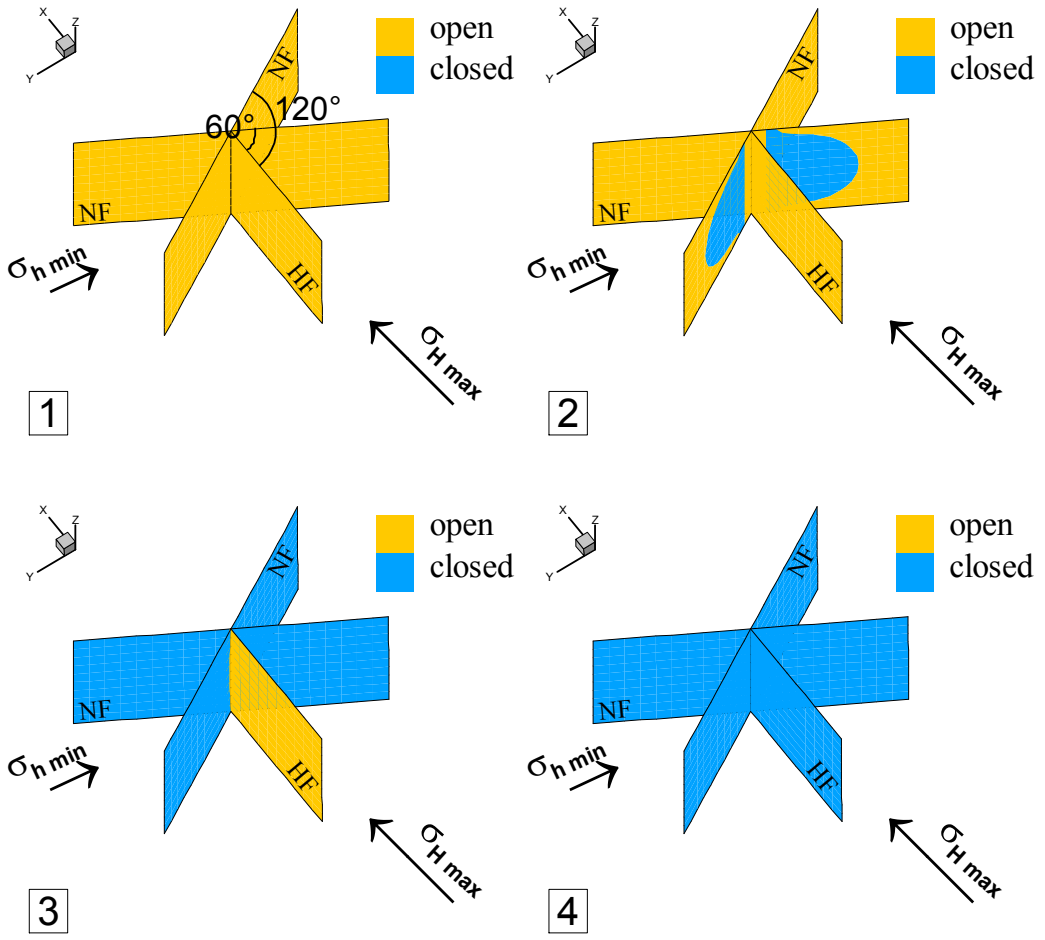

Fig. 5. 14. HF-NF closure sequence for a conjugate set of natural fractures.

Fig. 5. 15 shows the pressure decline and the Gdp/dG for this example. The onset of natural fracture closure is marked by a green circle showing a sudden change of slope in the Gdp/dG plot. Natural fracture closure is then followed by the closure of the hydraulic fracture which is marked by the blue circle on Gdp/dG. The G-function analysis shows two distinct signatures indicating the closure of two or more features. The tangent method is also applied to compare the interpreted closure pressure obtained from this method (26.8 MPa [3900 psi]) and the stiffness/compliance method (~27.9 MPa [4050 psi]). The tangent method often underestimates the closure pressure and hence the net pressure. Using this

pressure could affect the outcome of the stimulation especially when designing for the naturally fractured reservoirs. It has been shown in several studies (Kamali and Ghassemi, 2018; Sesetty and Ghassemi, 2017; Ye et al., 2018) that the stimulation mechanism varies depending on the level of the injection pressure with respect to the minimum in-situ stress.

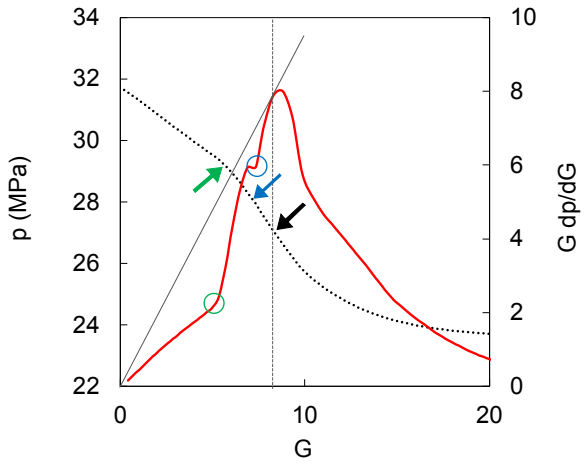

Fig. 5. 15. Pressure profile and Gdp/dG for a hydraulic fracture intersecting a conjugate natural fracture set.

5. 3. 6. Multiple fracture sets

The last simulation example involves a hydraulic fracture intersecting two conjugate natural fracture sets as shown in Fig. 5. 16. The conjugate set's geometry is similar to the previous example, however, the hydraulic fracture is not connected to the center of the natural fractures (their intersection line). Moreover, the conjugate sets are separated by horizontal offsets of 8.5 m and 6.0 m in the *x*- and *y*-directions, respectively.

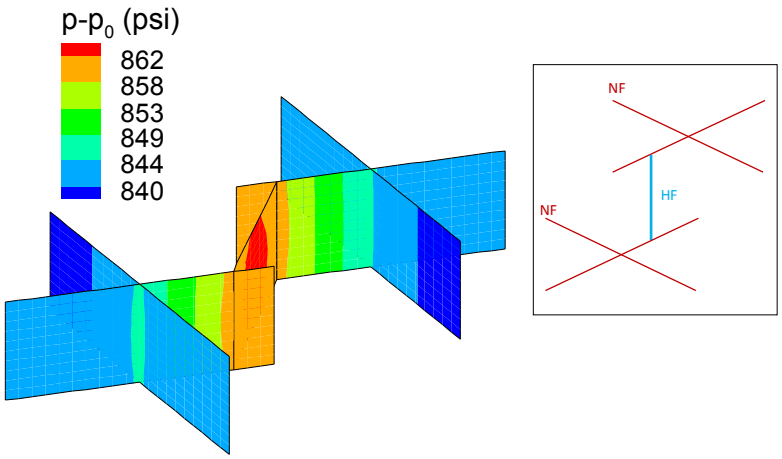

Fig. 5. 16. Pressure distribution before shut-in in a HF-NF system with two conjugate natural fracture sets.

The closure sequence of this HF-NF set is shown in Fig. 5. 17. It can be seen in this figure that the closure behavior is more complicated than the previous examples. The mechanical interaction between the fractures (i.e., stress shadowing) causes additional compression or tension in certain regions which results in a complicated closure trend. This implies that the closure process is more involved than ideally envisioned even for natural fractures under the same normal stress.

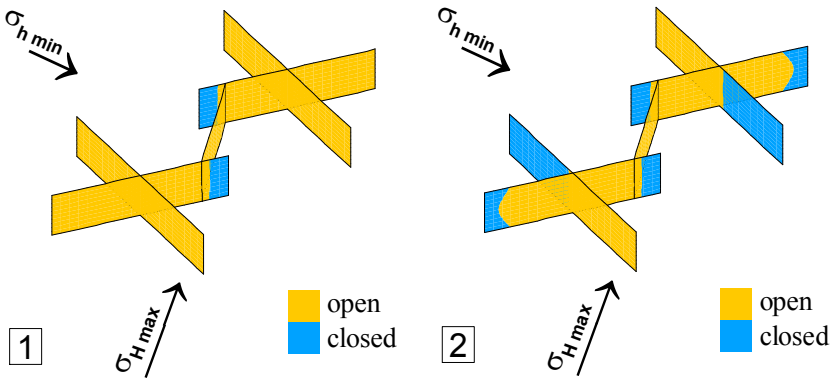

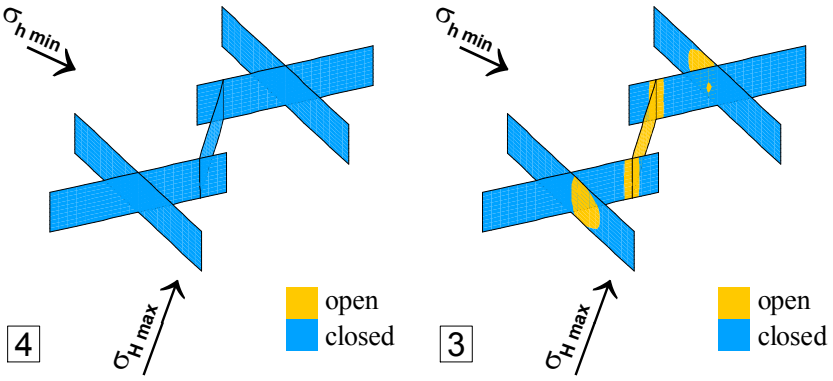

Fig. 5. 17. Closure sequence for a hydraulic fracture intersection two conjugate sets of natural fractures. (1) Shows the opening status before shut-in and (2)-(4) show opening status after shut-in.

The pressure decline and Gdp/dG plots are shown in Fig. 5. 18. Despite the complex behavior of the fracture closure of this system, it can be seen the pressure profile and Gdp/dG show two clear signatures indicating change of the system stiffness: one corresponding to the onset of NF closure and the other for the HF. Although the natural fractures did not close at once and the process was gradual, the closure plot shows only the signature indicating the onset of closure. The second signature corresponds to the closure of the hydraulic fracture (blue circle and arrow). The closure pressure obtained from the stiffness and tangent method are 27.9 MPa (4050 psi) and 27.2 MPa (3950 psi), respectively.

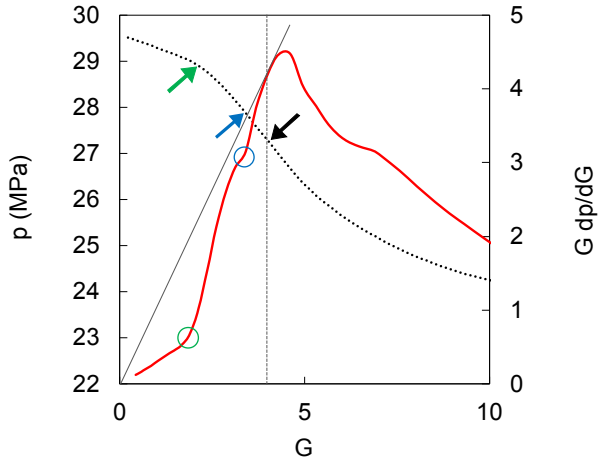

Fig. 5. 18. Pressure profile and Gdp/dG of the HF-NF system with two NF conjugate set. The closure of the hydraulic fracture is marked by the blue circle and arrow. The slop change after G of 6 is where the fracture aperture reaches its residual value and remains unchanged afterwards.

5. 3. 7. FORGE field data

FORGE which stands for "Frontier Observatory for Research in Geothermal Energy" is a department of energy (DOE) project dedicated to advancing technologies in the field of enhanced geothermal systems (EGS) through research, testing, and implementation. This project concerns sustaining a fracture network for an efficient heat exchange between the injected water and the basement rock to facilitate EGS commercialization. The FORGE site covers a 25 km^2 area in the Milford energy corridor in Beaver County, Utah.

A DFIT test has been conducted on the FORGE site along with several injection/fall-off tests to determine the minimum stress, and permeability among other parameters. The DFIT cycle is of interest as it shows a peculiar behavior which challenges the conventional approach to closure stress interpretation. Fig. 5. 19 shows the pressure and its derivative,

Gdp/dG, during the shut-in period. Using the tangent method (tangents are shown as T1, and T2), the closure stress from the first and second hump are 5400 and 4400 psi, respectively. The second closure stress reading is in a better agreement with the results obtained from the other injection tests (Moore et al., 2018). It can be seen in this figure that the G dp/dG plot has two humps, one very early in the test and another less distinct one afterwards. This behavior raises many questions and poses a challenge to the interpretation of the closure pressure. One explanation might be the closure of natural fractures which precedes that of the main hydraulic fracture resulting in an early closure signature (as shown in examples above). However, the Gdp/dG plots obtained from the HF-NF examples above did not show multiple humps that are separated far apart. It is also likely that the closure of the HF is accompanied by the closure of a second NF that is parallel/subparallel to the main HF and orthogonal to the first NF. Nevertheless, the possibility of natural fracture closure cannot be ruled out since different HF-NF configurations have different effects. Therefore, at this time, one can assume that the second hump corresponds to the hydraulic fracture closure because the hydraulic fracture is the last fracture to close as shown previously.

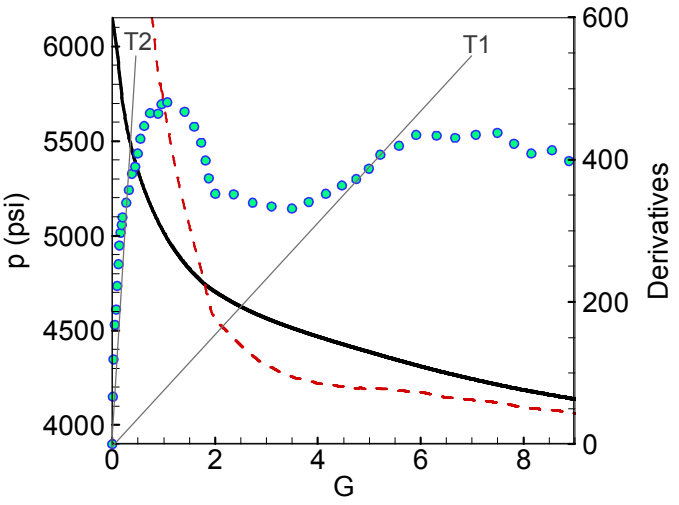

Fig. 5. 19. Pressure and its derivative obtained from a FORGE DFIT test. The semi-log derivative shows two humps indicating multiple closure events possibly due to the closure of natural fractures (data obtained from stress measurement report by Moore et al., 2018).

A stress measurement report by Moore et al. (2018) provides an estimate of the in-situ stresses and pore pressure. The elastic properties such as the Young's modulus and the Poisson's ratio (Fig. 5. 20) are chosen based on the field measurements in the FORGE site. Table 5. 3 summarizes the input parameters used in the field example.

Table 5. 3. Input parameters used in the DFIT analysis.

parameter	Unit	value
measured depth	m [ft]	2265 [7430]
Young's modulus	GPa [Mpsi]	55.2 [8.0]
Poisson's ratio	-	0.25
matrix permeability	m^2 [mD]	$4.0x10^{-17}$ [0.04]
matrix porosity	-	0.025
injected fluid	Pa.s [cP]	0.001 [1.0]
total compressibility	Pa^{-1} [psi^{-1}]	$5.0x10^{-10}$ [$3.45x10^{-6}$]
S_h	MPa [psi]	31.5 [4580]

S_H	MPa [psi]	37.6 [5450]
S_v	MPa [psi]	55.2 [8000]
p_0	MPa [psi]	27.6 [4000]
NF length	m [ft]	45.0 [147.6]
NF height	m [ft]	5.0 [16.4]
Intersection angle	°	90, 60, 45
NF friction angle	°	20
NF cohesion	MPa [psi]	0.0 [0.0]
NF initial aperture	mm [in]	0.20 [7.9×10^{-3}]
NF normal stiffness	GPa/m [Mpsi/in]	40.0 [1.47×10^{-1}]
NF shear stiffness	GPa/m [Mpsi/in]	40.0 [1.47×10^{-1}]
HF normal stiffness	GPa/m [Mpsi/in]	2.0 [7.4×10^{-3}]
HF shear stiffness	GPa/m [Mpsi/in]	2.0 [7.4×10^{-3}]

It is our objective to investigate the impact of natural fractures on the pressure transient of the FORGE and to determine whether the double hump on the G plot could be caused by the presence of natural fractures. Fig. 5. 21 shows a schematic of the problem where a hydraulic fracture intersects a natural fracture at an intersection angle α. Several simulations were carried out by tuning the normal stiffness of the natural and hydraulic fractures and their intersection angle to obtain a reasonable pressure match. The resulting pressure derivative, Gdp/dG, reflects the overall trend shown in the field data by capturing two distinct humps during the test. Matching the derivative was, however, proved almost impossible in our simulation iterations.

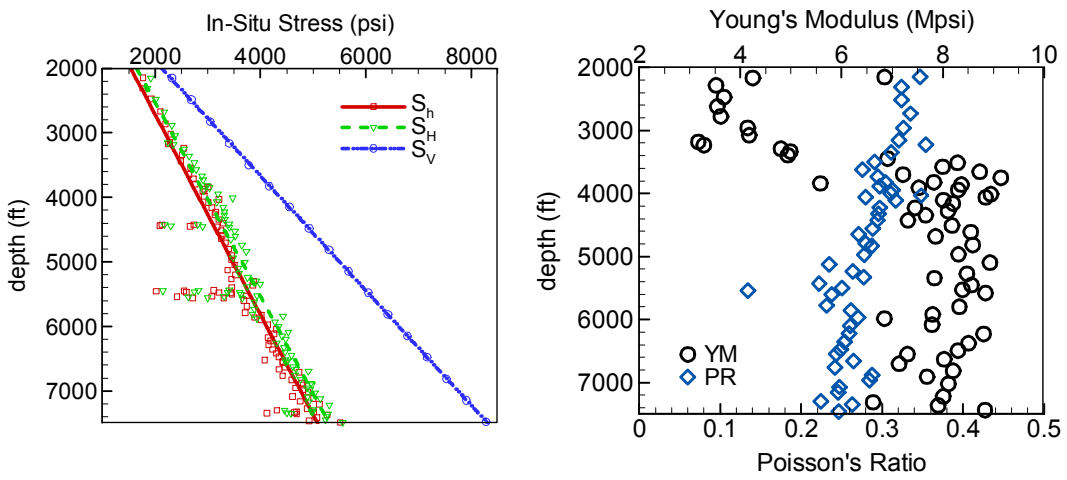

Fig. 5. 20. The variation of the in-situ stresses (Moore et al., 2018) and the elastic properties obtained in the FORGE site.

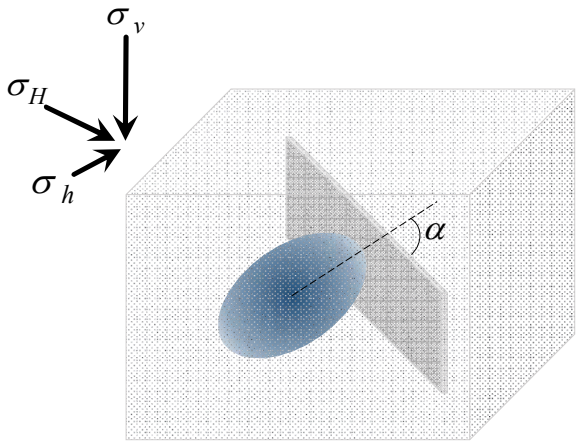

Fig. 5. 21. A schematic showing the hydraulic and natural fractures and the in-situ stresses.

The final matched case involves a hydraulic fracture intersecting a single natural fracture orthogonally. Therefore the natural fracture is initially closed under the maximum horizontal stress. Continuous injection into the HF opens the natural fracture before shut-in. The pump is then shut-in to study the pressure decline and the G function. Fig. 5. 22 shows the pressure profile obtained using our model and the field pressure corresponding

to the FORGE DFIT (cycle 5). The pressure decline curve shows a good agreement with the field data by capturing the magnitude and the trend of the pressure decline throughout the shut-in period. The pressure decline was found to be mainly influenced by the matrix permeability, hydraulic and natural fracture stiffness, and initial reservoir pressure.

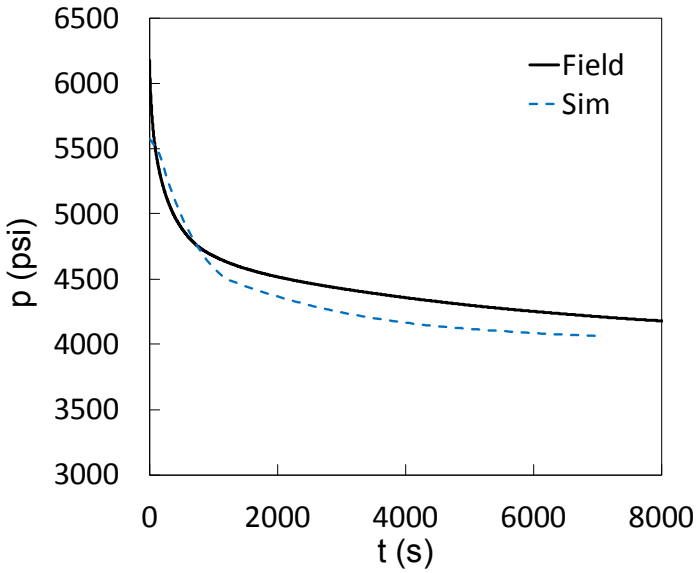

Fig. 5. 22. Field and simulation pressure profiles.

Unlike the pressure profile, it is almost impossible to match the semi-log pressure derivatives (i.e., Gdp/dG) given the strong dependency of such functions on the variations of the pressure. However, the model should reflect the overall Gdp/dG trend assuming that the DFIT is, in fact, influenced by the natural fractures and not any other phenomenon. Fig. 5. 23 shows the Gdp/dG (solid line) for the final simulation case. This figure shows that Gdp/dG consists of two humps; one fully-developed and distinct hump early in the test (like what is observed in the field) and a second hump which is flatter and of a smaller magnitude later in the test. Comparing with the G plot in Fig. 5. 19, it is clear that the trend

obtained from the simulation resembles that of the field data. This confirms that the double hump could in fact be caused by an interacting hydraulic and natural fracture set.

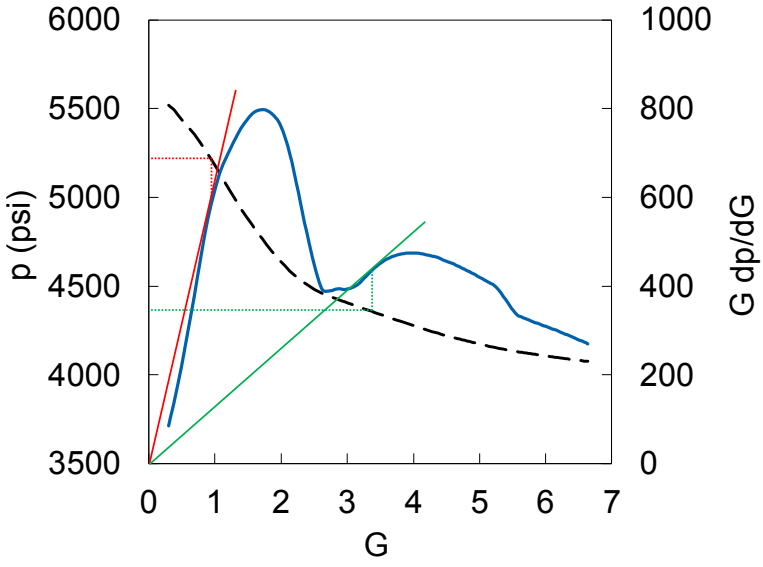

Fig. 5. 23. Pressure (dashed line) and G dp/dG (solid line) for the base case example. The closure stress for the NF and HF using the tangent method is 5200 psi (35.9 MPa) and 4400 psi (30.3 MPa), respectively.

5. 4. Discussion and Summary

A 3D displacement discontinuity model is used to cast light on the pressure transient of hydraulic fractures in the presence of natural fractures. The model is applied to a range of HF-NF sets from simpler geometries to multiple sets of conjugate natural fractures. We focused on the fracture opening distribution, closure sequence, and pressure decline behavior throughout the shut-in period in our analysis. The results indicate that the interaction between hydraulic and natural fractures impact the overall pressure transient. It was shown in the simulations that the stress shadow from the hydraulic fracture generates a non-uniform opening distribution on the natural fracture. The smaller fracture widths in

the area with sharper angles complicate the proppant transport process. Additionally, the compressive stress shadow on certain parts of the natural fractures results in an earlier fracture closure translating into a gradual closure behavior. Our results show that the closure of natural fractures which often precedes that of the HF could result in a signature similar to the ones caused by the change of system stiffness/compliance. Therefore, the system stiffness approached should be should applied properly to avoid misinterpretations.

Chapter 6

Highlights and Recommendations

This dissertation outlined the underlying mechanisms involved in the stimulation of naturally-fractured reservoirs. State-of-the-art simulators were developed and used to study different aspects of reservoir stimulation in naturally-fractured rocks. The model development was broken into stages. First, a 2D elastic model was developed which coupled rock deformation and fluid flow by combining a displacement discontinuity method (DDM) with a finite difference (FD) scheme. Fracture propagation was treated rigorously by using a mixed-mode propagation scheme and enforcing the critical stress intensity criterion. Closed natural fractures were explicitly modeled using contact elements. Mohr-Coulomb criterion was used to determine the contact status of the closed fractures in the transverse direction. Fracture coalescence was also implemented in the model to capture the realistic interaction of natural fractures during stimulation. Shear fracture propagation was incorporated into the model by conducting stress analysis in the vicinity of the kink points. Therefore, the model allows for coexistence of tensile wing-cracks and shear cracks emanating and growing from the same tip.

Several analyses were conducted using the 2D coupled elastic model to investigate the impact of in-situ stress conditions, and elastic properties on the outcome of reservoir stimulation. Our simulation results indicate that wing-cracks can initiate from natural fracture that slip, at injection pressures below the minimum in-situ stress. This implies that, the commonly accepted hydro-shearing concept in EGS cannot exclude wing-crack

propagation. In fact, wing or shear crack formation is a likely scenario when the injection well is in direct contact with the natural fractures. The results show that the stimulation is mostly in the form of wing-crack propagation when natural fractures are shorter whereas dilation is the dominant stimulation mechanism for longer natural fractures. It was found that high differential and low confining stresses are conducive to the formation of wing-cracks. The stimulation results revealed that 5 mm to approximately 1 cm of shear slip is sufficient to initiate wing-cracks in most of our examples where the natural fracture's length was in the range of 5 to 10 m. Our results also indicate that higher confining stresses hinder wing-crack propagation while higher differential stresses promote it. Although, tensile wing-cracks are relatively dominant, shear cracks can also observed in rocks with lower shear strength. A dense array of smaller cracks near the tip of the natural fractures could potentially reduce the rock's shear strength leading to higher chances of shear propagation (a plausible scenario in the Soultz EGS). The propagation of natural fractures in a simple *en echelon* configuration revealed that, fracture coalescence could happen as a result of wing-cracks intersecting with the neighboring fractures. This is, in fact, regarded as a plausible stimulation mechanism in geothermal reservoir.

The 2D elastic model was then extended to account for the poroelastic effects on the stimulation of naturally-fractured rocks. This was accomplished by replacing the elastic DD kernels with a poroelastic displacement discontinuity model. A time-marching algorithm was utilized to capture the transient behavior of poroelastic stresses. The poroelastic DD model was then coupled with our fluid flow model to study the response of natural fracture to injection. The poroelastic model enabled us to study the more likely case of injection into the rock matrix rather than only injection directly into the natural fractures.

Our simulation results indicated that under necessary conditions, wing-crack propagation is an integral part of the reservoir stimulation when there is direct contact between the well and the natural fractures. Some of the conditions include critically-stressed natural fractures that are favorably oriented for shear, lower cohesion and friction angle of the natural fractures to enhance shear slip, tightly-spaced natural fractures that can form a connected network as a result of injection.

By examining the role of poroelasticity through a number sensitivity analysis on reservoir permeability, initial pore pressure, and pumping rate, it has been revealed that lower matrix permeability, higher initial pore pressure, and higher pumping rate promote wing-crack propagation. The simulation results can help further understanding of non-DC seismic events due to simultaneous shear-tensile behavior that is observed along the pre-existing fracture/faults and the wing-cracks. The growing number of micro-seismic and seismic activities near the geothermal sites with earthquake profiles different from that of the double-couple (DC) earthquakes has made researchers to revisit the conventional DC models. Some studies have attributed the non-DC profile to the simultaneous shear and tensile behavior along the faults/fractures. This mechanism, in fact, requires intersecting shear and tensile faults which together can exhibit a simultaneous shear-tensile behavior. This study predicts fracture geometries consisting of tensile segments (wing-cracks) and shear segments (pre-existing fracture). Therefore, the ultimate fracture geometry could show paired shear-tensile behavior confirming the proposed mechanism as one possible explanation of the non-DC events.

The next step in the model development was integrating a natural fracture module with a 3D hydraulic fracture model to study HF-NF interaction in 3D. A 3D natural fracture model

was incorporated into a fully 3D hydraulic fracture simulator based on BEM for rock deformation and FEM for transport processes. A unique and first-of-its-kind HF-NF model was innovated to study hydraulic fracturing in the presence of natural fractures without any major assumptions regarding the type of intersection and geometry. This is in contrast to previous investigations of HF-NF intersection which were limited to 2D, and pseudo-3D models with constant fracture height and simple intersection types. The current model allows for different HF propagation geometries, mechanical and hydraulic interaction with the natural fractures, intersection with natural fractures with any dip angle and strike, different modes of intersection such as arrest, cross, and the engulfing pattern.

The treatment pressure and the potential signatures caused by the HF-NF interaction and coalescence was discussed in details to further the understanding of reservoir stimulation in naturally-fractured reservoirs. The natural fracture intersection was found to be followed by a sudden pressure drop in most cases. Simulations showed that the hydraulic fracture recovers from the pressure drop and continues to propagate as a result of continuous injection. The pressure difference between the approaching HF and the natural fractures in addition to the size of the natural fracture were found to be some of the factors governing the pressure drop upon intersection. The simulation results indicate that the zone of maximum fracture opening is likely to shift away from injection well as a result of intersection with natural fractures leading to non-uniform proppant distributions. Moreover, the results show that the stress shadow from the hydraulic fracture can reduce the natural fracture width near the HF-NF intersection line which could result in proppant bridging and an inefficient stimulation. Fracture propagation was examined under the combined effect of stress barriers and natural fractures. The results show that the hydraulic

fracture conforms to the propagation barriers resulting in complex geometries. Our simulation results indicate that a hydraulic fracture that is partially arrested by a natural fracture can still grow in other directions away from the natural fracture. The 2D analysis of the same problem leads to the conclusion that the approaching HF fully terminates when arrested by a natural fracture.

The key contributions of this study are as follows:

- Development of a fully-coupled displacement discontinuity model used for modelling mixed-mode fracture propagation from closed natural fractures in response to injection.
- Implementation of a robust propagation scheme capable of capturing tensile wing-cracks, shear crack segments, coexistence of wing and shear cracks, and fracture coalescence in a hydro-mechanically coupled simulator.
- Extending the 2D elastic model to account for the role of poroelasticity in the stimulation of naturally-fractured reservoirs. Demonstrating wing-crack propagation is more a likely outcome when injection is directly into the natural fractures. And proving wing-crack propagation and fracture coalescence as a viable stimulation mechanism in EGS, in addition to the formerly known concept of hydro-shearing.
- Extending a fully 3D HF simulator to an integrated 3D HF-NF simulator capable of modelling hydraulic fracture propagation near natural fractures. Complex fracture geometries resulting from fracture crossing, and arresting can be predicted for a wide range of natural fracture dip angles and strikes.

- Demonstrating the injection pressure profiles for several cases of hydraulic and natural fracture intersection with a thorough analysis of the pressure profiles.

The current model can be further improved by:

- Including thermoelastic stresses given the difference between the temperature of the injected fluid and the reservoir particularly in geothermal applications.
- Using structured mesh and same element shapes in both the hydraulic and natural fracture to reduce the difficulties experienced in the implementation of the fracture coalescence in 3D. This, however, limits the application of the 3D HF-NF simulator to only certain fracture geometries.
- Simplifying the HF-NF intersection scheme for extension to the field problems. Major simplifications include using rectangular elements to avoid extra treatment of the elements near the intersection zone which also mitigates the need for constant remeshing upon and after intersection.

References

Aguilera, R.F. (1980). Naturally Fractured Reservoirs. Tulsa, Oklahoma. PennWell Books

Aliabadi, M. H., & Rooke, D. P. (1991). Numerical fracture mechanics (Vol. 8). Springer Science & Business Media

AlDajani OA, Germaine JT, Einstein HH (2018) Hydraulic Fracture of Opalinus Shale under Uniaxial Stress: Experiment Design and Preliminary Results. In 52nd US Rock Mechanics/Geomechanics Symposium. American Rock Mechanics Association

Anderson, G. D. (1981). Effects of friction on hydraulic fracture growth near unbonded interfaces in rocks. Society of Petroleum Engineers Journal, 21(01), 21-29

Asgian, M. (1988). A numerical study of fluid flow in a deformable, naturally fractured reservoir: The influence of pumping rate on reservoir response. Paper presented at the The 29th US Symposium on Rock Mechanics (USRMS).

Ashby, M. F., & Hallam, S. D. (1986). The Failure of Brittle Solids Containing Small Cracks under Compressive Stress States. *Acta Metallurgica, 34*(3), 497-510. doi: Doi 10.1016/0001-6160(86)90086-6

Banerjee, P. K., & Butterfield, R. (1981). Boundary element methods in engineering science (Vol. 17, p. 578). London: McGraw-Hill

Barree, R. D., Mukherjee, H. (1996). Determination of Pressure Dependent Leakoff and Its Effect on Fracture Geometry. Society of Petroleum Engineers. doi:10.2118/36424-MS

Batchelor, G.K. (1967). An introduction to fluid dynamics. Cambridge University Press

Berchenko, I., 1998. "Thermal Loading of Saturated Rock Mass: Field Experiment and Modeling Using Thermoporoelastic Singular Solutions", Ph.D. Dissertation, University of Minnesota

Biot MA (1941) General theory of three-dimensional consolidation. *Journal of Applied Physics*, 12(2), 155-164. doi: 10.1063/1.1712886

Bird RB, Stewart WE, Lightfoot EN (1960) Transport phenomena. 1960. Madison, USA

Blanton, T. L. (1982). An experimental study of interaction between hydraulically induced and pre-existing fractures. In SPE unconventional gas recovery symposium. Society of Petroleum Engineers

Bobet, A., & Einstein, H. H. (1998a). Fracture coalescence in rock-type materials under uniaxial and biaxial compression. *International Journal of Rock Mechanics and Mining Sciences, 35*(7), 863-888. doi: Doi 10.1016/S0148-9062(98)00005-9

Bobet, A., & Einstein, H. H. (1998b). Numerical modeling of fracture coalescence in a model rock material. *International Journal of Fracture, 92*(3), 221-252. doi: Doi 10.1023/A:1007460316400

Bombolakis, E. G. (1973). Study of Brittle-Fracture Process under Uniaxial Compression. *Tectonophysics, 18*(3-4), 231-248. doi: Doi 10.1016/0040-1951(73)90048-6

Brace, W. F., & Bombolakis, E. G. (1963). A Note on Brittle Crack Growth in Compression. *Journal of Geophysical Research, 68*(12), 3709-&. doi: Doi 10.1029/Jz068i012p03709

Castillo, J. L. (1987). Modified Fracture Pressure Decline Analysis Including Pressure-Dependent Leakoff. Society of Petroleum Engineers. doi:10.2118/16417-MS

Carvalho, J. L. (1991). Poroelastic effects and influence of material interfaces on hydraulic fracture behavior. Ph.D. dissertation. University of Toronto

Carter JP, Booker JR (1981) Consolidation due to lateral loading of a pile. In International Conference on Soil Mechanics and Foundation Engineering, 10th, 1981, Stockholm, Sweden (Vol. 2)

Cheng AHD (2016) Poroelasticity (Vol. 27). Berlin: Springer

Chiang, W. T. (1978). Fracture criteria for combined mode cracks. Paper presented at the ICF4, Waterloo (Canada) 1977

Cleary, M. P. (1977). Fundamental solutions for a fluid-saturated porous solid. International Journal of Solids and Structures, 13(9), 785-806

Cleary MP (1980) Analysis of Mechanisms And Procedures For Producing Favorable Shapes Of Hydraulic Fractures. Paper presented at the SPE Annual Technical Conference and Exhibition Dallas, Texas

Cornet, F. H., Berard, T., & Bourouis, S. (2007). How close to failure is a ganite rock mass at a 5 km depth? *International Journal of Rock Mechanics and Mining Sciences, 44*(1), 47-66. doi: 10.1016/j.ijrmms.2006.04.008

Craig, D. P., Eberhard, M. J., Odegard, C. E., Ramurthy, M., Mullen, R. (2002). Permeability, Pore Pressure, and Leakoff-Type Distributions in Rocky Mountain Basins. Society of Petroleum Engineers. doi:10.2118/75717-MS

Crouch, S. L. (1976). Solution of plane elasticity problems by the displacement discontinuity method. I. Infinite body solution. International Journal for Numerical Methods in Engineering, 10(2), 301-343

Crouch, S. L., & Starfield, A. M. (1983). *Boundary Element Methods in Solid Mechanics, with Applications in Rock Mechanics and Geological Engineering*. London: Allen & Unwin

Curran J, Carvalho JL (1987) A Displacement Discontinuity Model For Fluid-saturated Porous Media. Paper presented at the 6th ISRM Congress, Montreal, Canada

Dahi Taleghani, A., & Olson, J. E. (2013). How natural fractures could affect hydraulic-fracture geometry. SPE journal, 19(01), 161-171

Daneshy, A. (1974). Hydraulic fracture propagation in the presence of planes of weakness. In SPE European spring meeting. Society of Petroleum Engineers

Dobroskok, A., Ghassemi, A., & Linkov, A. (2005). Extended structural criterion for numerical simulation of crack propagation and coalescence under compressive loads. *International Journal of Fracture, 133*(3), 223-246. doi: 10.1007/s10704-005-4042-4

Dyskin, A. V., Sahouryeh, E., Jewell, R. J., Joer, H., & Ustinov, K. B. (2003). Influence of shape and locations of initial 3-D cracks on their growth in uniaxial compression. *Engineering Fracture Mechanics, 70*(15), 2115-2136. doi: 10.1016/S0013-7944(02)00240-0

Economides MJ, Nolte KG (2000) Reservoir stimulation (3rd edition). Wiley, New York

Erdogan, F., & Sih, G. C. (1963). On the Crack Extension in Plates Under Plane Loading and Transverse Shear. *Journal of Basic Engineering, 85*(4), 519-525. doi: 10.1115/1.3656897

Evans, K. F. (2005). Permeability creation and damage due to massive fluid injections into granite at 3.5 km at Soultz: 2. Critical stress and fracture strength. *Journal of Geophysical Research: Solid Earth, 110*(B4), n/a-n/a. doi: 10.1029/2004JB003169

Evans, K. F., Genter, A., & Sausse, J. (2005). Permeability creation and damage due to massive fluid injections into granite at 3.5 km at Soultz: 1. Borehole observations. *Journal of Geophysical Research: Solid Earth, 110*(B4), n/a-n/a. doi: 10.1029/2004JB003168

Fairhurst, C., & Cook, N. G. W. (1966). The of Phenomenon of Rock Splitting Parallel to the Direction of Maximum Compression In the Neighbourhood of a Surface. Paper presented at the 1st ISRM Congress

Farmahini-Farahani, M., & Ghassemi, A. (2016). Simulation of micro-seismicity in response to injection/production in large-scale fracture networks using the fast multipole displacement discontinuity method (FMDDM). *Engineering Analysis with Boundary Elements, 71*, 179-189

Foulger GR, Julian BR (2015) Non-Double-Couple Earthquakes. In: Beer M., Kougioumtzoglou I., Patelli E., Au IK. (eds) Encyclopedia of Earthquake Engineering. Springer, Berlin, Heidelberg

Gale, J. F., Reed, R. M., & Holder, J. (2007). Natural fractures in the Barnett Shale and their importance for hydraulic fracture treatments. AAPG bulletin, 91(4), 603-622

Garagash, D. I. (2006). Propagation of a plane-strain hydraulic fracture with a fluid lag: Early-time solution. International journal of solids and structures, 43(18-19), 5811-5835

Ghassemi A, Zhang Q (2006) Poro-thermoelastic response of a stationary crack using the displacement discontinuity method. ASCE J. Engineering Mechanics, 132(1), 26-33

Ghassemi A, Zhou X (2011) A three-dimensional thermo-poroelastic model for fracture response to injection/extraction in enhanced geothermal systems. *Geothermics*, 40(1), pp.39-49

Ghassemi, A., & Roegiers, J. C. (1996). A three-dimensional poroelastic hydraulic fracture simulator using the displacement discontinuity method. Paper presented at the 2nd North American Rock Mech. Symp., Montreal, Quebec, Canada

Ghassemi, A., & Tao, Q. (2016). Thermo-poroelastic effects on reservoir seismicity and permeability change. *Geothermics, 63*, 210-224

Goodman, R. E. (1989). Introduction to rock mechanics. New York: Wiley

Goodman, R. E., Taylor, R. L., & Brekke, T. L. (1968). A model for the mechanics of jointed rocks. *Journal of Soil Mechanics & Foundations Div*.

Gringarten AC (1984) Interpretation of tests in fissured and multilayered reservoirs with double-porosity behavior: theory and practice. *Journal of petroleum technology*, 36(04), pp.549-564

Griffith, A. A. (1921). The Phenomena of Rapture and Flow in Solids. Phil. Trans. Roy. Soc.

Gu, H., Weng, X., Lund, J. B., Mack, M. G., Ganguly, U., & Suarez-Rivera, R. (2012). Hydraulic fracture crossing natural fracture at nonorthogonal angles: a criterion and its validation. SPE Production & Operations, 27(01), 20-26

Guiggiani, M., Krishnasamy, G.., Rudolphi, T. J., & Rizzo, F. J. (1992). A general algorithm for the numerical solution of hypersingular boundary integral equations

Hanson, M., Shaffer, R. J., & Anderson, G. D. (1981). Effects of various parameters on hydraulic fracturing geometry. Society of Petroleum Engineers Journal, 21(04), 435-443

Hoek, E., & Bieniawski, Z. T. (1965). Brittle Fracture Propagation in Rock under Compression. *International Journal of Fracture Mechanics, 1*(3), 137-155

Horii, H., & Nematnasser, S. (1986). Brittle Failure in Compression - Splitting, Faulting and Brittle-Ductile Transition. *Philosophical Transactions of the Royal Society a-Mathematical Physical and Engineering Sciences, 319*(1549), 337-374. doi: DOI 10.1098/rsta.1986.0101

Huang J, Ghassemi A (2015) A poroelastic model for evolution of fractured reservoirs during gas production. J. Pet. Sci. & Engng. 10.1016/j.petrol.2015.10.007

Huang J, Ghassemi A (2017) Poro-viscoelastic modeling of production from shale gas reservoir: An adaptive dual permeability model. J. Pet. Sci. Eng. 158, 336-350

Huang, K., Zhang, Z., & Ghassemi, A. (2013). Modeling three-dimensional hydraulic fracture propagation using virtual multidimensional internal bonds. *International Journal for Numerical and Analytical Methods in Geomechanics, 37*(13), 2021-2038. doi: 10.1002/nag.2119

Hussain, M., Pu, S., & Underwood, J. (1974). Strain energy release rate for a crack under combined mode I and mode II. Paper presented at the Fracture Analysis: Proceedings of the 1973 National Symposium on Fracture Mechanics, Part II

Irgens, F. (2008). Continuum mechanics. Springer Science & Business Media

Irwin, G. R. (1957). Analysis of Stresses and Strains Near the End of a Crack Traversing a Plate. *J. Appl. Mech.* doi: citeulike-article-id:810675

Jeffrey, R. G., Vandamme, L., & Roegiers, J. C. (1987). Mechanical interactions in branched or subparallel hydraulic fractures. In Low Permeability Reservoirs Symposium. Society of Petroleum Engineers

Jung, R. (2013). EGS — Goodbye or Back to the Future. Paper presented at the ISRM International Conference for Effective and Sustainable Hydraulic Fracturing, Brisbane, Australia.

Kachanov, M. (1993). Elastic solids with many cracks and related problems. In Advances in applied mechanics (Vol. 30, pp. 259-445). Elsevier.

Kamali, A., & Ghassemi, A. (2016a). Analysis of Natural Fracture Shear Slip and Propagation in Response to Injection. Paper presented at the 41st Workshop on Geothermal Reservoir Engineering, Stanford, California.

Kamali, A., & Ghassemi, A. (2016b). On the Reservoir Stimulation Mechanisms in Fractured Reservoirs. Paper presented at the 50th U.S. Rock Mechanics/Geomechanics Symposium, Houston, Texas.

Kamali, A., & Ghassemi, A. (2016). Poroelastic Analysis of Natural Fracture Propagation and Coalescence. In Kamali A, Ghassemi A. Poroelastic Analysis of Natural Fracture Propagation and Coalescence. Geothermal Resource Council, 2016 Annual Meeting. Sacramento, California. October 23rd-26th

Kamali A, Ghassemi A (2017) Reservoir Stimulation in Naturally Fractured Poroelastic Rocks. In 51st US Rock Mechanics/Geomechanics Symposium. American Rock Mechanics Association

Kamali A, Ghassemi A (2018) Analysis of Injection-Induced Shear Slip and Fracture Propagation in Geothermal Reservoir Stimulation. *Geothermics*, 76, pp.93-105

Kamali, A. and Ghassemi, A. (2019), January. DFIT Considering Complex Interactions of Hydraulic and Natural Fractures. In SPE Hydraulic Fracturing Technology Conference and Exhibition. Society of Petroleum Engineers

Kamali, A., & Ghassemi, A. (2019). Robust 3D Modeling of Hydraulic Fracture Propagation in Naturally Fractured Reservoirs. In SPE/AAPG/SEG Unconventional Resources Technology Conference. Unconventional Resources Technology Conference

Kamali, A., and Ghassemi, A. (2020). On the Role of Poroelasticity in the Propagation Mode of Natural Fractures in Reservoir Rocks. Rock Mechanics and Rock Engineering, 1-20

Kellogg, O.D. (1929). Foundations of Potential Theory. Berlin Verlag Von Julius Springer.

Koshelev, V., & Ghassemi, A. (2003). Hydraulic fracture propagation near a natural discontinuity. In Proceedings of the 28th Workshop on Geothermal Reservoir Engineering

Kumar, D., & Ghassemi, A. (2016). A three-dimensional analysis of simultaneous and sequential fracturing of horizontal wells. *Journal of Petroleum Science and Engineering, 146*, 1006-1025.

Kumar D, Ghassemi A (2015) 3D simulation of mixed-mode poroelastic fracture propagation for reservoir stimulation. In 39th GRC Annual Meeting, Reno, Nevada (pp. 1-11)

Kumar D, Ghassemi A (2018) Three-Dimensional Poroelastic Modeling of Multiple Hydraulic Fracture Propagation from Horizontal Wells. *International Journal of Rock Mechanics and Mining Sciences*, 105, 192-209

Lamont, N., & Jessen, F. W. (1963). The effects of existing fractures in rocks on the extension of hydraulic fractures. Journal of Petroleum Technology, 15(02), 203-209

Lehner, F., & Kachanov, M. (1996). On modelling of "winged" cracks forming under compression. *International Journal of Fracture, 77*(4), R69-R75. doi: Doi 10.1007/Bf00036257

Lomize,G. M., Flow in Fractured Rocks (1951), 127pp.,Gosenergoizdat, Moscow (In Russian)

Lutz, S. J., Hickman, S., Davatzes, N., Zemach, E., Drakos, P., & Robertson-Tait, A. (2010). Rock mechanical testing and petrologic analysis in support of well stimulation activities at the Desert Peak Geothermal Field, Nevada. Paper presented at the Proceedings 35th Workshop on Geothermal Reservoir Engineering

Mayerhofer, M. J., Economides, M. J. (1997). Fracture-Injection-Test Interpretation: Leakoff Coefficient vs. Permeability. Society of Petroleum Engineers. doi:10.2118/28562-PA

McClintock, F. (1962). Friction on Griffith cracks in rocks under pressure. Paper presented at the Proc. 4th US Nat. Congr. Appl. Mech.

McClure, M. W., Jung, H., Cramer, D. D., Sharma, M. M. (2016). The Fracture-Compliance Method for Picking Closure Pressure from Diagnostic Fracture-Injection Tests (see associated supplementary discussion/reply). Society of Petroleum Engineers. doi:10.2118/179725-PA

Melin, S. (1986). When Does a Crack Grow under Mode-Ii Conditions. *International Journal of Fracture, 30*(2), 103-114

Min, K. S., Zhang, Z., & Ghassemi, A. (2010). Numerical Analysis of Multiple Fracture Propagation In Heterogeneous Rock. Paper presented at the 44th U.S. Rock Mechanics Symposium and 5th U.S.-Canada Rock Salt Lake City, Utah

Moore, J., McLennan, J., Handwerger, D., Finnila, A., and Forbes, B. (2018). In Situ stress Measurements, FORGE Utah Technical Report, Report to Department of Energy, Geothermal Technologies Office

Mukherjee, H., Larkin, S., Kordziel, W. (1991). Extension of Fracture Pressure Decline Curve Analysis to Fissured Formations. Society of Petroleum Engineers. doi:10.2118/21872-MS

Murphy, H., Brown, D., Jung, R., Matsunaga, I., & Parker, R. (1999). Hydraulics and well testing of engineered geothermal reservoirs. *Geothermics, 28*(4-5), 491-506. doi: Doi 10.1016/S0375-6505(99)00025-5

Nelson, R. (2001). Geologic analysis of naturally fractured reservoirs. Elsevier

Nolte, K. G. (1979). Determination of Fracture Parameters from Fracturing Pressure Decline. Society of Petroleum Engineers. doi:10.2118/8341-MS

Petit, J. P., & Barquins, M. (1988). Can Natural Faults Propagate under Mode-Ii Conditions. *Tectonics, 7*(6), 1243-1256. doi: Doi 10.1029/Tc007i006p01243

Pine, R. J., & Batchelor, A. S. (1984). Downward Migration of Shearing in Jointed Rock during Hydraulic Injections. *International Journal of Rock Mechanics and Mining Sciences, 21*(5), 249-263. doi: Doi 10.1016/0148-9062(84)92681-0

Raaen, A. M., Horsrud, P., Kjørholt, H., Økland, D. (2006). Improved routine estimation of the minimum horizontal stress component from extended leak-off tests. International Journal of Rock Mechanics and Mining Sciences, 43(1), 37-4

Raaen, A. M., Skomedal, E., Kjørholt, H., Markestad, P., Økland, D. (2001). Stress determination from hydraulic fracturing tests: the system stiffness approach. International Journal of Rock Mechanics and Mining Sciences, 38(4), 529-541

Renshaw, C. E., & Pollard, D. D. (1995). An experimentally verified criterion for propagation across unbounded frictional interfaces in brittle, linear elastic materials. In International journal of rock mechanics and mining sciences & geomechanics abstracts (Vol. 32, No. 3, pp. 237-249)

Rice JR, Cleary MP (1976) Some Basic Stress Diffusion Solutions for Fluid-Saturated Elastic Porous-Media with Compressible Constituents. *Reviews of Geophysics*, 14(2), 227-241. doi: 10.1029/Rg014i002p00227

Rao, Q. H., Sun, Z. Q., Stephansson, O., Li, C. L., & Stillborg, B. (2003). Shear fracture (Mode II) of brittle rock. *International Journal of Rock Mechanics and Mining Sciences, 40*(3), 355-375. doi: 10.1016/S1365-1609(03)00003-0

Safari, R., & Ghassemi, A. (2015). 3D thermo-poroelastic analysis of fracture network deformation and induced micro-seismicity in enhanced geothermal systems. *Geothermics, 58*, 1-14

Safari, R., & Ghassemi, A. (2016). Three-dimensional poroelastic modeling of injection induced permeability enhancement and microseismicity. *International Journal of Rock Mechanics and Mining Sciences, 84*, 47-58

Salamon, M. D. G. (1964). Elastic Analysis of Displacements and Stresses Induced by the Mining of Seam or Reef Deposits, Part II. Journal of the South African Institute of Mining and Metallurgy, 64(6), 197-218

Sesetty, V., & Ghassemi, A. (2012). Simulation of hydraulic fractures and their interactions with natural fractures. In 46th US Rock Mechanics/Geomechanics Symposium. American Rock Mechanics Association

Sesetty V, Ghassemi A (2017) Complex Fracture Network Model for Stimulation of Unconventional Reservoirs. In 51st US Rock Mechanics/Geomechanics Symposium. American Rock Mechanics Association

Sesetty, V., & Ghassemi, A. (2015). A numerical study of sequential and simultaneous hydraulic fracturing in single and multi-lateral horizontal wells. *Journal of Petroleum Science and Engineering, 132*, 65-76

Sesetty V, Ghassemi A (2018) Effect of rock anisotropy on wellbore stresses and hydraulic fracture propagation. International Journal of Rock Mechanics and Mining Sciences, 112, 369-384

Schettler, P. D., Parmely, C. R., & Lee, W. J. (1989). Gas storage and transport in Devonian shales. SPE Formation Evaluation, 4(03), 371-376

Shen, B., & Stephansson, O. (1994). Modification of the G-Criterion for Crack-Propagation Subjected to Compression. *Engineering Fracture Mechanics, 47*(2), 177-189. doi: Doi 10.1016/0013-7944(94)90219-4

Sneddon IN (1946) The Distribution of Stress in the Neighbourhood of a Crack in an Elastic Solid. Proceedings of the Royal Society of London Series a-Mathematical and Physical Sciences, 187(1009), 229-260. doi: 10.1098/rspa.1946.0077

Steif, P. S. (1984). Crack Extension under Compressive Loading. *Engineering Fracture Mechanics, 20*(3), 463-473. doi: Doi 10.1016/0013-7944(84)90051-1

Stone, T. J., & Babuska, I. (1998). A numerical method with a posteriori error estimation for determining the path taken by a propagating crack. *Computer Methods in Applied Mechanics and Engineering, 160*(3-4), 245-271. doi: Doi 10.1016/S0045-7825(97)00303-4

Tao, Q., Ghassemi, A., & Ehlig-Economides, C. A. (2011). A fully coupled method to model fracture permeability change in naturally fractured reservoirs. *International Journal of Rock Mechanics and Mining Sciences, 48*(2), 259-268

Thiercelin, M., & Makkhyu, E. (2007). Stress field in the vicinity of a natural fault activated by the propagation of an induced hydraulic fracture. In 1st Canada-US Rock Mechanics Symposium. American Rock Mechanics Association

Timoshenko, S. P., & Goodier , J. N. (1970). *Theory of Elasticity* (3rd ed.). New York: McGraw Hill

Vandamme, L. (1986). A three-dimensional displacement discontinuity model for analysis of hydraulically propagated fracture. Ph.D. Dissertation, Dept. Civil Engineering. University of Toronto, Toronto

Vandamme L, Detournay E, Cheng AHD (1989) A Two-Dimensional Poroelastic Displacement Discontinuity Method for Hydraulic Fracture Simulation. *International Journal for Numerical and Analytical Methods in Geomechanics*, 13(2), 215-224. doi: 10.1002/nag.1610130209

Vandamme, L., & Curran, J. (1989). A three-dimensional hydraulic fracturing simulator. *International Journal for Numerical Methods in Engineering, 28*(4), 909-927

Vandamme L, Roegiers JC (1990) Poroelasticity in Hydraulic Fracturing Simulators. *Journal of Petroleum Technology*, 42(9), 1199-1203

Verde, A., & Ghassemi, A. (2015). Modeling injection/extraction in a fracture network with mechanically interacting fractures using an efficient displacement discontinuity method. *International Journal of Rock Mechanics and Mining Sciences, 77*, 278-286

Verruijt A (1969) Elastic storage of aquifers, In: Flow through Porous Media, (ed.) R.J.M. DeWiest, Academic Press, New York, 1969

Warren JE, Root PJ (1963) The Behavior of Naturally Fractured Reservoirs. *Society of Petroleum Engineers Journal*, 3(03), pp.245-255

Warpinski, N. R., & Teufel, L. W. (1987). Influence of Geologic Discontinuities on Hydraulic Fracture Propagation (includes associated papers 17011 and 17074). Society of Petroleum Engineers. doi:10.2118/13224-PA

Witherspoon, P. A., Wang, J. S. Y., Iwai, K., & Gale, J. E. (1980). Validity of Cubic Law for fluid flow in a deformable rock fracture. *Water Resources Research, 16*(6), 1016-1024. doi: 10.1029/WR016i006p01016

Yan, X. (2004). A special crack tip displacement discontinuity element. *Mechanics Research Communications, 31*(6), 651-659

Ye Z, Ghassemi A (2018a) Experimental study on injection-induced fracture propagation and coalescence for EGS stimulation. In Proc., 43rd Workshop on Geothermal Reservoir Engineering. Stanford, CA: Stanford Univ

Ye Z, Ghassemi A (2018b) Injection-induced Fracture Propagation and Coalescence Under Triaxial Loading. In 52nd US Rock Mechanics/Geomechanics Symposium. American Rock Mechanics Association

Ye Z, Ghassemi A, Riley S (2018) Stimulation Mechanisms in Unconventional Reservoirs. In Unconventional Resources Technology Conference, Houston, Texas, 23-25 July 2018 (pp. 3072-3080). Society of Exploration Geophysicists, American Association of Petroleum Geologists, Society of Petroleum Engineers

Zhou, X, Ghassemi A (2011) Three-dimensional poroelastic analysis of a pressurized natural fracture. *International Journal of Rock Mechanics and Mining Sciences*, 48(4), pp.527-534

Zhou, J., & Xue, C. (2011). Experimental investigation of fracture interaction between natural fractures and hydraulic fracture in naturally fractured reservoirs. In SPE Europec/Eage Annual Conference and Exhibition. Society of Petroleum Engineers

Zimmerman, R. W., & Bodvarsson, G. S. (1996). Hydraulic conductivity of rock fractures. *Transport in Porous Media, 23*(1), 1-30. doi: 10.1007/bf00145263

Appendix

Appendix-A

2D Elastic and Poroelastic Stress Kernels:

The shear stress, normal stress and pore pressure induced by a unit continuous fluid source over a DD element of size 2a are summarized below:

$$\sigma_{xx}^{q} = \frac{\alpha\mu(1-2v)}{8\pi k(1-v)}\left\{\left[-(x-x')\left(\frac{1}{\xi^2}-\frac{e^{-\xi^2}}{\xi^2}+E_1(\xi^2)\right)\right]_{-a}^{+a} - 2\int_{-a}^{+a}E_1(\xi^2)dx'\right\} \tag{AP-1}$$

$$\sigma_{yy}^{q} = \frac{\alpha\mu(1-2v)}{8\pi k(1-v)}\left[+(x-x')\left(\frac{1}{\xi^2}-\frac{e^{-\xi^2}}{\xi^2}+E_1(\xi^2)\right)\right]_{-a}^{+a} \tag{AP-2}$$

$$\sigma_{xy}^{q} = \frac{\alpha\mu(1-2v)}{8\pi k(1-v)}\left[-y\left(\frac{1}{\xi^2}-\frac{e^{-\xi^2}}{\xi^2}+E_1(\xi^2)\right)\right]_{-a}^{+a} \tag{AP-3}$$

$$p = \frac{\mu}{4\pi k}\int_{-a}^{+a}E_1(\xi^2)dx' \tag{AP-4}$$

where the exponential integral E_1 and its argument ξ^2 are defined as:

$$E_1(z) = \int_z^{\infty}\frac{e^{-u}}{u}du \tag{AP-5}$$

$$\xi^2 = \frac{r^2}{4ct} = \frac{(x-x')^2+y^2}{4ct} \tag{AP-6}$$

where c is the diffusivity constant.

The shear and normal stresses induced by a unit constant DD of length 2a are summarized below:

$$\sigma_{xx} = 2GD_x(+2f_{,xy}+yf_{,xyy})+2GD_y(f_{,yy}+yf_{,yyy}) \tag{AP-7}$$

$$\sigma_{yy} = 2GD_x(-2f_{,xyy}) + 2GD_y(f_{,yy} - yf_{,yyy}) \tag{AP-8}$$

$$\sigma_{xy} = 2GD_x(f_{,yy} + yf_{,yyy}) + 2GD_y(-yf_{,xyy}) \tag{AP-9}$$

Where function $f(x,y)$ is defined,

$$f(x,y) = \frac{-1}{4\pi(1-\nu)}[y(\arctan\frac{y}{x-a} - \arctan\frac{y}{x+a}) - (x-a)\ln\sqrt{(x-a)^2+y^2} + (x+a)\ln\sqrt{(x+a)^2+y^2}] \tag{AP-10}$$

Second and third derivatives of this function that are used in AP-7 through AP-9 are given as follows:

$$f_{,xx} = -f_{,yy} = \frac{+1}{4\pi(1-\nu)}\left[\frac{x-a}{(x-a)^2+y^2} - \frac{x+a}{(x+a)^2+y^2}\right] \tag{AP-11}$$

$$f_{,xy} = \frac{+1}{4\pi(1-\nu)}\left[\frac{y}{(x-a)^2+y^2} - \frac{y}{(x+a)^2+y^2}\right] \tag{AP-12}$$

$$f_{,xyy} = -f_{,xxx} = \frac{+1}{4\pi(1-\nu)}\left[\frac{(x-a)^2-y^2}{\{(x-a)^2+y^2\}^2} - \frac{(x+a)^2-y^2}{\{(x+a)^2+y^2\}^2}\right] \tag{AP-13}$$

The influence of element *j* on element *i* can be obtained by applying the proper coordinate and stress transformation:

$$\bar{x}_i = (x_i - x_j)\cos\beta_j + (y_i - y_j)\sin\beta_j \tag{AP-14}$$

$$\bar{y}_i = -(x_i - x_j)\sin\beta_j + (y_i - y_j)\cos\beta_j \tag{AP-15}$$

$$\sigma^{i}_{\bar{x}'\bar{x}'} = \sigma^{i}_{\bar{x}\bar{x}}\cos^2(\beta_i - \beta_j) + \sigma^{i}_{\bar{y}\bar{y}}\sin^2(\beta_i - \beta_j) + 2\sigma^{i}_{\bar{x}\bar{y}}\sin(\beta_i - \beta_j)\cos(\beta_i - \beta_j) \tag{AP-16}$$

$$\sigma^{i}_{\bar{y}'\bar{y}'} = \sigma^{i}_{\bar{x}\bar{x}}\sin^2(\beta_i - \beta_j) + \sigma^{i}_{\bar{y}\bar{y}}\cos^2(\beta_i - \beta_j) - 2\sigma^{i}_{\bar{x}\bar{y}}\sin(\beta_i - \beta_j)\cos(\beta_i - \beta_j) \tag{AP-17}$$

$$\overset{i}{\sigma}_{\bar{x}'\bar{y}'} = -(\overset{i}{\sigma}_{\bar{x}\bar{x}} - \overset{i}{\sigma}_{\bar{y}\bar{y}})\sin(\beta_i - \beta_j)\cos(\beta_i - \beta_j) + \overset{i}{\sigma}_{\bar{x}\bar{y}}(\cos^2(\beta_i - \beta_j) - \sin^2(\beta_i - \beta_j)) \quad \text{(AP-18)}$$

Appendix-B

This appendix demonstrates how the coupled equations are solved in each time step in the following flowchart. It should be noted that the fluid intensity source (i.e., diffusion/leakoff) is determined using equation AP-4 in Appendix-A. This term controls the poroelastic stresses and also affect the ratio of the stored to leakoff volume during injection.

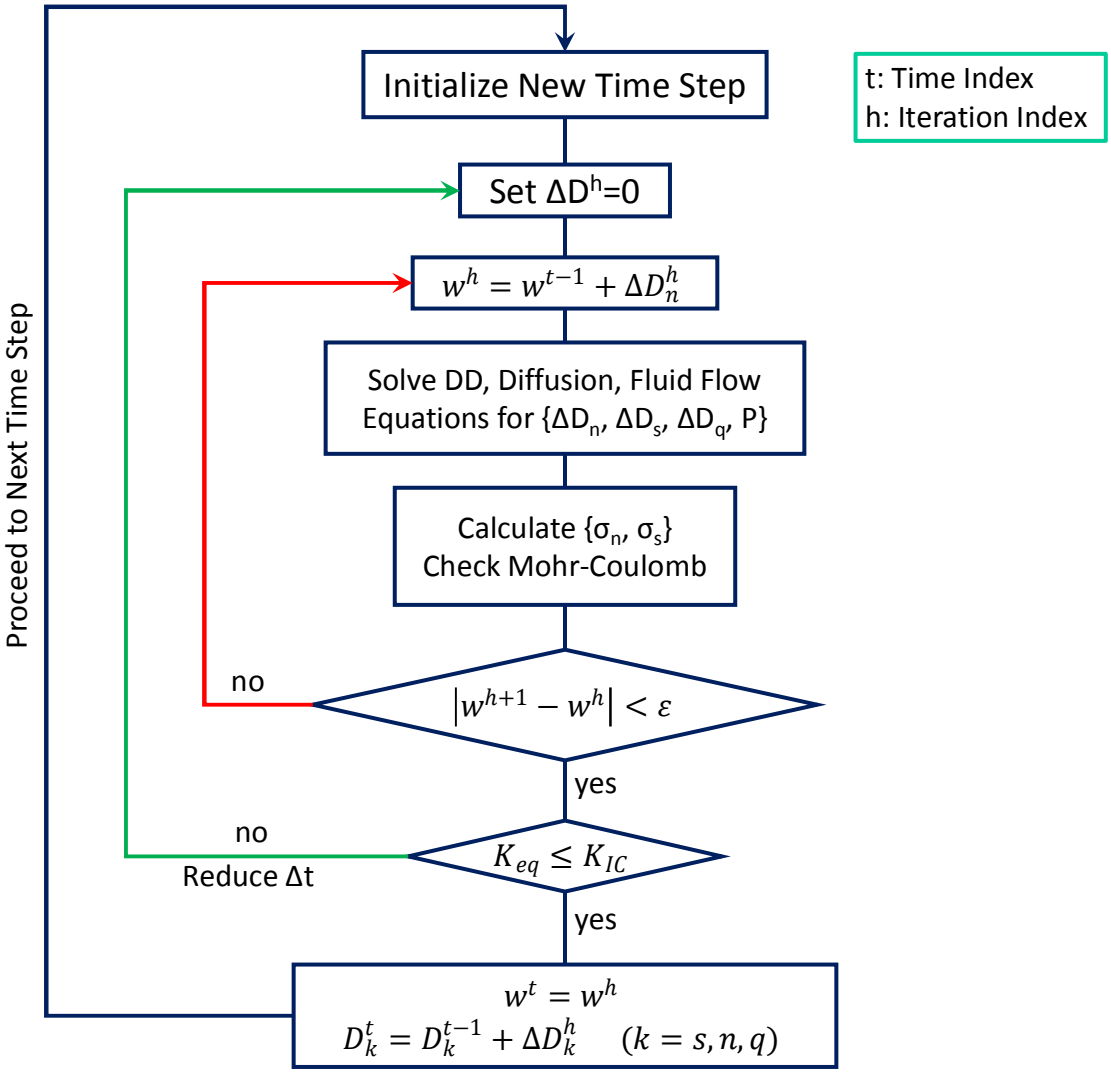

Fig. B1 Simulation flowchart showing the coupling strategy

Appendix-C

The stress fields around a crack in elastic and poroelastic rocks are compared in this appendix. A constant injection rate was applied in both cases. The injection parameters were chosen such that the pre-existing crack does not mechanically open during the injection. The induced normal stresses (i.e., $\Delta\sigma_{xx}$, $\Delta\sigma_{yy}$) at the center of the crack are not significant because the crack remained mechanically closed. The pressure buildup resulted in shear slip and that is why the stress field around the crack resembles that of shear loading and not tensile loading. The stress fields are compared with the stress fields caused by mode II (shear) loading provided by Kachanov (1993).

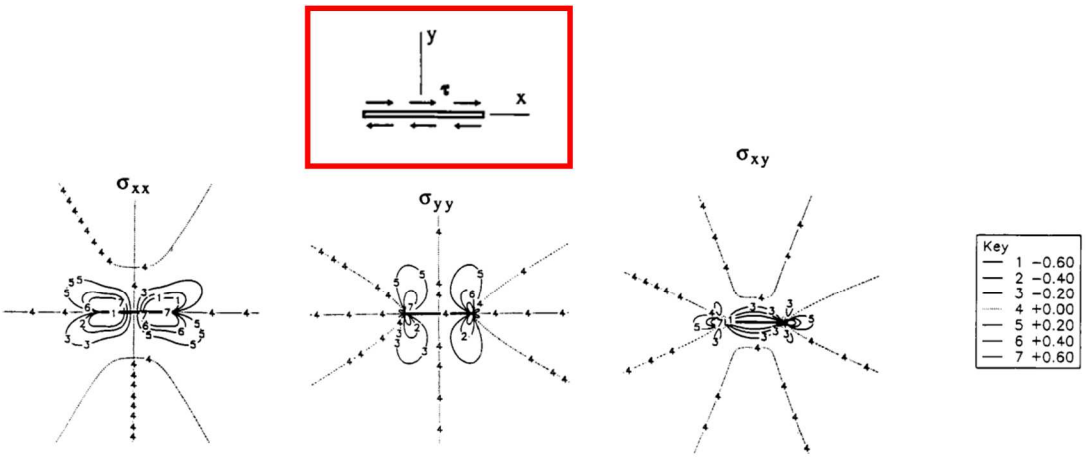

Mode II standard stress field (Kachanov 1993).

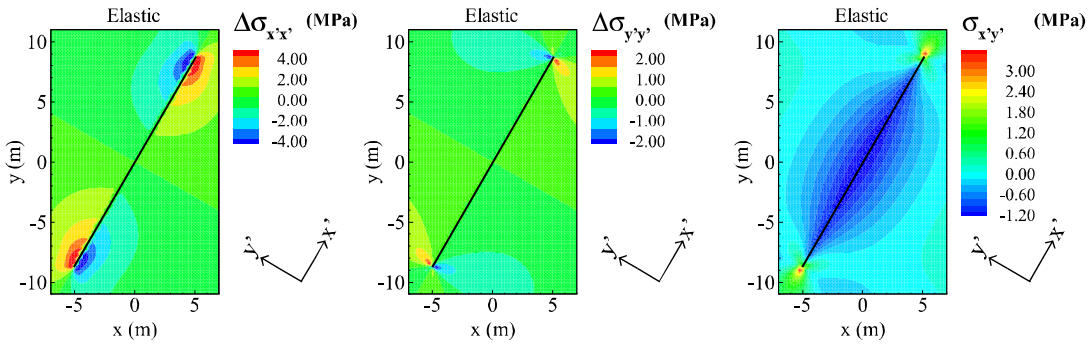

Fig. C1 comparison between the stress fields (top row) caused by mode II loading (Kachanov 1993) and (bottom row) the ones caused by shear slip as a response to injection (this study).

Appendix-D

The following analysis sheds light on the role of the initial pore pressure on the leakoff volume during stimulation. We analyze the impact of the initial reservoir pore pressure on the leakoff volume and the corresponding poroelastic stress acting normal to the natural fracture. Water is injected into a 10 m fracture at a constant rate of 1.0x10-6 m^3/s. The natural fracture is subjected to 10 MPa of compression and the initial pore pressure values are assumed to be 2.0 and 6.0 MPa. The leakoff volume and injection pressure are monitored during 3.50 hours of injection. It should be emphasized that a stationary fracture is used in this problem and fracture propagation is intentionally neglected to simplify the pressure analysis.

It can be observed in the following figures that the leakoff volume is indeed lower when the initial pore pressure is higher (pressure-dependent leakoff). It is interesting to note that the leakoff volumes are initially the same. This is because the leakoff rate is controlled by the pressure difference between the fracture and the matrix. After the injection pressures start to increase at different rates, the leakoff volumes differ from one another. The injection pressures would rise at the same rate if the one with the higher initial pore pressure did not open. The onset of separation in the leakoff volumes are marked by the dashed blue line. It can be seen on the pressure plot that the pressure difference between the matrix and the fracture is 4 MPa (10-6 when Po is 6.0, and 4 i.e., (6-2) when Po is 2.0 MPa) when the leakoff volumes are the same.

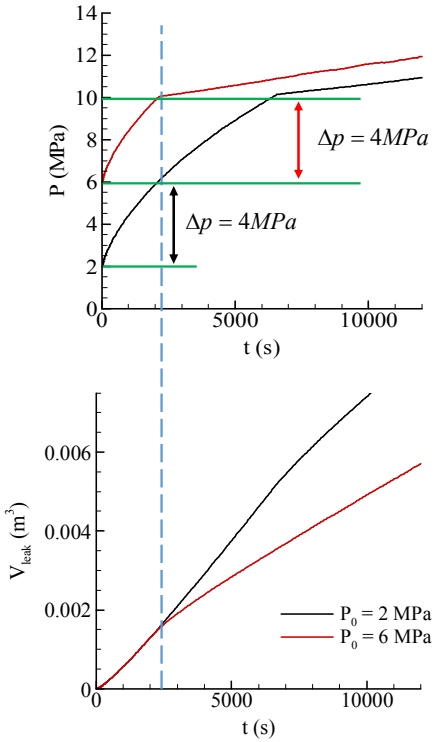

Fig. D1 (top) Injection pressure profile obtained using different initial pore pressures (bottom) comparison between the leakoff volumes

The influence of initial pore pressure on the back-stress is investigated using the fracture opening pressure. This parameter can provide a good measure of the poroelastic stresses. In other words, the natural fracture should ideally open when the pressure is equal to the normal stress in the absence of poroelastic stresses. The following figure shows that the crack opens at a higher pressure when the initial pore pressure is lower. This, in fact, confirms that the back-stress is higher in the example with lower pore pressure. The difference, as pointed out, might be low but it shows the role of diffusion induced stresses.

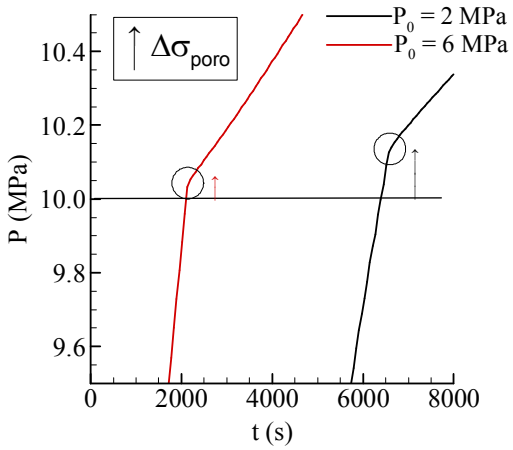

Fig. D2 Comparison between the fracture opening pressure for a crack subject to different initial pore pressure values

Appendix-E

This appendix provides a detailed analysis of the impact of pumping rate on the leakoff and stored volume. It was already shown that the higher pumping rate results in a longer fracture for the same amount of injection. It is interesting to take a closer look at the fracture (stored) volume and the leakoff volume versus the total injected volume. The simulation is stopped once 12 Liters of water is injected using two different rates of 5.0×10^{-6} m^3/s and 2.5×10^{-6} m^3/s. The following plots show that the fracture volume is higher when the fluid is injected at a higher rate. Given the different length of fractures at the end of simulation, the fracture volume is not a true representation of the fracture width. However, the leakoff volume plot clearly indicates that the leakoff volume is higher when the pumping rate is smaller even though the resulting crack is shorter.

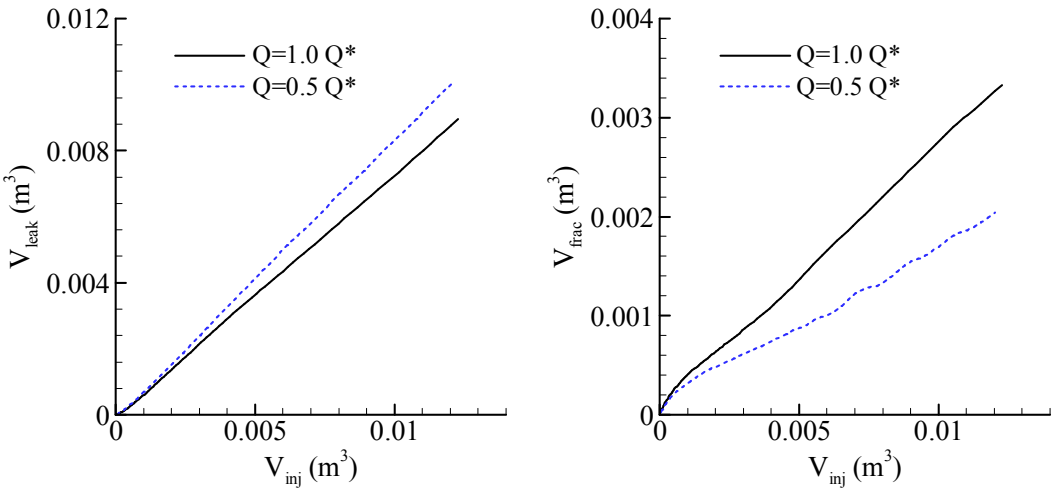

Fig. E1 (left) Comparison between the leakoff volume under different injection rates (right) comparison between the stored fracture volume under different injection rates

To illustrate the impact of the pumping rate on the fracture opening pressure, the injection pressure is plotted against the normal displacement discontinuity. The transition from a

mechanically closed fracture (positive Dn) to mechanically open fracture state (negative Dn) can be used to find the fracture opening pressure. As shown in the following plot, the fracture opens at a relatively higher pressure (~0.15 MPa) when the injection rate is smaller.

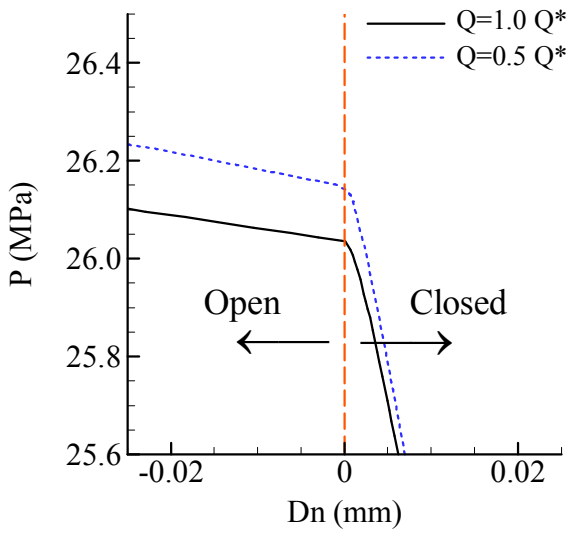

Fig. E2 Injection pressure vs. fracture opening for different injection rates.